DEPARTMENT OF PHYSICS

Experimental study of laser-driven electron and proton acceleration

by

Salima Abuazoum

A thesis presented for the partial fulfilment of the requirements for the degree of Doctor of Philosophy in Physics

2012

Copyright Declaration

Signed:

Date:
December 23, 2012

To my husband, Salim Alfitoryai Salim,

my Mum, Mabroka,

my brothers, Hosin, Mohamed and Ali.

Abstract

This thesis addresses two important topics in the field of laser-driven plasma accelerators. Firstly, the research investigates the generation of relativistic electron beams through laser-wakefield acceleration (LWFA) by applying novel tapered capillary discharge waveguide accelerators, produced by femtosecond laser micromachining. A stable plasma waveguide is formed in a hydrogen-filled capillary driven by an all-solid state high-voltage pulser, specially constructed for this purpose. A longitudinal density taper has been confirmed by measurement of the transverse plasma density profiles at both ends of the waveguide and efficient guiding of low intensity ($\sim 10^{12}$ W/cm^2), ultra-short duration (50 fs) laser pulses is demonstrated.

For optimal high-power laser conditions (intensity of 1.6×10^{18} W/cm^2), electron beams are produced and compared in positively tapered, negatively tapered and straight capillaries with similar plasma densities of 3-6 $\times 10^{18}$ cm^{-3} over a length of 4 cm. In all three capillaries, low charge (<3 pC), low divergence (<4 mrad) monoenergetic electron beams are produced with resolution-limited energy spreads down to 1%. Significantly, an energy enhancement of 22% is obtained in the positive tapered capillary to obtain bunch energies up to 290 MeV, which may arise from the density taper. In addition, the negatively tapered capillary gives the best shot-to-shot pointing stability of the electron beam (mean r.m.s. fluctuation of 1.7 mrad).

Secondly, enhanced yields of protons and ions from laser interactions with solid targets have been investigated. Using a second high power laser system (intensity of $\sim 4 \times 10^{19}$ W/cm^2), hydrogen-doped foils of Au, Cu and Ti have been used as targets to identify the effect of hydrogen implantation on the produced proton beam. From these novel experiments, it has been demonstrated that an enhancement in the proton yield by approximately a factor of 3 is obtained from hydride Au and Cu targets for proton energies of $\sim$3 MeV.

Acknowledgements

My ultimate thanks are to Allah who created me and gave me strength and knowledge.

I would like to express my sincere thanks to everyone who has contributed directly or indirectly to the achievements of this work.

First and foremost, I would like to express my sincere gratitude to my PhD supervisor, Prof. Dino Jaroszynski. His continuous support in addition to his patience and attention to detail has been most valuable during the time of research. I really appreciate the encouragement he has given to me which has brought me up to this point and for that I owe him many thanks. I must also thank him for the host of invaluable opportunities he made available to me, without which this thesis would not have happened.

I would also like to thank so much Dr Mark Wiggins who I was lucky to be his student. During the experiments he was with me day by day and he gave me so many opportunities and he was always there to guide me through them. His dedication and work ethic has been the cornerstone of the many successful experimental campaigns that I had the chance to be involved in. I am grateful to him for his fruitful discussions and helpful assistance during the time of this work. Without his advice, I would never have had the confidence to achieve this.

My particular gratitude also goes to Prof. Ken Ledingham for the support, suggestions and encouragements. He has provided me with much needed confidence and made life with the research more enjoyable.

A special thank goes to Dr Gregory Vieux for his laser guiding expertise, for helpful discussions and for taking the time to sort out issues with the experimental equipment.

I would also like to thank Dr Gregor Welsh for his help and patience during hard days in the lab, to Dr Ranaul Islam and Dr Bernhard Ersfeld for their theoretical advice and to Mr David Clark and Mr Tom McCanny for their technical support.

I would like to express my thanks to all of my colleagues, both past and present members of the Strathclyde Intense Laser Interaction Studies (SILIS) group.

I owe many thanks to my brother: Mohamed Abuazoum for continuous encouragement he has given to me.

I am most indebted to my mama for her prayers and invaluable support for me to finish my study. Also, for my brothers and sisters, many thanks for your support.

Finally, I would to express my deepest gratitude to my husband to whom this thesis is dedicated.

List of publications

1. S. Abuazoum, S. M. Wiggins, B. Ersfeld, K. Hart, G. Vieux, X. Yang, G. H. Welsh, R. C. Issac, M. P. Reijnders, D. R. Jones, and D. A. Jaroszynski**,** *Linearly tapered discharge capillary waveguides as a medium for a laser plasma wakefield accelerator*. Applied Physics Letters, 2012. **100**(1):p. 014106.

2. S. Abuazoum, S. M. Wiggins, R. C. Issac, G. H. Welsh, G. Vieux, M. Ganciu, and D. A. Jaroszynski, *A high voltage pulsed power supply for capillary discharge waveguide applications*. Review of Scientific Instruments, 2011. **82**(6):p. 063505.

3. S. M. Wiggins, M. P. Reijnders, S. Abuazoum, K. Hart, G. Vieux, G. H. Welsh, R. C. Issac, X. Yang, D. R. Jones, and D. A. Jaroszynski, *Straight and linearly tapered capillaries produced by femtosecond laser micromachining*. Journal of Plasma Physics, 2012. **78**(4):p. 355-361.

4. S. M. Wiggins, M. P. Reijnders, S. Abuazoum, K. Hart, G. H. Welsh, R. C. Issac, D. R. Jones, and D. A. Jaroszynski, *Note: femtosecond laser micromachining of straight and linearly tapered capillary discharge waveguides*. Review of Scientific Instruments, 2011. **82**(9): p. 096104.

Contents

List of Figures

List of Tables

CHAPTER 1

Introduction

1.1 High energy particle accelerators

Accelerated elementary particles have a very wide range of applications in science, engineering and medicine. Advances in nuclear and particle physics, and cosmology in particular, depend on reaching ever higher particle energies. Conventional radio frequency (RF) particle accelerators [1] are capable of producing highly energetic bunches of charged particles but there are several limits associated with these accelerators.

RF acceleration is achieved in a transfer of energy from long-wavelength electromagnetic radiation modes in resonant cavities to particles travelling through the cavities. The strength of the electric field that can be maintained in each cavity is limited by surface breakdown, which limits the *maximum accelerating gradient* to typically a few 10s of MV/m (for electrons). High-energy, GeV- and TeV-scale accelerators are enormous and expensive to construct and maintain. The largest accelerator facilities cost billions of euros. One example, the Large Hadron Collider (LHC) is the largest and most powerful particle accelerator in the world. This is located in Geneva, Switzerland, and is designed to observe elusive elementary particles such as the Higgs Boson [2]. The LHC is a proton-proton collider operating at energies up to 7 TeV; for the Higgs particle to be detected, energies of more than 100 GeV are required. As a result, the LHC is a circular accelerator (storage ring) with a circumference of 27 km and its building cost was around $3B.

The next large planned colliders are the International Linear Collider (ILC) and the Compact Linear Collider (CLIC). The ILC, will collide together 500 GeV

or 1 TeV electrons and positrons, and is designed to be 31 km long and will have a projected cost of $6.5B [3]. CLIC would be a 48 km long structure for 3 TeV electron-positron collisions [4]. Despite using the most advanced RF techniques, the accelerating gradients are projected to increase up to only ~100 MeV/m, which would require accelerator lengths to reach these energies. It appears that the large size and cost of conventional accelerators is slowing progress of scientific research and technological applications of high energy particles.

These limitations also apply to advanced third generation light sources, such as synchrotrons and free-electron lasers (FELs), which utilise oscillating high-energy particles to radiate very bright pulses of ultra-violet, soft X-ray and hard X-ray radiation [5]. These sources are used by very large user communities across many areas of science and industry. The U.K. is served by a synchrotron called the Diamond Light Source located at the Harwell Science and Innovation Campus in Oxfordshire. By accelerating electrons to near light-speed, Diamond generates brilliant beams of light from the infra-red to X-rays.

The world's first operational X-ray FEL is the Linac Coherent Light Source (LCLS) at the Stanford Linear Accelerator Center (SLAC), U.S.A. which produces pulses of X-rays more than a billion times brighter than the most powerful alternative sources [6]. It uses a 3 km long linear accelerator (linac) to reach electron energies of up to 50 GeV.

The European XFEL that is currently under construction [7] at DESY in Hamburg, Germany will use a 20 GeV beam which is distributed into several beam lines. This allows the electron beam to be used by several parallel operating experiments.

To reduce the size of these accelerators, a technology capable of much higher accelerating gradients will be required. A promising technique to generate extremely large electric fields to significantly reduce the size of accelerators is the plasma accelerator. In such accelerators electric fields of 100s of GV/m can be sustained and energetic particles can be accelerated to high energies over lengths measured in millimetres.

1.2 Plasma acceleration of relativistic electrons

The field of laser plasma wakefield acceleration (LWFA) was theoretically introduced in the late 1970s by Tajima and Dawson [8]. Plasmas are gases that are already broken down into electrons and ions, therefore, they can sustain arbitrarily high electric fields, typically of the order of 10-1000 GV/m. By focussing a high intensity ($\sim 10^{18}$ W/cm^2), short duration laser pulse through underdense plasma the ponderomotive force of the laser pulse displaces the plasma electrons and establishes electron density oscillations (plasma waves). These density oscillations propagate at the speed of the driving laser pulse and trail behind it as a wake, analogous to the wake of a boat travelling across water. The electrostatic fields of the wakefield are ~1 GeV/cm and can accelerate electrons trapped in the wake to very high energies very rapidly [9-12].

A second type of electron plasma accelerator is the particle-driven wakefield acceleration (PWFA), where the plasma waves are driven by high charge density electron beams, rather than by laser pulses. These plasma waves can be used to accelerate particles to high energies, which have already been experimentally verified [13]. The most notable experimental demonstration was achieved at SLAC in 2007 where a small fraction of a conventional RF accelerated electron bunch at 42 GeV has been accelerated up to 85 GeV after propagating in a 85 cm long PWFA [14]. The average wakefield accelerating gradient of 51 GV/m is much larger than the corresponding gradient of 0.013 GV/m in the RF accelerator. Future developments may also see PWFA applied to high energy proton [15] and positron [16] beam lines since the wakefield technique is not restricted to negatively charged particles.

1.2.1 Development of LWFA for accelerating electrons

To put the work presented in this thesis into perspective, it is necessary to review the history of LWFA. In the early 2000s, the rapid development of laser technology, most notably the development of the chirped pulse amplification (CPA) laser enabled powers of multi-TW levels to be reached, which stimulated rapid development of LWFA systems. Using a single short pulse from a powerful

femtosecond laser (with duration comparable with the plasma oscillation period), plasma waves in the so-called “bubble” regime are excited [17]. In the bubble regime an evacuated cavity free from cold plasma electrons is formed behind the laser pulse. In 2002, 1 J energy and 30 fs duration Ti:sapphire laser pulses were focused into 2×10^{19} cm^{-3} density gas jets to produce the first demonstration of accelerating trapped electrons up to 200 MeV, with 100% energy spread [18].

The big breakthrough experimentally came in 2004 when three groups independently showed that monoenergetic electron beams could be accelerated to an energy over 100 MeV with less than 10% energy spread in gas jets driven by 100 TW-level laser pulses [19-21]. In 2006, the energy gain was increased up to 1 GeV by guiding similar laser pulses inside a 33 mm long gas-filled capillary discharge waveguide [22, 23]. The production of monoenergetic electron beams has been a vital step in the development of the technology because it shows the potential of electron beams with the necessary quality required for applications. Recently, electron beams with low energy spread <1% [24], low transverse emittance $\sim 1\,\pi$ mm mrad [25] and high peak current [24, 26] have been produced.

For optimal LWFA operation, reliable plasma sources are required. High density (10^{17}– 10^{19} cm^{-3}), low temperature (3-5 eV), stable plasmas must be generated by these sources. A common device used to produce such plasma sources is the gas-filled capillary discharge waveguide, which is the main focus of this thesis. By applying a high-voltage electrical pulse of several kV across a capillary (several 10s of mm long) filled with a low atomic number gas, plasma is produced in the capillary. Hydrogen is normally used as the gas medium because it is has an atomic number of 1 and is easily ionised. Hard materials such as alumina are required for the capillary material to be resistant to damage from the high voltage and the high intensity laser pulses.

An alternative to filling the capillary with gas is to produce the plasma from breakdown of the capillary walls that are made of softer materials such as glass or polypropylene ($[CH_2]_n$). These are known as ablative capillary discharges,

which suffer from a shorter lifetime compared to gas-filled capillaries [27, 28]. In LWFA experiments, the hydrogen-filled capillary discharge is an important plasma source to extend the length of the high intensity laser plasma interactions because of the parabolic radial profile of the density that acts as a waveguide [29, 30]. High intensity laser pulses can be efficiently guided over several centimetres thus making them suitable for generating GeV-scale electron energies. Capillaries also allow additional control parameters such as the initial gas pressure or the charging voltage and delay relative to the arrival of the laser pulse, which allows a fine control of the plasma density and channel properties.

The energy gain in homogeneous plasma is limited by dephasing (when electrons out-run the accelerating phase of the wake and enter the decelerating phase of the wake). The method of increasing the dephasing length while maintaining the accelerating gradient by using a longitudinal plasma density gradient (tapering) was originally suggested in the 1980s [31]. Theoretical studies predict a significant energy increase [32, 33]. This thesis presents the first experimental evidence of energy enhancement in a laser wakefield accelerator using a tapered plasma density profile (increasing with distance).

The applications of high quality electron beams produced in LWFA experiments are now being reported. These novel sources, which produce femtosecond duration pulses of high brightness radiation from micron-scale sources, offer a remarkable potential for many applications. One very important application is a LWFA-driven XFEL [34], which would greatly reduce the size of such devices. The first demonstration of undulator radiation generated by LWFA electron beams was reported in 2008 [35] for the visible region of the electromagnetic spectrum and extended to the extreme ultra-violet range in 2009 [36] .

However, to produce stimulated emission in an XFEL, very high quality electron beam properties, such as 0.1% energy spread at high energy (~1 GeV), are required [37]. Energetic electron beams can also be applied to generate gamma-ray radiation for the production of short-lived radioisotopes such as ^{11}C

and ^{18}F which are used in Positron Emission Tomography (PET) scans in hospitals [38]. Another important medical application of laser-accelerated high energy electrons is in radiotherapy, which is introduced in the following section.

1.2.2 LWFA electrons for radiotherapy

Currently, several million patients throughout the world suffer from cancer each year and a significant fraction of them are treated with X-rays of energies of a few MeV [39]. X-rays are used in the majority of cancer radiotherapy treatment and can be conveniently generated using relatively compact and flexible conventional linear accelerators.

One of the most interesting applications of energetic electron beams produced using laser–plasma accelerators is in clinical radiation treatment, either directly or after conversion to ultrashort X-ray pulses. Higher quality and more energetic electron beams, created by laser–plasma accelerators, could be used for radiotherapy to give better clinical results. It has been reported that these beams are well suited to producing a high dose peaked along the propagation axis in a narrow and sharp transverse beam, combined with a deep penetration [40]. Comparison of dose deposition for 250 MeV laser accelerated electrons with that of 6 MeV X-rays showed significant improvement for a clinically approved prostate treatment plan [39].

The feasibility of using laser electron accelerators for radiation and, particularly, their properties for clinical application have been discussed in a study published in 2004 [41]. This study concluded that the present compact terawatt laser accelerators could produce therapeutic electron beams with acceptable pulse flatness, penetration and fall-off depth dose but using laser pulse energies of typically 1 J at 10 Hz repetition rate to deliver the required clinical electron beam dose in a few minutes as required for clinical use.

1.3 Plasma acceleration of ions and protons

The acceleration of ions driven by intense laser-plasma interactions has been studied for more than two decades with proton and ion beams produced with

energies of the order of tens of MeV [42]. To achieve this, high intensity laser pulses are focused onto the front surface of a thin metal foil, i.e., a solid target, in contrast to LWFA electron acceleration that uses gas targets. At the present time, the mechanisms responsible for ion acceleration are the subject of intensive research by several groups around the world. The dominant mechanism for this kind of acceleration at moderate laser intensities (up to 10^{19} W/cm^2) is Target Normal Sheath Acceleration (TNSA)[43], which involves the production of large electrostatic fields by space charge effects when electrons leave the foil target. Ions ejected from the target are rapidly accelerated in these fields. For this reason, a thin (~few microns) and low atomic number target is best suited to accelerate ions and protons by allowing the electrons to easily exit the target and form the fields.

1.3.1 Development of plasma acceleration of ion and proton beams

First measurements of proton beams generated from laser-solid interactions were made in the 1980s by two groups [42, 44]. In these studies, the protons were generated originally from a contaminated layer (hydrocarbon) on the surface of the target. Using picosecond laser pulses with intensities in 10^{18} - 10^{19} W/cm^2, later measurements in the 1990s [45] generated protons of energies with a Maxwellian distribution in the MeV range. More recently [46, 47], multi-MeV protons have been observed using very high laser intensities up to 10^{20} W/cm^2. In these experiments, the targets were metallic foils and the protons originated from contamination layers on the surface of the target.

The need for such high laser intensities has largely restricted experimental progress to a few selected laser facilities around the world, mainly at the Rutherford Appleton Laboratory (RAL) in the U.K., with the VULCAN laser system [48], and the Lawrence Livermore National Laboratory (LLNL) in the U.S.A., with the NOVA laser system [49]. In early 2000, using long pulse lasers on VULCAN with intensities of 5×10^{19} W/cm^2 [50], energetic proton beams were generated with an energy up to 18 MeV. Simultaneously, high power laser

experiments at petawatt levels were performed at LLNL with several hundred Joule pulses with intensities up to 3×10^{20} W/cm^2 incident on solid targets to produce protons with energies up to 55 MeV.

In 2002, collimated carbon ion beams were observed from the rear surface of thin targets up to 100 MeV [51]. In a recent measurement in 2006, the production of monoenergetic protons from microstructured targets was reported [52]. At VULCAN, experimental investigations of low and medium mass ion acceleration from heated thin targets irradiated at intensities up to 5×10^{20} W/cm^2 were reported [53]. It was found that the ions have an energy spectrum up to the several MeV/nucleon. In very recent developments, enhancement of the efficiency of laser-produced proton beams led to 30 MeV beams (few times increase in the maximum energy compared with Au flat-foil targets) [54]. This experiment was performed at the 30-TW Trident facility [55] at the Los Alamos National Laboratory (LANL) using flat-top cone targets.

The 200 TW Trident laser (~80 J, 600 fs) was used to produce the highest proton energies reported to date of ~70 MeV [56]. More recent reports suggest the detection of protons with energies above 100 MeV. This progress in the generation of multi-tens of MeV protons from the interaction of a high intensity laser beam incident on a thin foil make this an exciting area for several potential applications such as fast ignition [57], charged particle radiography [58] and the most promising application to date: proton beam radiation therapy, which is introduced in the following section.

1.3.2 Plasma-accelerated beams for hadron therapy

Hadron therapy is a type of radiotherapy that applies protons, carbon and other heavy ions to irradiate tumours. Protons from conventional accelerators have been used in radiotherapy on approximately 100,000 patients worldwide [59]. From successful clinical results it appears that hadron therapy is a particularly promising method for the treatment of deep tumours [60]. The advantage of proton therapy over the widely used X-ray radiotherapy is the ability to confine the radiation dose to the tumour [61] with the possibility of

stopping the protons at the prescribed depth, so that the healthy tissues located behind the tumour can be spared. Also, the increase of ionisation losses near the so-called Bragg peak result in a considerably raised dose in the tumour compared with that delivered to healthy tissues along the proton path. On the other hand, the dose deposited by an X-ray beam reduces slowly with depth from the surface causing a lot of damage to surrounding healthy cells. The comparison between the relative depth dose distribution for proton and X-ray beams is presented in Fig. 1.1(a).

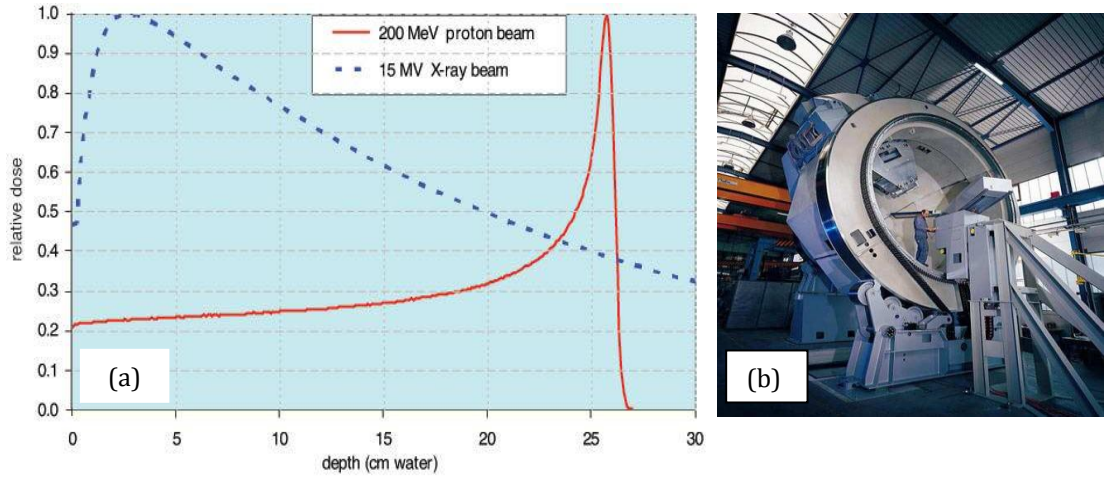

Figure 1.1: (a) Relative depth dose distribution for a 200 MeV proton beam (solid red line) and a 15 MeV X-ray beam (dashed blue line) and (b) a gantry to be used to direct proton beams under construction [62].

Although hadron therapy is considered to be effective, its use is still strongly limited by the large size and high cost of the conventional linacs and synchrotron ion accelerators. Also, the gantries that enable a large variety of tumours to be treated are expensive to build and require a lot of space, as seen in Fig. 1.1(b). With the rapid progress in laser development and research on laser plasma accelerators, many projects aim to greatly reduce the cost and size of proton and hadron accelerators for treatment. Recent studies have investigated the potential of laser-driven hadron therapy [63-65]. These show that several factors make the laser-based accelerator very attractive. These are:

- Its compactness.

- Lower requirement of radiation shielding (thus lowering the cost).
- Large gantries (which are expensive) are no longer required.

The production of proton and ions by laser plasma acceleration, require several conditions to be met before considering this approach for medical applications:

- The proton energy has to be increased to 200 MeV, which requires petawatt class lasers [66, 67].
- At this energy, a flux of about 10^{11} protons s^{-1} is required for treatment [40].
- The accuracy of dose control and addressing quality assurance for patient safety needs to be developed.
- Greater shot-to-shot stability of the laser–plasma accelerator is required.

For hadron therapy, a number of experimental groups are developing laser proton sources up to a few MeV, which are used for biological studies. For example, in a recent study in 2009, the demonstration of DNA double-strand breaking in cancer cells has been reported [68].

1.4 Thesis outline

This thesis presents an experimental investigation of laser-plasma acceleration of two different types of particles. The initial focus of research is on the use of straight and tapered hydrogen-filled capillary discharge plasma waveguides for laser wakefield acceleration of relativistic electrons. These LWFA experiments have been performed at the University of Strathclyde using the Advanced Laser Plasma High-energy Accelerators towards X-rays (ALPHA-X) wakefield accelerator beam line [24], shown in Fig. 1.2. The second study is on the interaction of high-power laser pulses with a thin hydride metal solid target to generate energetic proton and ion pulses. For these experiments, the JETI laser at the Friedrich-Schiller-University in Jena (Fig. 1.3) has been utilised [52].

Figure 1.2: The Advanced Laser Plasma High-Energy Accelerators towards X-rays (ALPHA-X) laser wakefield beam line.

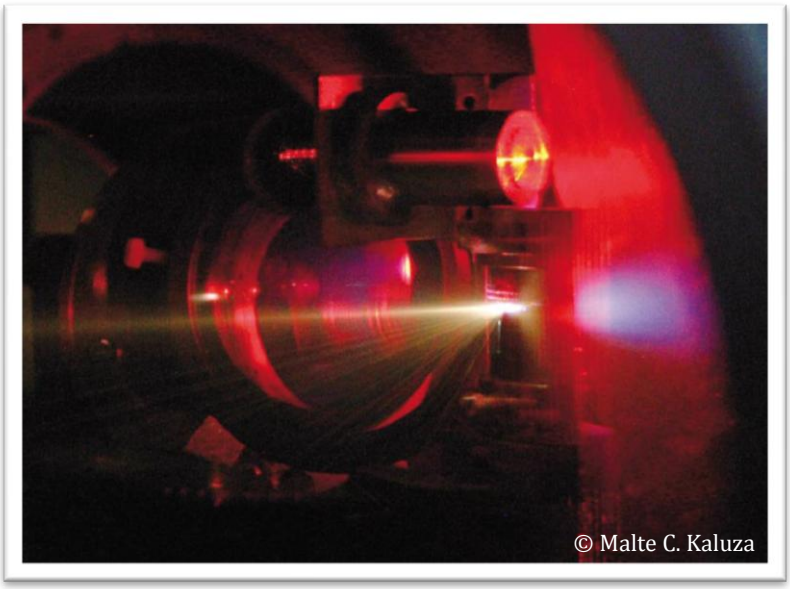

Figure 1.3: The JETI laser pulses are focused onto a thin metal foil from the right, generating plasma. Due to recombination at later times, the plasma radiates in the visible range. Starting from the metal foil, a jet of energetic ions is emitted to the left.

This thesis highlights the first demonstration of acceleration of LWFA electron beams in tapered capillary discharge waveguides and is outlined as follows:

Chapter 2: A brief overview of the general physics of laser-plasma interactions at relativistic laser intensities is given. The basic principle behind LWFA is outlined and the theory that is relevant to the analysis and the experimental results are described. The theoretical background of laser-plasma acceleration of protons and ions is introduced.

Chapter 3: The mechanism for guiding intense laser beams through plasma in a hydrogen-filled capillary discharge waveguide is introduced. A study of straight and tapered hydrogen-filled capillary discharge waveguides, which have been manufactured by a femtosecond laser micromachining technique developed at the University of Strathclyde, is presented. A new design of a high-voltage pulsed power supply for capillary waveguides used in the laser wakefield accelerator experiment is also presented.

Chapter 4: The measurements of the time-integrated plasma density, based on Stark broadening of hydrogen Balmer lines, are presented for both types of capillaries, showing that this diagnostic technique is effective. The results of efficient guiding with high energy transmission of the fundamental Gaussian mode of a low intensity laser pulse for both types of capillary waveguide are presented in this chapter.

Chapter 5: The LWFA experiments carried out on the ALPHA-X beam line at Strathclyde are described in detail. The methods for recording data from the experimental diagnostics are outlined. The results of the experiments for all types of capillary waveguide are presented in full, including both directions of the longitudinal taper, i.e., laser propagating along either an increasing or decreasing plasma density gradient.

Chapter 6: The experiments using the JETI laser at Jena for proton and ion acceleration in laser plasmas using hydride solid targets are detailed. As shown in this chapter, the results are obtained for the first time from hydride gold,

copper and titanium targets and new physics has been extracted from these findings.

Chapter 7: The results of the thesis are summarised and future work is outlined.

References

1. W.K.H. Panofsky and M. Breidenbach, *Accelerators and detectors.* Reviews of Modern Physics, 1999. **71**(2): p. S121-S132.
2. P.W. Higgs, *Broken symmetries, massless particles and gauge fields.* Physics Letters, 1964. **12**(2): p. 132-133.
3. M.C. Ross, N.J. Walker, and A. Yamamoto, *Present status of the ILC project and developments.* Proceedings of IPAC2011, San Sebastián, Spain, 2011. p. 16-20.
4. R. Tomas, *Overview of the Compact Linear Collider.* Physical Review Special Topics - Accelerators and Beams, 2010. **13**(1): p. 014801.
5. J.M.J. Madey, *Stimulated Emission of Bremsstrahlung in a Periodic Magnetic Field.* Journal of Applied Physics, 1971. **42**(5): p. 1906-1913.
6. http://lcls.slac.stanford.edu/aboutlcls.aspx, 06/04/2012.
7. http://xfel.desy.de, 06/04/2012.
8. T. Tajima and J.M. Dawson, *Laser Electron Accelerator.* Physical Review Letters, 1979. **43**(4): p. 267-270.
9. J.M. Dawson, *Nonlinear Electron Oscillations in a Cold Plasma.* Physical Review, 1959. **113**(2): p. 383-387.
10. R.D. Ruth and P. Chen, *Plasma Accelerators*. 1985, SLAC Summer Institute on Particle Physics: Stanford , California.
11. P. Chen, J.J. Su, J.M. Dawson, K.L.F. Bane, and P.B. Wilson, *Energy Transfer in the Plasma Wake-Field Accelerator.* Physical Review Letters, 1986. **56**(12): p. 1252-1255.
12. J.M. Dawson, *Plasma Particle Accelerators.* Scientific American, 1987. **260**(3): p. 54-61.

13. P. Chen, J.M. Dawson, R.W. Huff, and T. Katsouleas, *Acceleration of Electrons by the Interaction of a Bunched Electron Beam with a Plasma.* Physical Review Letters, 1985. **54**(7): p. 693-696.
14. I. Blumenfeld, C.E. Clayton, F.J. Decker, M.J. Hogan, C. Huang, R. Ischebeck, R. Iverson, C. Joshi, T. Katsouleas, N. Kirby, W. Lu, K.A. Marsh, W.B. Mori, P. Muggli, E. Oz, R.H. Siemann, D. Walz, and M. Zhou, *Energy doubling of 42GeV electrons in a metre-scale plasma wakefield accelerator.* Nature, 2007. **445**(7129): p. 741-744.
15. G. Xia, R. Assmann, R.A. Fonseca, C. Huang, W. Mori, L.O. Silva, J. Vieira, F. Zimmermann, and P. Muggli, *A proposed demonstration of an experiment of proton-driven plasma wakefield acceleration based on CERN SPS.* Plasma Physics, 2012. **78**(4): p. 347-353.
16. W.B. Mori, W. An, V.K. Decyk, W. Lu, F.S. Tsung, R.A. Fonseca, S.F. Martins, J. Vieira, L.O. Silva, M. Chen, E. Esarey, C.G.R. Geddes, W.P. Leemans, C.B. Schroeder, J.L. Vay, K. Amyx, D.L. Bruhwiler, J.R. Cary, E. Cormier-Michel, B. Cowan, P. Messmer, C. Huang, and T. Antonsen, *Dream beams: Extreme-scale computing enabling new accelerator technologies for the energy and intensity frontiers.* Proceedings Scientific Discovery through Advanced Computing 201, 2010. **201**: p. 261-276.
17. A. Pukhov and J. Meyer-ter-Vehn, *Laser wake field acceleration: the highly non-linear broken-wave regime.* Applied Physics B: Lasers and Optics, 2002. **74**(4): p. 355-361.
18. V. Malka, S. Fritzler, E. Lefebvre, M.M. Aleonard, F. Burgy, J.P. Chambaret, J.F. Chemin, K. Krushelnick, G. Malka, S.P.D. Mangles, Z. Najmudin, M. Pittman, J.P. Rousseau, J.N. Scheurer, B. Walton, and A.E. Dangor, *Electron Acceleration by a Wake Field Forced by an Intense Ultrashort Laser Pulse.* Science, 2002. **298**(5598): p. 1596-1600.
19. J. Faure, Y. Glinec, A. Pukhov, S. Kiselev, S. Gordienko, E. Lefebvre, J.P. Rousseau, F. Burgy, and V. Malka, *A laser-plasma accelerator producing monoenergetic electron beams.* Nature, 2004. **431**(7008): p. 541-544.

20. C.G.R. Geddes, C. Toth, J. van Tilborg, E. Esarey, C.B. Schroeder, D. Bruhwiler, C. Nieter, J. Cary, and W.P. Leemans, *High-quality electron beams from a laser wakefield accelerator using plasma-channel guiding.* Nature, 2004. **431**(7008): p. 538-541.
21. S.P.D. Mangles, C.D. Murphy, Z. Najmudin, A.G.R. Thomas, J.L. Collier, A.E. Dangor, E.J. Divall, P.S. Foster, J.G. Gallacher, C.J. Hooker, D.A. Jaroszynski, A.J. Langley, W.B. Mori, P.A. Norreys, F.S. Tsung, R. Viskup, B.R. Walton, and K. Krushelnick, *Monoenergetic beams of relativistic electrons from intense laser-plasma interactions.* Nature, 2004. **431**(7008): p. 535-538.
22. W.P. Leemans, B. Nagler, A.J. Gonsalves, C.s. Toth, K. Nakamura, C.G.R. Geddes, E. Esarey, C.B. Schroeder, and S.M. Hooker, *GeV electron beams from a centimetre-scale accelerator.* Nature, 2006. **2**(10): p. 696-699.
23. K. Nakamura, B. Nagler, C. Toth, C.G.R. Geddes, C.B. Schroeder, E. Esarey, W.P. Leemans, A.J. Gonsalves, and S.M. Hooker, *GeV electron beams from a centimeter-scale channel guided laser wakefield accelerator.* Physics of Plasmas, 2007. **14**(5): p. 056708.
24. S.M. Wiggins, R.C. Issac, G.H. Welsh, E. Brunetti, R.P. Shanks, M.P. Anania, S. Cipiccia, G.G. Manahan, C. Aniculaesei, B. Ersfeld, M.R. Islam, R.T.L. Burgess, G. Vieux, W.A. Gillespie, A.M. MacLeod, S. B. van der Geer, M. J. de Loos, and D.A. Jaroszynski, *High quality electron beams from a laser wakefield accelerator.* Plasma Physics and Controlled Fusion, 2010. **52**(12): p. 124032.
25. E. Brunetti, R.P. Shanks, G.G. Manahan, M.R. Islam, B. Ersfeld, M.P. Anania, S. Cipiccia, R.C. Issac, G. Raj, G. Vieux, G.H. Welsh, S.M. Wiggins, and D.A. Jaroszynski, *Low Emittance, High Brilliance Relativistic Electron Beams from a Laser-Plasma Accelerator.* Physical Review Letters, 2010. **105**(21): p. 215007.
26. O. Lundh, J. Lim, C. Rechatin, L. Ammoura, A. Ben-Ismail, X. Davoine, G. Gallot, J.P. Goddet, E. Lefebvre, V. Malka, and J. Faure, *Few femtosecond, few kiloampere electron bunch produced by a laser-plasma accelerator.* Nature, 2011. **7**(3): p. 219-222.

27. Y. Ehrlich, C. Cohen, A. Zigler, J. Krall, P. Sprangle, and E. Esarey, *Guiding of High Intensity Laser Pulses in Straight and Curved Plasma Channel Experiments.* Physical Review Letters, 1996. **77**(20): p. 4186-4189.
28. T. Palchan, D. Kaganovich, P. Sasorov, P. Sprangle, C. Ting, and A. Zigler, *Electron density in low density capillary plasma channel.* Applied Physics Letters, 2007. **90**(6): p. 061501.
29. D.J. Spence and S.M. Hooker, *Investigation of a hydrogen plasma waveguide.* Physical Review E, 2000. **63**(1): p. 015401.
30. A.J. Gonsalves, T.P. Rowlands-Rees, B.H.P. Broks, J.J.A.M. van der Mullen, and S.M. Hooker, *Transverse Interferometry of a Hydrogen-Filled Capillary Discharge Waveguide.* Physical Review Letters, 2007. **98**(2): p. 025002.
31. T. Katsouleas, *Physical mechanisms in the plasma wake-field accelerator.* Physical Review A, 1986. **33**(3): p. 2056-2064.
32. P. Sprangle, J.R. Penano, B. Hafizi, R.F. Hubbard, A. Ting, D.F. Gordon, A. Zigler, and J. T. M. Antonsen, *GeV acceleration in tapered plasma channels.* Physics of Plasmas, 2002. **9**(5): p. 2364-2370.
33. W. Rittershofer, C.B. Schroeder, E. Esarey, F.J. Gruner, and W.P. Leemans, *Tapered plasma channels to phase-lock accelerating and focusing forces in laser-plasma accelerators.* Physics of Plasmas, 2010. **17**(6): p. 063104.
34. W.P. Leemans, E. Esarey, J. van Tilborg, P.A. Michel, C.B. Schroeder, C. Toth, C.G.R. Geddes, and B.A. Shadwick, *Radiation from laser accelerated electron bunches: coherent terahertz and femtosecond X-rays.* IEEE Transactions on Plasma Science, 2005. **33**(1): p. 8-22.
35. H.P. Schlenvoigt, K. Haupt, A. Debus, F. Budde, O. Jackel, S. Pfotenhauer, H. Schwoerer, E. Rohwer, J.G. Gallacher, E. Brunetti, R.P. Shanks, S.M. Wiggins, and D.A. Jaroszynski, *A compact synchrotron radiation source driven by a laser-plasma wakefield accelerator.* Nature, 2008. **4**(2): p. 130-133.
36. M. Fuchs, R. Weingartner, A. Popp, Z. Major, S. Becker, J. Osterhoff, I. Cortrie, B. Zeitler, R. Horlein, G.D. Tsakiris, U. Schramm, T.P. Rowlands-

Rees, S.M. Hooker, D. Habs, F. Krausz, S. Karsch, and F. Gruner, *Laser-driven soft-X-ray undulator source.* Nature, 2009. **5**(11): p. 826-829.

37. F. Gruner, S. Becker, U. Schramm, T. Eichner, M. Fuchs, R. Weingartner, D. Habs, J. Meyer-ter-Vehn, M. Geissler, M. Ferrario, L. Serafini, B. van der Geer, H. Backe, W. Lauth, and S. Reiche, *Design considerations for table-top, laser-based VUV and X-ray free electron lasers.* Applied Physics B: Lasers and Optics, 2007. **86**(3): p. 431-435.
38. K.W.D. Ledingham, P. McKenna, T. McCanny, S. Shimizu, J.M. Yang, L. Robson, J. Zweit, J.M. Gillies, J. Bailey, G.N. Chimon, R.J. Clarke, D. Neely, P.A. Norreys, J.L. Collier, R.P. Singhal, M.S. Wei, S.P.D. Mangles, P. Nilson, K. Krushelnick, and M. Zepf, *High power laser production of short-lived isotopes for positron emission tomography.* Journal of Physics D: Applied Physics, 2004. **37**(16): p. 2341.
39. V. Malka, J. Faure, Y.A. Gauduel, E. Lefebvre, A. Rousse, and K.T. Phuoc, *Principles and applications of compact laser-plasma accelerators.* Nature, 2008. **4**(6): p. 447-453.
40. K.W.D. Ledingham and W. Galster, *Laser-driven particle and photon beams and some applications.* New Journal of Physics, 2010. **12**(4): p. 045005.
41. C. Chiu, M. Fomytskyi, F. Grigsby, F. Raischel, M.C. Downer, and T. Tajima, *Laser electron accelerators for radiation medicine: A feasibility study.* Medical Physics, 2004. **31**(7): p. 2042-2052.
42. S.J. Gitomer, R.D. Jones, F. Begay, A.W. Ehler, J.F. Kephart, and R. Kristal, *Fast ions and hot electrons in the laser-plasma interaction.* Physics of Fluids, 1986. **29**(8): p. 2679-2688.
43. R.A. Snavely, M.H. Key, S.P. Hatchett, T.E. Cowan, M. Roth, T.W. Phillips, M.A. Stoyer, E.A. Henry, T.C. Sangster, M.S. Singh, S.C. Wilks, A. MacKinnon, A. Offenberger, D.M. Pennington, K. Yasuike, A.B. Langdon, B.F. Lasinski, J. Johnson, M.D. Perry, and E.M. Campbell, *Intense High-Energy Proton Beams from Petawatt-Laser Irradiation of Solids.* Physical Review Letters, 2000. **85**(14): p. 2945-2948.

44. Y. Kishimoto, K. Mima, T. Watanabe, and K. Nishikawa, *Analysis of fast-ion velocity distributions in laser plasmas with a truncated Maxwellian velocity distribution of hot electrons.* Physics of Fluids, 1983. **26**(8): p. 2308-2315.

45. F.N. Beg, A.R. Bell, A.E. Dangor, C.N. Danson, A.P. Fews, M.E. Glinsky, B.A. Hammel, P. Lee, P.A. Norreys, and M. Tatarakis, *A study of picosecond laser-solid interactions up to 10^{19} W/cm^2* Physics of Plasmas, 1997. **4**(2): p. 447-457.

46. K. Krushelnick, E.L. Clark, Z. Najmudin, M. Salvati, M.I.K. Santala, M. Tatarakis, A.E. Dangor, V. Malka, D. Neely, R. Allott, and C. Danson, *Multi-MeV Ion Production from High-Intensity Laser Interactions with Underdense Plasmas.* Physical Review Letters, 1999. **83**(4): p. 737-740.

47. M.I.K. Santala, M. Zepf, F.N. Beg, E.L. Clark, A.E. Dangor, K. Krushelnick, M. Tatarakis, I. Watts, K.W.D. Ledingham, T. McCanny, I. Spencer, A.C. Machacek, R. Allott, R.J. Clarke, and P.A. Norreys, *Production of radioactive nuclides by energetic protons generated from intense laser-plasma interactions.* Applied Physics Letters, 2001. **78**(1): p. 19-21.

48. C.N. Danson, P.A. Brummitt, R.J. Clarke, J.L. Collier, B. Fell, A.J. Frackiewicz, S. Hancock, S. Hawkes, C. Hernandez-Gomez, P. Holligan, M.H.R. Hutchinson, A. Kidd, W.J. Lester, I.O. Musgrave, D. Neely, D.R. Neville, P.A. Norreys, D.A. Pepler, C.J. Reason, W. Shaikh, T.B. Winstone, R.W.W. Wyatt, and B.E. Wyborn, *Vulcan Petawatt—an ultra-high-intensity interaction facility.* Nuclear Fusion, 2004. **44**(12): p. S239.

49. S.P. Hatchett, C.G. Brown, T.E. Cowan, E.A. Henry, J.S. Johnson, M.H. Key, J.A. Koch, A.B. Langdon, B.F. Lasinski, R.W. Lee, A.J. Mackinnon, D.M. Pennington, M.D. Perry, T.W. Phillips, M. Roth, T.C. Sangster, M.S. Singh, R.A. Snavely, M.A. Stoyer, S.C. Wilks, and K. Yasuike, *Electron, photon, and ion beams from the relativistic interaction of Petawatt laser pulses with solid targets.* Physics of Plasmas, 2000. **7**(5): p. 2076-2082.

50. E.L. Clark, K. Krushelnick, J.R. Davies, M. Zepf, M. Tatarakis, F.N. Beg, A. Machacek, P.A. Norreys, M.I.K. Santala, I. Watts, and A.E. Dangor,

Measurements of Energetic Proton Transport through Magnetized Plasma from Intense Laser Interactions with Solids. Physical Review Letters, 2000. **84**(4): p. 670-673.

51. M. Hegelich, S. Karsch, G. Pretzler, D. Habs, K. Witte, W. Guenther, M. Allen, A. Blazevic, J. Fuchs, J.C. Gauthier, M. Geissel, P. Audebert, T. Cowan, and M. Roth, *MeV Ion Jets from Short-Pulse-Laser Interaction with Thin Foils.* Physical Review Letters, 2002. **89**(8): p. 085002.
52. H. Schwoerer, S. Pfotenhauer, O. Jackel, K.U. Amthor, B. Liesfeld, W. Ziegler, R. Sauerbrey, K.W.D. Ledingham, and T. Esirkepov, *Laser-plasma acceleration of quasi-monoenergetic protons from microstructured targets.* Nature, 2006. **439**(7075): p. 445-448.
53. P. McKenna, F. Lindau, O. Lundh, D.C. Carroll, R.J. Clarke, K.W.D. Ledingham, T. McCanny, D. Neely, A.P.L. Robinson, L. Robson, P.T. Simpson, C.-G. Wahlström, and M. Zepf, *Low- and medium-mass ion acceleration driven by petawatt laser plasma interactions.* Plasma Physics and Controlled Fusion, 2007. **49**(12B): p. B223.
54. K.A. Flippo, E. d'Humieres, S.A. Gaillard, J. Rassuchine, D.C. Gautier, M. Schollmeier, F. Nurnberg, J.L. Kline, J. Adams, B. Albright, M. Bakeman, K. Harres, R.P. Johnson, G. Korgan, S. Letzring, S. Malekos, N. Renard-LeGalloudec, Y. Sentoku, T. Shimada, M. Roth, T.E. Cowan, J.C. Fernandez, and B.M. Hegelich, *Increased efficiency of short-pulse laser-generated proton beams from novel flat-top cone targets.* Physics of Plasmas, 2008. **15**(5): p. 056709.
55. N.K. Moncur, R.P. Johnson, R.G. Watt, and R.B. Gibson, *Trident: a versatile high-power Nd:glass laser facility for inertial confinement fusion experiments.* Applied Optics, 1995. **34**(21): p. 4274-4283.
56. S.A. Gaillard, K.A. Flippo, M.E. Lowenstern, J.E. Mucino, J.M. Rassuchine, D.C. Gautier, J. Workman, and T.E. Cowan, *Proton acceleration from ultrahigh-intensity short-pulse laser-matter interactions with Cu micro-cone targets at an intrinsic ~10^{-8} contrast.* Journal of Physics: Conference Series, 2010. **244**(2): p. 022034.

57. M. Roth, T.E. Cowan, M.H. Key, S.P. Hatchett, C. Brown, W. Fountain, J. Johnson, D.M. Pennington, R.A. Snavely, S.C. Wilks, K. Yasuike, H. Ruhl, F. Pegoraro, S.V. Bulanov, E.M. Campbell, M.D. Perry, and H. Powell, *Fast Ignition by Intense Laser-Accelerated Proton Beams.* Physical Review Letters, 2001. **86**(3): p. 436-439.
58. M. Borghesi, D.H. Campbell, A. Schiavi, M.G. Haines, O. Willi, A.J. MacKinnon, P. Patel, L.A. Gizzi, M. Galimberti, R.J. Clarke, F. Pegoraro, H. Ruhl, and S. Bulanov, *Electric field detection in laser-plasma interaction experiments via the proton imaging technique.* Physics of Plasmas, 2002. **9**(5): p. 2214-2220.
59. http://ptcog.web.psi.ch, 10/04/2012.
60. Y.E. Dubrova, M. Plumb, B. Gutierrez, E. Boulton, and A.J. Jeffreys, *Genome stability: Transgenerational mutation by radiation.* Nature, 2002. **405**(6782): p. 37-40.
61. R.R. Wilson, *Radiological Use of Fast Protons.* Radiology, 1946. **47**(5): p. 487-491.
62. Varian Medical Systems. Palo Alto. California.
63. S.V. Bulanov, T.Z. Esirkepov, V.S. Khoroshkov, A.V. Kuznetsov, and F. Pegoraro, *Oncological hadrontherapy with laser ion accelerators.* Physics Letters A, 2002. **299**(2): p. 240-247.
64. S.V. Bulanov, H. Daido, T.Z. Esirkepov, V.S. Khoroshkov, J. Koga, K. Nishihara, F. Pegoraro, T. Tajima, and M. Yamagiwa, *Feasibility of Using Laser Ion Accelerators in Proton Therapy.* AIP Conference Proceedings, 2004. **740**(1): p. 414-429.
65. E. Fourkal, J.S. Li, M. Ding, T. Tajima, and C.M. Ma, *Particle selection for laser-accelerated proton therapy feasibility study.* Medical Physics, 2003. **30**(7): p. 1660-1670.
66. V. Malka, S. Fritzler, E. Lefebvre, E. d'Humieres, R. Ferrand, G. Grillon, C. Albaret, S. Meyroneinc, J.-P. Chambaret, A. Antonetti, and D. Hulin, *Practicability of protontherapy using compact laser systems.* Medical Physics, 2004. **31**(6): p. 1587-1592.

67. E. Fourkal, J.S. Li, W. Xiong, A. Nahum, and C.M. Ma, *Intensity modulated radiation therapy using laser-accelerated protons: a Monte Carlo dosimetric study.* Physics in Medicine and Biology, 2003. **48**(24): p. 3977.

68. A. Yogo, K. Sato, M. Nishikino, M. Mori, T. Teshima, H. Numasaki, M. Murakami, Y. Demizu, S. Akagi, S. Nagayama, K. Ogura, A. Sagisaka, S. Orimo, M. Nishiuchi, A.S. Pirozhkov, M. Ikegami, M. Tampo, H. Sakaki, M. Suzuki, I. Daito, Y. Oishi, H. Sugiyama, H. Kiriyama, H. Okada, S. Kanazawa, S. Kondo, T. Shimomura, Y. Nakai, M. Tanoue, H. Sasao, D. Wakai, P.R. Bolton, and H. Daido, *Application of laser-accelerated protons to the demonstration of DNA double-strand breaks in human cancer cells.* Applied Physics Letters, 2009. **94**(18): p. 181502.

CHAPTER 2

Physics of intense laser-plasma interactions

For more than two decades, electron and ion acceleration, driven by intense laser-plasma interaction, has been an area of huge interest both theoretically and experimentally. Several mechanisms have been introduced to describe electron and ion acceleration but, so far, no single theoretical model exists that can adequately describe all the main aspects of the interaction physics.

This chapter contains the general background theory necessary to describe laser-plasma interaction from basic principles, the theory of laser wakefield acceleration and also the theory of laser-accelerated ion and proton beams. The chapter starts with the interaction of a high-intensity laser with a single electron. Subsequently, electron acceleration processes are discussed. Finally, two different mechanisms for proton and ion acceleration at the front and the rear side of the target are described.

2.1 The interaction of a high intensity laser with plasma

During the interaction of high intensity laser pulses with matter at intensities in the range of $I = 10^{18} \ldots 10^{20}$ W/cm^2, the relativistic regime has to be considered [1]. The electric field of such laser pulses can reach values of order of $E \sim 10^{10} \ldots 10^{11}$ V/cm and the electrons are torn away from the nucleus creating plasma with temperatures of millions of Kelvin. This interaction gives rise to several new collective plasma effects. To understand these effects some relevant quantities and concepts need to be introduced.

2.1.1 The motion of an electron in a high intensity laser field

When an intense laser is focused onto a solid or a gas target, the motion of an electron with charge e and mass m_e in the electric field of laser becomes relativistic, with a quiver velocity given by:

$$\boldsymbol{v}_{osc} = \frac{e\boldsymbol{E}}{m_e\omega}, \tag{2.1}$$

where $\boldsymbol{E}$ is the amplitude of the electric field, ω is the frequency of laser and c is the speed of light in vacuum. This quiver motion is characterised by a parameter a_0 known as the normalised vector potential, which can be written as [2, 3]:

$$a_0 = \frac{e\boldsymbol{E}}{m_e c\omega} = \frac{\boldsymbol{p}_{osc}}{m_e c} = \left(\frac{I\,\lambda^2}{1.37\times10^{18}}\right)^{1/2}, \tag{2.2}$$

where $\boldsymbol{p}_{osc}$ is transverse quiver momentum, I is the intensity of the laser and λ is the wavelength in microns.

The normalised vector potential defines three regimes of the interaction of the laser with matter. For 1 μm wavelength and for $a_0 \ll 1$, the electron motion is classical and the regime corresponds to intensities below the 5×10^{14} W/cm^2 limit. For $0.02 \leq a_0 \leq 1$, the interaction is classed as a high intensity regime. This regime corresponds to intensities between 5×10^{14} and 10^{18} W/cm^2. When $a_0 \gg 1$, the regime is known as the relativistic regime and the intensity is above the 10^{18} W/cm^2 limit [4].

In the high intensity regime, the motion of the electron can be described by the Lorentz force equation:

$$\frac{d\boldsymbol{p}}{dt} = -e(\boldsymbol{E} + \boldsymbol{v}\times\boldsymbol{B}), \tag{2.3}$$

where $\boldsymbol{p} = \gamma\, m_e\boldsymbol{v}$ is the relativistic momentum of the electron, $\gamma = \sqrt{1+(p/\ m_e c)^2} = 1/\sqrt{1-\beta^2}$ is the relativistic factor , $\beta = v/c$ is the electron velocity normalised to the speed of light and **B** is the magnetic field strength.

In the classical case, the term $(e\boldsymbol{E})$ is the dominant force and the electrons oscillate only along the laser polarisation direction. The term $e(\boldsymbol{v}\times\boldsymbol{B})$ becomes very significant in the relativistic case and the result of this force component is to push the electrons in the direction of laser propagation.

2.1.2 The ponderomotive force

When an electromagnetic wave propagates in plasma, the nonlinear force which is responsible for direct momentum transfer to the plasma is called the ponderomotive force [5]. Many nonlinear phenomena have a simple explanation in terms of the ponderomotive force. The description of an acceleration mechanism which allows electrons to gain energy from the laser field can be obtained by introducing the ponderomotive force of the laser acting on the electrons [6].

To derive this force, consider Eq. (2.3) for the electron's motion for the classical case $\gamma \approx 1$

$$\frac{d}{dt}(\ m_e \boldsymbol{v}) = -e\big(\boldsymbol{E}(\boldsymbol{r}) + v \times \boldsymbol{B}(\boldsymbol{r})\big), \tag{2.4}$$

assuming the electric field has the form

$$\boldsymbol{E} = \boldsymbol{E_s}(\boldsymbol{r})\cos(\omega t), \tag{2.5}$$

where $\boldsymbol{E_s}(\boldsymbol{r})$ contains the spatial dependence. To first order, the electron responds only to the laser electric field, neglecting the $\boldsymbol{v} \times \boldsymbol{B}$ term in the equation of the motion, and the electric field is taken to be that at the initial position ($\boldsymbol{r}_0$) of the electron. Hence,

$$m_e \frac{d}{dt}\boldsymbol{v_1} = -e\boldsymbol{E}(\boldsymbol{r_0})\ , \tag{2.6}$$

$$\frac{d\boldsymbol{r}_1}{dt} = \boldsymbol{v}_1 = -(e/\ m_e\omega)\boldsymbol{E}_s si\, n(\omega t), \tag{2.7}$$

$$\boldsymbol{\delta r_1} = (e/\ m_e\omega^2)\boldsymbol{E}_s\cos(\omega t), \tag{2.8}$$

where $\delta \boldsymbol{r}_1$ is the displacement of the electron in the electric field from its initial position. Going to second order, $\boldsymbol{E}(\boldsymbol{r})$ can be Taylor-expanded around the initial position of the electrons as

$$\boldsymbol{E}(\boldsymbol{r}) = \boldsymbol{E}(\boldsymbol{r_0}) + (\boldsymbol{\delta r_1}.\boldsymbol{\nabla})\boldsymbol{E}|_{r=r_0} + \ldots \tag{2.9}$$

Now the term $\boldsymbol{v_1} \times \boldsymbol{B}_1$ must be added using Maxwell's equation to derive the magnetic field

$$\boldsymbol{\nabla} \times \boldsymbol{E} = \frac{\partial \boldsymbol{B}}{\partial t},$$

$$\boldsymbol{B}_1 = -(1/\omega)\boldsymbol{\nabla} \times \boldsymbol{E}_s|_{r=r_0}\sin(\omega t), \tag{2.10}$$

and the second order term of Eq. (2.4) is then

$$m_e \frac{d\boldsymbol{v}_2}{dt} = -e[(\boldsymbol{\delta r}_1.\boldsymbol{\nabla})\boldsymbol{E} + \boldsymbol{v}_1 \times \boldsymbol{B}_1]. \quad (2.11)$$

Inserting Eqs. (2.7), (2.8) and (2.10) into (2.11) and averaging over time, it is found that

$$m_e \langle \frac{d\boldsymbol{v}_2}{dt} \rangle = -\frac{1}{2} \frac{e^2}{m_e \omega^2} \ [(\boldsymbol{E}_s \,.\boldsymbol{\nabla})\boldsymbol{E}_s + \boldsymbol{E}_s \times (\boldsymbol{\nabla} \times \boldsymbol{E}_s)] = \ \boldsymbol{F}_{pond}, \quad (2.12)$$

where the factor $1/2$ arises from the averaging over a laser cycle such that $\langle \cos^2(\omega t) \rangle = \langle \sin^2(\omega t) \rangle = 1/2$. Now by using the vector identity $\boldsymbol{A} \times (\boldsymbol{B} \times \boldsymbol{C}) = \boldsymbol{B}\,(\boldsymbol{A}.\boldsymbol{C}) - \boldsymbol{C}\,(\boldsymbol{A}\,.\boldsymbol{B})$, the equation of motion becomes

$$\boldsymbol{F}_{pond} = -\frac{1}{4} \frac{e^2}{m_e \omega^2} \ \boldsymbol{\nabla}(E_s{}^2) \ . \quad (2.13)$$

From this equation, it can be noted that an electron is expelled from regions of high intensity of the laser focus along the laser intensity gradient, which is proportional to the $\boldsymbol{E}_s{}^2$.

The scattering angle, with respect to laser propagation axis, is defined by the ratio between the transverse and longitudinal momenta of the electron and can be determined by Eq. (2.14) [7],

$$\theta = \arctan \sqrt{\frac{2}{\gamma - 1}}. \quad (2.14)$$

Experimentally, this equation has been confirmed by Moore *et al*. [8], where this angle was observed from the laser focus.

The Eq. (2.13) is only the force on a single electron. The force acting on the plasma is this force times the plasma density *n* expressed in terms of the plasma frequency ω_p which depends on plasma electron density, n_e

$$\omega_p = \sqrt{\frac{n_e e^2}{m_e \varepsilon_o}} \ . \quad (2.15)$$

Since $\boldsymbol{E}_s{}^2 = 2\langle \boldsymbol{E^2} \rangle$, the ponderomotive force is given by

$$\boldsymbol{f}_{pond} = -\frac{1}{2} \frac{\omega_p{}^2}{\omega^2} \ \boldsymbol{\nabla} \langle \varepsilon_o \boldsymbol{E^2} \rangle, \quad (2.16)$$

and the relativistic expression for the ponderomotive potential, $\boldsymbol{U}_{pond}$ using Eq. (2.2) is

$$U_{pond} = m_e c^2 (\gamma - 1) = m_e c^2 (\sqrt{1 + {a_0}^2} - 1)$$

$$= 0.511 \left(\sqrt{1 + \frac{I\lambda^2}{1.37 \times 10^{18}}} - 1 \right) MeV. \quad (2.17)$$

Since the distribution of electron energy can be described by the relativistic equation $E^2 \exp(-E/kT)$ where k is Boltzmann's constant and T is the electron temperature [9], the average value of kT is found to be U_{pond} [2]. Table 2.1 presents the range of U_{pond}, for λ = 800 nm, over the range of relevant laser intensities 10^{13} ... 10^{21} Wcm^{-2} using Eq. (2.17). This illustrates the onset of relativistic effects around $a_0 \sim 1$ where U_{pond} approaches the electron rest mass.

I (W/cm^2)	a_0	U_{pond} (MeV)
10^{13}	0.00214	1.168×10^{-6}
10^{14}	0.00676	1.167×10^{-5}
10^{15}	0.02138	1.167×10^{-4}
10^{16}	0.06761	0.00117
10^{17}	0.21381	0.01155
10^{18}	0.67612	0.10584
10^{19}	2.13809	0.69516
10^{20}	6.76123	2.98158
10^{21}	21.3809	10.42658

Table 2.1: Ponderomotive potential (U_{pond}) and normalised vector potential (a_0) as a function of laser intensity (I).

2.1.3 Propagation of electromagnetic waves in plasma

The collective behaviour of electrons instead of single electron motion has to be considered for the investigation of laser-plasma interactions. The combined result of the collective motion of plasma electrons and the self-generated electric and magnetic fields will be produced. If the electrons are displaced from the positive ion background by an external perturbation, a restoring force builds

up due to the electric fields arising from the charge separation. When the perturbation ceases, the electrons start to oscillate around the position of charge equilibrium with frequency ω_p.

2.1.3.1 Linear propagation

To describe linear propagation of electromagnetic radiation in a plasma one must derive the linear dispersion relation for an electromagnetic wave propagating through a plasma. The electrostatic force acting on the electrons is

$$m_e \frac{d^2\boldsymbol{r}}{dt^2} = -e\boldsymbol{E}, \tag{2.18}$$

where $\boldsymbol{E}$ is the electric field, which is written as $\boldsymbol{E} = E_O \cos(kx - \omega t)\hat{X}$ and k is the wavenumber of the electromagnetic wave. Assuming a small density perturbation and quasi-neutrality ($\rho = 0$), the wave equation can be derived from Maxwell's equations [10] such that

$$\nabla^2\boldsymbol{E} - \mu_0 \frac{\partial \boldsymbol{J}}{\partial t} = \frac{1}{c^2}\frac{\partial^2 \boldsymbol{E}}{\partial t^2}, \tag{2.19}$$

where ($J = -en_e\, dr/dt$) is the current density. Now from

$$\boldsymbol{E} = E_O \cos(kx - \omega t)$$

$$\nabla^2\boldsymbol{E} = -k^2\boldsymbol{E}, \qquad \frac{\partial^2 \boldsymbol{E}}{\partial t^2} = -\omega^2\boldsymbol{E}, \qquad \frac{\partial \boldsymbol{J}}{\partial t} = en_e\frac{e\boldsymbol{E}}{m}. \tag{2.20}$$

Inserting (2.20) into (2.19) gives the dispersion relation for an electromagnetic wave propagating through a plasma

$$\omega^2 - \omega_p^2 = k^2c^2 \ . \tag{2.21}$$

From this equation it is seen that, for $\omega < \omega_p$, the value $\sqrt{\omega^2 - \omega_p^2}/c = k$ becomes imaginary, so the laser pulse cannot propagate in plasma and, for $\omega > \omega_p$, laser pulses can propagate. From the threshold condition $\omega = \omega_p$, the critical plasma density can be defined as

$$n_{cr} = \frac{\varepsilon_o\ m_e\omega^2}{e^2}\ , \tag{2.22}$$

which defines the maximum plasma density into which a pulse with a specified frequency can penetrate. The critical plasma density describes two different

categories of plasma: underdense plasma where $n_e < n_{cr}$ and overdense plasma where $n_e > n_{cr}$.

The phase velocity of the electromagnetic wave propagating in plasma can be calculated by using the dispersion relation Eq. (2.21)

$$v_{ph} = \frac{\omega}{k} = c/\sqrt{1 - {\omega^2}_p/\omega^2} \ , \tag{2.23}$$

and the group velocity is given by

$$v_g = \frac{\partial \omega}{\partial k} = c\sqrt{1 - {\omega^2}_p/\omega^2} \ , \tag{2.24}$$

where $\sqrt{1 - {\omega^2}_p/\omega^2} = \sqrt{1 - n_e/n_{cr}} = \eta$ is the refractive index of the plasma.

As the refractive index in a plasma is always smaller than 1, with $n_e < n_{cr}$, the phase velocity and group velocity are always, respectively, larger and smaller than *c*.

2.1.3.2 Nonlinear propagation

In the relativistic regime, the key effect which needs to be taken into consideration is the increase of the relativistic mass of plasma electrons, γm_e. In this case, the relativistic plasma frequency is given by

$$\omega_{p,rel} = \sqrt{\frac{n_e e^2}{\langle\gamma\rangle \ m_e \ \varepsilon_o}} \ , \tag{2.25}$$

and the refraction index is

$$\eta_{rel} = \sqrt{1 - n_e/\langle\gamma\rangle n_{cr}} \ , \tag{2.26}$$

where $\langle\gamma\rangle$ is averaged both over the fast laser field oscillation and a large number of electrons

$$\langle\gamma\rangle = \sqrt{1 + a_0^2} \, . \tag{2.27}$$

The intensity dependence of the refractive index via the Lorentz factor has deep consequences for the propagation of laser pulses of relativistic intensities in plasmas. Relativistic self-focusing is the phenomenon of a high intensity laser pulse reducing in size, i.e., focusing when propagating in underdense plasma. There are two mechanisms responsible for the relativistic self-focusing effect. The first one is the averaged electron mass, $\gamma \, m_e$, increasing during the

oscillation in the laser field, which causes a decrease of the plasma frequency. The second mechanism is the expelling of electrons out of the focal spot by the ponderomotive force. This will decrease the local plasma density and therefore the local plasma frequency. Consequently, the refractive index is higher at the centre of the beam than at the beam edges. This causes the plasma to act like a positive lens and the laser will self-focus [11, 12]. For the Gaussian envelope approximation, the critical power P_{cr} for self-focusing is given by

$$P_{cr} = 2\left(\frac{\omega}{\omega_p}\right)^2 P_0 \,, \tag{2.28}$$

where

$$P_0 = \frac{m_e^2\, c^5}{e^2} = 8.7 \text{ GW} \,. \tag{2.29}$$

When this condition is fulfilled, the self-focusing of the laser balances the natural diffraction and the laser effectively propagates in a self-made channel over distances much longer than the Rayleigh range (see section 2.2.2.3).

2.2 Laser- driven electron acceleration

In the previous section, the processes by which nonlinear propagation of a laser pulse through the plasma affects the characteristics of the pulse were described. For laser electron acceleration one has to take a closer look at how the highly intense laser pulse drives the plasma. Tajima and Dawson in their paper [13] proposed use of the large electric fields in a plasma wave for particle acceleration. In this scheme, plasma wave oscillation is excited when electrons are collectively displaced by the ponderomotive force of an intense laser pulse. The plasma wave propagates with a phase velocity close to the speed of light in the wake behind the intense laser pulse (hence the term wakefield acceleration). This means that highly relativistic electrons can move in phase with the plasma wave and 'surf' the wave potential over relatively long distances. This technique for electron acceleration by plasma waves can sustain electric fields of approximately 3-4 orders of magnitude greater than those that can be achieved with conventional RF technology.

2.2.1 Laser wakefield acceleration

The basic explanation of this phenomenon is as follows. A high intensity laser pulse ($a \geq 1$) propagating through underdense plasma expels electrons from high intensity regions by the ponderomotive force and a low density region of electron follows in the wake of the pulse. Behind the laser pulse, the Coulomb force between the background ions and the electrons attracts the electrons back towards the axis, driving them into an oscillation that produces a plasma density wave. The group velocity of the driving laser pulse equals the phase velocity of the plasma wave,

$$v_g = \eta c = v_p = \frac{\omega_p}{k_p}. \tag{2.30}$$

A number of theoretical articles address ponderomotive excitation of plasma waves in the laser-wakefield regime [14-16]. An important result is that there is an optimum pulse duration for which the plasma wave is resonant with the laser pulse envelope. For a Gaussian laser pulse, and for a linear plasma wave and non-relativistic laser intensities, the oscillation reaches its maximum amplitude when the laser pulse length is equal to half the plasma wavelength

$$c\tau = \frac{\lambda_p}{2} = \frac{\pi c}{\omega_p}, \tag{2.31}$$

where τ is the laser pulse full-width at half-maximum (FWHM) duration. When this condition is satisfied, a large amplitude plasma wave is excited and electrons from the plasma background can be injected into or trapped in the laser wakefield and then accelerated to high energy. The acceleration mechanism is analogous to the acceleration of a surfer catching and being swept along by a large ocean wave. The principle of a laser wakefield accelerator is shown schematically in Fig 2.1. The maximum accelerating electric field in the plasma is estimated by [17]

$$E_{max} = \frac{m_e c\, \omega_p}{e} \cong 0.096 \sqrt{n_e\ [\mathrm{m}^{-3}]}\quad [\mathrm{V/m}], \tag{2.32}$$

such that, theoretically, for an electron plasma density range of (10^{18} – 10^{19} cm^{-3}) electric fields of the order of 100-300 GV/m are possible.

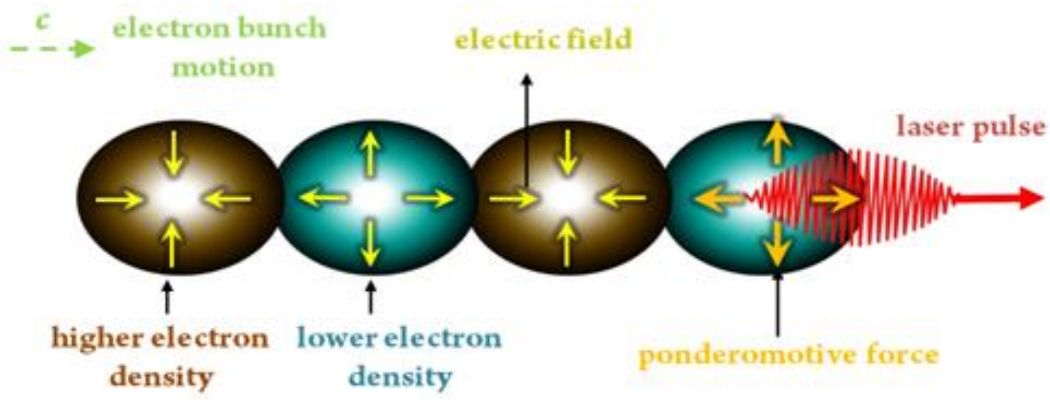

Figure 2.1: Interaction between an intense laser pulse and underdense plasma creates a high gradient accelerating structure. A laser pulse propagates through the plasma at velocity v_g. The plasma density oscillations are set up by the ponderomotive force of the laser pulse, causing a wake to trail the pulse. A co-propagating bunch of electrons gains energy from the accelerating phase of the wake's longitudinal electric field.

During plasma wave motion, if the electrons that form the wave move with the same velocity as the wave itself they will reduce the electron density at the peak of the wave, dampning it and wave-breaking can occur. Wave-breaking limits the growth of the plasma wave and the maximum electric field that can be generated. It is important because it is a mechanism by which background plasma electrons can be injected and accelerated. If this self-injection mechanism can be controlled, it eliminates the need for complicated external injection schemes [18], significantly decreasing the experimental complexity.

In the relativistic case, the electric field required for wave breaking can be estimated using Eq. (2.33)[19]

$$E_{wb} = E_{max}\sqrt{2\left(\omega/\omega_p - 1\right)}\ , \qquad (2.33)$$

where $\omega/\omega_p = \gamma_g = 1/\sqrt{1 - v_g^2/c^2}$ is the relativistic factor associated with the plasma wave. This shows that the relativistic wave-breaking amplitude can be much larger in strength than E_{max}. For example, an 800 nm laser pulse

passing through a plasma of density of 10^{18} cm^{-3} can drive electric fields approximately eight times greater than E_{max} .

2.2.2 Energy gain limitations

Although the acceleration gradients produced by laser wakefield acceleration are very large, there are several fundamental limits on acceleration which limit the length over which acceleration can be achieved, and that will limit the maximum energy gain produced in a single stage of a LWFA [16]. The two main limitations for channel-guided LWFA are electron dephasing and pump depletion. Diffraction of the laser pulse is also a severe effect, but this can be overcome through the use of a plasma channel to guide the laser pulse [20]. In the following discussion, the laser power is considered to be less than the critical power for self-focusing, and instabilities are neglected.

2.2.2.1 Dephasing

Since there is a small, but non-negligible, difference between the group velocity of the driving laser pulse ($v_g < c$), and the longitudinal velocity of the accelerated electrons, the electrons eventually reach the centre of the plasma wave where the electric field changes sign and slips into decelerating phase of the plasma wave. The propagation length to reach this crossing point is known as the dephasing length (l_d) [21].

To estimate the dephasing length, consider an accelerated electron with velocity c and assume the phase velocity of the wakefield is taken to be the group velocity of the laser pulse. Hence, the difference in velocity between the electron and wakefield velocities is

$$\Delta v = c\sqrt{1 - \left(\omega_p/\omega\right)^2} - c \approx \frac{1}{2}\, c\, \left(\omega_p/\omega\right)^2 \quad . \tag{2.34}$$

For the linear regime ($a_0^2 \ll 1$) , if an electron is injected at the peak of the plasma wave (at the back of the wake), dephasing occurs when it has moved half a plasma wavelength ($\lambda_p/2$) and the dephasing length is the length that the

electron moves during this time, $(\lambda_p/2\,)/\,\Delta v$. From this it can be shown that the dephasing length in this regime is

$$l_d = c\left(\frac{\lambda_p}{2}\right)/\,\Delta v \;\; = \;\; {\lambda_p}^3/\lambda^2\,. \tag{2.35}$$

The electrons will lose energy if they continue to interact with the wake beyond l_d. For the nonlinear regime (bubble regime) $(a_0^2 > 1)$, the dephasing length becomes [22]

$$l_d \approx \; a_0\,{\lambda_p}^3/\lambda^2\;\,. \tag{2.36}$$

It is clear that the dephasing length increases for higher intensities and also by operating at lower densities.

2.2.2.2 Laser energy depletion

As the laser drives the wake, it loses its energy to the plasma [21, 23] and, clearly, this process cannot continue indefinitely since the laser energy is finite. In order to estimate the length over which this energy depletion effect becomes important, we define a laser depletion length l_{dep} as the distance the pulse travels for loss of one-half of its initial energy. This is calculated by equating the energy deposited into the wakefield with the laser pulse energy [16].

In the linear regime, the pump depletion length can be estimated by equating the laser pulse energy to the energy left behind in the wake [24, 25]

$$l_{dep} \approx \;\; {\lambda_p}^3/{a_0}^2\lambda^2\,. \tag{2.37}$$

In this regime, it is clear that the pulse depletion length is longer than the dephasing length; in fact, it shows that the laser energy is not being used efficiently.

In the nonlinear regime, the description of pulse depletion is given by [24, 25]

$$l_{dep} \approx \;\; a_0\,{\lambda_p}^3/\,\lambda^2\;\,, \tag{2.38}$$

and here the pulse depletion length increases for higher a_0 and it can be increased further by operating at lower densities. In this case the pump depletion length can equal the dephasing length which means the energy of the

laser pulse is being used efficiently, and also that the length of plasma should be chosen to match the dephasing length.

2.2.2.3 Diffraction

The high intensity ($\geq 10^{15}$ W/cm^2) that is required for many applications of high-intensity laser pulses, such as laser wakefield acceleration, high harmonic generation (HHG) and X-ray lasers is achieved by focusing the laser energy into a small area. In the absence of guiding, the beam diverges rapidly through diffraction and remains intense only over a short distance. This often limits the useful output.

For a Gaussian beam, the transverse intensity profile $I\,(r,z)$ of a laser beam propagating along the z-axis with a power P is shown in Fig. 2.2 and it can be described by [26]

$$I\,(r,z)\;=\;\frac{2P}{\pi w^2(z)}\;e^{-2\,(r/w(z))^2}\,, \tag{2.39}$$

where r represents the radial distance from the central z-axis and $w(z)$ is the beam radius where the amplitude decreases to $1/e$ of its value on-axis. The beam radius $w(z)$ varies along the z-axis as

$$w(z)=w(0)\sqrt{\left(\frac{z}{z_R}\right)^2+1}\,, \tag{2.40}$$

where $w(0)$ is the minimum beam radius at $z=0$ and z_R is the Rayleigh length, equal to

$$z_R=\;\pi\;w(0)^2/\lambda\,. \tag{2.41}$$

The Rayleigh length is the distance from the focus at z = 0 to where the intensity on-axis is reduced by a factor of two and is a measure of the distance over which the laser pulse remains at or close to its highest intensity. One can also say that the beam radius is increased by a factor $\sqrt{2}$ over the Rayleigh length. As an example, a focused laser beam with a wavelength of 800 nm focused to a spot size of 20 μm has a Rayleigh length of 1.6 mm.

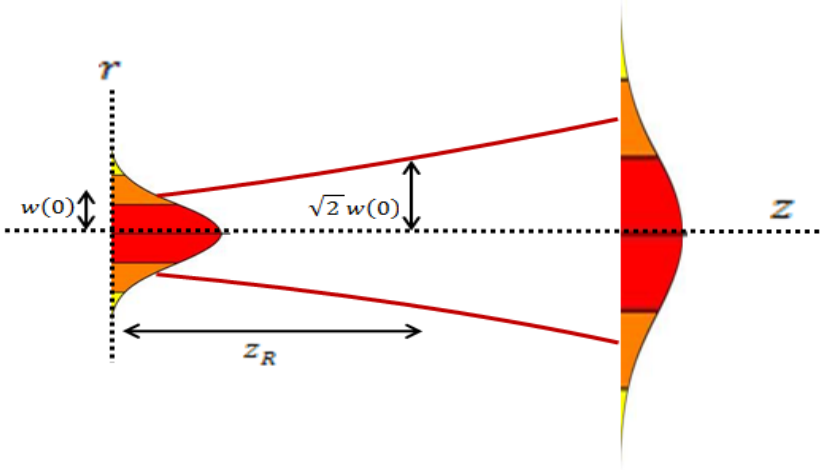

Figure 2.2: The evolution of a Gaussian laser beam along the z-direction with an initial radius w and the beam waist w(0) located at the minimum. The Rayleigh length, z_R is also indicated.

The Gaussian beam propagates with a curved phase front with radius $R(z)$ given by

$$\frac{1}{R(z)} = \frac{z}{z^2 + z_R^2}, \tag{2.42}$$

and the curvature is also shown in Fig 2.2 where, at $z = 0$, the phase front is completely flat. From Eq. (2.41), by using $w \cong \lambda_p$ and the expression for the dephasing length Eq. (2.35), it can be shown that the diffraction-limited acceleration length is

$$z_R = l_{diff} = l_d\,(\pi\ \lambda/\lambda_p)\,, \tag{2.43}$$

from which it is clear that $l_{diff} \ll l_d$, so diffraction is a significant effect for the LWFA since the length over which the laser has sufficiently high intensity to generate a large amplitude wakefield can be severely limited. This can be overcome, however, with the use of a plasma channel to guide the laser pulse. As described in the following chapter, overcoming diffraction with optical guiding is of key importance to increasing the energy gain of a laser wakefield accelerator.

2.2.3 Electron energy gain scaling

After the discussion of the limitations to the energy gain of the wakefield accelerator, the maximum electron energy gain can be calculated by integrating

the longitudinal electric field strength over the distance over which the particle experiences the accelerating field. Scaling laws describing the energy gain in the LWFA can be derived and three different cases are considered. The first is for uniform plasma where the acceleration length is limited by vacuum diffraction. The second is for a plasma channel where the acceleration length is limited by electron dephasing and the third is a plasma channel where the acceleration length is limited by pump depletion. In all cases, the laser power is assumed to be less than the critical power for self-focusing in plasma. The scaling laws for the energy gain can be summarised as follows:

If the acceleration distance is limited by diffraction, then $l_{acc} \cong \pi z_R$ and the energy gain in linear regime in practical units is [27]

$$E_{diff}[\text{MeV}] \cong 576\left(\lambda\ /\lambda_p\right) P[\text{TW}]. \tag{2.44}$$

and, for nonlinear regime, the energy gain in practical units is [28]

$$\Delta E_{diff}[\text{MeV}] \cong 740\left(\lambda\ /\lambda_p\right)\left(1 + {a_0}^2/2\right)^{-1/2} P[\text{TW}]\ . \tag{2.45}$$

If the acceleration distance is limited by the dephasing length, $l_{acc} \cong\ \ l_d$, in linear regime in practical units is [28]

$$\Delta E_d[\text{MeV}] \cong (630\ I[\text{W/cm}^2])/n_e[\ \text{cm}^{-3}], \tag{2.46}$$

and, for the nonlinear regime, the energy gain in practical units is

$$\Delta E_d[\text{MeV}] \cong (2/\pi)\ (630\ I[\text{W/cm}^2])/n_e[\ \text{cm}^{-3}], \tag{2.47}$$

If the acceleration distance is limited by the depletion length, $l_{acc} \cong\ \ l_{dep}$, the energy gain in linear regime in practical units is [28]

$$\Delta E_{dep}[\text{MeV}] \cong (3.4 \times 10^{21})/(n_e[\ \text{cm}^{-3}]\ \lambda^2[\mu\text{m}]), \tag{2.48}$$

and, for the nonlinear regime, the energy gain in practical units is

$$\Delta E_{dep}[\text{MeV}] \cong (400\ I[\text{W/cm}^2])/n_e[\ \text{cm}^{-3}]\ . \tag{2.49}$$

From these scaling laws it becomes apparent that the energy gain is larger for lower plasma densities and higher laser intensities. Using laser systems that produce peak powers of the order of a few tens of TW and by extending the acceleration distance beyond z_R, electron beams in the GeV range can be produced. As an example, in the high intensity regime, the dephasing length is approximately equal to the depletion length which implies higher efficiency and larger energy gains. Consider the ALPHA-X beam line with a 20 TW, 40 fs

Ti:sapphire laser operating at a wavelength of 800 nm focused to a (radius at $1/e^2$) waist of 20 μm in a plasma of density 10^{18} cm^{-3}. This corresponds to $a_0 = 0.9$ and $I_0 = 1.6 \times 10^{18}$ Wcm^{-2}. The maximum energy gain is $\Delta E_{diff} = 300$ MeV in an acceleration length of L_{acc} = 5 mm versus $\Delta E_d = 650$ MeV in $l_d = 5$ cm. Here, for this simple description the pump depletion-limited energy gain of the laser beam is not included.

Energies of laser-accelerated electrons have increased with the advance of laser technology and better control and understanding of the experiments [20, 29-43]. Leemans *et al.* [29] reported GeV laser acceleration of electrons using 40 TW, 40 fs laser pulses with a 3.3 cm long plasma channel. With these and other more recent experiments [30-40], it is now evident that the laser accelerated electron energy scales with laser intensity and scales inversely with the plasma density, as predicted by Tajima and Dawson [13].

Experimental data utilising the existing large energy lasers are summarised and shown in Fig. 2.3. From this figure it can be seen that there is a clear dependence of the energy gain on the laser intensity where the energy increases with increasing the intensity ($\Delta E \propto a_0$) as represented by the pink area which gives the range of a_0 from 2-10. This figure also shows the clear tendency of energy gain as a function of the plasma density n_e ($\Delta E \propto {n_e}^{-1}$). This presents the community with opportunities to consider designs of experiments toward 10 GeV electron energy based on laser wakefield acceleration [19, 20, 44].

2.2.4 Electron energy gain improvement

The scaling law shows that the LWFA can accelerate electrons to higher energy at lower plasma density. This is because the dephasing length increases as density decreases. However, it is only possible to benefit from the enhancement in the dephasing length if the laser can drive a wakefield for that entire length. This is many Rayleigh lengths and, although self-focusing can extend the interaction length to some extent, its effect decreases as the electron density is decreased. If the laser pulse is guided by an external guiding structure, then electron densities can be chosen for which $z_R \ll l_d$.

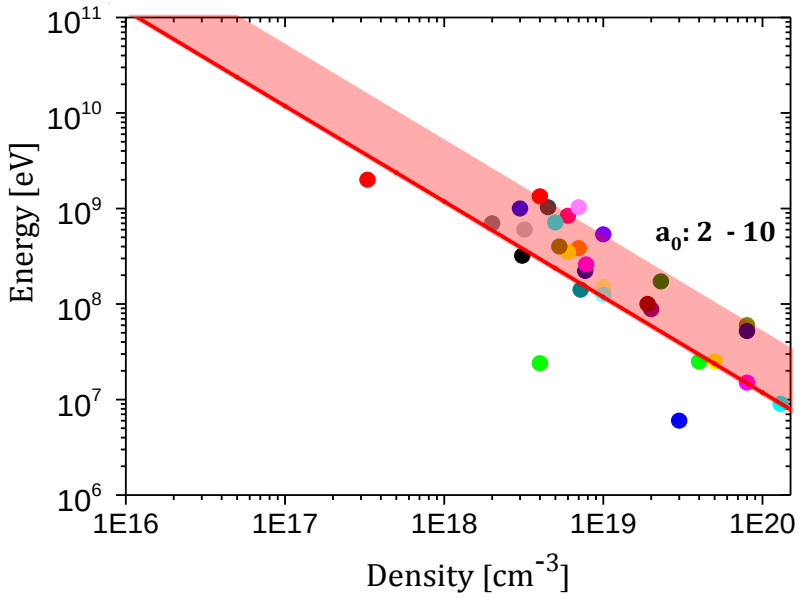

Figure 2.3: Electron energy as a function of laser intensity and plasma density observed in the experiments [20, 29-43]. The pink area gives the range of a_0 and the red solid line shows the fitted curve of $\Delta E \propto n_e^{-1}$.

The result is that for a given laser power, electrons can be accelerated to higher energies over the extended propagation length. Initial work using laser plasma channels produced by lasers [20] and discharges [29, 45] has demonstrated that the energy gain of a single LWFA stage can be raised significantly if the laser is effectively guided. Techniques to avoid the diffraction of the laser beam are discussed in chapter 3, and one of the subjects of this thesis is the application of the hydrogen-filled capillary discharge waveguide for laser wakefield acceleration.

2.3 Laser-driven proton and ion acceleration

As the development of multi-terawatt laser technology becomes more common, exciting new areas of research grow and continue to develop in the interaction of lasers beams with solids. Using high intensity lasers to irradiate thin metal foils, it has become possible to generate high energy ion beams [46, 47].

A number of the experiments have demonstrated that protons and even heavier ions can be efficiently accelerated from both the front and rear target surfaces [48-50] in ultra-high intensity laser-solid interactions. To explain the observed MeV protons, two reasonable acceleration scenarios have been proposed. The first explanation [46, 49, 51] proposes that the protons come from the front surface of the target due to the laser plasma induced charge separation and ponderomotive force.

The second explanation [47, 52] proposes that the protons come from the rear surface of the target. In this case, the acceleration mechanism is initiated by hot electrons propagating through the target which then form an electrostatic potential sheath capable of ionising and accelerating protons and heavy ions at the rear surface.

2.3.1 Front side acceleration mechanism

Front surface acceleration was studied by Y. Sentoku *et al.* [51]. This mechanism accelerates protons at the front side of the target in the vicinity of the laser focus. When the main pulse of relativistic intensity with a normalised vector potential $a_0 > 1$ arrives at the relativistic critical surface, electrons are expelled out of the focal region by the ponderomotive force until the generated electrostatic potential, U_e, arising from the charge separation is approximately equal to the ponderomotive potential, U_{pond}, of the laser, given by Eq. (2.16)

$$U_e = U_{\text{pond}} = m_e c^2 \left(\sqrt{1 + a_0^2} - 1 \right). \tag{2.50}$$

The maximum energy for protons accelerated by this field is found [53] to be

$$E_{\text{proton}}^{\text{front}} = 1.25\, K_B T \tag{2.51}$$

As an example, for $U_{pond} \approx K_B T$, consider the case of a 1 J laser beam, 80 fs operating at λ = 800 nm and focal point diameter of ~ 6 μm (JETI laser system). Such a laser gives an intensity of $I = 4.4 \times 10^{19}$ W/cm^2 and maximum proton energy of $E_{\text{cutoff}} = 2.3$ MeV. This value is in agreement with Sentoku *et al.* [51], which yields for $I = 4.0 \times 10^{19}$ W/cm^2 a maximum proton energy of 2.2 MeV.

The proposed front side mechanism plays a certain role for laser plasma acceleration, but the experimental and theoretical work shows that the acceleration from the rear side dominates in most experiments and this mechanism will be presented in the following section.

2.3.2 Rear side acceleration mechanism: target normal sheath acceleration

Many different possible mechanisms have been proposed for laser-driven proton beams from the rear side in the interaction of a high intensity laser with a thin foil. The main mechanism of significance for the experimental work in this thesis is Target Normal Sheath Acceleration (TNSA) [54], which is graphically shown in Fig. 2.4. It is the most widely accepted theory used to explain the production of energetic protons and heavy ions from the rear side of a thin foil.

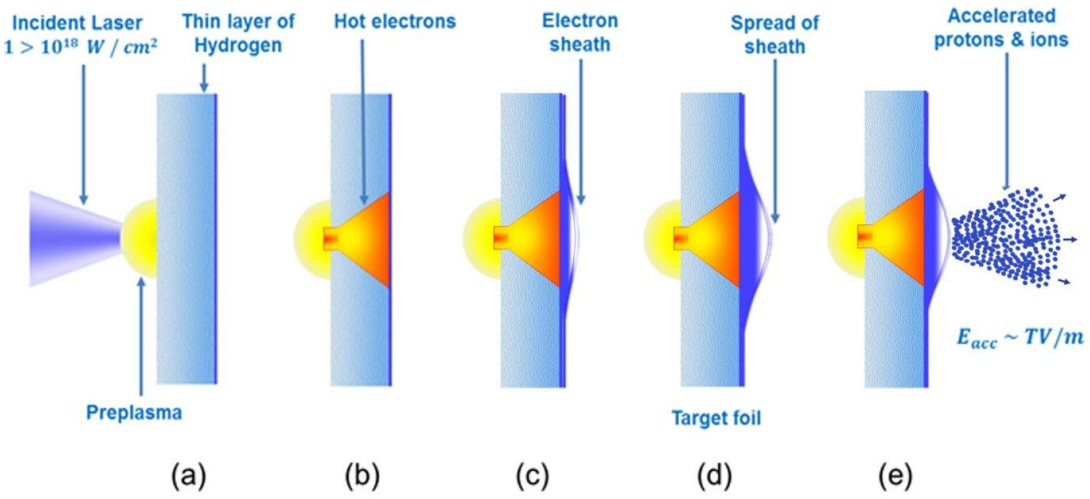

Figure 2.4: A summary of the TNSA is shown: (a) Laser pulse creates pre-plasma. (b) Main pulse accelerates electrons to MeV-energies. (c) Electron sheath generates electric field on rear side. (d) Transverse spread of sheath with speed of light. (e) Field ionisation and ion acceleration in the normal direction.

In this mechanism, when the laser pulse is focused onto the front surface of a thin metal foil, a part of the laser pulse is reflected and a considerable amount of laser energy is converted into electrons. These hot electrons are accelerated by

the laser pulse to relativistic energies (~MeV) and propagate through the target material. Upon reaching the target rear surface, these electrons break out into the vacuum forming a charged cloud that extends over several Debye lengths where the Debye length λ_D is given by

$$\lambda_D = \sqrt{\frac{\varepsilon_0 k_B T_e}{e^2 n_e}} = 0.24\ (\mu m) \sqrt{\frac{k_B T_e\ (MeV)}{n_e / 10^{21} cm^{-3}}}\ . \tag{2.52}$$

Typically this is a few μm [52, 55] for the conditions of the experiments presented in this thesis ($k_B T_e \sim$ 2.3 MeV and $n_e \sim 10^{21}$ cm^{-3}).

The break out of the electron population leaves the bulk of the target positively charged. As a consequence, a space charge field is generated on the target rear surface that is sufficiently strong to decelerate and eventually pull back all subsequent electrons. This leads to the formation of a thin, quasistatic electron sheath at the rear side of the target. At the rear surface of this electron sheath, huge electric fields as high as several teravolt per meter (TV/m) are generated. The strength of this electrostatic field can be estimated by

$$E \cong \frac{k_B T_e}{e\ \lambda_D}\ . \tag{2.53}$$

For an electron energy $k_B T_e \sim$ 1 MeV and $\lambda_D = 1\ \mu m$, a sheath field of ~ 1 TV/m is predicted. This field is strong enough to ionise the surface of the target and accelerate the resulting ions to energy in the tens of MeV range.

Recently, theoretical works [56, 57] have reported that with the increase in the power of the large laser systems, it is becoming possible to reach a new more efficient acceleration mechanism, known as laser radiation pressure (RPA) [57]. RPA dominates the acceleration of ions for high enough laser intensities. The total radiation pressure on target can be estimated by [58]

$$P_R = \frac{2RI_0}{c}\ . \tag{2.54}$$

where R is the plasma reflectivity (≈ 1 for solid plasma density).

It has been shown that the RPA acceleration mechanism could be reached with laser intensities in the range 10^{21} – 10^{23} W/cm^2 and mono-energetic ion beams are expected from solid targets of nanometre thickness with a maximum

energy in the GeV range. With the power of the large laser systems available today, the RPA is still at the lower limit and the TNSA mechanism is still the dominant acceleration process.

2.3.3 Proton energy gain scaling

Several experimental [59, 60] and theoretical [61-63] results have been reported on the maximum achievable proton energy as a function of various laser pulse parameters. Recently, scaling laws for laser-produced proton beams based on laser intensity, pulse duration and energy have been experimentally determined [64, 65]. However, as they cannot be fully compared owing to the different sets of parameters used, no clear picture has yet appeared of the relative importance of the target thicknesses and laser parameters pulse energy, pulse duration, peak intensity and focal spot size.

The comparison between the results of several experimental groups is presented in Fig. 2.5, which shows the maximum proton energy as a function of laser intensity on the target. Maximum energies reached with short pulse lasers such as ASTRA, ATLAS and LUND were generally only a few MeV, as illustrated by the data points numbered 1, 2, 3, respectively. Energy of 10 MeV has been reached with 40 fs laser pulses by the LOA laser system, labelled 4. For lasers such as Z-100TW at SNL, NOVA and DRACO, maximum proton energies above 10 MeV have been observed as shown by the points labelled 5, 6 and 7 respectively. For the results of a series of experiments of high-power lasers such as VULCAN, LULI and TRIDENT, clear scaling of the maximum proton energies with the square root of the laser intensity has been established experimentally. From Fig. 2.5 and Table 2.2, it can be seen that longer pulses typically result in higher proton energy.

The scaling of $E_{\max}$ with I_0 ($E \propto I_0$) for the RPA mechanism is much more favourable than with the square root of the laser intensity for TNSA [66].

Laser system	Location	Intensity (W/cm^2)	Pulse duration (fs)	Maximum proton energy (MeV)	Reference
ASTRA	Rutherford Appleton Laboratory, U.K.	6×10^{18}	60	1.5	[67]
ATLAS	Max Planck Institute for Quantum Optics, Germany	1.3×10^{19}	150	4	[68]
LUND	Lund Laser Centre, Sweden	1×10^{19}	33	4	[69]
LOA	Laboratory of Applied Optics, France	6×10^{19}	40	10	[70]
DRACO	Research Center Dresden Rossendorf, Germany	1×10^{21}	25	17	[71]
LULI	Laboratory for Intense Lasers, France	6×10^{19}	320	20	[64]
Z-100 TW (SNL)	Sandia National Laboratories, United States	9.2×10^{19}	1000	30	[72]
VULCAN	Rutherford Appleton Laboratory, UK	6×10^{20}	1000	55	[65]
TRIDENT	Los Alamos National Laboratory, United States	1.5×10^{20}	600	70	[73]
NOVA	Lawrence Livermore National Laboratory, United States	3×10^{20}	500	58	[47]

Table 2.2: Comparison of the maximum proton energy for various experiments using different laser systems.

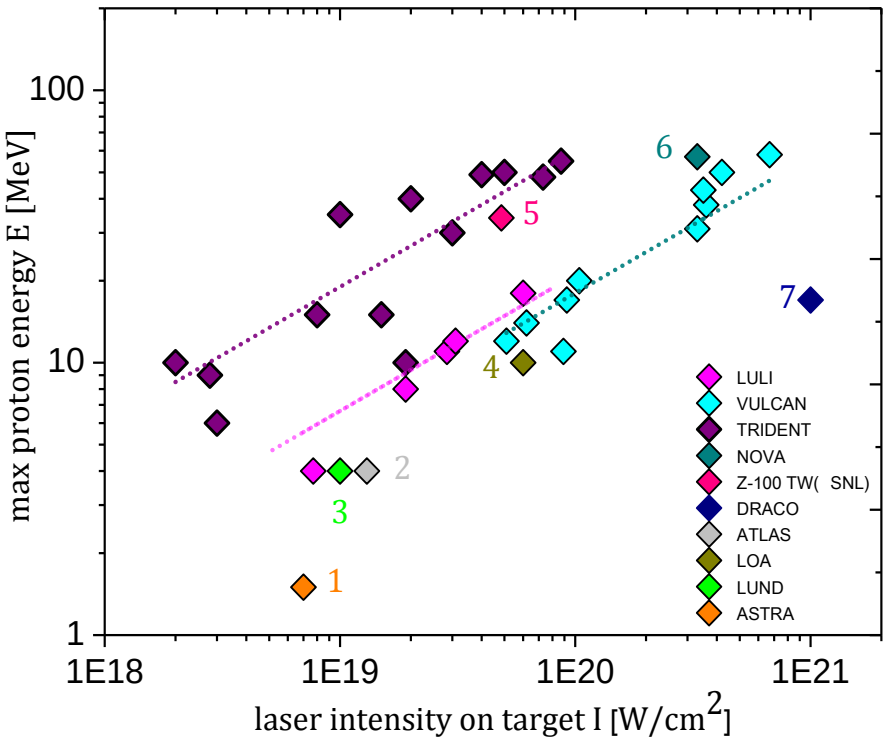

Figure 2.5: Maximum energy of the proton beam as a function of the laser intensity on the target from several groups at several laser systems. Colour short dot lines represent scaling of the maximum proton energies with the square root of the laser intensity for VULCAN (cyan), LULI (magenta) and TRIDENT (purple) respectively.

References

1. Y.I. Salamin, S.X. Hu, K.Z. Hatsagortsyan, and C.H. Keitel, *Relativistic high-power laser–matter interactions.* Physics Reports, 2006. **427**(2–3): p. 41-155.
2. G. Malka and J.L. Miquel, *Experimental Confirmation of Ponderomotive-Force Electrons Produced by an Ultrarelativistic Laser Pulse on a Solid Target.* Physical Review Letters, 1996. **77**(1): p. 75-78.
3. S.C. Wilks and W.L. Kruer, *Absorption of ultrashort, ultra-intense laser light by solids and overdense plasmas.* IEEE Journal of Quantum Electronics 1997. **33**(11): p. 1954-1968.
4. G.A. Mourou, T. Tajima, and S.V. Bulanov, *Optics in the relativistic regime.* Reviews of Modern Physics, 2006. **78**(2): p. 309-371.

5. R. Dendy, *Plasma Physics*. 1993, Cambridge University Press: Cambridge.
6. F.F. Chen, *Introduction to Plasma Physics*. 1974, Plenum Press: New York.
7. F.V. Hartemann, S.N. Fochs, G.P. Le Sage, N.C. Luhmann, Jr., J.G. Woodworth, M.D. Perry, Y.J. Chen, and A.K. Kerman, *Nonlinear ponderomotive scattering of relativistic electrons by an intense laser field at focus.* Physical Review E, 1995. **51**(5): p. 4833-4843.
8. C.I. Moore, J.P. Knauer, and D.D. Meyerhofer, *Observation of the Transition from Thomson to Compton Scattering in Multiphoton Interactions with Low-Energy Electrons.* Physical Review Letters, 1995. **74**(13): p. 2439-2442.
9. K.W.D. Ledingham, I. Spencer, T. McCanny, R.P. Singhal, M.I.K. Santala, E. Clark, I. Watts, F.N. Beg, M. Zepf, K. Krushelnick, M. Tatarakis, A.E. Dangor, P.A. Norreys, R. Allott, D. Neely, R.J. Clark, A.C. Machacek, J.S. Wark, A.J. Cresswell, D.C.W. Sanderson, and J. Magill, *Photonuclear Physics when a Multiterawatt Laser Pulse Interacts with Solid Targets.* Physical Review Letters, 2000. **84**(5): p. 899-902.
10. J.D. Jackson, *Classical Electrodynamics*. 1999, Wiley: New York.
11. A.B. Borisov, A.V. Borovskiy, V.V. Korobkin, A.M. Prokhorov, O.B. Shiryaev, X.M. Shi, T.S. Luk, A. McPherson, J.C. Solem, K. Boyer, and C.K. Rhodes, *Observation of relativistic and charge-displacement self-channeling of intense subpicosecond ultraviolet (248 nm) radiation in plasmas.* Physical Review Letters, 1992. **68**(15): p. 2309-2312.
12. P. Monot, T. Auguste, P. Gibbon, F. Jakober, G. Mainfray, A. Dulieu, M. Louis-Jacquet, G. Malka, and J.L. Miquel, *Experimental Demonstration of Relativistic Self-Channeling of a Multiterawatt Laser Pulse in an Underdense Plasma.* Physical Review Letters, 1995. **74**(15): p. 2953-2956.
13. T. Tajima and J.M. Dawson, *Laser Electron Accelerator.* Physical Review Letters, 1979. **43**(4): p. 267-270.

14. L.M. Gorbunov and V.I. Kirsanov, *Excitation of plasma waves by an electromagnetic wave packet.* Experimental and Theoretical Physics Letters, 1987. **93**(0044-4510): p. 509-518.
15. P. Sprangle, E. Esarey, A. Ting, and G. Joyce, *Laser wakefield acceleration and relativistic optical guiding.* Applied Physics Letters, 1988. **53**(22): p. 2146-2148.
16. E. Esarey, P. Sprangle, J. Krall, and A. Ting, *Overview of plasma-based accelerator concepts.* IEEE Transactions on Plasma Science, 1996. **24**(2): p. 252-288.
17. J.M. Dawson, *Nonlinear Electron Oscillations in a Cold Plasma.* Physical Review, 1959. **113**(2): p. 383-387.
18. A. Irman, M.J.H. Luttikhof, A.G. Khachatryan, F.A. van Goor, J.W.J. Verschuur, H.M.J. Bastiaens, and K.J. Boller, *Design and simulation of laser wakefield acceleration with external electron bunch injection in front of the laser pulse.* Journal of Applied Physics, 2007. **102**(2): p. 024513-024513-7.
19. A. Pukhov and J. Meyer-ter-Vehn, *Laser wake field acceleration: the highly non-linear broken-wave regime.* Applied Physics B: Lasers and Optics, 2002. **74**(4): p. 355-361.
20. C.G.R. Geddes, C. Toth, J. van Tilborg, E. Esarey, C.B. Schroeder, D. Bruhwiler, C. Nieter, J. Cary, and W.P. Leemans, *High-quality electron beams from a laser wakefield accelerator using plasma-channel guiding.* Nature, 2004. **431**(7008): p. 538-541.
21. T. Katsouleas, C. Joshi, J.M. Dawson, F.F. Chen, C. Clayton, W.B. Mori, C. Darrow, and D. Umstadter, *Plasma accelerators.* AIP Conference Proceedings, 1985. **130**(1): p. 63-98.
22. E. Esarey, B.A. Shadwick, C.B. Schroeder, and W.P. Leemans, *Nonlinear Pump Depletion and Electron Dephasing in Laser Wakefield Accelerators.* AIP Conference Proceedings, 2004. **737**(1): p. 578-584.

23. A. Ting, E. Esarey, and P. Sprangle, *Nonlinear wake-field generation and relativistic focusing of intense laser pulses in plasmas.* Physics of Fluids B: Plasma Physics, 1990. **2**(6): p. 1390-1394.
24. W. Horton and T. Tajima, *Pump depletion in the plasma-beat-wave accelerator.* Physical Review A, 1986. **34**(5): p. 4110-4119.
25. S.V. Bulanov, I.N. Inovenkov, V.I. Kirsanov, N.M. Naumova, and A.S. Sakharov, *Nonlinear depletion of ultrashort and relativistically strong laser pulses in an underdense plasma.* Physics of Fluids B: Plasma Physics, 1992. **4**(7): p. 1935-1942.
26. H. Haus, *Waves and fields in optoelectronics*. 1984, Prentice-Hall: Englewood Cliffs
27. W.P. Leemans, C.W. Siders, E. Esarey, N.E. Andreev, G. Shvets, and W.B. Mori, *Plasma guiding and wakefield generation for second-generation experiments.* IEEE Transactions on Plasma Science, 1996. **24**(2): p. 331-342.
28. W. Leemans, E. Esarey, C. Geddes, C. Schroeder, and C. Tóth, *Laser guiding for GeV laser–plasma accelerators.* Philosophical Transactions of the Royal Society A: Mathematical, Physical and Engineering Sciences, 2006. **364**(1840): p. 585-600.
29. W.P. Leemans, B. Nagler, A.J. Gonsalves, C.s. Toth, K. Nakamura, C.G.R. Geddes, E. Esarey, C.B. Schroeder, and S.M. Hooker, *GeV electron beams from a centimetre-scale accelerator.* Nature, 2006. **2**(10): p. 696-699.
30. E. Miura, K. Koyama, S. Kato, N. Saito, M. Adachi, Y. Kawada, T. Nakamura, and M. Tanimoto, *Demonstration of quasi-monoenergetic electron-beam generation in laser-driven plasma acceleration.* Applied Physics Letters, 2005. **86**(25): p. 251501.
31. S.P.D. Mangles, C.D. Murphy, Z. Najmudin, A.G.R. Thomas, J.L. Collier, A.E. Dangor, E.J. Divall, P.S. Foster, J.G. Gallacher, C.J. Hooker, D.A. Jaroszynski, A.J. Langley, W.B. Mori, P.A. Norreys, F.S. Tsung, R. Viskup, B.R. Walton, and K. Krushelnick, *Monoenergetic beams of relativistic electrons from intense laser-plasma interactions.* Nature, 2004. **431**(7008): p. 535-538.

32. J. Faure, Y. Glinec, A. Pukhov, S. Kiselev, S. Gordienko, E. Lefebvre, J.P. Rousseau, F. Burgy, and V. Malka, *A laser-plasma accelerator producing monoenergetic electron beams.* Nature, 2004. **431**(7008): p. 541-544.

33. A. Yamazaki, H. Kotaki, I. Daito, M. Kando, S.V. Bulanov, T.Z. Esirkepov, S. Kondo, S. Kanazawa, T. Homma, K. Nakajima, Y. Oishi, T. Nayuki, T. Fujii, and K. Nemoto, *Quasi-monoenergetic electron beam generation during laser pulse interaction with very low density plasmas.* Physics of Plasmas, 2005. **12**(9): p. 093101.

34. T. Hosokai, K. Kinoshita, T. Ohkubo, A. Maekawa, M. Uesaka, A. Zhidkov, A. Yamazaki, H. Kotaki, M. Kando, K. Nakajima, S.V. Bulanov, P. Tomassini, A. Giulietti, and D. Giulietti, *Observation of strong correlation between quasimonoenergetic electron beam generation by laser wakefield and laser guiding inside a preplasma cavity.* Physical Review E, 2006. **73**(3): p. 036407.

35. C.T. Hsieh, C.M. Huang, C.L. Chang, Y.C. Ho, Y.S. Chen, J.Y. Lin, J. Wang, and S.Y. Chen, *Tomography of Injection and Acceleration of Monoenergetic Electrons in a Laser-Wakefield Accelerator.* Physical Review Letters, 2006. **96**(9): p. 095001.

36. B. Hidding, K.U. Amthor, B. Liesfeld, H. Schwoerer, S. Karsch, M. Geissler, L. Veisz, K. Schmid, J.G. Gallacher, S.P. Jamison, D. Jaroszynski, G. Pretzler, and R. Sauerbrey, *Generation of Quasimonoenergetic Electron Bunches with 80-fs Laser Pulses.* Physical Review Letters, 2006. **96**(10): p. 105004.

37. M. Mori, M. Kando, I. Daito, H. Kotaki, Y. Hayashi, A. Yamazaki, K. Ogura, A. Sagisaka, J. Koga, K. Nakajima, H. Daido, S.V. Bulanov, and T. Kimura, *Transverse dynamics and energy tuning of fast electrons generated in sub-relativistic intensity laser pulse interaction with plasmas.* Physics Letters A, 2006. **356**(2): p. 146-151.

38. S.P.D. Mangles, A.G.R. Thomas, M.C. Kaluza, O. Lundh, F. Lindau, A. Persson, F.S. Tsung, Z. Najmudin, W.B. Mori, C.G. Wahlström, and K. Krushelnick, *Laser-Wakefield Acceleration of Monoenergetic Electron*

Beams in the First Plasma-Wave Period. Physical Review Letters, 2006. **96**(21): p. 215001.

39. S. Kneip, S.R. Nagel, S.F. Martins, S.P.D. Mangles, C. Bellei, O. Chekhlov, R.J. Clarke, N. Delerue, E.J. Divall, G. Doucas, K. Ertel, F. Fiuza, R. Fonseca, P. Foster, S.J. Hawkes, C.J. Hooker, K. Krushelnick, W.B. Mori, C.A.J. Palmer, K.T. Phuoc, P.P. Rajeev, J. Schreiber, M.J.V. Streeter, D. Urner, J. Vieira, L.O. Silva, and Z. Najmudin, *Near-GeV Acceleration of Electrons by a Nonlinear Plasma Wave Driven by a Self-Guided Laser Pulse.* Physical Review Letters, 2009. **103**(3): p. 035002.
40. D.H. Froula, C.E. Clayton, T. Döppner, K.A. Marsh, C.P.J. Barty, L. Divol, R.A. Fonseca, S.H. Glenzer, C. Joshi, W. Lu, S.F. Martins, P. Michel, W.B. Mori, J.P. Palastro, B.B. Pollock, A. Pak, J.E. Ralph, J.S. Ross, C.W. Siders, L.O. Silva, and T. Wang, *Measurements of the Critical Power for Self-Injection of Electrons in a Laser Wakefield Accelerator.* Physical Review Letters, 2009. **103**(21): p. 215006.
41. E. Brunetti, R.P. Shanks, G.G. Manahan, M.R. Islam, B. Ersfeld, M.P. Anania, S. Cipiccia, R.C. Issac, G. Raj, G. Vieux, G.H. Welsh, S.M. Wiggins, and D.A. Jaroszynski, *Low Emittance, High Brilliance Relativistic Electron Beams from a Laser-Plasma Accelerator.* Physical Review Letters, 2010. **105**(21): p. 215007.
42. S.M. Wiggins, R.C. Issac, G.H. Welsh, E. Brunetti, R.P. Shanks, M.P. Anania, S. Cipiccia, G.G. Manahan, C. Aniculaesei, B. Ersfeld, M.R. Islam, R.T.L. Burgess, G. Vieux, W.A. Gillespie, A.M. MacLeod, S. B. van der Geer, M. J. de Loos, and D.A. Jaroszynski, *High quality electron beams from a laser wakefield accelerator.* Plasma Physics and Controlled Fusion, 2010. **52**(12): p. 124032.
43. S. Cipiccia, M.R. Islam, B. Ersfeld, R.P. Shanks, E. Brunetti, G. Vieux, X. Yang, R.C. Issac, S.M. Wiggins, G.H. Welsh, M.-P. Anania, D. Maneuski, R. Montgomery, G. Smith, M. Hoek, D.J. Hamilton, N.R.C. Lemos, D. Symes, P.P. Rajeev, V.O. Shea, J.M. Dias, and D.A. Jaroszynski, *Gamma-rays from*

harmonically resonant betatron oscillations in a plasma wake. Nature Physics, 2011. **7**(11): p. 867-871.

44. J.L. Vay, C.G.R. Geddes, E. Esarey, C.B. Schroeder, W.P. Leemans, E. Cormier-Michel, and D.P. Grote, *Modeling of 10 GeV-1 TeV laser-plasma accelerators using Lorentz boosted simulations.* Physics of Plasmas, 2011. **18**(12): p. 3103.
45. K. Nakamura, B. Nagler, C. Toth, C.G.R. Geddes, C.B. Schroeder, E. Esarey, W.P. Leemans, A.J. Gonsalves, and S.M. Hooker, *GeV electron beams from a centimeter-scale channel guided laser wakefield accelerator.* Physics of Plasmas, 2007. **14**(5): p. 056708.
46. E.L. Clark, K. Krushelnick, J.R. Davies, M. Zepf, M. Tatarakis, F.N. Beg, A. Machacek, P.A. Norreys, M.I.K. Santala, I. Watts, and A.E. Dangor, *Measurements of Energetic Proton Transport through Magnetized Plasma from Intense Laser Interactions with Solids.* Physical Review Letters, 2000. **84**(4): p. 670-673.
47. R.A. Snavely, M.H. Key, S.P. Hatchett, T.E. Cowan, M. Roth, T.W. Phillips, M.A. Stoyer, E.A. Henry, T.C. Sangster, M.S. Singh, S.C. Wilks, A. MacKinnon, A. Offenberger, D.M. Pennington, K. Yasuike, A.B. Langdon, B.F. Lasinski, J. Johnson, M.D. Perry, and E.M. Campbell, *Intense High-Energy Proton Beams from Petawatt-Laser Irradiation of Solids.* Physical Review Letters, 2000. **85**(14): p. 2945-2948.
48. P. McKenna, K.W.D. Ledingham, J.M. Yang, L. Robson, T. McCanny, S. Shimizu, R.J. Clarke, D. Neely, K. Spohr, R. Chapman, R.P. Singhal, K. Krushelnick, M.S. Wei, and P.A. Norreys, *Characterization of proton and heavier ion acceleration in ultrahigh-intensity laser interactions with heated target foils.* Physical Review E, 2004. **70**(3): p. 036405.
49. A. Maksimchuk, S. Gu, K. Flippo, D. Umstadter, and V.Y. Bychenkov, *Forward Ion Acceleration in Thin Films Driven by a High-Intensity Laser.* Physical Review Letters, 2000. **84**(18): p. 4108-4111.
50. A.J. Mackinnon, M. Borghesi, S. Hatchett, M.H. Key, P.K. Patel, H. Campbell, A. Schiavi, R. Snavely, S.C. Wilks, and O. Willi, *Effect of Plasma Scale*

Length on Multi-MeV Proton Production by Intense Laser Pulses. Physical Review Letters, 2001. **86**(9): p. 1769-1772.

51. Y. Sentoku, T.E. Cowan, A. Kemp, and H. Ruhl, *High energy proton acceleration in interaction of short laser pulse with dense plasma target.* Physics of Plasmas, 2003. **10**(5): p. 2009-2015.
52. M. Hegelich, S. Karsch, G. Pretzler, D. Habs, K. Witte, W. Guenther, M. Allen, A. Blazevic, J. Fuchs, J.C. Gauthier, M. Geissel, P. Audebert, T. Cowan, and M. Roth, *MeV Ion Jets from Short-Pulse-Laser Interaction with Thin Foils.* Physical Review Letters, 2002. **89**(8): p. 085002.
53. M.C. Kaluza, *Characterisation of Laser-Accelerated Proton Beams.* (PhD thesis), 2004. Max Planck Institute of Quantum Optics: Garching.
54. S.C. Wilks, A.B. Langdon, T.E. Cowan, M. Roth, M. Singh, S. Hatchett, M.H. Key, D. Pennington, A. MacKinnon, and R.A. Snavely, *Energetic proton generation in ultra-intense laser-solid interactions.* Physics of Plasmas, 2001. **8**(2): p. 542-549.
55. S.P. Hatchett, C.G. Brown, T.E. Cowan, E.A. Henry, J.S. Johnson, M.H. Key, J.A. Koch, A.B. Langdon, B.F. Lasinski, R.W. Lee, A.J. Mackinnon, D.M. Pennington, M.D. Perry, T.W. Phillips, M. Roth, T.C. Sangster, M.S. Singh, R.A. Snavely, M.A. Stoyer, S.C. Wilks, and K. Yasuike, *Electron, photon, and ion beams from the relativistic interaction of Petawatt laser pulses with solid targets.* Physics of Plasmas, 2000. **7**(5): p. 2076-2082.
56. T. Esirkepov, M. Borghesi, S.V. Bulanov, G. Mourou, and T. Tajima, *Highly Efficient Relativistic-Ion Generation in the Laser-Piston Regime.* Physical Review Letters, 2004. **92**(17): p. 175003.
57. A.P.L. Robinson, M. Zepf, S. Kar, R.G. Evans, and C. Bellei, *Radiation pressure acceleration of thin foils with circularly polarized laser pulses.* New Journal of Physics, 2008. **10**(1): p. 013021.
58. A. Macchi, S. Veghini, and F. Pegoraro, *"Light Sail" Acceleration Reexamined.* Physical Review Letters, 2009. **103**(8): p. 085003.
59. E.L. Clark, K. Krushelnick, M. Zepf, F.N. Beg, M. Tatarakis, A. Machacek, M.I.K. Santala, I. Watts, P.A. Norreys, and A.E. Dangor, *Energetic Heavy-Ion*

and Proton Generation from Ultraintense Laser-Plasma Interactions with Solids. Physical Review Letters, 2000. **85**(8): p. 1654-1657.

60. M. Allen, Y. Sentoku, P. Audebert, A. Blazevic, T. Cowan, J. Fuchs, J.C. Gauthier, M. Geissel, M. Hegelich, S. Karsch, E. Morse, P.K. Patel, and M. Roth, *Proton spectra from ultraintense laser-plasma interaction with thin foils: Experiments, theory, and simulation.* Physics of Plasmas, 2003. **10**(8): p. 3283-3289.
61. E. Fourkal, I. Velchev, and C.M. Ma, *Coulomb explosion effect and the maximum energy of protons accelerated by high-power lasers.* Physical Review E, 2005. **71**(3): p. 036412.
62. J. Schreiber, F. Bell, F. Grüner, U. Schramm, M. Geissler, M. Schnürer, S. Ter-Avetisyan, B.M. Hegelich, J. Cobble, E. Brambrink, J. Fuchs, P. Audebert, and D. Habs, *Analytical Model for Ion Acceleration by High-Intensity Laser Pulses.* Physical Review Letters, 2006. **97**(4): p. 045005.
63. T. Esirkepov, M. Yamagiwa, and T. Tajima, *Laser Ion-Acceleration Scaling Laws Seen in Multiparametric Particle-in-Cell Simulations.* Physical Review Letters, 2006. **96**(10): p. 105001.
64. J. Fuchs, P. Antici, E. Humieres, E. Lefebvre, M. Borghesi, E. Brambrink, C.A. Cecchetti, M. Kaluza, V. Malka, M. Manclossi, S. Meyroneinc, P. Mora, J. Schreiber, T. Toncian, H. Pepin, and P. Audebert, *Laser-driven proton scaling laws and new paths towards energy increase.* Nature, 2006. **2**(1): p. 48-54.
65. L. Robson, P.T. Simpson, R.J. Clarke, K.W.D. Ledingham, F. Lindau, O. Lundh, T. McCanny, P. Mora, D. Neely, C.G. Wahlstrom, M. Zepf, and P. McKenna, *Scaling of proton acceleration driven by petawatt-laser-plasma interactions.* Nature, 2007. **3**(1): p. 58-62.
66. C.A.J. Palmer, N.P. Dover, I. Pogorelsky, M. Babzien, G.I. Dudnikova, M. Ispiriyan, M.N. Polyanskiy, J. Schreiber, P. Shkolnikov, V. Yakimenko, and Z. Najmudin, *Monoenergetic Proton Beams Accelerated by a Radiation Pressure Driven Shock.* Physical Review Letters, 2011. **106**(1): p. 014801.

67. I. Spencer, K.W.D. Ledingham, P. McKenna, T. McCanny, R.P. Singhal, P.S. Foster, D. Neely, A.J. Langley, E.J. Divall, C.J. Hooker, R.J. Clarke, P.A. Norreys, E.L. Clark, K. Krushelnick, and J.R. Davies, *Experimental study of proton emission from 60-fs, 200-mJ high-repetition-rate tabletop-laser pulses interacting with solid targets.* Physical Review E, 2003. **67**(4): p. 046402.

68. M. Kaluza, J. Schreiber, M.I.K. Santala, G.D. Tsakiris, K. Eidmann, J. Meyer-ter-Vehn, and K.J. Witte, *Influence of the Laser Prepulse on Proton Acceleration in Thin-Foil Experiments.* Physical Review Letters, 2004. **93**(4): p. 045003.

69. D. Neely, P. Foster, A. Robinson, F. Lindau, O. Lundh, A. Persson, C.-G. Wahlstrom, and P. McKenna, *Enhanced proton beams from ultrathin targets driven by high contrast laser pulses.* Applied Physics Letters, 2006. **89**(2): p. 021502.

70. S. Fritzler, K.T. Phuoc, V. Malka, A. Rousse, and E. Lefebvre, *Ultrashort electron bunches generated with high-intensity lasers: Applications to injectors and x-ray sources.* Applied Physics Letters, 2003. **83**(19): p. 3888-3890.

71. K. Zeil, S.D. Kraft, S. Bock, M. Bussmann, T.E. Cowan, T. Kluge, J. Metzkes, T. Richter, R. Sauerbrey, and U. Schramm, *The scaling of proton energies in ultrashort pulse laser plasma acceleration.* New Journal of Physics, 2010. **12**(4): p. 045015.

72. S. Marius, *Optimization and control of laser-accelerated proton beams*. 2008, Institute of Nuclear Physics: Southwest German.

73. S.A. Gaillard, K.A. Flippo, M.E. Lowenstern, J.E. Mucino, J.M. Rassuchine, D.C. Gautier, J. Workman, and T.E. Cowan, *Proton acceleration from ultrahigh-intensity short-pulse laser-matter interactions with Cu micro-cone targets at an intrinsic ~10^{-8} contrast.* Journal of Physics: Conference Series, 244, 2010: p. 022034.

CHAPTER 3

Capillary discharge waveguides: development and design

In order to design an experiment for the first demonstration of laser wakefield acceleration using tapered plasma waveguides, as the first step, the mechanism of laser guiding in a pre-formed plasma channel is reviewed in the first section of this chapter. Following this, the experimental development of both non-tapered (straight) and tapered plasma waveguides is described. Lastly, a description of a new high voltage pulsed power supply, together with testing results for capillary discharging, is presented.

3.1 Plasma waveguides

In laser wakefield acceleration, optical guiding of high-intensity laser pulses is required to extend the acceleration length up to the dephasing length. This is important to obtain maximum bunch energy from the acceleration process. In the absence of guiding, the acceleration length is fundamentally limited by diffraction to a characteristic distance determined by the Rayleigh length (section 2.2.2.3) as illustrated in Fig. 3.1(a).

An attractive technique to guide a high-intensity laser pulse is to couple the beam into a pre-formed plasma channel as shown in Fig. 3.1(b). A plasma waveguide suitable for guiding has a parabolic electron density profile [1] n_e, which is described by

$$n_e = n_e(0) + \Delta n_e \left(\frac{r}{r_{ch}}\right)^2, \qquad (3.1)$$

where $n_e(0)$ is the on-axis density, Δn_e is the channel depth, r is the radial coordinate and r_{ch} is the channel radius. An example of the parabolic electron density profile, according to Eq. (3.1), has been plotted in Fig. 3.2 for typical capillary parameters:

$n_e(0) = 1.5 \times 10^{18}$ cm^{-3}, $\Delta n_e = 2 \times 10^{18}$ cm^{-3} and $r_{ch} = 140$ μm .

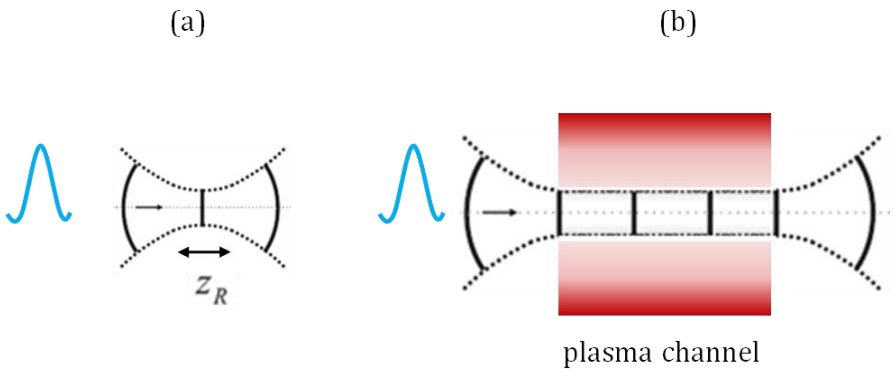

Figure 3.1: (a) A focused laser pulse diffracts with a characteristic distance determined by the Rayleigh length (z_R). (b) A pre-formed plasma channel, providing a balance between focusing and diffraction, can guide a laser pulse over distances beyond the Rayleigh length.

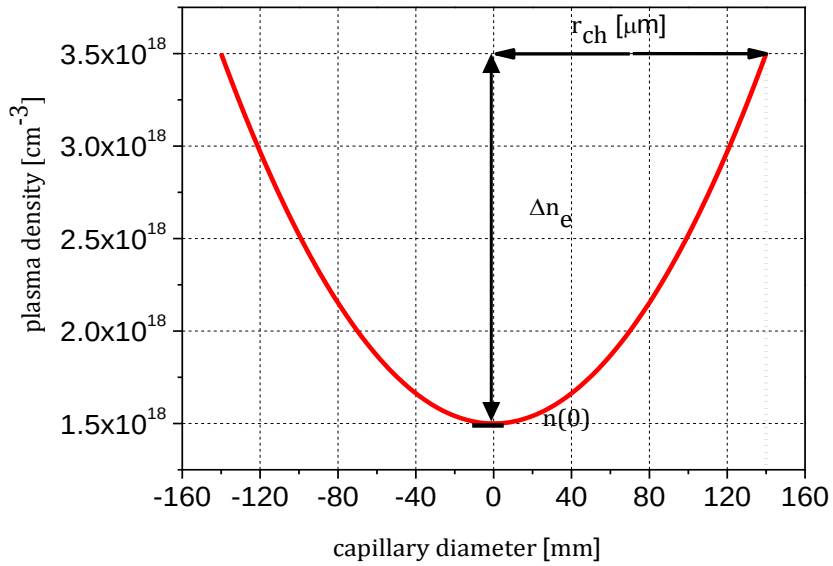

Figure 3.2: Example parabolic distribution of the radial electron density in a plasma waveguide.

The refractive index of the plasma channel, η(r), has a parabolic radial profile with a maximum on-axis and, therefore, the channel behaves as a continuous focusing lens with

$$\eta(r) = \sqrt{1 - \frac{n_e(r)e^2}{m_e \varepsilon_0 \omega^2}} \quad . \tag{3.2}$$

The refractive index profile that corresponds to the parabolic electron density profile, from Fig. 3.2, has been plotted in Fig. 3.3. The continual focusing applied to the laser beam along the channel is the mechanism for keeping the laser from diffracting, i.e., the channel acts as a waveguide.

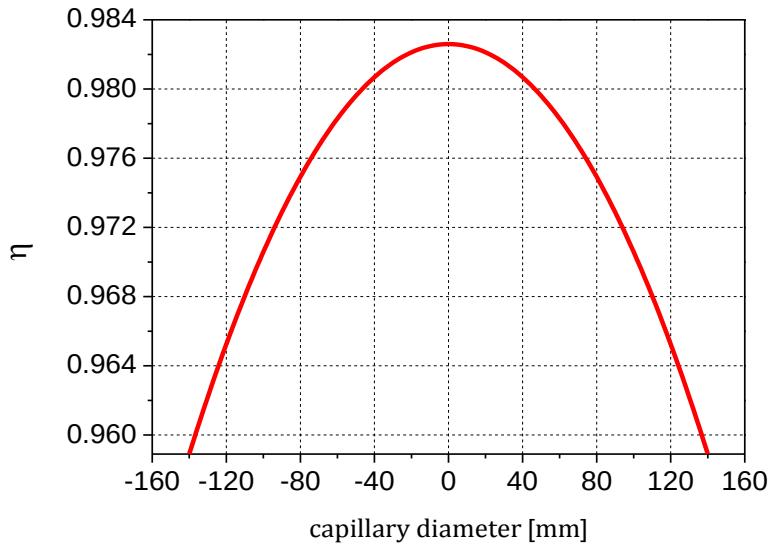

Figure 3.3: Refractive index profile for a plasma with the following parameters: $n_e(0) = 1.5 \times 10^{18}$ cm^{-3}, $\Delta n_e = 2 \times 10^{18}$ cm^{-3} and $r_{ch} = 140$ µm .

3.1.1 Matched laser beam size

When a Gaussian laser beam travels through a parabolic plasma channel, under certain conditions it can be guided without variation of its transverse profile [2]. The beam is said to be matched to the channel, dependent on the initial beam size and the channel parameters. The condition for matching the laser beam to the parabolic plasma channel can be derived by starting with the wave equation

$$\nabla^2 E + \frac{\omega^2}{c^2}\eta^2 E = 0 \quad , \tag{3.3}$$

where the electric field E is written as a wave propagating in the z-direction

$$E = E_1 e^{i\beta z} \quad , \tag{3.4}$$

and β is the wavenumber in direction of propagation. Substituting this into the wave equation Eq. (3.3) results in

$$\nabla^2 E_1 + (k^2\eta^2 - \beta^2)\, E_1 = 0\,, \tag{3.5}$$

where η is the refractive index, given by Eq. (3.2), and E_1, for a Gaussian beam profile with an initial beam waist w_0 and amplitude E_0, is

$$E_1 = E_0\, e^{-r^2/\, {w_0}^2} \quad . \tag{3.6}$$

The refractive index distribution and electric field of the Gaussian beam both depend only on *r* and are cylindrical symmetric. Then the wave equation can be written in cylindrical coordinates

$$\frac{1}{r}\frac{\partial}{\partial r}\left(r\frac{\partial}{\partial r}\right) E_1 + (k^2\eta^2 - \beta^2)\, E_1 = 0,$$

$$\left(\frac{-4}{{w_0}^2} + \frac{4r^2}{{w_0}^2}\right) e^{-r^2/\, {w_0}^2} + \left[k^2\left(1 - \frac{n_e(r)e^2}{m_e\varepsilon_0\omega^2}\right) - \beta^2\right] e^{-r^2/\, {w_0}^2} = 0\ . \tag{3.7}$$

From this equation, the condition for matched guiding ($w_0 = w_{\mathrm{M}}$) occurs when

$$\frac{4r^2}{{w_{\mathrm{M}}}^2} = k^2\Delta n_e \left(\frac{r}{r_{ch}}\right)^2 \frac{e^2}{m_e\varepsilon_0\omega^2} \quad , \tag{3.8}$$

which can also be written to give the matched spot size w_{M} in the form

$$w_{\mathrm{M}} = \left(\frac{1}{\pi r_e \Delta n_e}\right)^{\frac{1}{4}} \sqrt{r_{ch}} \tag{3.9}$$

where r_e is the classical electron radius. It can be seen that the matched spot size does not depend on the laser wavelength.

A study by Bobrova *et al.* [3] applied a simple plasma model in which thermal equilibrium is assumed to predict the matched spot size for a capillary discharge waveguide as a function of the capillary diameter and initial gas pressure, and obtained an estimate for the matched spot size of

$$w_{\mathrm{M}}[\mu\mathrm{m}] \approx \ 1.48 \times 10^5\, (n_e[\mathrm{cm}^{-3}])^{-1/4} \sqrt{r_{\mathrm{ch}}\,[\mu\mathrm{m}]} \quad . \tag{3.10}$$

From this equation it is clear that the matched spot size is proportional to the square root of the capillary radius. As an example, for a typical straight capillary with $r_{\mathrm{ch}} \approx 140$ μm and taking initial hydrogen pressure of 60 mbar and plasma density of $\approx 1.5 \times 10^{18}\mathrm{cm}^{-3}$, it is found that $w_{\mathrm{M}} \approx 50$ μm. Such a matched spot size is much larger than the diffraction-limited spot size for an 800 nm laser

pulse so it can be readily obtained using conventional focusing optics such as a high *f*-number spherical mirror or an off-axis parabolic mirror.

3.1.2 Beam radius oscillations

Assuming an electromagnetic wave propagating in a plasma channel has a Gaussian profile, then the evolution of the laser waist $w(z)$ along the z-direction is described by the differential equation

$$\frac{d^2w(z)}{dz^2} = \frac{1}{k^2 w(z)^3}\left[1 - \frac{w(z)^4}{(w_{\mathrm{M}})^4}\right] \tag{3.11}$$

and when ($w_0 = w_{\mathrm{M}}$), the laser beam will propagate with a stable transverse intensity profile [4].

The general solution of Eq. (3.11) in the straight channel case (uniform longitudinal density), when $w_0 \neq w_{\mathrm{M}}$, can be obtained using the initial conditions at the focus $w(z) = w_0,\ z = 0$ and $dw(0)/dz = 0\ as$

$$w(z) = \frac{w_0}{\sqrt{2}}\left[1 + \frac{{w_M}^4}{{w_0}^4} + \left(1 - \frac{{w_M}^4}{{w_0}^4}\right)\cos\left(\frac{4z}{k\,{w_M}^2}\right)\right]^{1/2} \tag{3.12}$$

and it can be seen that if the initial waist size is not equal to the matched spot size of the plasma channel, then the beam will oscillate between w_0 and ${w_{\mathrm{M}}}^2/\,w_0$. This behaviour is called ''scalloping '' and it can also lead to losses in the energy transmission of the beam [5].

For an example of beam scalloping, consider the behaviour of a laser pulse of wavelength 800 nm propagating through a 4 cm long straight capillary with $w_{\mathrm{M}} = 50$ μm, for three different values of w_0. The evolution of the beam size along the waveguide is presented in Fig. 3.4 for the three cases obtained using Eq. (3.12). The matched condition is clear when $w_0 = w_{\mathrm{M}}$ and the constant spot size is maintained throughout the capillary.

During laser pulse propagation, when the pulses are not matched into the capillary waveguide, they experience oscillations in their radius, with an oscillation wavelength ≈ 31 mm (scalloping period given by ${\pi^2 w_{\mathrm{M}}}^2/\lambda$ [4]). When $w_0 < w_{\mathrm{M}}$, the beam initially diffracts and when $w_0 > w_{\mathrm{M}}$, the beam initially focuses. It can be concluded therefore that, if the laser pulse is not

matched to the plasma channel during high-power LWFA experiments, then the initial size of the beam with respect to the matching condition will, in combination with relativistic self-focusing, have a large influence on the evolution of the laser pulse profile in the waveguide.

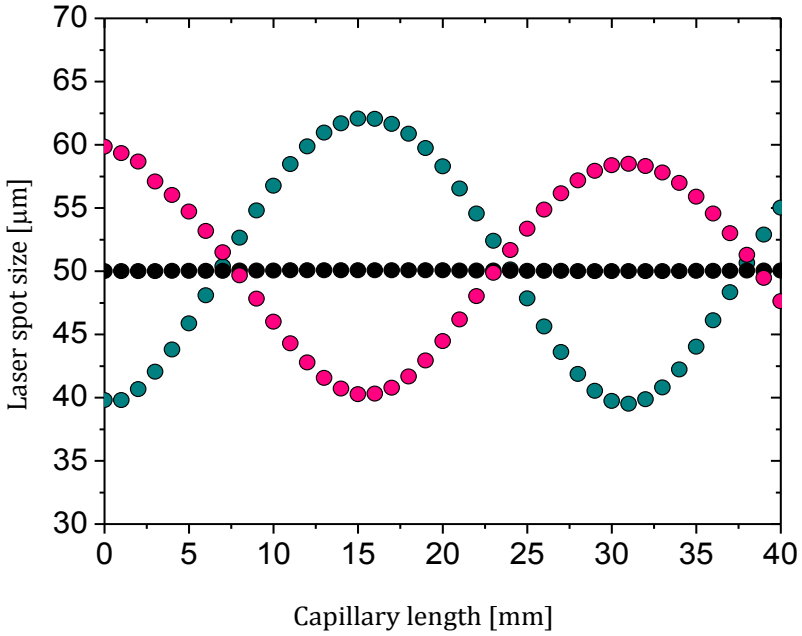

Figure 3.4: Variation of the laser spot size through a capillary waveguide with the matched spot size $w_{\mathrm{M}} = 50$ μm. Initial laser beam waists of 40, 50 and 60 μm are indicated by green, black and pink circles respectively.

3.2 Tapered plasma waveguides

In LWFA, the maximum electron energy is determined by dephasing (section 2.2.2.1), which also sets the maximum length of the accelerator. For example, with a straight capillary (uniform density), higher energies can simply be achieved by lowering the overall density since this increases l_d , i.e., l_d scales inversely with n_e. At any given density, however, the energy can be enhanced by introducing a positive density taper (increasing along the accelerator) such that plasma wavelength, λ_p decreases as the laser, wake, and electrons propagate [6, 7]. During acceleration, the wake contracts in size ($R \cong (1/\pi)\sqrt{\gamma\,\lambda_p}$, where γ is the relativistic factor), which has the effect of continually advancing the dephasing point, as shown in Fig. 3.5.

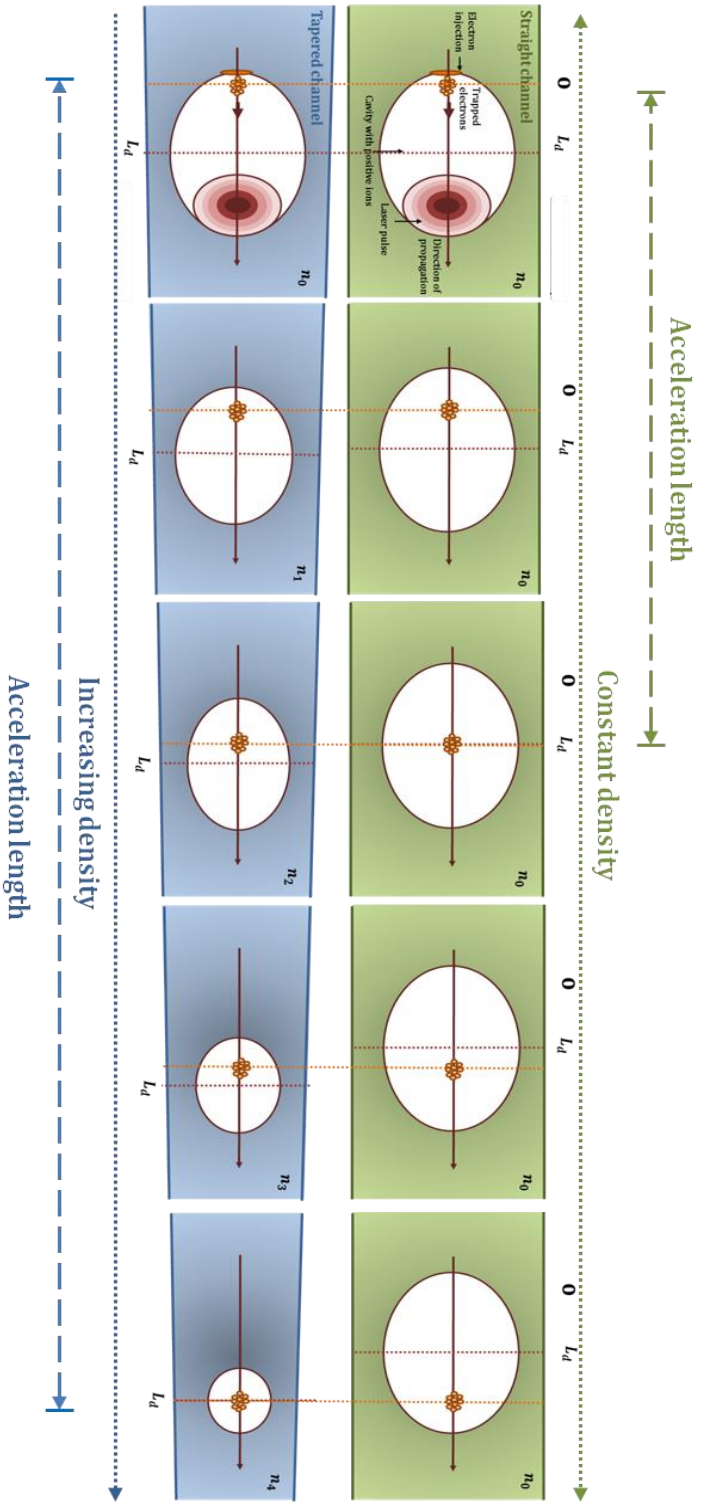

Figure 3.5: Schematic representation of electron acceleration showing the difference between laser-plasma interaction in uniform density and positively tapered density. In the tapered case, the electrons experience a greater acceleration over a longer distance.

Therefore, the electrons are maintained in the accelerating region of the wake over a longer distance and, consequently, both l_d and the maximum electron energy achievable are increased. These parameters, in the tapered case, scale as $dn(z)/dz$, where $n(z)$ is the rate of change of density along is longitudinal coordinate z and n_0 is the entrance density. A recent analytical study [8] investigated the enhancement of the energy both for an ideal non-linear taper and a linear taper, noting that the latter could be realisable experimentally. The study reported that, although a linear taper is not optimal, it can still increase the final energy by a factor of 3 compared with that of a uniform plasma channel (neglecting laser energy depletion).

Tapered channels, therefore, have the capacity to increase the maximum electron energy achievable for both 10-100 TW and larger petawatt-scale laser systems and a lower power, high repetition laser could furthermore be used for LWFA-driven undulator radiation sources (section 1.2.1).

3.2.1 Beam size oscillations in tapered waveguides

In the tapered channel case (longitudinally varying density), from Eq. (3.11), the matched spot size is given by

$$w_{\mathrm{M}}(z) = 2\sqrt{\frac{r_{ch}(z)c}{\omega_p(z)}} \quad . \tag{3.13}$$

Introducing non-dimensional variables $\zeta = kz$, $\rho = kw(z)$, $\rho_m = kw_{\mathrm{M}}(z)$, $k = 2\pi/\lambda$ and substituting into Eq. (3.11) results in [9]

$$\rho''(\zeta) = 1/\rho^3 - \rho/\rho_M^4 = -4\delta/\rho_{\mathrm{M}}^4 + O(\delta^2) \tag{3.14}$$

with $\delta = \rho - \rho_M$.

The solution of Eq. (3.14) is obtained as

$$\rho(\zeta) = \rho_{\mathrm{M}}(\zeta)\left[1 + (\delta_0 \cos(\varphi(\zeta))/\rho_{\mathrm{M0}}) - (\delta_0\, \rho'_M(\zeta) \sin(\varphi(\zeta)/2)\right] \tag{3.15}$$

$$w(z) = \frac{\rho(\zeta)}{k}, \tag{3.16}$$

where the initial delta parameter,

$\delta_0 = k\,(w_0 - w_{M0})$, $\varphi(\zeta) = 2\int_0^{L\zeta} 1/\rho_M(\zeta)^2 d\zeta$, normalised capillary length, $L\zeta = k * L$ and $\rho_{M0} = k(w_{M0})$ [9].

As an example of beam scalloping for a tapered capillary (112 μm to 77 μm), consider the behaviour of a laser pulse of wavelength 800 nm propagating through a 4 cm long channel with initial plasma density $n_0 = 2 \times 10^{18}\text{cm}^{-3}$ and w_M = 41 μm, for three different values of w_0. The evolution of the beam size along the waveguide is presented in Fig. 3.6 for the three cases obtained using Eqs (3.15) and (3.16). The matched condition is clear when $w_0 = w_M$ and the constant spot size is maintained throughout the capillary. During laser pulse propagation, when the pulses are not matched into the capillary waveguide, they experience oscillations in their radius and the exit waist is insensitive to the entrance waist in this particular case. Clearly, there is a non-uniform scalloping period because of the density gradient but, apart from that, behaviour is similar to that in a straight capillary.

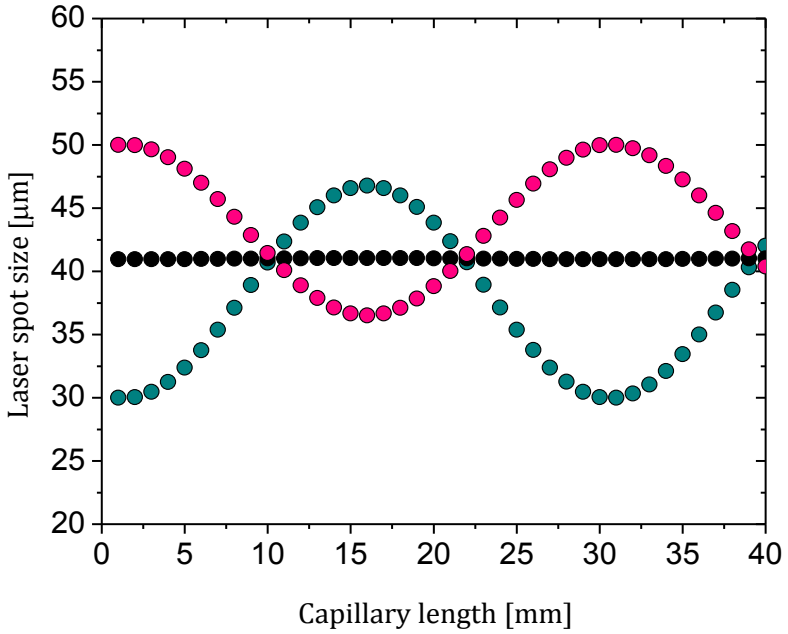

Figure 3.6: Variation of the laser spot size through a tapered capillary waveguide with the matched spot size $w_M = 41\ \mu m$. Initial laser beam waists of 30, 41 and 50 μm are indicated by green, black and pink circles respectively.

3.3 Hydrogen-filled capillary discharge waveguide

A promising technique used to create the described type of plasma channel is the gas-filled (usually hydrogen) capillary discharge waveguide [2, 4]. The waveguide serves as a cylindrical cavity in which to confine plasma and guide a laser pulse [3]. Numerical simulations for a gas-filled capillary discharge waveguide have been conducted by Bobrova *et al.* [3] and the results are shown in Fig. 3.7. From these results, the dynamics of the H-filled capillary discharge waveguide have been identified as occurring in three stages.

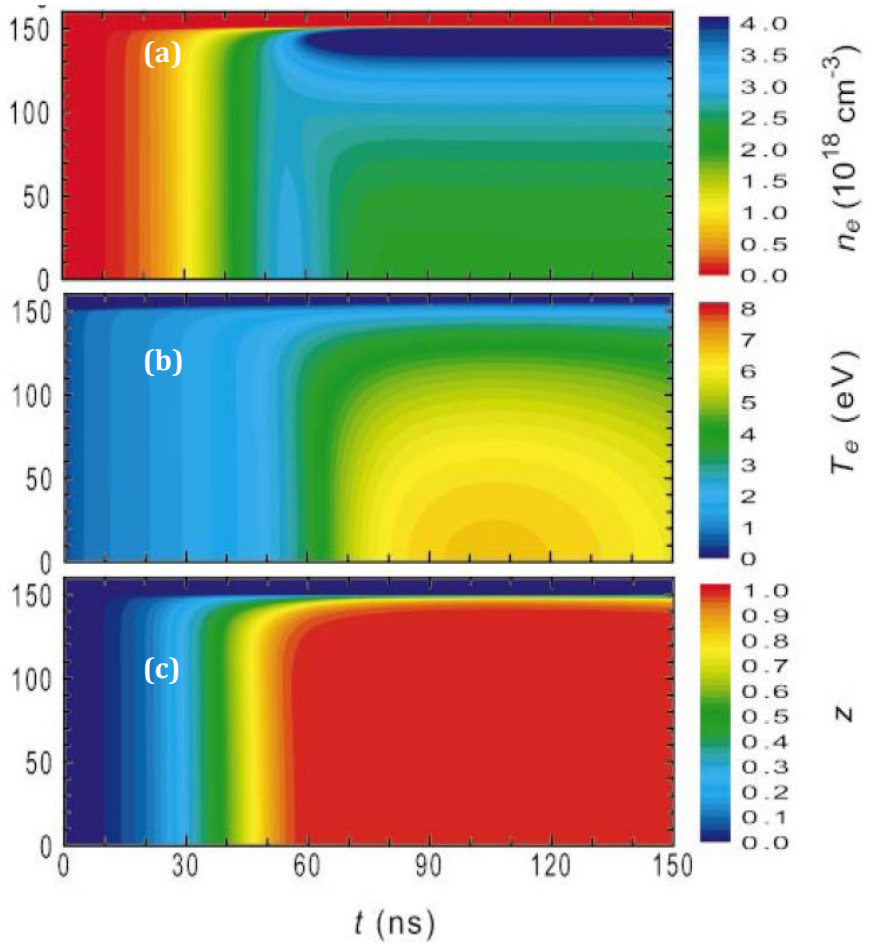

Figure 3.7: Results of a simulation of capillary discharge dynamics for an alumina capillary of 300 μm inner diameter pre-filled with 67 mbar of hydrogen. (a) and (b) show distributions in the (r, t) plane of electron density in units of 10^{18} cm^{-3} and temperature in units of eV, respectively. (c) shows the distribution of the degree of ionisation of hydrogen. From Bobrova *et al.*[3].

In the first stage, the electron density, temperature and degree of ionisation distribution remain homogenous because the pressure inside the capillary remains constant. The three plasma parameters grow linearly with time until full ionisation is reached. In the second stage (quasi-equilibrium), the increasing electric current induces enhancement of the plasma temperature. The plasma is cooled near the wall, producing a heat flow due to thermal conduction. The radial plasma temperature distribution is inhomogeneous.

The last stage involves quasi-equilibrium between Ohmic heating and cooling to the capillary wall. The radial distribution of the plasma parameters stays almost constant in time because the timescales of thermal conduction (~10 ns) and penetration of the electric field into the plasma (~2 ns) are much less than the discharge time (~200 ns). The plasma pressure in this quasi-steady-state equilibrium is almost constant across the capillary. Assuming that the electron temperature is equal to the ion temperature and there is no thermal radiation, the plasma distribution is determined by the balance between Ohmic heating on-axis and cooling to the wall.

3.3.1 Inverse bremsstrahlung heating

Absorption is a physical process or collection of processes that take place when the energy transfers from the laser pulse to the plasma. One of the most dominant absorption mechanisms is inverse bremsstrahlung absorption [10]. In this mechanism, an incident laser field cannot impart any energy since the electron has no net gain of energy over a cycle of the electric field. However, in plasma during oscillation, if the electron collides with an ion, the energy will transfer from the electron to the ion. This means that the laser pulse energy will decrease as its energy is transferred initially to the electrons and the temperature of electron plasma will increase. Then there is an increase in the ion-plasma temperature because the electrons in turn collide with the ions.

In a hydrogen-filled capillary discharge waveguide, the absorption rate of the laser beam intensity can be evaluated. During the collision between the electron and the ion in the plasma, the electron-ion collision frequency ν is given by [11]

$$\nu = \frac{{m_e}^{1/2}\omega_p^2 Z^2 e^2 \, ln\,(\,\lambda_D/b_0)}{4\pi\varepsilon_0 T^{3/2}} = \omega_p \, \frac{ln(\,\lambda_D/b_0)}{(\,\lambda_D/b_0)} \quad , \tag{3.17}$$

where λ_D is Debye length $= \sqrt{T\epsilon_0/n_e\, e^2}$, b_0 is the impact parameter $= Ze^2/4\pi\varepsilon_0 T$, Z is the atomic number of fully ionised plasma and T is the temperature of the plasma. It can be seen that $\nu \propto T^{-3/2}$.

The imaginary part of the refractive index is the absorption coefficient k which is related to the absorption constant K is [12]

$$K = 2\omega\, k/c = (2\omega/c)\sqrt{0.5(A-B)} \quad , \tag{3.18}$$

where $A = B^2 + \left[(\nu/\omega)\left(\omega_p^2/(\,\omega^2+\nu^2)\right)\right]^2$, $B = 1 - (\omega_p^2/(\,\omega^2+\nu^2))$ and ω is the laser frequency.

The meaning of the absorption constant K and the effect of the plasma temperature on absorbed laser energy can be seen in the special case of plasma from the attenuation of the laser intensity I of the laser light passing along the x direction by [12]

$$I/I_0 = \exp(-Kx) \ . \tag{3.19}$$

For a capillary of diameter 280 μm and length 4 cm and an 800 nm laser pulse propagating in hydrogen plasma (Z = 1) with density of n_e = 1.5 × $10^{18}\ cm^{-3}$, the dependence of the absorption rate on the plasma temperature is shown in Fig. 3.8. It can be clearly seen that the absorption rate sharply falls with increasing the plasma temperature. For experimental parameters relevant to the work in this thesis, the plasma temperature is typically < 10 eV [5]. These relatively low temperatures mean that the laser energy absorption through inverse bremsstrahlung heating cannot be neglected since it will decrease the laser transmission efficiency through the waveguide.

However, these values of temperature have to be corrected as soon as the electrons start oscillating in the electromagnetic field of the laser pulse to take into account the new temperature. The corrected temperature can be obtained from the corrected velocity which is given by

$$v_{el} = \sqrt{{v_{ei}}^2 + {v_0}^2} \tag{3.20}$$

where v_{el} is thermal velocity of electron in the electromagnetic field of the laser, v_{ei} is thermal electron velocity without the electromagnetic field and $v_0 = (a_0 c)$ is the maximum amplitude of the quiver velocity in the E-field of the laser pulse. The average over the velocities of v_{el} has been performed to express the velocity as a function of the corrected thermal temperature $T = m_e {v_{el}}^2$. The dependence of the corrected plasma temperature on laser intensity is presented in Fig. 3.9 and it shows that an intensity increase leads to an increase in the plasma temperature which, in turn, will lead to a decrease in the laser energy absorption.

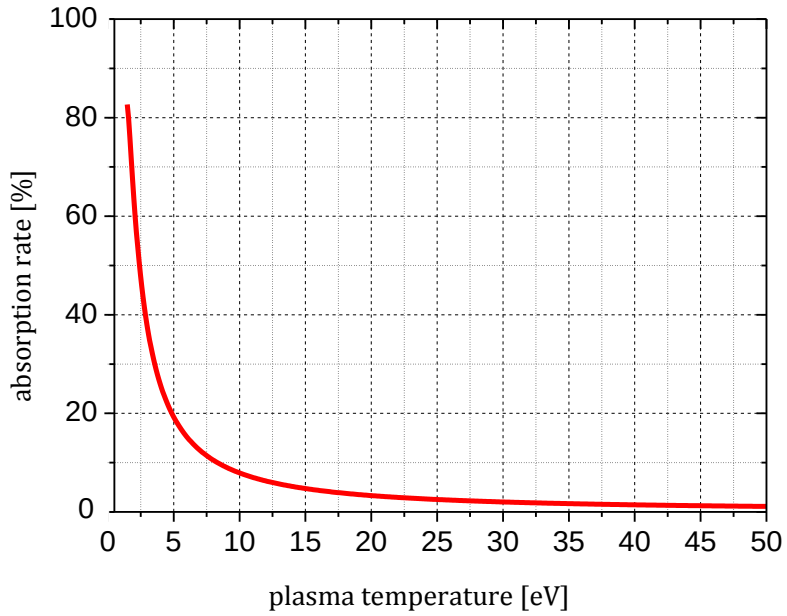

Figure 3.8: Absorption rate after propagation of laser light (800 nm) in a 4 cm long plasma channel with density of 1.5×10^{18} cm^{-3}.

At higher intensities, the laser energy transmission increases to close to 100% [13, 14] where the absorption due to inverse bremsstrahlung heating is reduced. However, at relativistic intensities, the transmission typically drops to ~60-70% for ultra-short duration laser pulses due to generation of a plasma wake and, therefore, significantly increased absorption [13-15].

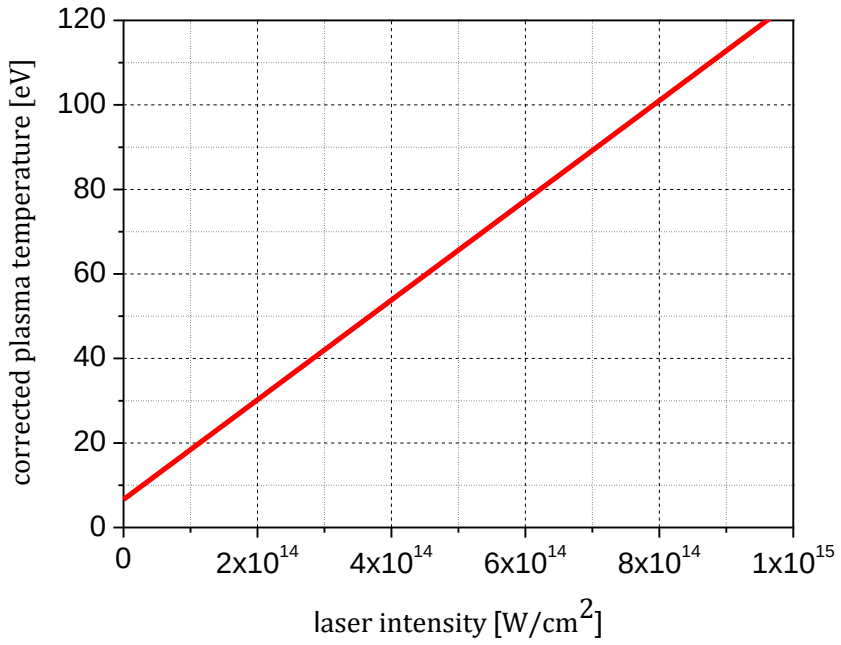

Figure 3.9: The corrected plasma temperature as a function of laser intensity.

3.4 Design of the hydrogen-filled capillary discharge waveguide

The design of the Strathclyde hydrogen-filled capillary discharge waveguide is suitable for both types of capillary (straight and linearly tapered capillaries) investigated in this thesis. They have been produced using a femtosecond micromachining technique [16].

The channel is formed by machining semi-circular channels of diameter d into two alumina (ceramic) or sapphire (crystalline) blocks, which are then carefully sandwiched together to form a narrow capillary of length L. These materials have high electrical resistivity, high dielectric strength, high thermal conductivity and impressive thermal stability [17]. Therefore, because of the excellent insulation properties, they are very reliable materials in high-power electronics. However, due to their hardness, it is difficult and expensive to machine. Femtosecond micromachining allows large band-gap materials, such as these, to be machined with minimal thermally and mechanically produced defects [17].

3.4.1 Machining straight capillaries

Machining capillaries is achieved by scanning a focused, high repetition rate, femtosecond laser beam over surface of the plates. One of the plates has additional surface grooves or bore holes micromachined into it to allow for gas to be injected into the capillary. The surface groove method requires careful plate alignment to enable a good O-ring seal around the gas fittings; therefore, the bore hole method is preferred (hole dimensions $\sim 700 \times 200$ μm, located 5 mm from the ends). Copper electrodes, connected to the output of a high voltage pulsed power supply, are positioned at either end of the capillary. On-axis apertures enable the laser pulses to be transmitted into the channel.

The experimental setup to perform femtosecond laser micromachining is shown in Fig. 3.10. Machining is achieved using the Strathclyde Terahertz to Optical Pulse Source (TOPS) femtosecond laser system [18] (intensity $\approx 10^{14}$ W/cm^2, duration = 50 fs, focal spot radius at a waist (radius at $1/e^2$) of 12 μm and 1 kHz pulse repetition rate). The focusing lens is mounted on a *Z*-axis translation stage for precise location of the focal position at the surface plane of the plates that are mounted together on *XY- axes* translation stages.

There are two key aspects of the femtosecond laser micromachining process that have a bearing on the scheme for obtaining a circular cross-section. Firstly, the laser focal spot size is much smaller than the capillary diameter. Secondly, as a laser beam scans across the target surface, the cross-sectional area of ablated material $A_{\text{scan line}}$, is inversely proportional to the scanning velocity v, $\left(A_{\text{scan line}} = V_{\text{pulse}} f\ (1/v)\right)$, where V_{pulse} is the volume removed by one pulse for a particular energy and f is the pulse repetition frequency. The individual pulses overlap, therefore, for the relevant velocity range and the laser can be assumed to be continuous. Hence, a complete capillary is formed by a series of many longitudinal scans (57 in this case, each repeated 16 times) at different radial positions [Fig. 3.11(c)], where the scan velocity is low close to the axis, and high at the outer edges [Fig. 3.11(a)].

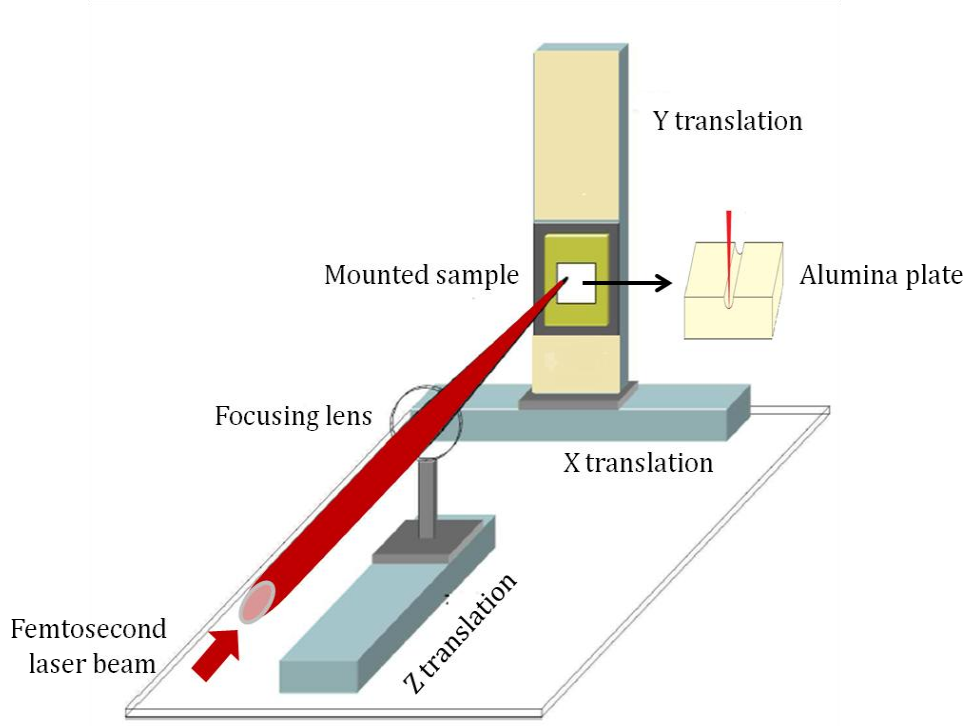

Figure 3.10: Micromachining setup showing the translation stages for both control of the sample position with respect to the laser position and precise positioning of the laser focus at the surface plane of the sample.

To machine uniform, straight capillary, the velocity motion of the scanning laser beam is constant along the longitudinal direction, utilising this velocity-to-depth mapping. A photograph of a completed capillary is displayed in Fig. 3.12 and optical microscope images of segments of straight capillary are shown in Fig. 3.13. The latter alumina capillary is 40 mm long and has a nominal design diameter of 280 μm. The laser pulse energy was 150 μJ (corresponding to an intensity of 10^{14} W/cm^2).

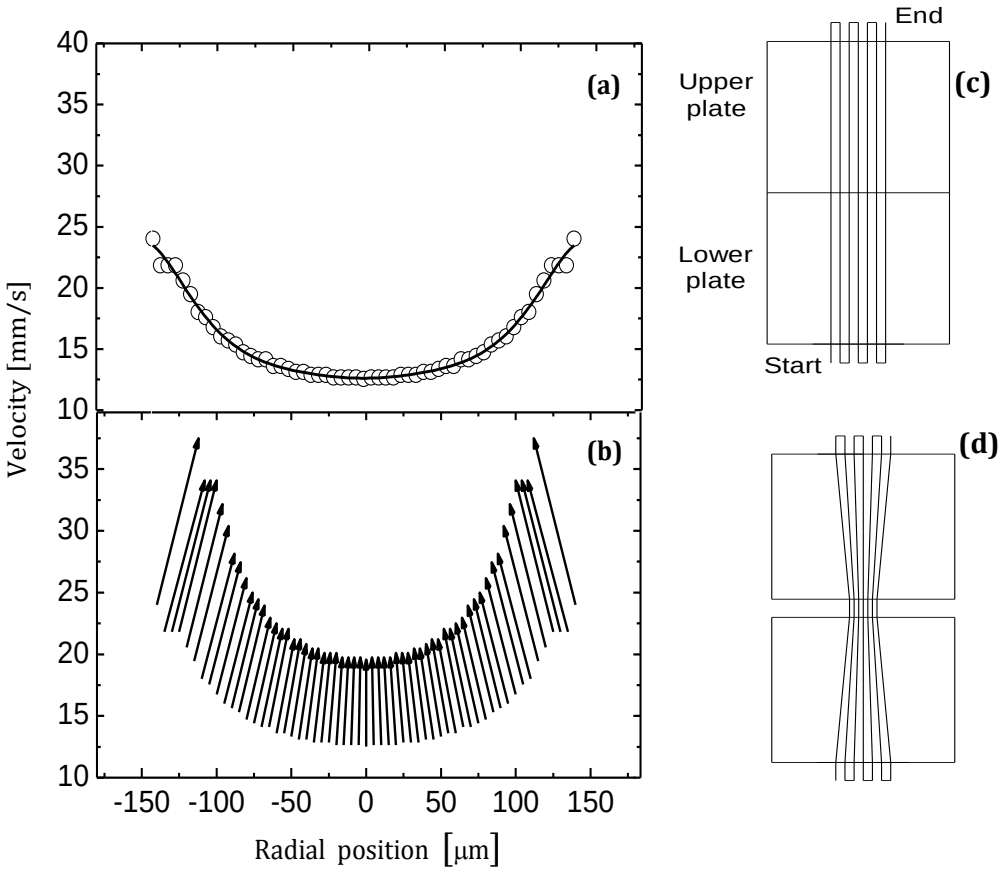

Figure 3.11: (a) Velocity profile used for machining straight capillary for a diameter of 280 μm over 40 mm, where the solid red line is a best-fit quadratic. (b) The start-to-end velocities of each scan line implemented for a diameter taper of 280 μm $\rightarrow$ 224 μm over 40 mm. (c) and (d) Scanning laser schematics for machining straight and tapered capillaries respectively.

Figure 3.12: Photograph of a complete used alumina capillary (length 40 mm). Dark carbonisation adjacent to the cathode location is seen around the waveguide entrance and the two gas inlets are visible on the top surface.

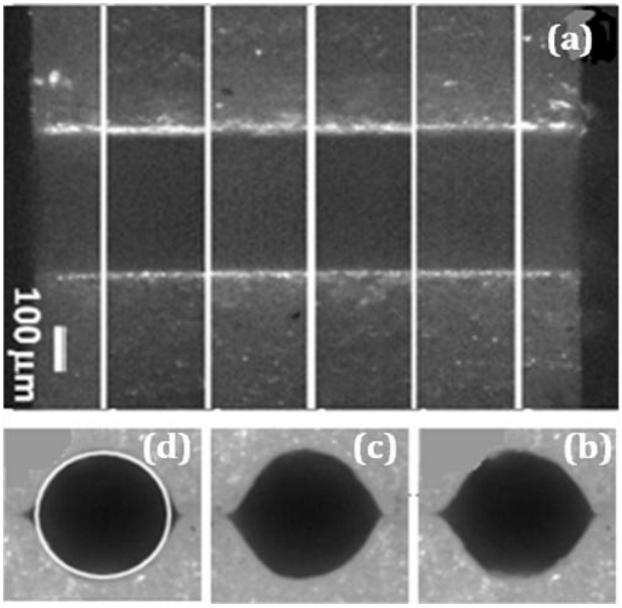

Figure 3.13: Optical microscope images of a straight capillary showing (a) sampled longitudinal positions along one plate and (b) and (c) both ends of the aligned capillary. (d) One end with a superimposed circle of diameter 280 μm. The indicated scale applies to all images.

3.4.2 Machining linearly tapered capillaries

The tapered capillaries are micromachined in a similar technique to straight capillaries but require two modifications. Firstly, the scanning direction is no longer only parallel to one axis. Secondly, as the scanning laser progresses from the wide end to the narrow end, its velocity must increase to maintain a semicircular ablation depth (which is inversely proportional to the velocity). Hence, the scanning laser is now accelerating instead of moving at constant velocity.

To determine the tapered capillary trajectory equations describing the evolution of the scanning laser position $x(t)$, velocity $v(t)$, and acceleration $a(t)$ as a function of time t, per scan line, consider the profile of a linearly tapered channel given by [16]

$$r(x) = r + \propto x \ , \tag{3.21}$$

where $\propto = (r_2 - r_1)/L$ describes the rate of tapering, r_1 and r_2 are the start and end radii, respectively, and L is the capillary length.

As with the straight capillary, the number of scan lines is constant, however in this case the step size is smaller at the end because of the smaller radius. For tapering, the start and end velocities will therefore be different, and the ratio of the two are proportional to the square of the ratio of the radii

$$\frac{v(L)}{v(0)} = \left(\frac{r_1}{r_2}\right)^2 \quad , \tag{3.22}$$

where v (0) is the initial velocity for that particular scan line. In general, this results in v (x) varying as

$$v(x) = \frac{r_1^2\, v(0)}{(r_1 + \alpha x)^2} \quad . \tag{3.23}$$

From this, the expressions for the linearly tapered capillary channel trajectories can be derived

$$x(t) = \frac{1}{\alpha}\left(\sqrt[3]{3tr_1^2 v(0)\alpha + r_1^3} - r_1\right) \quad , \tag{3.24}$$

$$v(t) = r_1^2 v(0)/[r_1^2 3tv(0)\alpha + r_1^3]^{2/3} \quad , \tag{3.25}$$

$$a(t) = -2r_1^4 v(0)^2\alpha/-r_1^2[-3tv(0)\alpha + r_1]^{5/3} \quad . \tag{3.26}$$

Optical microscope images of a strongly linearly tapered capillary are shown in Fig. 3.14. The alumina capillary has a length of 40 mm and nominal design diameter of 280 μm → 168 μm ($\alpha = 1.4 \times 10^{-3}$ and laser pulse energy is ~150 μJ). Images of the longitudinal capillary widths [Fig. 3.14(a) and (b)] demonstrate that a smooth taper from the wide end to the narrow end has been machined into both plates. The end-on images, after aligning the two plates, are shown in Fig. 3.14(c) and (d). Dimensions of the major and minor axes for each best-fit ellipse are 330 × 280 μm and 196 × 170 μm, respectively.

3.5 New design of a high-voltage pulsed power supply for discharge capillary waveguides

Applications for the hydrogen-filled capillary discharge waveguide for LWFA [19-21] and Raman amplification [22, 23] requires stable plasma formation for consistent and reproducible synchronisation with the laser system. Plasma is generated in the capillary after applying a potential difference of ~20 kV across

the capillary (typically 30-40 mm in length) and subsequent rapid avalanche breakdown. Formation of a high current (~300 A) discharge pulse is evidence of near complete ionisation of the gas in the capillary [2].

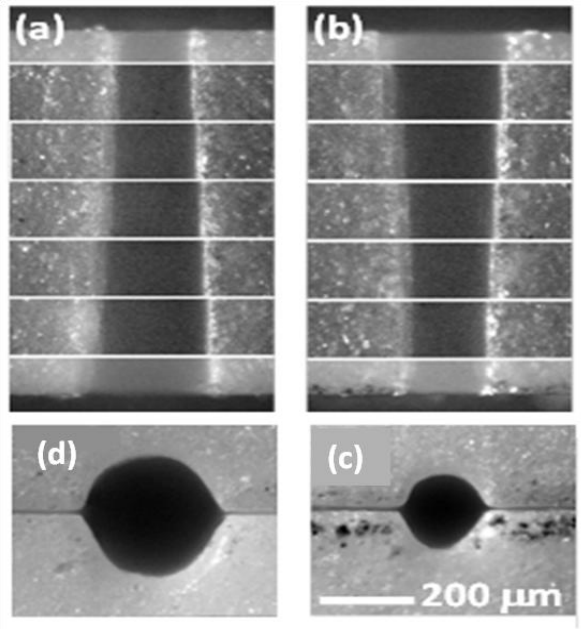

Figure 3.14: (a) Optical microscopy images of a linearly tapered capillary at regular longitudinal positions along the (a) lower and (b) upper plate surfaces. (c) and (d) show each end of the aligned capillary. The indicated scale applies to all images.

The plasma only needs to exist for the short time it takes for the laser pulse to propagate through the waveguide, that is, much less than 1 ns. Therefore, pulsed systems are an efficient method both for gas injection into the capillary on the ms timescale and plasma formation on the 100s of ns or μs timescale.

Many conventional high-voltage power supply designs can be used to produce the short duration voltage pulse to form the plasma discharge [24, 25]. Temporal jitter in the induced current pulse arises from the stochastic nature of the avalanche ionisation process and is crucially dependent on the rise time of the voltage pulse, which should be minimised. It is also a desirable characteristic to minimise the applied voltage for full ionisation to reduce electrical noise in the experimental environment.

Previous hydrogen-filled capillary discharge waveguide research at Strathclyde used a pulsed power supply unit that was based on toroidal magnetic transformer technology, which was used in Raman amplification studies [26, 27]. However, the large jitter from this power supply was problematic. Temporal fluctuations were not reproducible and were very large (many 10s of ns) at times, which made synchronisation of the laser pulse with the discharge extremely difficult, which has an impact on guiding and laser wakefield acceleration. As a solution, an all solid-state high-voltage pulsed power supply was designed and constructed, which helped to minimise temporal jitter.

3.5.1 Power supply circuit

The circuit of the new high voltage pulser based on a transmission line transformer is shown in Fig. 3.15. A DC power supply charges up a capacitor network (capacitance C = 118 nF) via a current-limiting resistor (resistance R = 2 MΩ). The maximum charging voltage is 7 kV, safely below the maximum rating of the capacitors. The positive terminal of the capacitor network, at *+HV*, is momentarily discharged to ground by a high peak current, high voltage solid-state switch (Behlke, HTS-121-160-FI with integrated free-wheeling diode). This drives the negative terminal of the capacitor network, initially at ground potential, to *–HV*, forcing a negative high voltage pulse to drive the transmission line transformer (TLT) connected to the load. The capillary initially acts as an open circuit but its impedance rapidly collapses on breakdown.

In Fig. 3.16, the circuit for the input side of the transformer is presented. With R limiting the current to 3.5 mA, capacitor charging to V = +7 kV is achieved. A network arrangement of 16 low cost capacitors keeps the size compact. A total storage capacitance of 118 nF gives a charging time constant of RC = 236 ms, compatible with discharge capillary operation at a pulsed repetition rate of 1 Hz. Furthermore, the total stored energy $E_{cap} = CV^2/2$ = 2.9 J is also minimised without introducing excessive voltage droop in the final output pulse. Switching is achieved with a 3 μs duration, +5 V voltage pulse applied to the Behlke switch

trigger input. The switch echoes this trigger behaviour, i.e., it closes for a duration of 3 μs before re-opening. A suite of protection circuitry including a pair of fast diode assembly (FDA) units (Behlke, FDA-160-150) is installed.

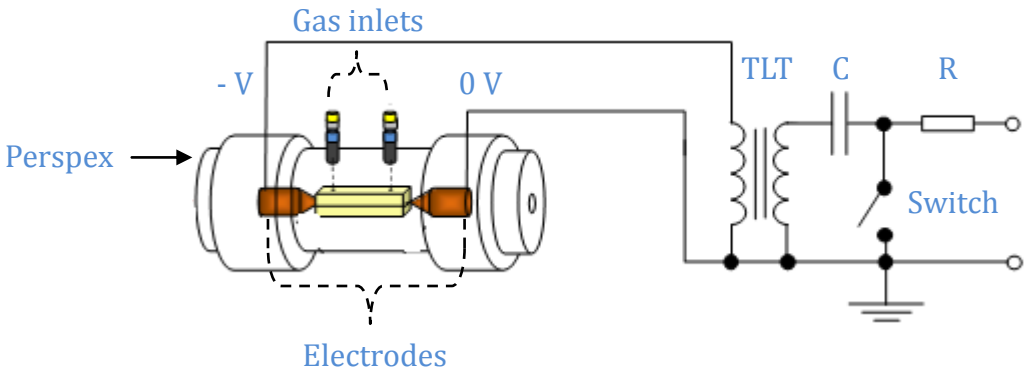

Figure 3.15: Schematic representation of the high voltage pulser connected to a capillary waveguide. The total storage capacitance (C) is 118 nF and the current-limiting resistance (R) is 2 MΩ.

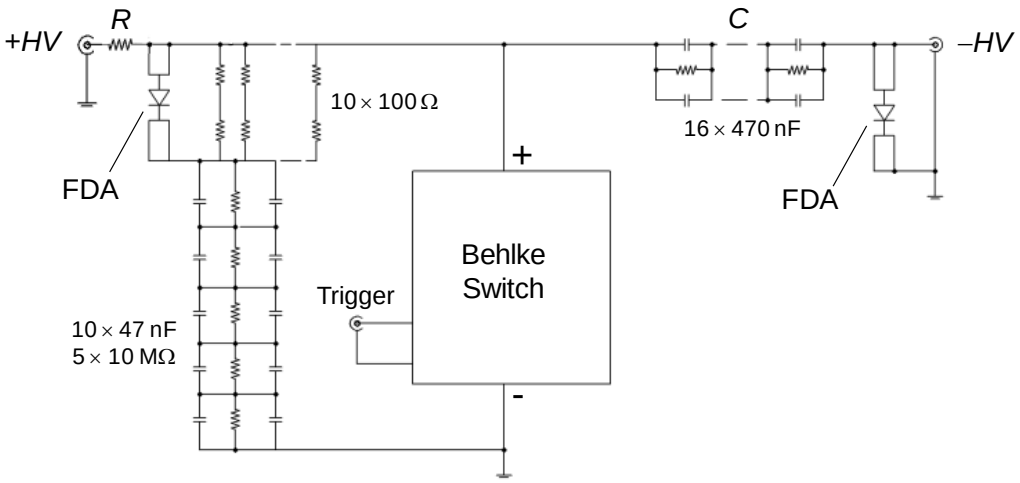

Figure 3.16: Circuit diagram of the pulser front end. A pair of fast diode assembly (FDA) units provides protection for the switch. Trigger is an applied +5 V pulse.

The basic circuit of the transformer and post-transformer can be seen in Fig. 3.17(a) and a photograph of the transformer is shown in Fig. 3.17(b). The transmission line transformer (TLT) is constructed using twelve lengths of coaxial cable (RG58C/U with characteristic impedance $Z_{cable} = 50\ \Omega$), each of which is 82 m long. The double-pass transit time for the voltage pulse is $2L/v$ =

0.84 μs, where v = 2.0×10^8 ms^{-1} is the velocity of propagation in the coaxial cable. The transmission line inputs are connected in parallel and the outputs in series; consequently, the voltage gain of an ideal TLT is simply equal to the number of transmission lines in the stack [28]. The transformer was wound through a single wooden core (for all stages of the transformer). The winding/core structure and each stage was electrically isolated using Mylar. The overall height and diameter of the transformer was 25 cm and 21 cm, respectively.

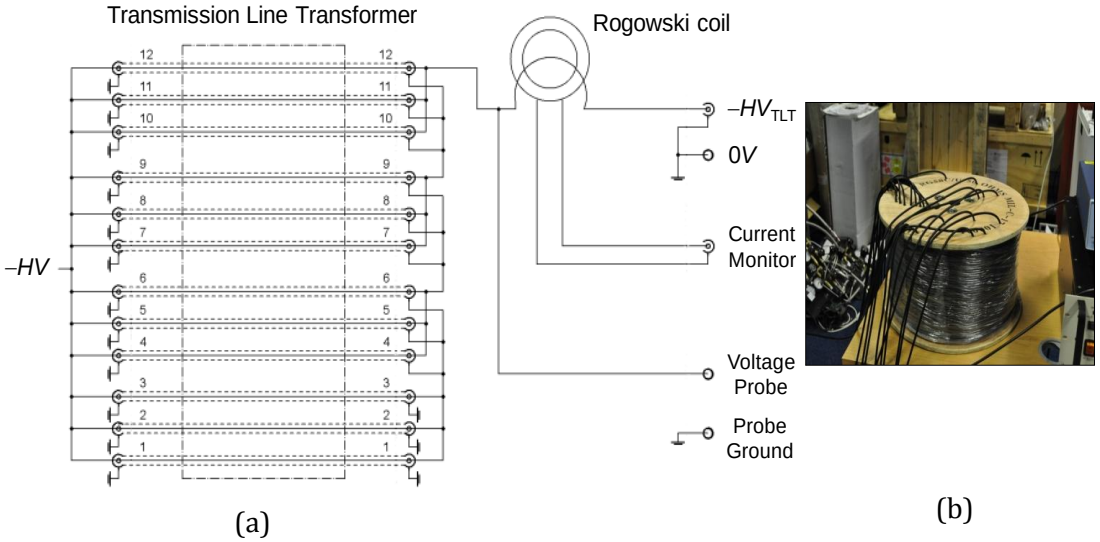

Figure 3.17: (a) Circuit diagram of the transmission line transformer and output end. The $-HV_{TLT}$ and $0V$ signals are output to the capillary electrodes along a pair of coaxial cable assemblies. (b) Photograph of the complete transformer.

Monitoring on the $-HV_{TLT}$ output line consists of a voltage probe (Tektronix, P6015A) and a current transformer (Stangenes Industries, 2–0.1W) coupled to a 1 GHz digital phosphor oscilloscope (Tektronix, TDS7104). The high voltage pulse is coupled to the capillary electrodes using insulated cable assemblies and vacuum grade electrical feed-throughs.

The global design is a four-stage TLT system with each stage comprising three coaxial cables in parallel [29] to give a total impedance of each stage of $Z_{stage} = Z_{cable}/3$ = 17 Ω. This ensures that the current limit due to the cables is now V/Z_{stage} = 412 A, i.e., well above that required (~250 – 300 A) for the

desired plasma density, instead of V/Z_{cable} = 140 A. The four-stage TLT has a measured voltage gain of 3.2, i.e., efficiency of 80%, such that the maximum applied voltage across the capillary can be 22.4 kV.

3.5.2 Testing the new high-voltage pulsed power supply

The pulsed power supply was initially tested in a vacuum chamber using two capillaries (straight and tapered) for plasma production. The straight sapphire crystal capillary was 4 cm long with a constant diameter of ~280 μm. The 4 cm tapered capillary has an internal structure that tapers linearly from about 330 μm to 280 μm. Hydrogen gas backing pressure was in the range 50–100 mbar. A photograph of the visible light emission from the plasma discharge is shown in Fig. 3.18. Uniform emission along the entire length of the capillary is evidence of good plasma channel formation.

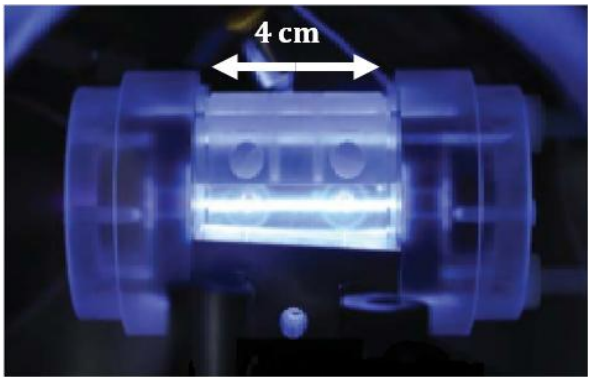

Figure 3.18: Photograph of plasma discharge formed by HV pulser with TLT in a sapphire capillary with gas backing pressure of 70 mbar.

The measurements of the voltage, current and rise time at different settings of the DC charging voltage are presented in Table 3.1. As the DC charging voltage increases, there is a clear increase in the peak voltage across the capillary as well as a decrease in the voltage pulse rise time. This is probably because with increasing the DC voltage the capacitor is charging much faster and therefore reaching the breakdown voltage much quicker.

Breakdown, as is evident from the current flow, is initiated for peak voltages between 6.4 and 9.1 kV. Typical voltage and current pulses are shown in

Fig. 3.19. The current reaches a maximum value of 284 A indicating a high degree of ionisation, the full-width at half-maximum pulse duration of the main peak is 900 ns and greater than 90% of the peak value is maintained for ~500 ns.

DC voltage (kV)	Voltage peak (kV)	Current peak (A)	Rise time (ns)
1	3.2	-	-
2	6.44	-	-
3	9.12	101	195
4	10.7	148	150
5	11.7	193	121
6	12.2	235	103
7	12.9	277	93

Table 3.1: Voltage, current and voltage pulse rise time measurements at different settings of DC charging voltage.

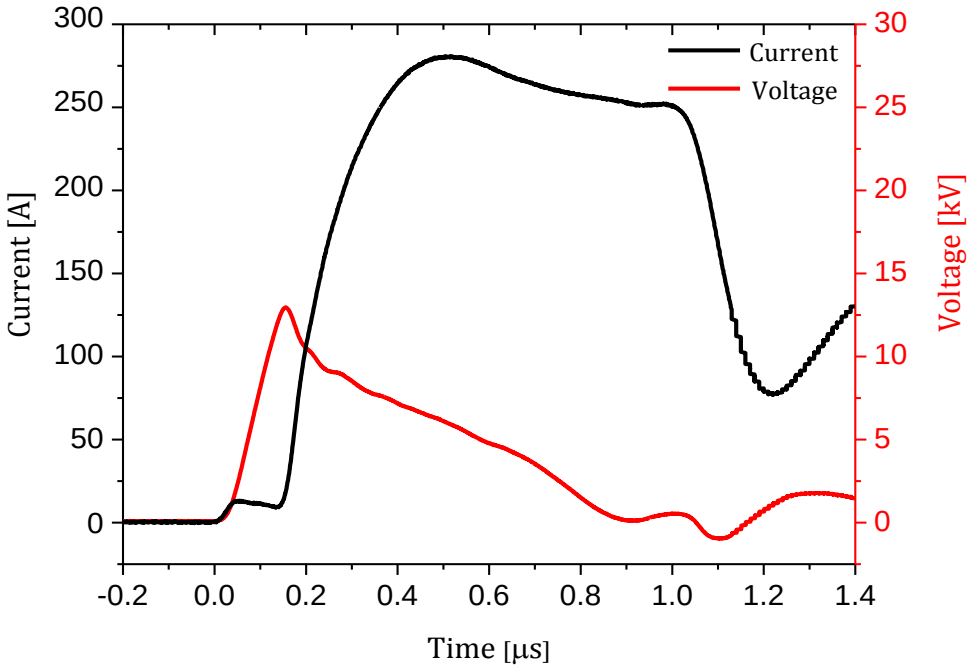

Figure 3.19: Typical discharge current and voltage traces for the straight capillary at the maximum applied voltage (21 kV) and at backing pressure of 100 mbar.

Temporal jitter in the leading edge of the current pulse is measured to be as low as 4.0 ns, as shown in Fig. 3.20. This is because the fast rise time (93 ns at backing pressure of 103 mbar) of the driving voltage pulse, as presented in Fig. 3.19, leads to rapid avalanche ionisation. The effect of the pressure of hydrogen on the jitter at the maximum DC voltage has been investigated (Fig. 3.21). There is a clear dependence with backing pressure and the lowest jitter (4 ns) is obtained at the highest pressure studied.

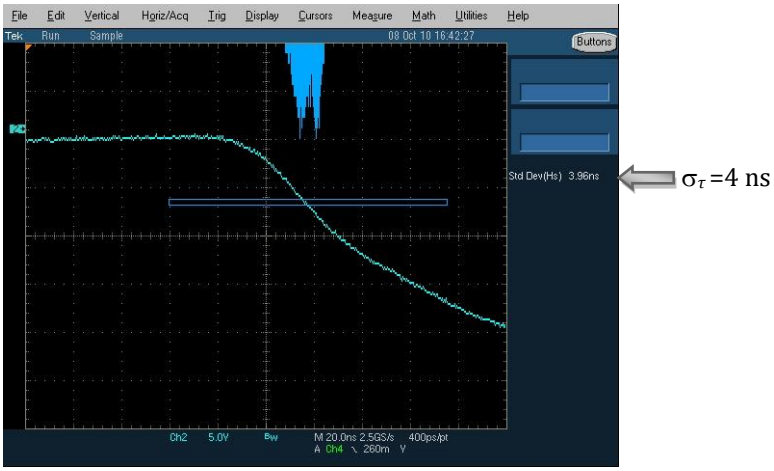

Figure 3.20: Oscilloscope screen shot showing histogram of 100 shots with a current pulse r.m.s. jitter σ_τ = 4.0 ns. DC charging voltage is 7 kV and backing pressure is 103 mbar.

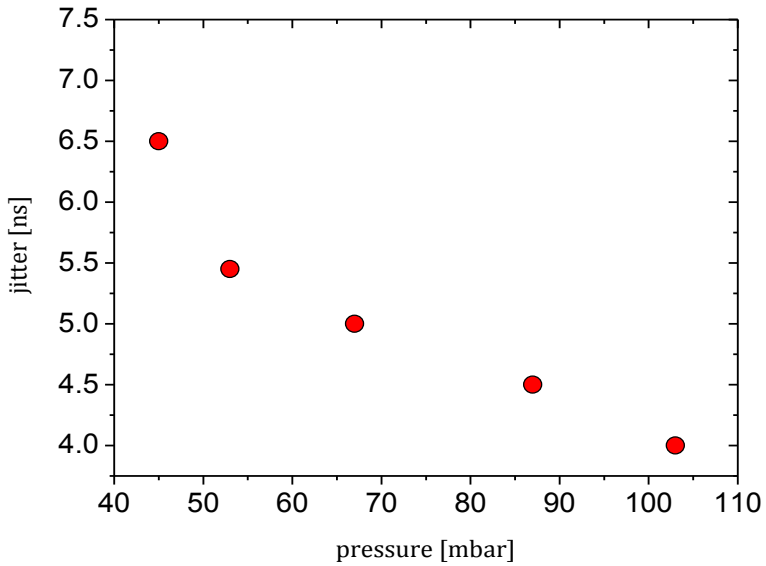

Figure 3.21: Current pulse r.m.s. temporal jitter as a function of gas backing pressure.

A comparison has been made between the new pulser and the old ferrite toroid power supply. The latter pulser applies a maximum of 16 kV across the capillary and has historically suffered from significant shot-to-shot fluctuations of the current pulse profile and relatively large temporal jitter. The voltage pulse produced by the old high voltage power supply is compared with that produced by the new high voltage pulser in Fig. 3.22. Note that the new pulser shows a marked improvement in the pulse rise time (95 ns as compared with 300 ns) and this is borne out in the subsequent current pulse jitter, as shown in Fig. 3.23, which shows a factor of ~ 8 reduction for the new solid-state-based pulser.

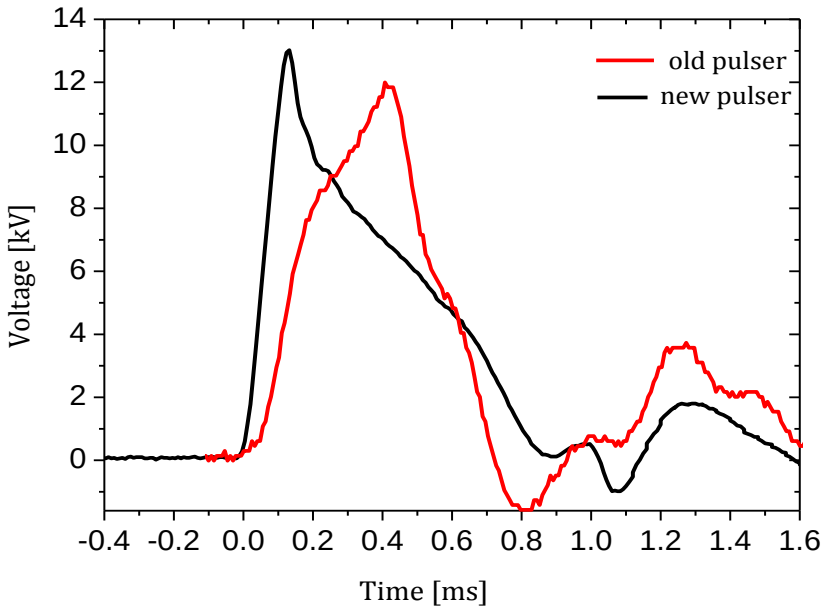

Figure 3.22: Comparison between the respective voltage pulses for old and new pulsers. The voltage pulses for the old and new pulsers are shown by the red and the black traces respectively.

A similar behaviour is found on testing a tapered capillary. The shot-to-shot stability in the profile has also been investigated switching the cathode from the large end to the small end of the capillary for a tapered capillary of diameter 325 μm to 274 μm. Fig. 3.24 shows temporal jitter measurements for switched polarity electrodes measured as a function of the applied voltage across the capillary for a backing pressure of 100 mbar. It can be seen that measurements of temporal jitter (acquired over 50 shots) using the tapered capillary is

impressively low (4-5 ns) for the higher applied voltages. No significant difference in the measured jitter is measured switching cathodes from the large end to the small end of the tapered capillary.

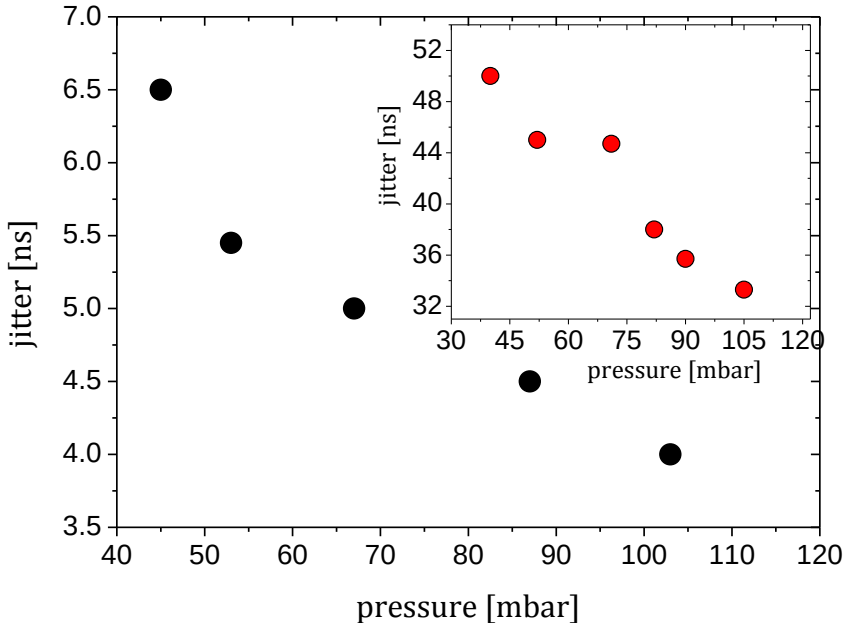

Figure 3.23: Comparison between the jitter from each pulser as a function of the pressure where the black and red solid circles denote the new pulser and old pulser respectively.

Also, as in the straight capillary, the current pulse jitter reduces at higher backing pressures, which is expected because higher densities of seed free electrons increase the ionising efficiency.

In both straight and tapered capillaries, the temporal fluctuations of the 900 ns current pulse are only ~0.4% of this period, which demonstrates excellent stability of the plasma current which is required for synchronisation with the femtosecond laser pulse.

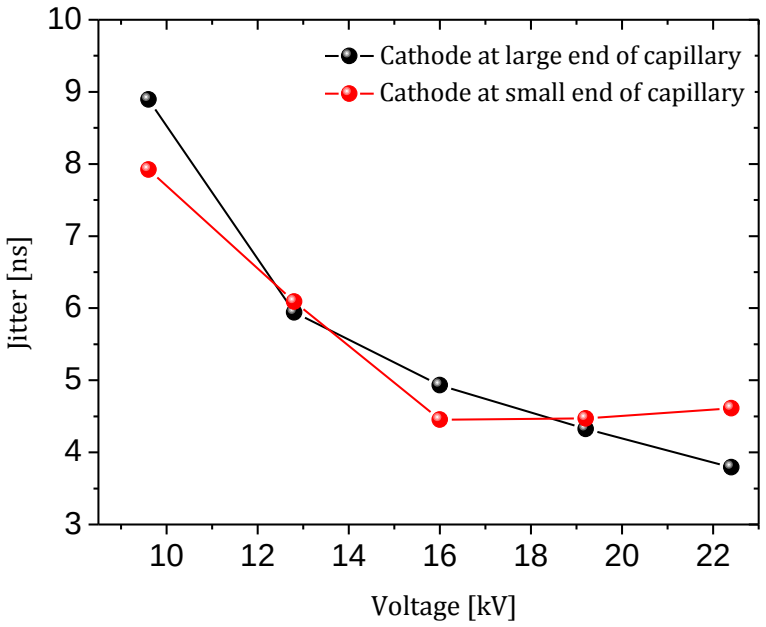

Figure 3.24: Comparison of temporal jitter measurements switching the polarity of the electrodes for a backing pressure of 100 mbar.

3.6 Conclusions

Hydrogen-filled capillary discharge waveguides suitable for LWFA experiments have been successfully produced and tested for producing plasma waveguides. Femtosecond laser micromachining is an effective technique for producing channels and appropriate acceleration of the scanning machining laser enables the formation of a linear tapered capillary cross-section. A strong taper of mean diameter 305 μm to 183 μm over a length of 40 mm shows that the range of diameters used in LWFA can be met by this technique. Micromachining controllability suggests that the final waveguide parameters can be tailor-made to suit particular applications and this may extend, in the future, to non-linear capillary structures for further enhancement of accelerator or Raman amplifier behaviour.

To apply plasma channels in experiments, a pulsed power supply unit has been developed. The new all solid-state pulser with TLT in a high voltage test chamber, provides a stable breakdown performance, which should be ideal for successful application in experiments. This is because the experiments require

stable plasma for consistent synchronisation with the high-power laser pulses arriving in the waveguide. Plasma generation in both straight and tapered capillaries has been shown to be comparable.

Low temporal jitter in the current pulse will be highly advantageous for these experiments where stable synchronisation between the formation of the plasma channel and the arrival time of the laser pulse is crucial. The temporal window (the time delay between the onset of the discharge current and the arrival of the laser pulse) for stable electron beam generation in the LWFA, for example, can be as narrow as 10 ns [14]. The pulser is relatively inexpensive, with the major costs being the high-voltage DC supply and the high-voltage switch.

References

1. D.J. Spence, P.D.S. Burnett, and S.M. Hooker, *Measurement of the electron-density profile in a discharge-ablated capillary waveguide.* Optics Letters, 1999. **24**(14): p. 993-995.
2. D.J. Spence and S.M. Hooker, *Investigation of a hydrogen plasma waveguide.* Physical Review E, 2000. **63**(1): p. 015401.
3. N.A. Bobrova, A.A. Esaulov, J.I. Sakai, P.V. Sasorov, D.J. Spence, A. Butler, S.M. Hooker, and S.V. Bulanov, *Simulations of a hydrogen-filled capillary discharge waveguide.* Physical Review E, 2001. **65**(1): p. 016407.
4. D.J. Spence, A. Butler, and S.M. Hooker, *First demonstration of guiding of high-intensity laser pulses in a hydrogen-filled capillary discharge waveguide.* Journal of Physics B: Atomic, Molecular and Optical Physics, 2001. **34**(21): p. 4103.
5. G. Vieux, *Broad-band linear Raman chirped pulse amplification in plasma.* (PhD Thesis), 2004. University of Strathclyde: Glasgow.
6. T. Katsouleas, *Physical mechanisms in the plasma wake-field accelerator.* Physical Review A, 1986. **33**(3): p. 2056-2064.
7. P. Sprangle, J.R. Penano, B. Hafizi, R.F. Hubbard, A. Ting, D.F. Gordon, A. Zigler, and J. T. M. Antonsen, *GeV acceleration in tapered plasma channels.* Physics of Plasmas, 2002. **9**(5): p. 2364-2370.

8. W. Rittershofer, C.B. Schroeder, E. Esarey, F.J. Gruner, and W.P. Leemans, *Tapered plasma channels to phase-lock accelerating and focusing forces in laser-plasma accelerators.* Physics of Plasmas, 2010. **17**(6): p. 063104.
9. B. Ersfeld, [private communication].
10. G. Pert, *Plasmas and laser light*. 1975, Wiley: New York.
11. R.J. Goldston and P.H. Rutherford, *Introduction to Plasma Physicsis*. 1995, Institute of Physics Press: Bristol.
12. H. Hora and H. Wilhelm, *Optical constants of fully ionized hydrogen plasma for laser radiation.* Nuclear Fusion, 1970. **10**(2): p. 111.
13. W.P. Leemans, B. Nagler, A.J. Gonsalves, C. Toth, K. Nakamura, C.G.R. Geddes, E. Esarey, C.B. Schroeder, and S.M. Hooker, *GeV electron beams from a centimetre-scale accelerator.* Nature, 2006. **2**(10): p. 696-699.
14. T.P. Rowlands-Rees, C. Kamperidis, S. Kneip, A.J. Gonsalves, S.P.D. Mangles, J.G. Gallacher, E. Brunetti, T. Ibbotson, C.D. Murphy, P.S. Foster, M.J.V. Streeter, F. Budde, P.A. Norreys, D.A. Jaroszynski, K. Krushelnick, Z. Najmudin, and S.M. Hooker, *Laser-Driven Acceleration of Electrons in a Partially Ionized Plasma Channel.* Physical Review Letters, 2008. **100**(10): p. 105005.
15. T.P.A. Ibbotson, N. Bourgeois, T.P. Rowlands-Rees, L.S. Caballero, S.I. Bajlekov, P.A. Walker, S. Kneip, S.P.D. Mangles, S.R. Nagel, C.A.J. Palmer, N. Delerue, G. Doucas, D. Urner, O. Chekhlov, R.J. Clarke, E. Divall, K. Ertel, P. Foster, S.J. Hawkes, C.J. Hooker, B. Parry, P.P. Rajeev, M.J.V. Streeter, and S.M. Hooker, *Investigation of the role of plasma channels as waveguides for laser-wakefield accelerators.* New Journal of Physics, 2010. **12**(4): p. 045008.
16. S.M. Wiggins, M.P. Reijnders, S. Abuazoum, K. Hart, G.H. Welsh, R.C. Issac, D.R. Jones, and D.A. Jaroszynski, *Note: Femtosecond laser micromachining of straight and linearly tapered capillary discharge waveguides.* Review of Scientific Instruments, 2011. **82**(9): p. 096104.
17. S.H. Kim, I.B. Sohn, and S. Jeong, *Ablation characteristics of aluminum oxide and nitride ceramics during femtosecond laser micromachining.* Applied Surface Science, 2009. **225**(24): p. 9717-9720.

18. D.A. Jaroszynski, B. Ersfeld, G. Giraud, S. Jamison, D.R. Jones, R.C. Issac, B.W.J. McNeil, A.D.R. Phelps, G.R.M. Robb, H. Sandison, G. Vieux, S.M. Wiggins, and K. Wynne, *The Strathclyde terahertz to optical pulse source (TOPS).* Nuclear Instruments and Methods in Physics 2000. **445**(1-3): p. 317-319.
19. T. Tajima and J.M. Dawson, *Laser Electron Accelerator.* Physical Review Letters, 1979. **43**(4): p. 267-270.
20. E. Esarey, C.B. Schroeder, and W.P. Leemans, *Physics of laser-driven plasma-based electron accelerators.* Reviews of Modern Physics, 2009. **81**(3): p. 1229-1285.
21. S.M. Wiggins, R.C. Issac, G.H. Welsh, E. Brunetti, R.P. Shanks, M.P. Anania, S. Cipiccia, G.G. Manahan, C. Aniculaesei, B. Ersfeld, M.R. Islam, R.T.L. Burgess, G. Vieux, W.A. Gillespie, A.M. MacLeod, S.B. van der Geer, M.J. de Loos, and D.A. Jaroszynski, *High quality electron beams from a laser wakefield accelerator.* Plasma Physics and Controlled Fusion, 2010. **52**(12): p. 124032
22. V.M. Malkin, G. Shvets, and N.J. Fisch, *Fast Compression of Laser Beams to Highly Overcritical Powers.* Physical Review Letters, 1999. **82**(22): p. 4448.
23. B. Ersfeld and D.A. Jaroszynski, *Superradiant Linear Raman Amplification in Plasma Using a Chirped Pump Pulse.* Physical Review Letters, 2005. **95**(16): p. 165002.
24. J. Jethwa, E.E. Marinero, and A. Muller, *Nanosecond risetime avalanche transistor circuit for triggering a nitrogen laser.* Review of Scientific Instruments, 1981. **52**: p. 989 - 991
25. V.K. Khanna, *Insulated Gate Bipolar Transistor IGBT Theory and Design*. 2003, John Wiley & Sons: New Jersey.
26. X. Yang, G. Vieux, A. Lyachev, J. Farmer, G. Raj, B. Ersfeld, E. Brunetti, M. Wiggins, R. Issac, and D.A. Jaroszynski, *Study of chirped pulse amplification based on Raman backscattering.* Proceedings of the SPIE, 2009. **7359**: p. 73590.

27. G. Vieux, A. Lyachev, X. Yang, B. Ersfeld, J.P. Farmer, E. Brunetti, R.C. Issac, G. Raj, G.H. Welsh, S.M. Wiggins, and D.A. Jaroszynski, *Chirped pulse Raman amplification in plasma.* New Journal of Physics, 2011. **13**(6): p. 063042.
28. P.N. Graneau, J.O. Rossi, and P.W. Smith, *The operation and modeling of transmission line transformers using a referral method.* Review of Scientific Instruments, 1999. **70**(7): p. 3180-3185.
29. R.A. Bendoyro, R.I. Onofrei, J. Sampaio, R. Macedo, G. Figueira, and N.C. Lopes, *Plasma Channels for Electron Accelerators Using Discharges in Structured Gas Cells.* IEEE Transactions on Plasma Science, 2008. **36**(4): p. 1728 - 1733.

CHAPTER 4

Capillary discharge waveguides: characterisation

In this chapter, the characterisation of plasma and laser guiding properties of the straight and linearly tapered capillary discharge waveguides, discussed in chapter 3, is presented. In the first section, the theory of Stark broadening of spectral lines of light produced by the plasma during discharge is given. This has been used experimentally as plasma density and temperature diagnostics. In the second section, the experimental setup for measuring the plasma properties and femtosecond laser guiding is presented. The characterisation of the plasma and demonstration of efficient guiding of low intensity, femtosecond duration laser pulses are presented for both capillary types and, finally, a conclusion is given.

4.1 Plasma density spectroscopic measurements using Stark broadening

Hydrogen neutrals in the plasma of capillary discharge waveguides emit light at optical wavelengths (Balmer lines) [1]. This light arises from electronic transitions between the atomic shells of hydrogen atoms of the background neutrals. By collecting that light plasma parameters such as the density and temperature can be measured by imaging the capillary exit plane onto the entrance slit of an optical spectrometer.

Measurement of the electron density in a plasma capillary is described in the following. The method is based on Stark broadening of the spectral lines of atomic hydrogen [2]. The creation of plasma is associated with a microscopic

electric field which interacts with the hydrogen atoms. Due to the statistical nature of this field, it results in broadening of atomic lines. For relatively cold and dense plasma, such as that produced inside the capillary, the linewidth is dominated by this effect. Two different spectral techniques have been used. Firstly, the Stark broadening of the Balmer lines yields information on the density. Secondly, the line intensity ratio between two lines provides information on the temperature, which is an important measurement for low temperatures because laser energy depletion due to inverse Bremsstrahlung can occur (section 3.3.1) [3].

4.1.1 Stark broadening of hydrogen Balmer lines

Line broadening in plasma is a result of two physical mechanisms. Firstly, Doppler broadening [4] occurs as a result of the thermal motion of radiators relative to the observer. Secondly, pressure broadening [5] is caused by the interaction of the radiators with surrounding particles and, in plasma, it is dominated by collisions between the radiators and charged perturbers. The electric fields cause Stark broadening.

The Doppler line profile is Gaussian, with a linewidth given by [4]

$$\Delta\lambda_D = 2\left[\frac{2kTln2}{mc^2}\right]^{1/2}\lambda_0\,, \tag{4.1}$$

where λ_0 is the unshifted wavelength, m is the radiator mass, k is Boltzmann's constant and c is the speed of light in vacuum. For the relevant temperature ($T < 10$ eV), the Doppler widths of the Balmer H_α (6562.7 Å) and H_β (4861.3 Å) lines are in the range of 0.3–0.8 Å. Stark broadening results from the interactions of radiator atoms with the electric field produced by the charged plasma particles at the location of the radiator. Thus it depends on the density of the charged particles in the plasma.

Hans Griem has calculated the details of Stark broadening in Hydrogen lines for diagnosing the plasma density from spectroscopic measurements [4]. The most investigated Stark-broadened spectral line is the Hydrogen Balmer H_α line. It is very popular because it lies in the visible spectrum and is very accessible

even at high densities. Ehrlich *et al.* used this technique to measure the density profile within the capillary waveguide [6]. The capillary was viewed longitudinally and a scan along the capillary diameter was used to obtain the radial electron density profile.

The electron density is determined from the linewidth of the hydrogen lines as [7]

$$n_e = 8.02 \times 10^{12} \left(\frac{\Delta\lambda_{1/2}}{\alpha_{1/2}} \right)^{3/2} , \qquad (4.2)$$

where the plasma density n_e is given in cm^{-3} and the full-width at half-maximum (FWHM) of the Lorentzian-shaped hydrogen Balmer line is given in Angstroms (after background subtraction). The parameter $\alpha_{1/2}$ depends on both the density of the plasma and weakly on its temperature; it is also different for each spectral line and values are tabulated in Griem's book [4].

In the set of measurements described here, the electron density was in the range of (10^{17}-10^{18} cm^{-3}). The Stark broadening width corresponding to these densities for H_α is of the order of (2-20 nm). This is why the Doppler broadening can be neglected.

Figure 4.1 summarises some experiments that have been performed to diagnose Stark broadening. In all these cases, the density was also measured with an independent diagnostic and the results were compared with Stark broadening of the H_α line [1, 8-10]. The dashed line shows the density from Stark broadening as predicted by Griem's theory [4] and the error bars account for temperature variations. It can be seen that the accuracy of the diagnostic decreases slightly at higher densities (> 2×10^{18} cm^{-3}).

4.1.2 Plasma temperature diagnostic

Another useful diagnostic is the intensity ratio of spectral lines. One of the most common tools is the ratio of the two major Balmer lines, H_α and H_β [11]. If the lines have Lorentzian shapes then the quasistatic theory can be applied and the population on each atomic shell can be assumed to follow Boltzmann distributions, which depends on the temperature of the plasma. Then the ratio

of the populations will be equal to the ratio of the spectral intensities of the lines, i.e. as the ratio of the two Boltzmann distributions as [11]

$$\frac{H_\beta}{H_\alpha} = 0.27 \left(\frac{\lambda_{\mathrm{H}\,\alpha}}{\lambda_{\mathrm{H}\,\beta}}\right)^3 e^{\frac{E_\alpha - E_\beta}{kT}}, \tag{4.3}$$

where the energy of each level in eV is $E_\alpha = 12.08$, $E_\beta = 12.74$ and $\lambda_{\mathrm{H}\alpha} = 656\,\mathrm{nm}$, $\lambda_{\mathrm{H}\beta} = 486\,\mathrm{nm}$. This equation can be solved for the plasma electron temperature kT in eV. Extra care has to be taken if the spectral lines are polluted with background radiation; then the pure line intensity has to be found out first by removing the background contributions. From Fig. 4.2, which shows the temperature dependence on this ratio for the two main Balmer lines, an estimate of plasma temperature can be found.

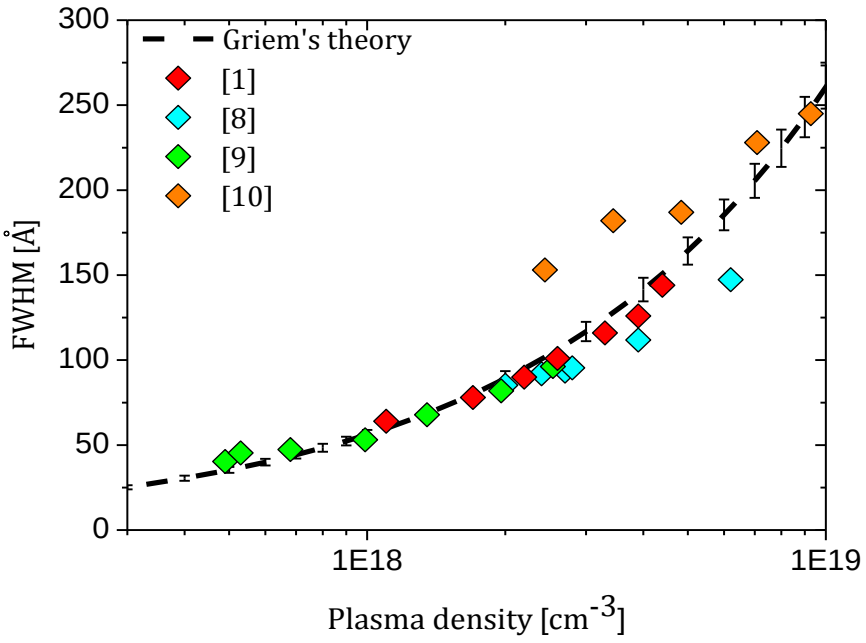

Figure 4.1: Comparison of experimental data [1, 8-10] of Stark broadening with Griem's theory.

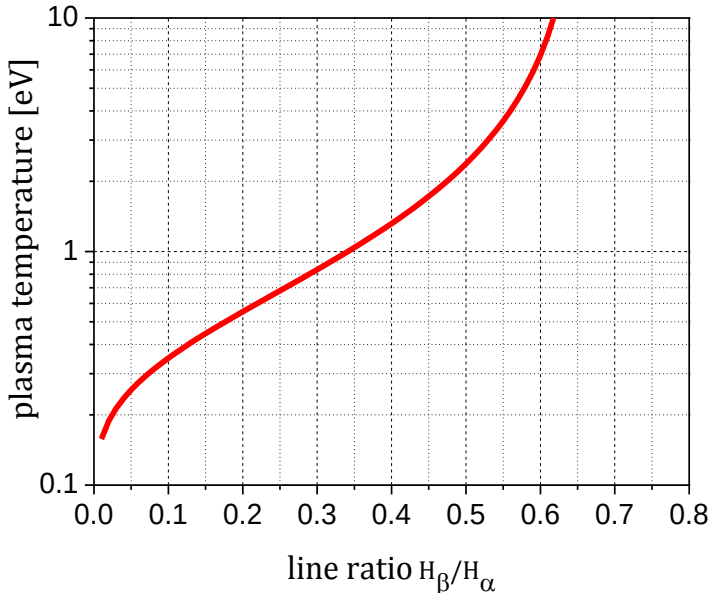

Figure 4.2: Plasma temperature as a function of the line intensity ratio of the Balmer lines.

4.2 Plasma diagnostics and laser guiding setup

The femtosecond laser system applied for the micromachining (and described in section 3.2.2.1) is strongly attenuated to a focal intensity of $\approx 10^{12}$ W/cm^2 for use in the guiding experiment, as shown in Fig. 4.3. The laser beam is focused to a spot size approximately equal to the correct matched spot size at the entrance of the waveguide using a 40 cm focal length lens. Further attenuation by a series of neutral density filters reduces the beam intensity for imaging onto a CCD camera (Point Grey Research, Flea2). The beam spot size is adjusted and aligned using variable apertures and the beam height set using a pair of pinholes. During guiding, several attenuation filters are removed to increase the ratio between laser light and the hydrogen emission light to reduce the background signal for accurate measurement of the guiding efficiency.

To help in the alignment of the femtosecond laser through the capillary, a low-power red laser diode is co-aligned with the path of the femtosecond beam and can be easily inserted with a removable mirror set on a magnetic base. This permits the multiple axes of the capillary housing to be carefully aligned, first

with the laser diode directed through the centre of the capillary and then with the femtosecond laser beam.

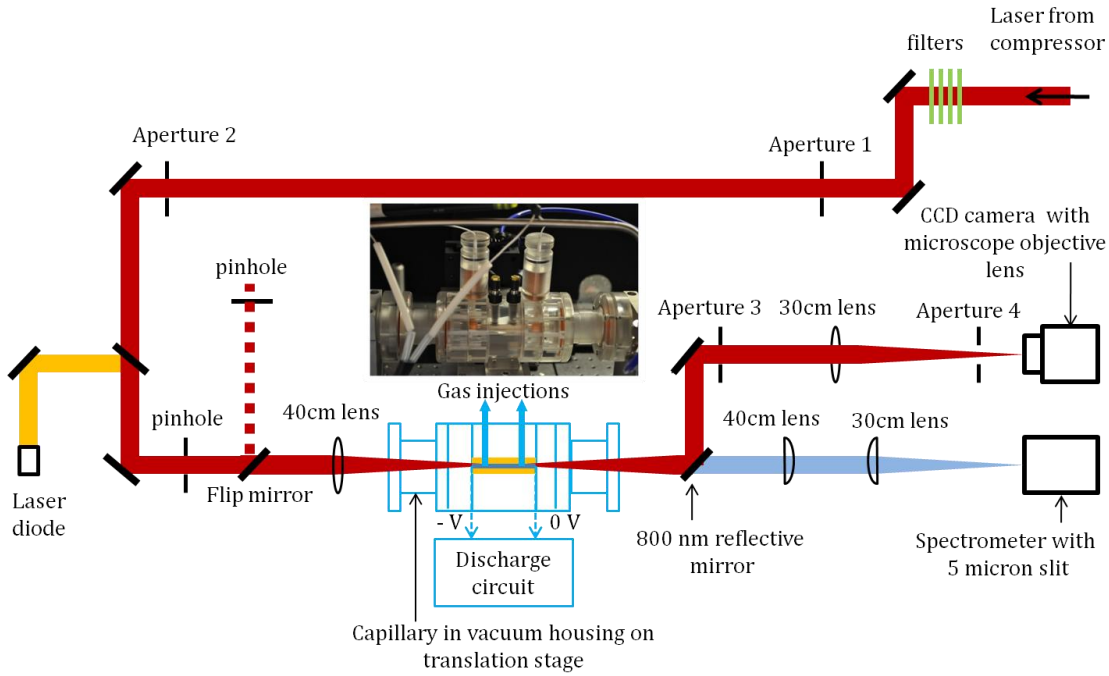

Figure 4.3: Schematic diagram of the experimental setup for characterising the plasma and laser guiding in the capillary discharge waveguide. The laser guiding set up shows the femtosecond laser path (solid red line) and the alignment laser diode path (yellow dotted line). The path for the plasma spectroscopy measurements is also presented as the solid blue line.

The waveguide structure is mounted on a 4-axis stage external to the vacuum system consisting of a linear transverse, linear vertical and two rotation stages. The translation stages are used to align the entrance of the capillary with the laser beam. This completes the basic alignment method used in the experiments.

After alignment, the femtosecond laser beam is imaged onto the CCD camera using an achromatic doublet lens and a microscope objective lens (×4 magnification), all of which are initially set to image the entrance plane of the capillary. This provides a reference laser beam input image for measuring the guiding efficiency of the laser pulses. With the capillary in place, for measuring the energy transmission of the guided pulse when the laser is synchronised with

the discharge, the entire imaging system is translated 4 cm back to capture the exit plane of the capillary.

Hydrogen is injected into the capillary by means of a pulsed solenoid valve connected to a hydrogen gas cylinder. The gas flow is pulsed at 1 Hz and synchronised to the discharge. The gas flow into the capillary (backing pressure) is controlled using a manual valve and monitored with a pressure gauge.

A waveform generator (LeCroy LW120) is used to trigger (1 Hz) the high voltage pulsed power supply (described in section 3.3) to apply a high voltage pulse across the capillary. Copper electrodes are mounted on each side of the capillary and connected to the negative and ground terminals of the high voltage pulser so that, when the capacitor network discharges via the TLT, it drives a negative high voltage pulse to the ground terminal through the capillary.

The timing of the discharge current with respect to a laser system driver signal (from a Medox Pockels cell driver unit) is monitored on an oscilloscope taking into account that the laser pulse arrives at the capillary 230 ns after the leading edge of the Medox driving pulse (measured with a photodiode). This allows the HV trigger pulse to be delayed with respect to the laser pulse using a delay generator, which is used to scan across a range corresponding to the 900 ns pulse duration of the discharge current.

For the plasma spectroscopy measurements, the plasma light emitted from the capillary is collected through two focusing lenses (f = 400 mm and 300 mm respectively) with a magnification factor (0.75) and imaged onto the entrance slit (width 5 μm) of an optical spectrometer (Ocean Optics, SD2000 spectrometer), which has a spectral range of 200-900 nm, a resolution of 1.1 nm and an integration time of 2 ms. The spectrometer is aligned using the laser diode focused into the capillary using a 40 cm focal length lens. The spatial resolution is determined by the size of the entrance slit of the spectrometer. The Stark broadening analysis of the hydrogen Balmer lines, particularly H_α and H_β, is applied to diagnose the plasma.

4.3 Experimental results

4.3.1 Plasma density and temperature measurements

In this section, the sets of data that investigate the dependence of the plasma density and temperature on the pressure are presented for both straight and tapered capillaries. The electron density is calculated using Eq. 4.2 and the plasma temperature is estimated, using Eq. 4.3, from the intensity ratio of the light emitted in the two principal Balmer lines.

4.3.1.1 Time-integrated density measurements

Plasma spectroscopy measurements confirm that the prerequisite underdense plasma with excellent shot-to-shot stability is generated in each capillary. An example of a measured hydrogen spectrum, showing the Balmer lines H_α (656.27 nm) and H_β (486.13 nm), is presented in Fig. 4.4. Since the integration time is longer than the discharge duration (the FWHM pulse duration of the main peak is 900 ns), it records the time-integrated plasma light spectra. Quantitative measurements of the density and temperature are presented in the following sections.

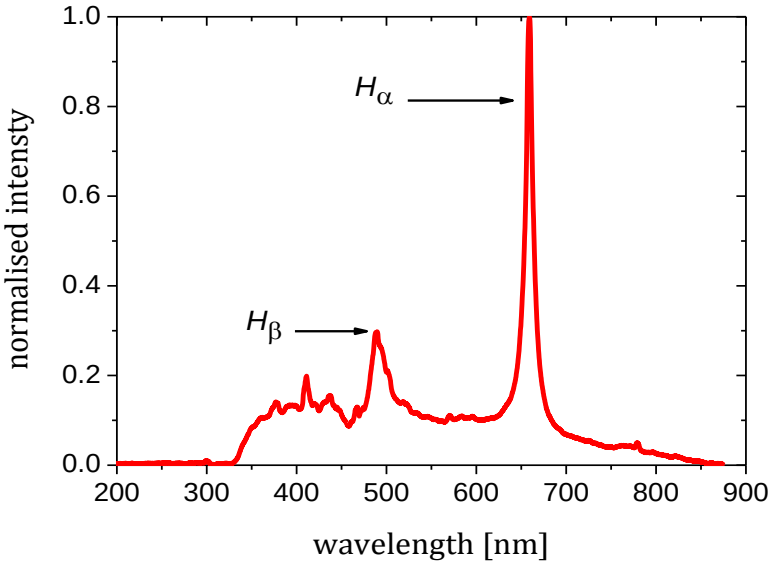

Figure 4.4: Typical hydrogen spectrum recorded with the Ocean Optics SD2000 spectrometer.

Plasma density dependence on capillary parameters

Here the dependence of the plasma density and temperature on the various parameters controlling a capillary discharge is investigated. This data is important because it allows design flexibility of plasma sources for plasma wakefield experiments.

- **Dependence on neutral gas pressure**

Here, firstly using a straight capillary (280 μm diameter, 40 mm length), a comparison is presented of spectra recorded for different neutral hydrogen pressures, ranging from 40 to 100 mbar for charging voltage 21 kV. The data for the H_α line are presented in Fig. 4.5. It is evident that higher plasma densities (wider linewidths) can be obtained for higher pressures. The linewidths of both lines increase, suggesting an increase in density. The same behaviour is also observed using a tapered capillary [the diameter reduces from (320 $\pm$ 5) μm to (270 $\pm$ 4) μm over the L = 40 mm length].

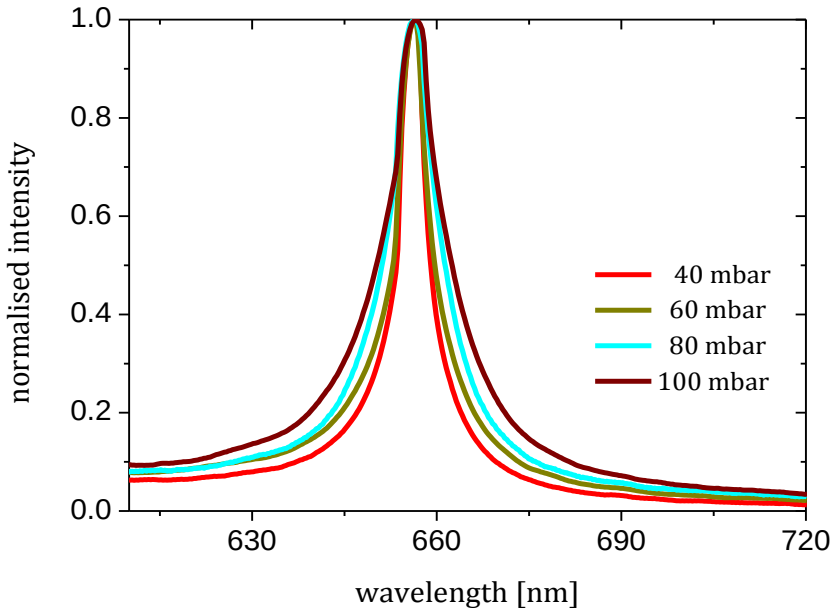

Figure 4.5: Normalised Balmer spectra recorded for increasing neutral hydrogen backing pressures.

- **Dependence on charging voltage**

Figure 4.6(a) shows measurements for different charging voltages (15kV, 18kV and 21kV) for the same straight capillary (280 μm diameter), with all other parameters remaining fixed.

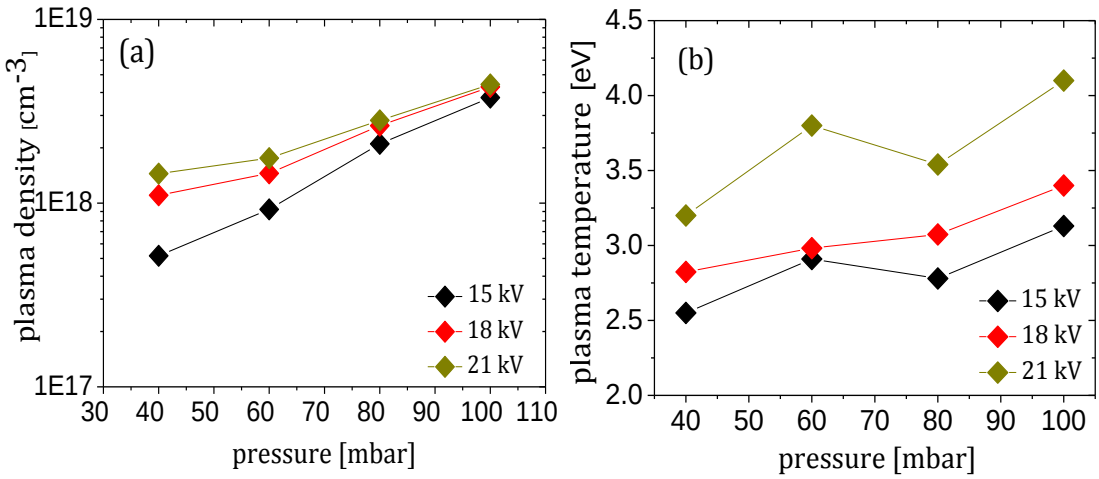

Figure 4.6: (a) Plasma density and (b) temperature at the centre of the straight capillary measured as a function of the charging voltage.

It is generally observed that at each given pressure (except at 100 mbar), when the charging voltage increases from 15 kV to 21 kV, the plasma density also increases. This is because as the applied voltage increases, the peak current increases, resulting in increase in plasmas density [7]. The experimental results here are similar to the results of other groups [12] with plasma density $\sim 1 \times 10^{18}$ cm^{-3} for backing pressure in the range ~50-100 mbar.

It is also observed that the plasma density is significantly increased when the charging voltage is increased from 15 kV to 18 kV, but little additional increase occurs when the voltage is increased to 21 kV. This indicates that the gas is fully ionised by 18 keV, and extra energy is deposited in to the plasma as kinetic energy of the plasma electrons rather than more ionisation. This is supported by the plasma temperature measurement that finds a significant increase in the temperature (up to 4.0 eV at 100 mbar) when the charging voltage is increased from 18 kV to 21 kV, as shown Fig. 4.6(b). Thus further increase of the charging voltage in this case is not expected to yield an increase in plasma density. From

Fig. 4.6(b) it is also shown that higher charging voltage creates a steady increase in the temperature with increasing the pressure. As a result, the charging voltage is fixed at 21 kV as an optimal charging voltage.

During the plasma spectroscopy experiments, the dependence of plasma density and plasma temperature on charging voltage has been also investigated for the tapered capillary [the diameter reduces from (320 $\pm$ 5) μm to (270 $\pm$ 4) μm over the L = 40 mm length resulting in the cross-sectional area reducing by a factor of 1.40 $\pm$ 0.04].

Results for the measured plasma density and plasma temperature at the small end of the tapered capillary are shown in Fig. 4.7. Figure 4.7(a) shows the plasma density measured as a function of the pressure for different charging voltages, 15 kV, 18 kV and 21 kV for the small end. The plasma density for a given pressure is higher when the charging voltage is increased from 15 kV to 21 kV, (except at 40 mbar). Here the same behaviour as found for the straight capillary has also been observed in tapered capillary case and once again it is noticed that the extra energy that is deposited in to the plasma when the charging voltage increased from 18 kV to 21 kV is transferred to the plasma temperature rather than density, as presented in Fig. 4.7(b). This figure shows the temperature dependence for the same small end of the tapered capillary. It is interesting to observe that the temperature also increases with increase of the charging voltage and there is a significant increase at 21 kV where the maximum temperature (4.2 eV) is reached at 80 mbar. In addition, lower charging voltages create variations in the measured plasma temperature.

From the comparison of the density and temperatures of the small end of the tapered capillary with the straight capillary (280 μm), it is seen that both give similar results. For the large end, the measurements of the plasma density and the temperature at the centre have been made at 60 mbar and 21 kV and the averaged results give $n_e \approx 1 \times 10^{18}$ cm^{-3} and $T_e \approx 3$ eV respectively, which provides useful information for the guiding experiment and the subsequent laser wakefield acceleration studies.

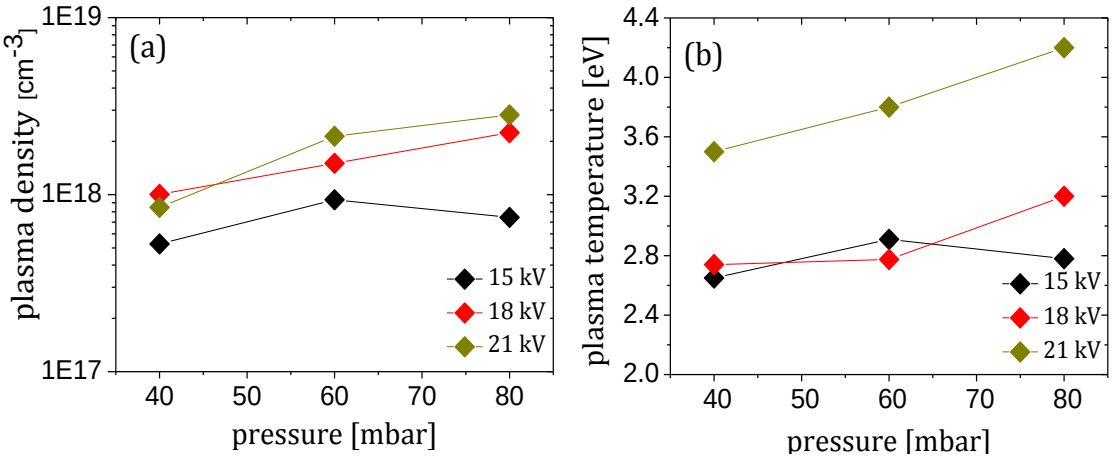

Figure 4.7: (a) Plasma density and (b) temperature, measured as a function of the charging voltage, at the centre of the small end of the tapered capillary.

- **Dependence on Capillary Radius**

Figure 4.8 shows a set of data that have been taken for 2 different straight capillary diameters (280 μm and 230 μm). The capillaries were 40 mm long and the charging voltage was set to 21 kV. It is seen from the figure that the narrower capillary provides a slight increase of the plasma density. The data shows, for example, at 60 mbar, the density increases 1.3 times from 1.55×10^{18} cm^{-3} (for the wider capillary) to 2.07×10^{18} cm^{-3} (for the narrower capillary).

Using this increasing measured value in the plasma density, the plasma density can be estimated for different diameters. As an example, the plasma density is increased to $\approx 5 \times 10^{18}$ cm^{-3} (an increase by 2.3 times) if the diameter is decreased by a factor of 2 from 280 μm to 140 μm. This observation is explained by the enhanced current density per unit area of the capillary ($A.\mu m^{-2}$). The current density is inversely proportional to the square of the diameter of the capillary and considering that the supplied current is the same for those discharges for both capillaries, the current density is higher in narrower capillary resulting in the enhancement in the plasma density. This behaviour has been previously observed when higher plasma densities are experimentally obtained at all given pressures with the smaller diameter

capillaries [13]. Although the observed increase in density is not large, it is still important because for low densities to be achieved [high maximum electron energy gain from LWFA (section 2.2.3)], a diameter as large as possible will be needed to be used.

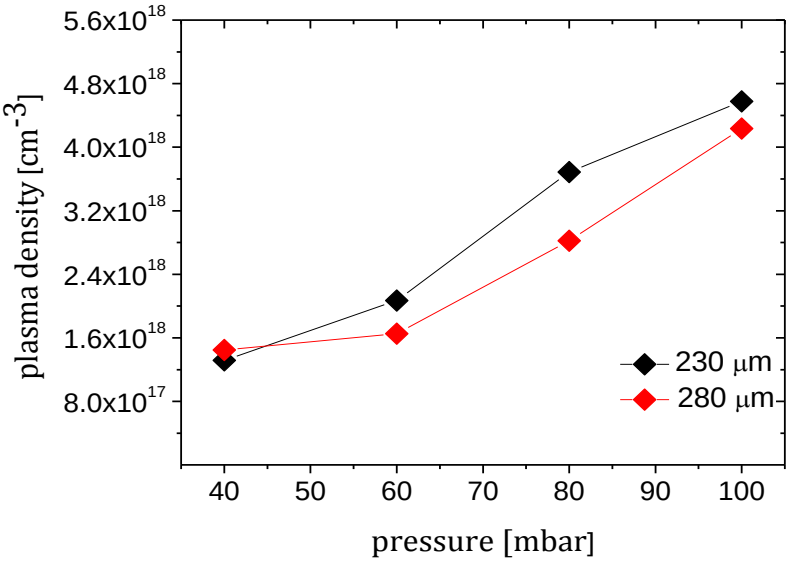

Figure 4.8: The dependence of the plasma density as a function of pressure for 2 different straight capillary diameters. The capillary lengths are 40 mm and the charging voltage 21 kV.

4.3.1.2 Channel density profile measurement

- **For straight capillary**

The Stark broadening technique has been extended to provide time-integrated measurements of the plasma electron density profile generated in the capillary. Excellent spatial resolution has been achieved by scanning across the capillary exit plane with a narrow entrance slit at the spectrometer. As the discharge current develops through time, increasing until the peak of the discharge whereby it then begins to decrease, the density of the plasma also develops producing spectral evolution of the plasma light for the duration of the discharge. However, the results shown here are all time integrated measurements due to the shutter of the spectrometer being open for ~2 ms and so capturing an averaged spectrum over the entire 900 ns discharge pulse. This technique still serves well for characterising the plasma density but the peak

discharge values could not be directly measured (the peak density is expected to be approximately double the time-averaged value).

Figure 4.9(a,b) shows the experimentally measured plasma density as a function of radial position across the straight capillary vertically and horizontally. The charging voltage was 21 kV for hydrogen pressure in the capillary of 60 mbar. From Fig. 4.9 it is seen that there is a clear density minimum $\sim (1.7 \pm 0.4) \times 10^{18}$ cm^{-3} at the centre of the capillary for vertical scan and $\sim (1.4 \pm 0.6) \times 10^{18}$ cm^{-3} for transverse scan giving an average of density $\sim (1.55 \pm 0.5) \times 10^{18}$ cm^{-3} and, thus, the peak density is expected to be ($\sim 3.1 \times 10^{18}\,\mathrm{cm}^{-3}$). Both the vertical and transverse scans show the characteristic parabolic shape of the capillary density centred on-axis with the density dropping off close to the walls [14, 15].

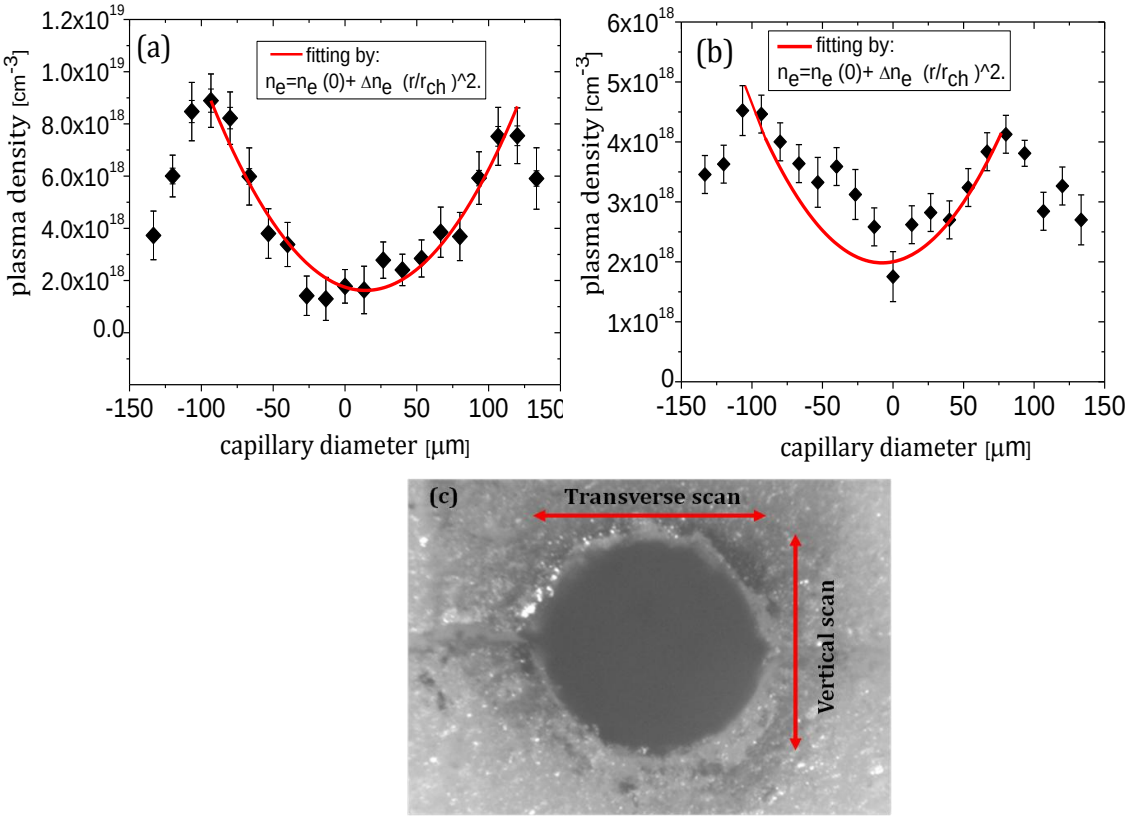

Figure 4.9: Plasma density profile for the 280 μm diameter straight capillary at 60 mbar and 21 kV. (a) Transverse (x-axis) scan with a parabolic fit (-94 to 120 μm). (b) Vertical (y-axis) scan with a parabolic fit (-106 to 80 μm). The parabolic fits exclude the data of the decrease in the density close to the walls. (c) Image of the capillary exit using an optical microscope.

These on-axis plasma density measurements are in good agreement with the on-axis density measured by Spence *et al.* [16] who previously measured an on-axis electron density of 2.7×10^{18} cm^{-3} for 300 μm alumina capillary with a hydrogen gas pressure of 67 mbar using interferometric measurement. The results here for the density profile are compared with the simulations of the electron density profile performed by Bobrova *et al.* [15] and it is found that the agreement between them is quite acceptable.

Recently, in other work [17], the spectroscopic measurement using the H_α line was also used for plasma density estimation in gas-filled capillary waveguides. Their results show that this technique can directly provide a rather good result for time–resolved density measurement to confirm that the spectroscopic measurement is a useful tool for measuring plasma density and temperature in capillary-based laser wakefield accelerators.

- **For tapered capillary**

Measurements of the plasma electron density profiles at both ends of a tapered capillary (where the diameter of the hole reduces from 325 μm to 274 μm over the L = 40 mm length) were made for both ends. In this case, hydrogen gas is injected with a backing pressure of 50 ± 5 mbar. The same imaging system coupled to the optical spectrometer described in the previous section, is used to measure the spectra of Stark-broadened hydrogen Balmer line emission from the background gas neutral atoms.

The transverse plasma density profiles at both ends of the capillary are shown in Fig. 4.10. Again, both show the characteristic parabolic shape of the capillary density centred on-axis with the density dropping off close to the walls but, most significantly, it verifies that the density is higher at the narrower end of the capillary. Assuming a smoothly varying plasma density variation along the smoothly varying tapered capillary structure, this shows that a longitudinal plasma density gradient has been successfully formed in the capillary. The mean time-averaged on-axis values are $(1.0 \pm 0.1) \times 10^{18}$ cm^{-3} and $(1.6 \pm 0.1) \times 10^{18}$ cm^{-3} for the wide and narrow ends respectively.

Hence, there is agreement between the entrance-to-exit density ratio (1.6 ± 0.3) and the corresponding capillary cross-sectional area ratio (1.40 ± 0.04), i.e. the density gradient is determined mainly by the cross-sectional area gradient (assuming a smooth density gradient along the tapered capillary). This correspondence between cross-section and density is an important indicator that optimal linearly tapered capillary, according to the desired LWFA experimental conditions, can be tailor-made with the femtosecond laser micromachining technique.

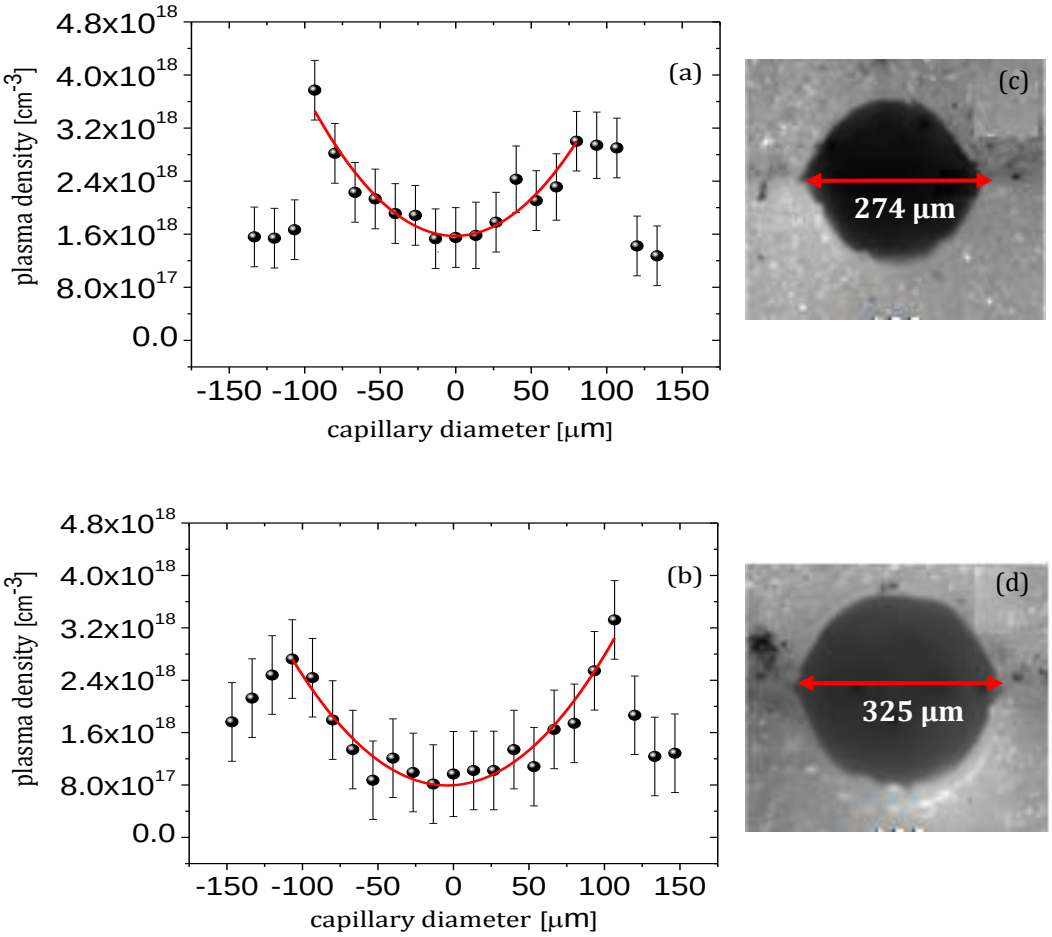

Figure 4.10: Experimentally measured horizontal time-averaged plasma density profile at the (a) narrow and (b) wide ends of the tapered capillary. The zero position denotes the centre of the capillary. The density profile curve at the narrow end is best-fit parabola from -94 to 80 μm and the curve at the wide end is best-fit parabola from -107 to 107 μm. For both narrow and wide ends, optical microscope images are shown in (c) and (d) respectively.

4.3.2 Femtosecond laser guiding

In this section, experiments to demonstrate the ability of the capillaries to act as waveguides are presented and guiding of low intensity femtosecond laser pulse is characterised for both types of capillary.

4.3.2.1 Guiding in a straight capillary

To determine the transmission of the guided laser beam in the plasma waveguide created in a straight capillary, both the input and output laser profiles are recorded. The capillary length is 40 mm, corresponding to approximately $3z_R$. A measurement is made without the capillary in place to calibrate the transmission (to establish the energy corresponding to 100% transmission). The timing of the laser pulse is measured using a photodiode, to give a delay of 230 ns behind the leading edge of the Medox pulse. For each measurement, the laser pulse delay is given as that relative to the Medox driver pulse for delay scans.

Part of the measured signal with the guided laser beam arises from radiation emitted from the plasma, which is also focused on the CCD camera. Images captured by the CCD camera detection system are shown in Fig. 4.11. For reference, the background plasma emission is displayed in Fig. 4.11(a). For quantitative measurements, this signal [Fig. 4.4], which occurs at radiation wavelengths shorter than the laser pulse wavelength (λ = 800 nm), is minimised with a colour filter. The residual plasma radiation signal without the laser present is also subtracted from the measured signals with a guided laser beam.

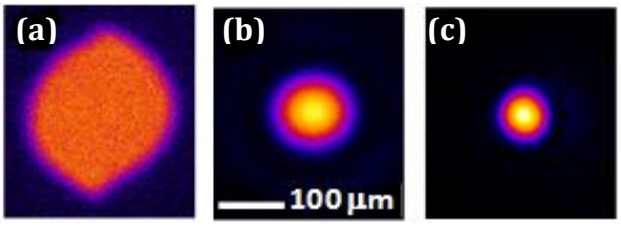

Figure 4.11: False colour CCD camera images showing (a) background plasma emission, (b) entrance laser pulse, (c) exit laser pulse optimally guided for the straight capillary of length 40 mm and diameter 280 µm.

The energy transmission ratio is calculated from the transmitted energy divided by the energy in the absence of the capillary. Energy transmission, presented in Fig. 4.12 and Fig. 4.13, is measured as a function of the time delay between the discharge and the laser pulses at a gas pressure of 50 mbar. For example, when the laser pulse is injected before the discharge pulse while the H_2 gas is still in the neutral state, only weak transmission of the laser pulse is observed, as shown in Fig. 4.12, with an irregular beam profile as shown in the first three images of Fig. 4.12 and Fig. 4.13 for (1, 2 and 3).

When the laser pulse is injected 0.2 μs after the onset of the discharge current pulse, a significant improvement in the transmitted beam profile occurs, as shown in image 4 of Fig. 4.12. Fig. 4.13 shows that the beam profile has a Gaussian profile distribution as expected for single-mode propagation through the plasma waveguide.

For injection times between 0.2 μs and 0.6 μs, significant transmission is observed, as shown in images 5 to 9 of Fig. 4.12. The beam profiles have Gaussian profile distributions, as seen in Fig. 4.13. Over this range the measured current through the capillary is also around its maximum value. This indicates that the plasma is at its highest degree of ionisation and that the desired channel structure of the plasma is formed. These observations are in good agreement with numerical simulations [15, 18].

Delays between 0.6 and 1.15 μs result in a degradation of the transmitted beam profile, as can be seen in images 10, 11 and 12. The measured current through the capillary decreases in this region. This indicates that the channel structure of the plasma has weakened and about to disappear. Plasma density measurements using interferometry [19] indicates that partial recombination of electrons and ions occurs in this period and the channel profile becomes more shallow, thus losing its guiding property. Furthermore, the time window for good guiding is estimated to be about 200 ns with an average energy transmission of (85 ± 5)%.

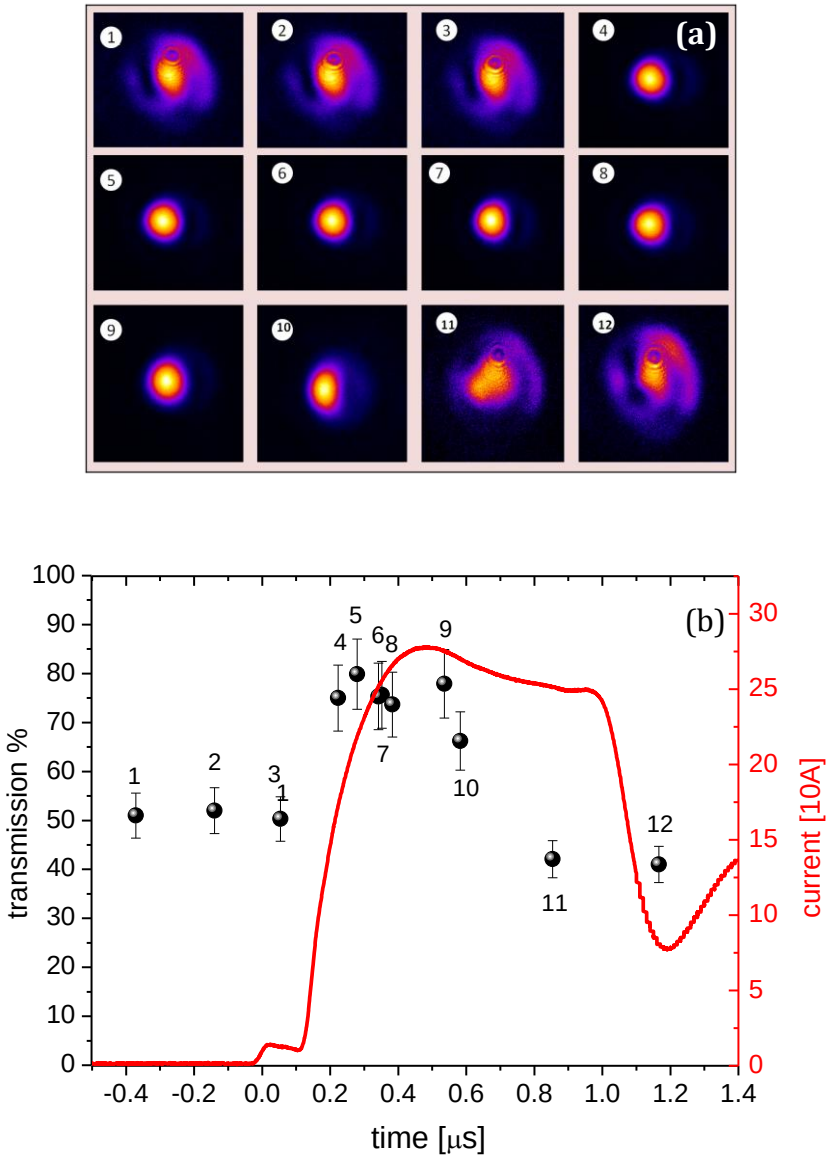

Figure 4.12: (a) Beam profiles of the transmitted laser pulses through the plasma channel. The images are recorded for different injection times of the laser pulse. Images 1, 2 and 3 are obtained for injection before the discharge pulse. Images 4 to 9 are recorded for injection between 0.2 and 0.5 μs, when the discharge current is a maximum. Images 10 to 12 are recorded for injection between 0.6 and 1.15 μs when the discharge current is decreasing. (b) The current through the capillary is shown together with the transmission as a function of the delay time.

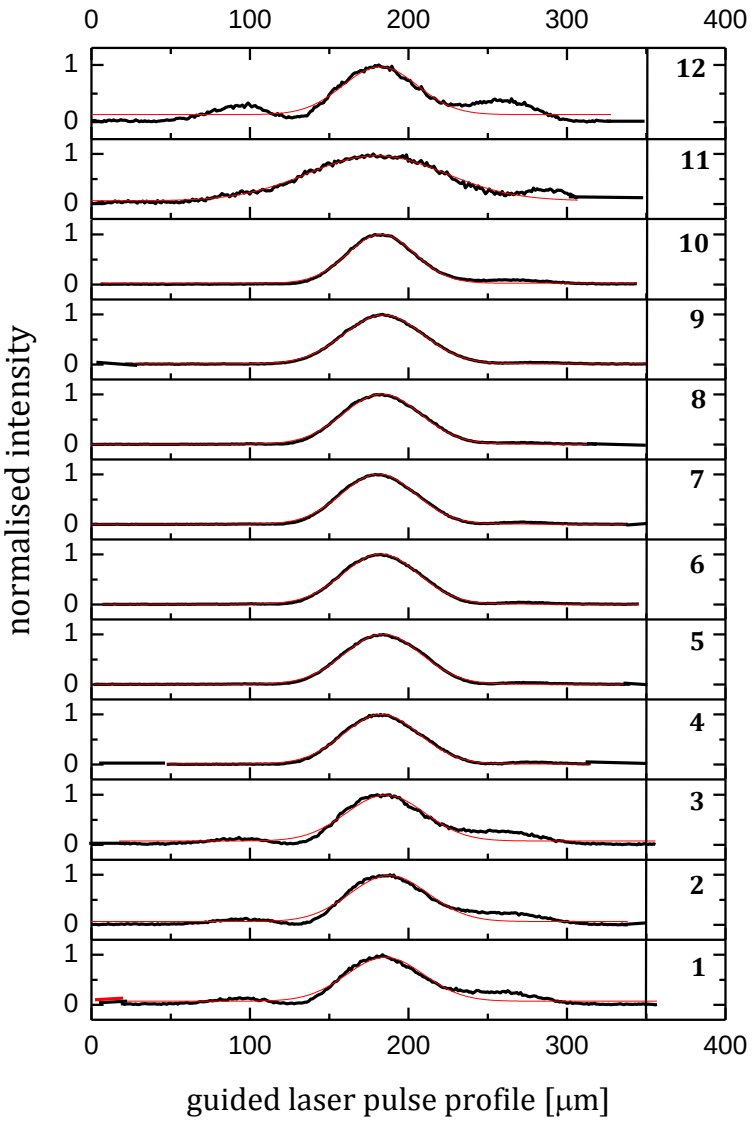

Figure 4.13: The evolution of the profile of transmitted laser pulses for the straight capillary from Fig 4.12. The red curves are Gaussian fits.

Because the matched spot size is ~35 μm for the estimated peak density of 3×10^{18} cm^{-3}, spot size oscillations (scalloping) occur along the waveguide (as described in section 3.1.1) and the exit beam size is smaller than that at the entrance (w_0 reduces from 81 μm to 47 μm) as shown in Fig. 4.11(b) and (c).

The laser energy loss (~15-20%) during propagation through the waveguide can be attributed to inverse bremsstrahlung absorption where, at low laser intensity, the absorption rate is determined by the plasma temperature. Energy

loss of 20% is predicted to be for a plasma temperature of 5 eV (section 3.3.1) which is close to our measured time-averaged on-axis plasma temperature of 3-4 eV [Fig. 4.6(b)]. The energy transmission should improve at higher intensity, before the onset of wave breaking, due to laser-driven plasma heating mitigating inverse bremsstrahlung absorption effects [20]. Note also that a non-circular cross-section has no impact on the laser waveguiding process.

4.3.2.2 Guiding in a tapered capillary

Guiding experiments have also been performed in the tapered capillary used for plasma density measurements. An imaging system is used to image the laser profile and measure the energy at the capillary entrance and exit planes respectively (section 4.3.1.2). The mean time-averaged on-axis density values are measured as $(1.0 \pm 0.1) \times 10^{18}$ cm^{-3} and $(1.6 \pm 0.1) \times 10^{18}$ cm^{-3} for the wide and narrow ends respectively.

The transmitted laser pulse mode profile is shown in Fig. 4.14 for different delays from the onset of the current pulse. When the laser pulse arrives early or late with respect to the peak of the current discharge pulse the output beam profile is grossly distorted (even though the measured transmission is high) indicating poor guiding and the excitation of transverse modes. At optimal synchronisation between the laser and current pulse (over a ~0.30 μs time range around the maximum current), a smooth Gaussian profile is evident and the transmission peaks at (79 ± 6)%. As for the straight capillary, the energy loss is dominated by inverse bremsstrahlung absorption, which is predicted here to be ~20% for a plasma temperature of ~5 eV.

The entrance laser waist is 89 μm, more than double the matched waist, ~41 μm at the capillary entrance for a peak density of $\sim 2 \times 10^{18}$ cm^{-3}, which leads to an exit beam of around half the entrance laser waist size (see Fig. 4.16). As shown in Fig. 4.15, high quality guiding with a Gaussian output profile with up to (82 ± 8)% energy transmission is found for input beam waists in the range ~50-100 μm, i.e. waists larger than the matched entrance waist. The exit waist is relatively insensitive to the entrance waist over a wide range of beam waists.

This shows that oscillation of the laser spot diameter in the capillary, due to mismatch does not lead to significant loss.

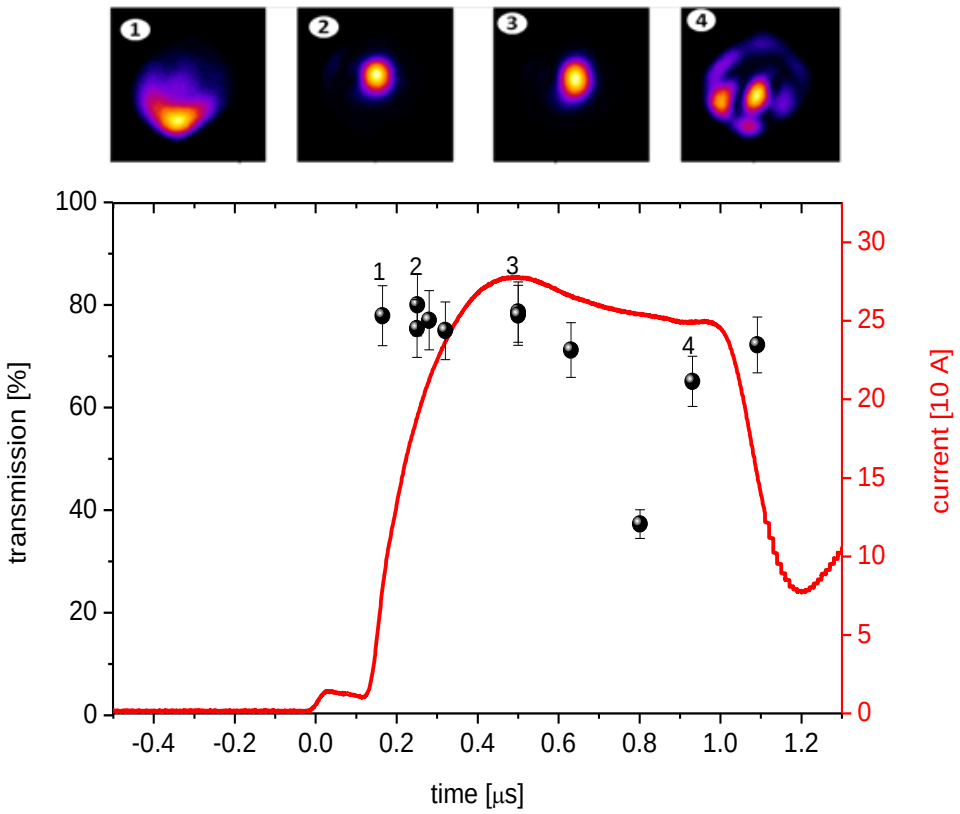

Figure 4.14: Laser energy transmission (black circles) measured as a function of delay with respect to the onset of the current discharge pulse (red solid line). Inset shows four corresponding laser pulse profiles measured at the capillary exit plane.

The corresponding evolution of a Gaussian laser beam in the tapered channel, discussed in section 3.2.2, is given by solutions of Eq. 3.11 for the investigated capillary (with an entrance-to-exit density ratio of 1.6), which are shown in Fig. 4.15 for different densities. Excluding the extreme datum for a small entrance waist where guiding is poor, the measured exit waists are reproduced by the model for a peak density increasing from (1.65) to (2.08) $\times 10^{18}$ cm^{-3}, as shown in Fig. 4.15. Best-fit agreement with experiment, given by the solid line of Fig. 4.15, corresponds to an entrance peak density of 1.95 $\times 10^{18}$ cm^{-3}, in good agreement with the measured time-averaged (~peak/2) plasma density. Note the invariant output waist predicted for an entrance peak density of

2.08×10^{18} cm^{-3} (dotted line of Fig. 4.15) indicates that, at this density, the beam waist always evolves to a matched exit waist, w_M (z=L), ~34 μm.

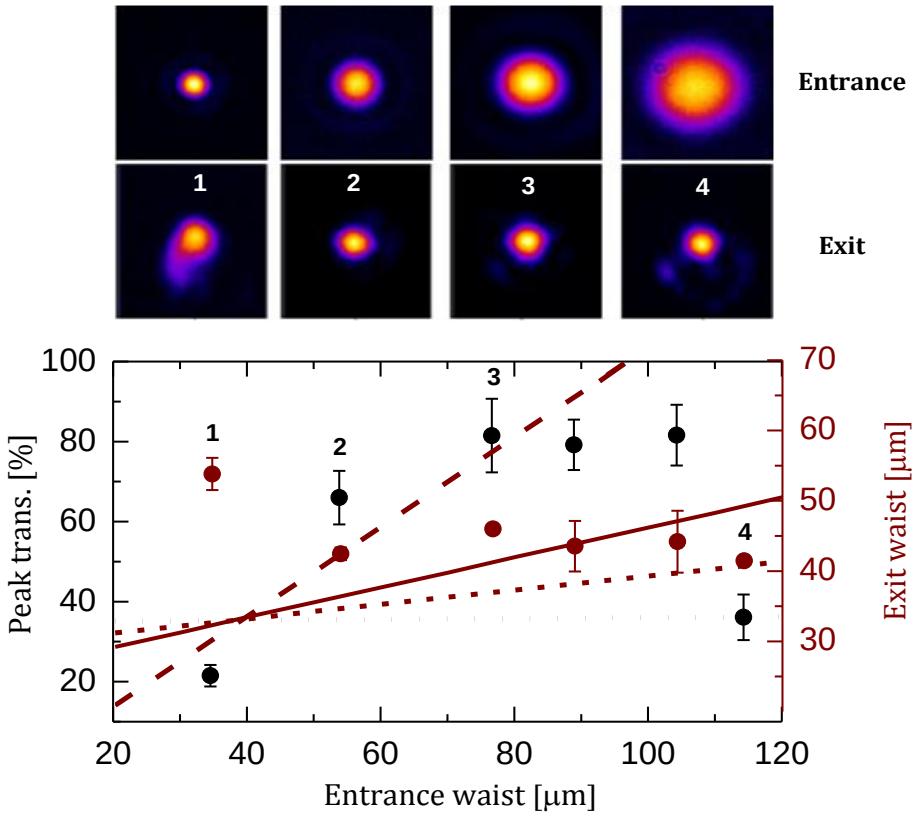

Figure 4.15: Laser energy transmission (black circles) and mean waist size of the output laser pulse at the capillary exit plane (brown circles) measured as a function of input laser pulse waist at the capillary entrance plane. Insets are four corresponding pairs of input and output laser pulse profiles. Waist error bars represent the degree of ellipticity of the exit beam. Exit waist dependences are shown for entrance plasma densities of (dashed line) 1.65×10^{18} cm^{-3}, (solid line) 1.95×10^{18} cm^{-3}, (short dashed line) 2.01×10^{18} cm^{-3}, and (dotted line) 2.08×10^{18} cm^{-3}, respectively.

The model also agrees with a single measurement of guiding conducted in the reverse direction, i.e. from the narrow end to the wide end, where the measured entrance and exit waists are 89 μm and 47 μm, respectively as shown in Fig. 4.17, and the corresponding best-fit modelled peak density decreases from 3.2 to 2.0×10^{18} cm^{-3}.

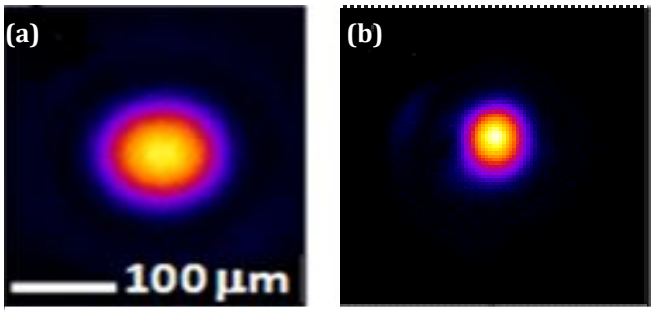

Figure 4.16: False colour CCD camera images showing (a) the entrance and (b) the optimally guided exit laser pulse, respectively, for a tapered capillary of length 40 mm with a diameter varying from 325 µm to 274 µm. The indicated scale applies to both images.

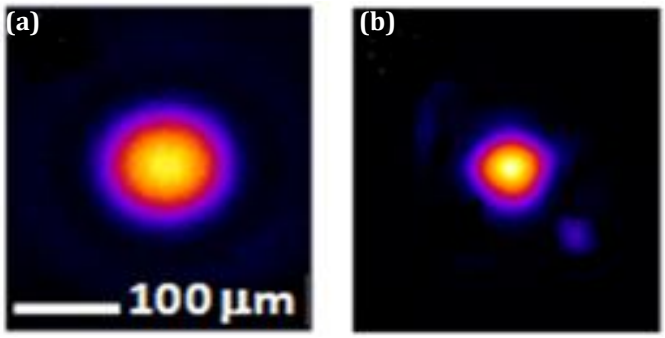

Figure 4.17: False colour CCD camera images showing (a) the entrance and (b) the optimally guided exit laser pulse, respectively for a tapered capillary (reverse direction) of length 40 mm and diameter 274 µm to 325 µm. The indicated scale applies to both images.

4.4 Conclusions

Interferometric techniques that are used to measure the plasma density [21] require a square capillary cross-section with optical quality sides. However, capillaries that are usually used for energetic electron production in LWFA experiments have circular cross-sections, which preclude the use of interferometric techniques. Therefore alternative methods are required for direct measurement of the capillary plasma density in these accelerators.

From the experimental data presented here for both straight and tapered capillaries, it can be concluded that one of the most promising ways of measuring the density is the spectroscopic method using the Stark broadening effect. The experimental data here show that the Stark broadening of the hydrogen line H_α is a very successful diagnostic for plasma densities in the

range of 10^{17}-10^{19} cm^{-3}. At these high densities, the plasma temperature can also be obtained by measuring the ratio of the two line intensities H_β/H_α.

The data shows that the density increases with increasing gas pressure, while increasing the charging voltage increases the amount of light emitted, which is attributed to the increase of the temperature and not due to an increase of the plasma density. The density also increases linearly with decreased capillary diameter due to the higher current density at the smaller radius end of the capillary.

From on-axis plasma density measurements, density profiles have reasonable parabolic fits, showing a radially increasing plasma density and centred on-axis with the density dropping off close to the walls. This is probably due to the plasma expanding and cooling that is sufficient for significant recombination near the capillary wall.

The experimental data using the tapered capillary show that measurements of the Stark-broadened Balmer line spectra confirm the existence of a longitudinal plasma density gradient, which is required in LWFA experiments exploiting a longitudinal plasma density gradient.

With a constant plasma density of $\sim 2.0 \times 10^{18}$ cm^{-3} and an internal diameter of 280 μm over a distance of 40 mm, the experimental data, obtained at laser intensity $\sim 10^{12}$ W/cm^2, show that guiding with an average energy transmission of (85 ± 5)% is suitable for LWFA driven by a laser intensity $\sim 10^{18}$ W/cm^2. The tapered capillary guided a laser pulse from an internal diameter of 325 μm to 274 μm along an increasing plasma density gradient from $(1.0 \pm 0.1) \times 10^{18}$ cm^{-3} and $(1.6 \pm 0.1) \times 10^{18}$ cm^{-3} for the wide and narrow ends respectively over 40 mm resulting in an average energy transmission of (80 ± 10)% (measured at low intensity). This transmission should increase to close to 100% at higher intensities [19, 22] where absorption due to inverse bremsstrahlung heating is reduced. However, at relativistic intensities, the transmission typically drops to ~60% -70% for ultra-short duration laser pulses due to driving a plasma wake [19, 22, 23].

References

1. S.A. Flih, E. Oks, and Y. Vitel, *Comparison of the Stark widths and shifts of the H-alpha line measured in a flash tube plasma with theoretical results.* Journal of Physics B: Atomic, Molecular and Optical Physics, 2003. **36**(2): p. 283–296.
2. W.L. Wiese, D.R. Paquette, and D.E. Kelleher, *Detailed Study of Stark-Broadening of Balmer Lines in a High-Density Plasma.* Physical Review A-General Physics, 1972. **6**(3): p. 1132–1153.
3. B. Vieux, *Broad-band linear Raman chirped pulse amplification in plasma.* (PhD Thesis), 2004. University of Strathclyde: Glasgow.
4. H.R. Griem, *Spectral Line Broadening by Plasmas*. 1974, Academic Press: New York.
5. H.M. Foley, *The Pressure Broadening of Spectral Lines.* Physical Review, 1946. **69**(11-12): p. 616-628.
6. Y. Ehrlich, C. Cohen, D. Kaganovich, A. Zigler, R.F. Hubbard, P. Sprangle, and E. Esarey, *Guiding and damping of high-intensity laser pulses in long plasma channels.* Journal of the Optical Society of America B-Optical Physics, 1998. **15**(9): p. 2416-2423.
7. J. Ashkenazy, R. Kipper, and M. Caner, *Spectroscopic Measurements of Electron-Density of Capillary Plasma Based on Stark-Broadening of Hydrogen Lines.* Physical Review A, 1991. **43**(10): p. 5568-5574.
8. A. Escarguel, E. Oks, J. Richou, and D. Volodko, *Highly nonlinear, sign-varying shift of hydrogen spectral lines in dense plasmas.* Physical Review E, 2000. **62**(2): p. 2667-2671.
9. S. Buscher, T. Wrubel, S. Ferri, and H.J. Kunze, *The Stark width and shift of the-hydrogen H alpha line.* Journal of Physics B-Atomic Molecular and Optical Physics, 2002. **35**(13): p. 2889-2897.
10. S. Boddeker, S. Gunter, A. Konies, L. Hitzschke, and H.J. Kunze, *Shift and Width of the H-Alpha Line of Hydrogen in Dense-Plasmas.* Physical Review E, 1993. **47**(4): p. 2785-2791.

11. G. Bekefi, *Principles of Laser Plasmas*. 1976, Wiley: New York.
12. M.S. Kim, D.G. Jang, H.S. Uhm, S.W. Hwang, I.W. Lee, and H. Suk, *Discharge Characteristics of a Gas-Filled Capillary Plasma for Laser Wakefield Acceleration.* IEEE Transactions on Plasma Science, 2011. **39**(8): p. 1638-1643.
13. C. Hao, E. Kallos, P. Muggli, T.C. Katsouleas, and M.A. Gundersen, *A High-Density Hydrogen-Based Capillary Plasma Source for Particle-Beam-Driven Wakefield Accelerator Applications.* IEEE Transactions on Plasma Science, 2009. **37**(3): p. 456-462.
14. D. Kaganovich, P. Sasorov, C. Cohen, and A. Zigler, *Variable profile capillary discharge for improved phase matching in a laser wakefield accelerator.* Applied Physics Letters, 1999. **75**(6): p. 772-774.
15. N.A. Bobrova, A.A. Esaulov, J.I. Sakai, P.V. Sasorov, D.J. Spence, A. Butler, S.M. Hooker, and S.V. Bulanov, *Simulations of a hydrogen-filled capillary discharge waveguide.* Physical Review E, 2001. **65**(1): p. 016407.
16. D.J. Spence, A. Butler, and S.M. Hooker, *Gas-filled capillary discharge waveguides.* Journal of the Optical Society of America B-Optical Physics, 2003. **20**(1): p. 138-151.
17. D.G. Jang, M.S. Kim, I.H. Nam, H.S. Uhm, and H. Suk, *Density evolution measurement of hydrogen plasma in capillary discharge by spectroscopy and interferometry methods.* Applied Physics Letters, 2011. **99**(14): p. 141502.
18. B.H.P. Broks, W. Van Dijk, J.J.A.W. van der Mullen, A.J. Gonsalves, T.P. Rowlands-Rees, and S.M. Hooker, *Modeling of a square pulsed capillary discharge waveguide for interferometry measurements.* Physics of Plasmas, 2007. **14**(2): p. 023501.
19. T.P. Rowlands-Rees, C. Kamperidis, S. Kneip, A.J. Gonsalves, S.P.D. Mangles, J.G. Gallacher, E. Brunetti, T. Ibbotson, C.D. Murphy, P.S. Foster, M.J.V. Streeter, F. Budde, P.A. Norreys, D.A. Jaroszynski, K. Krushelnick, Z. Najmudin, and S.M. Hooker, *Laser-Driven Acceleration of Electrons in a*

Partially Ionized Plasma Channel. Physical Review Letters, 2008. **100**(10): p. 105005.

20. T.P. Hughes, *Plasmas and Laser Light*. 1975, Adam Hilger: London.
21. A.J. Gonsalves, T.P. Rowlands-Rees, B.H.P. Broks, J.J.A.M. van der Mullen, and S.M. Hooker, *Transverse Interferometry of a Hydrogen-Filled Capillary Discharge Waveguide.* Physical Review Letters, 2007. **98**(2): p. 025002.
22. W.P. Leemans, B. Nagler, A.J. Gonsalves, C. Toth, K. Nakamura, C.G.R. Geddes, E. Esarey, C.B. Schroeder, and S.M. Hooker, *GeV electron beams from a centimetre-scale accelerator.* Nature, 2006. **2**(10): p. 696-699.
23. T.P.A. Ibbotson, N. Bourgeois, T.P. Rowlands-Rees, L.S. Caballero, S.I. Bajlekov, P.A. Walker, S. Kneip, S.P.D. Mangles, S.R. Nagel, C.A.J. Palmer, N. Delerue, G. Doucas, D. Urner, O. Chekhlov, R.J. Clarke, E. Divall, K. Ertel, P. Foster, S.J. Hawkes, C.J. Hooker, B. Parry, P.P. Rajeev, M.J.V. Streeter, and S.M. Hooker, *Investigation of the role of plasma channels as waveguides for laser-wakefield accelerators.* New Journal of Physics, 2010. **12**(4): p. 045008.

CHAPTER 5

Laser wakefield acceleration in straight and tapered capillary discharge waveguides

This chapter describes LWFA experiments using gas-filled tapered and straight capillary discharge waveguides, such as those characterised in chapter 4, that have been conducted on the Advanced Laser-Plasma High-energy Accelerators towards X-rays (ALPHA-X) accelerator beam line. Electron acceleration in tapered capillary waveguides has been demonstrated here for the first time.

The goal of these experiments has been to investigate the differences between linearly tapered and straight hydrogen-filled capillary discharge waveguides for laser wakefield acceleration for a range of conditions. Most significantly, enhancement of the electron energy is predicted from LWFA theory when the taper produces an increase in the longitudinal plasma density as a function of the propagation distance (section 3.2). The effect of propagating the laser pulse in the reverse sense, i.e., along a decreasing plasma density, has also been investigated.

The experimental setup of the ALPHA-X beam line is described in Section 5.1 followed by experimental results in section 5.2 that include measurements of the transmitted laser pulse as a method of determining the plasma density (the Stark-broadening spectroscopic technique has not been possible on the accelerator beam line set-up). Waveguide durability to a large number of high-

power laser shots is analysed in Section 5.3, followed by a discussion and conclusions in Section 5.4.

5.1 Experimental setup

Experiments to explore the effect of density tapering in capillary discharge waveguide accelerators have been conducted on the ALPHA-X beam line [1]. A Ti:sapphire laser pulse (energy = 800 mJ, full-width at half-maximum duration = 40 fs and wavelength λ = 800 nm) is focused to a waist w_0 = 20 μm (radius at $1/e^2$) at the entrance plane of the capillary under investigation such that, initially, the intensity I = 1.6×10^{18} W/cm^2 and the initial normalised vector potential $a_0 = \left(\frac{I\,\lambda^2}{1.37\times10^{18}}\right)^{1/2} = 0.9$. This accounts for ~50% of the laser energy being in the central spot.

The experimental arrangement is shown in Fig. 5.1. The exit of the waveguide is imaged onto diagnostics to allow the measurement of the laser spectrum and energy transmission. Electron beams generated from the laser wakefield accelerator have been diagnosed by scintillating Lanex screens and an electron spectrometer which allows measurement of their energy spectra and charge. Observation of the guiding properties of the waveguide and the resultant electron bunches have been made for a range of conditions.

5.1.1 Laser pulse imaging system

The position and size of the focal spot of the laser beam are crucial parameters for capillary-guided laser wakefield acceleration. The imaging system has been set up to observe and correctly adjust these parameters as shown in Fig. 5.2. The beam exiting the waveguide can be deflected, using a 2 inch diameter wedge, into an imaging system that is placed alongside the vacuum chamber, to image the laser beam. To properly align the laser focus at the entrance of, and through the capillary, a collimated lens, f = 1 m, is mounted on a longitudinal translation stage and placed directly in the line of the deflected

beam, to enable imaging of the beam focus and also, after a 4 cm translation, imaging the exit plane of the capillary.

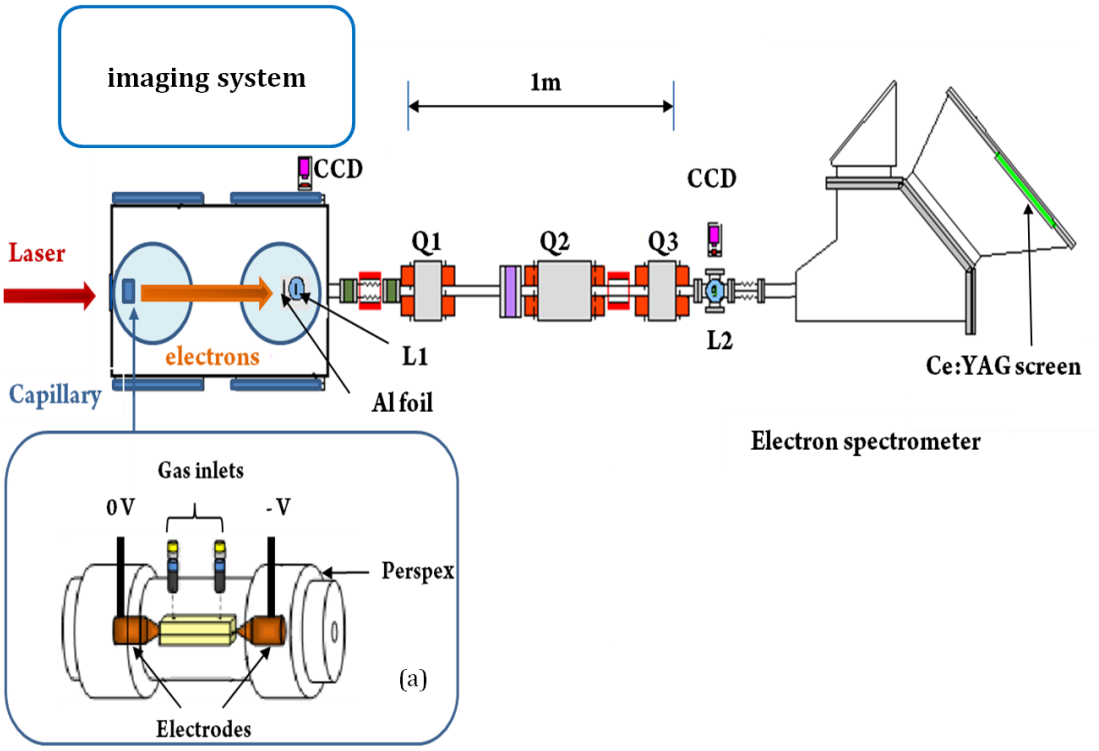

Figure 5.1: Schematic diagram of the ALPHA-X beam line for the capillary-guided laser wakefield accelerator. The plasma channel was formed in a hydrogen-filled capillary discharge waveguide [see inset (a)]. Hydrogen gas was introduced into the capillary waveguide using two gas inlets. A discharge is struck between two electrodes located at each end of the waveguide, using a high voltage pulsed power supply. The laser beam is focused onto the entrance of the capillary using an f/18 spherical mirror. A fraction of the laser light coming out from the waveguide is reflected by a removable wedge for the laser imaging diagnostics. Lanex screens are denoted by L1 and L2. Quadrupole magnets are denoted by Q1, Q2 and Q3.

The imaging system has been used to measure the energy transmission of the laser. The laser is focused by a converging lens, f = 1 m, and then reflected by two mirrors and a wedge, attenuating the beam intensity, into a microscope objective lens (×4 magnification) and a 16 bit CCD camera. It is very important to prevent damage to the CCD chip through the use of the wedge and neutral density filters of sufficient optical density.

During acceleration experiments, an important aspect of the set-up has been the plasma density measurement performed after capturing the laser spectrum following the interaction using an optical spectrometer (Ocean Optics SD4000) with an optical fibre placed directly in the line of the transmitted beam through the wedge.

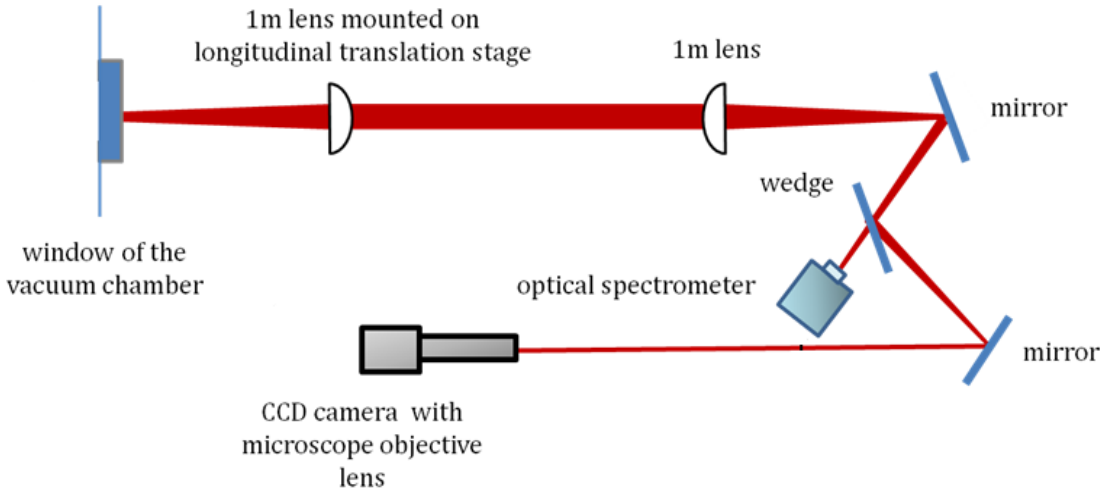

Figure 5.2: Schematic of the laser pulse imaging system.

5.1.2 Capillary alignment

Laser beam alignment through the capillary is very challenging and a vital part of the experimental setup. Careful steps have been taken with the aid of the imaging system. The gas-filled capillary discharge waveguide structure is mounted in a gimbal mount placed on a 3-axis stage. The translation stages are used to align the entrance of the capillary with the laser beam. The entrance of the capillary coincides with the centre of rotation of the gimbal mount allowing the exit of the capillary to be aligned without misaligning the entrance.

In the experiment the alignment steps proceed as follows: first, the laser focal spot size has been imaged by moving the capillary away from the optical axis, as shown in Fig. 5.3(a), where a good quality Gaussian profile of the main spot is obtained for both directions as shown in Fig. 5.3(b) and (c) respectively and the energy in the main central spot is shown to be ~50% of the total laser energy.

The transverse spatial profile of the focus [Fig. 5.3(b)] shows a small wing on one side of spot size with an intensity ~7 times smaller than the intensity at the waist.

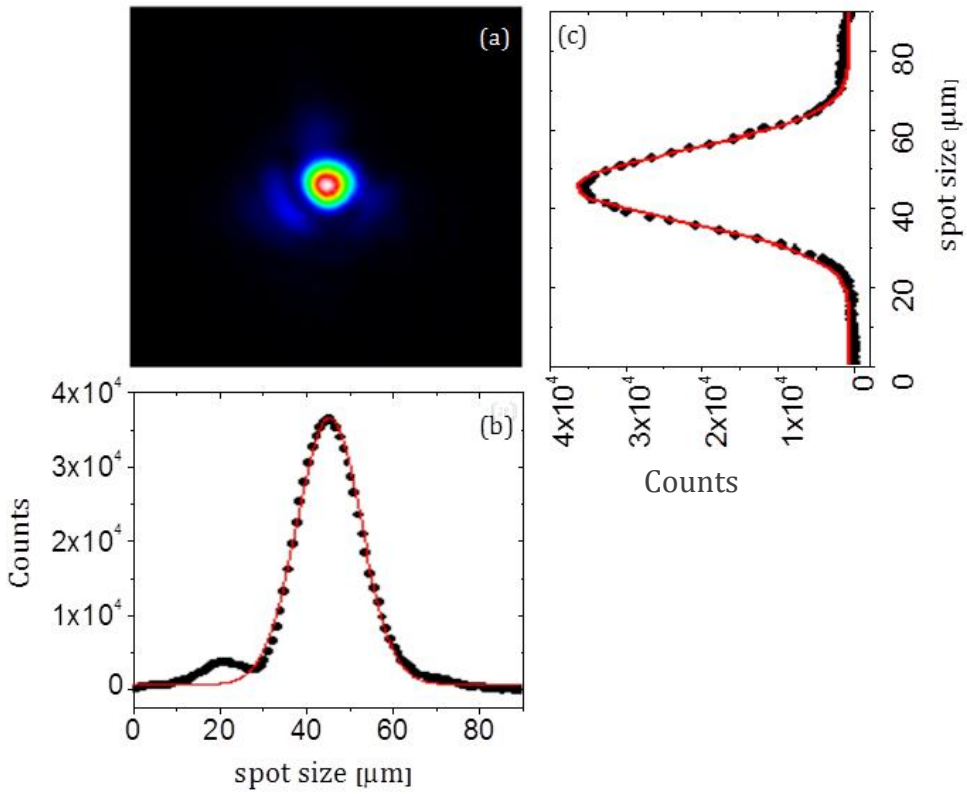

Figure 5.3: The laser pulse profile with maximum peak intensity. (a) Laser pulse image at the focus (w_0 = 20 μm). (b) Transverse and (c) vertical spatial profiles of the laser pulse where red curves are Gaussian fits.

The imaging system is then adjusted 4 cm further away. The waveguide structure is then moved back along the beam line using the three translation stages and adjusted longitudinally and horizontally until a sharp image of the exit plane of the capillary is observed on the CCD camera, as shown in Fig. 5.4. Such an image of the unguided laser pulse (no plasma discharge) indicates a well aligned capillary with a fairly symmetrical signal across the capillary and most of the laser energy on-axis.

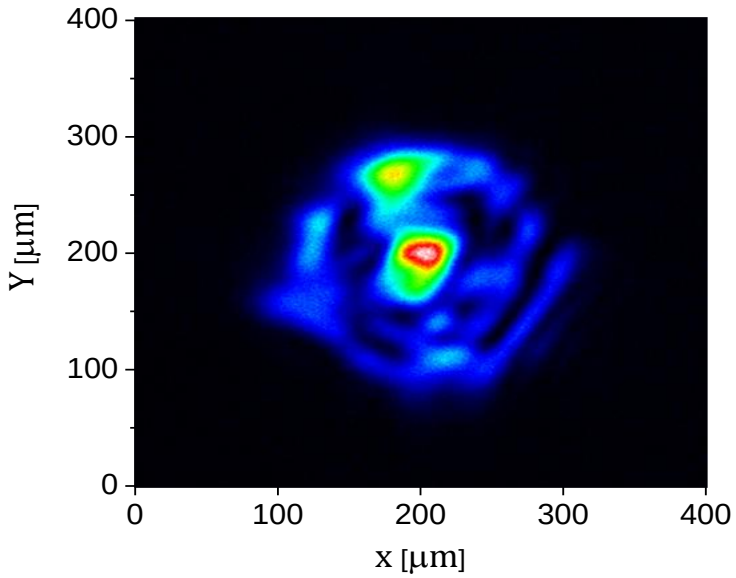

Figure 5.4: Transverse spatial profile of the laser pulse with lower laser energy (~ 0.5 mJ) at the exit plane of a capillary (diameter = 230 μm) without plasma discharge, i.e., for alignment purposes only.

During the alignment operation, the displacement of the laser pulse focus on the entrance of a capillary for 100 shots is measured with the optical system and presented in Fig. 5.5. Here, the pointing variation (the fluctuations of laser focus position) is defined in both the vertical and transverse directions by σ, where σ is the standard deviation of the distribution. One can see that the laser has very good stability in the vertical direction (σ_y = 1.5 μm) but suffers from larger fluctuations in the horizontal direction (σ_x = 6.7 μm) although this is still only a fraction (~ 0.3) of the focal spot size (w_0 = 20 μm). Pointing fluctuations of this type could be due to the way in which the vacuum chambers and optical mounts are fixed in position. It is believed that there is a coupling to vibrations in the laboratory walls that generates pointing fluctuations mostly on one axis of the laser at the accelerator location. However, the magnitude of these pointing fluctuations are acceptable for high-power capillary discharge waveguide operations with very low probability that the beam will strike the capillary wall for any laser shot causing damage.

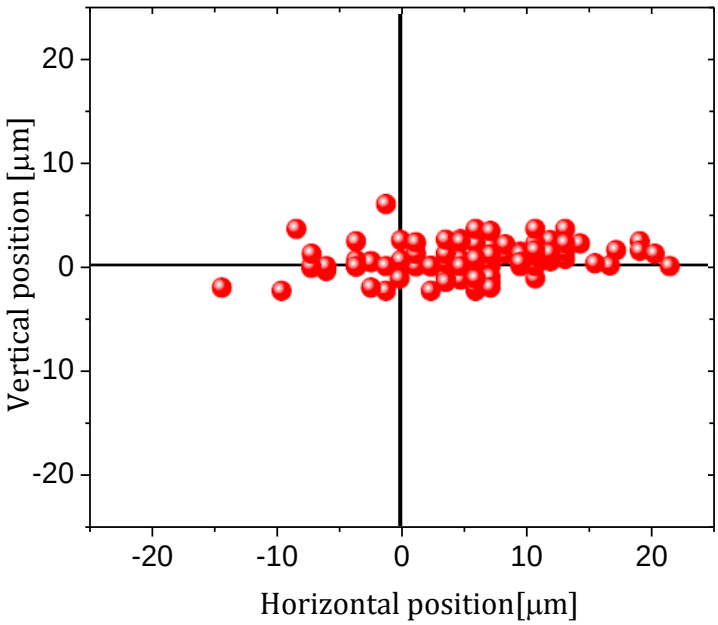

Figure 5.5: Laser beam pointing of the focal spot for 100 laser shots.

5.1.3 The waveguides

The hydrogen-filled capillary discharge waveguides used in these experiments are five alumina capillaries each of length L = 40 mm: two straight capillaries and three tapered capillaries with properties summarised in Table 5.1.

Waveguide	**Taper**	**Inner diameter D (μm) from entrance to exit**	**Capillary cross-sectional area ratio**	**Rate of capillary tapering (α)**
S1	Zero	230	1	0
S2	Zero	300	1	0
TP1	Positive	282 to 230	1.23	-0.625×10^{-3}
TN	Negative	206 to 268	0.77	0.800×10^{-3}
TP2	Positive	305 to 183	1.70	-1.525×10^{-3}

Table 5.1: Capillary parameters, taper rate $\alpha = \Delta D/2L$, where ΔD is the diameter change over length L (= 40 mm in each case).

Hydrogen is injected into the capillary by a pulsed valve (YAC-250 PSIG) connected to a hydrogen cylinder to control the flow of hydrogen with each laser shot and reduce the load on the vacuum pumps. The valve, which opens for a duration of 150 ms, is triggered using the pulse generator to operate every 15-20s, and synchronised to the discharge. The discharge is produced by a 22 kV, 900 ns voltage pulse with a rise time of ≈95 ns from the pulsed power supply based on solid-state switching and transmission line transformer described in section 3.5.

During the experimental setup, a photodiode connected to the timing oscilloscope measures the delay between the onset of the discharge current and the laser pulse arrival time. In these experiments for guiding and electron acceleration, the alignment of the laser at the entrance of the waveguide is sensitive to the laser pointing drift due to laboratory temperature variations and, for this reason, laser adjustments were required roughly once every 30 minutes.

5.1.4 Electron diagnostics

The electron diagnostics were separated from the optical diagnostics by thin aluminium foils (50 μm thickness) used to block the laser radiation but not significantly affecting electron beam. The accelerated electron bunch transverse profile is characterised using a standard technique (scintillating Lanex screens) [2], imaged onto CCD cameras, as shown in Fig. 5.1. The visible light emitted by each screen is recorded by the camera to give a 2-dimensional image of the electron beams as they passed through the detection plane. The use of this arrangement allows a spatially-resolved (~100 μm resolution) measurement of the electron beam profile.

The first Lanex screen (L1 in Fig. 5.1) is set up 64 cm from the exit plane of the waveguide to characterise the electron beam divergence and pointing stability directly after the accelerator. The second Lanex screen (L2) is located 1.40 m downstream from L1. The role of L2 is to make sure that the electron

beam is steered correctly through the centre of the vacuum pipe for correct transport to the electron spectrometer.

The energy of generated electrons is measured by a magnetic dipole imaging electron spectrometer. An electron in the electron spectrometer experiences a force given by

$$F_L = ev \times B \tag{5.1}$$

where F_L is the Lorentz force, e is the electron charge, v is its velocity and B is the magnetic field. When the electron propagates perpendicular to the magnetic field, the force is in the orthogonal direction to both the electron direction of motion and the magnetic field due to the cross product as shown in Fig. 5.6.

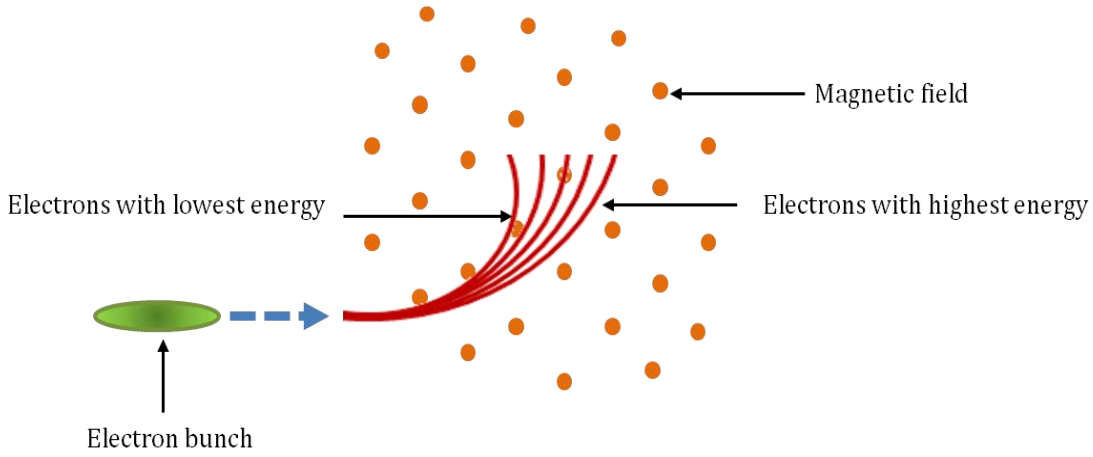

Figure 5.6: Illustration of the *v* x *B* force. Electrons emerging from the capillary are bent by the magnetic field (pointing out of the page). Different energies are bent to different positions.

The result of this force are circular electron orbits with the radius of curvature depending on the velocity, i.e., energy, of the electrons and magnitude of the magnetic field. By equating the magnetic force to the centripetal force, such that

$$evB = m_e v^2/r \tag{5.2}$$

and for an electron of energy E_e and relativistic mass γm_e, the orbit radius r is given by

$$r[mm] = \frac{\gamma m_e c}{eB} \cong \frac{3.34\, E_e[MeV]}{B[T]} \tag{5.3}$$

Therefore, the electron energy is given by

$$E_e[MeV] = \frac{r[mm]\,B[T]}{3.34} \tag{5.4}$$

where

$$B[T] = -3.923 \times 10^{-8}\, I^3 \; + \; 4.527 \times 10^{-6}\, I^2 \; + \; 8.357 \times 10^{-3}\, I \tag{5.5}$$

and I is the magnet current in Amps.

The spectrometer features a Browne–Buechner design [3] to provide strong focusing in the vertical plane thus enabling excellent energy resolution to be maintained over a wide range of energies. Two operating modes are possible: the first mode (high resolution) uses a high field strength to bend the electrons through approximately 90° with relatively narrow bandwidth, high resolution imaging at the focal plane. However, this mode is restricted to energy less than 105 MeV and has not been applied in the work presented here. The second mode (high energy) allows for wide bandwidth at the expense of a lower resolution, imaging beams with energies up to 660 MeV for a magnetic field strength up to B_{ES} = 1.8 T. Scintillating Ce:YAG crystals (1 mm thickness) positioned at the focal plane are used to image electrons exiting the spectrometer field and the image is captured on a CCD camera [see Fig 5.7(a)].

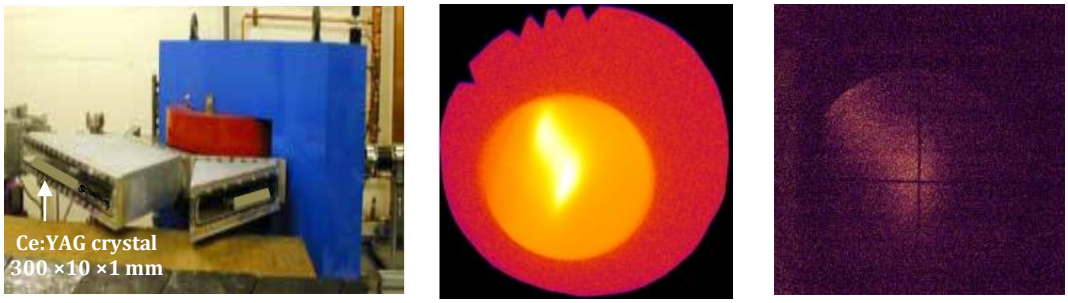

(a) **(b)** **(c)**

Figure 5.7: (a) Photograph of the electron spectrometer showing the position of the Ce:YAG screen in the high energy mode chamber, (b) example imaging plate image with electron beam charge = 1.86 pC and (c) corresponding Lanex 2 image captured simultaneously.

Ideal transport and focusing of electron beams is achieved entirely by the spectrometer magnetic field for the lower energy, high resolution mode but, for the high energy mode, external beam collimation is required for best results.

This is achieved by the electromagnetic quadrupole triplet (Q1, Q2 and Q3 in Fig. 5.1). In the experiments, the electron spectra are obtained with quadrupole magnet field strengths of 120 mT and spectrometer magnetic field strength in the range B_{ES} = 0.91-1.25 T.

Absolute charge measurements are made using imaging plates (Fujifilm, BAS-SR2025) inserted into the electron beam line, as shown in Fig. 5.7(b). This example imaging plate image shows 1.86 pC of charge and the simultaneous image for the Lanex 2 screen is shown in Fig. 5.7(c). Lanex 2 is thus calibrated directly and the electron spectrometer high energy Ce:YAG screen is cross-calibrated with Lanex 2 by averaging over many shots. The calibration value for the Ce:YAG screen is (Q[pC] = (number of electrons × e)/ 0.16×10^{-12}) [4].

5.2 Experimental results

In this section the results of the experiments are presented and significant trends are highlighted. Characterisation of the transmitted laser pulse and the accelerated electron beams are presented separately. The condition of the five used capillaries after high-power operation is also documented for future reference.

5.2.1 Characterisation of the transmitted laser pulse

5.2.1.1 High-power guiding

Characterisation of the guiding of low power femtosecond laser pulses through the capillaries (using a different laser system) has been presented in section 4.3.2. In this section, guiding is studied in-situ on the accelerator beam line set-up using the same high-power pulses as those used for wakefield experiments. Also, prior to the laser wakefield experiments, low power laser guiding performance is optimised by adjusting the initial gas density.

For complete optimal conditions, firstly using the S1 capillary, the energy transmission through the plasma channel is measured as a function of the time delay between the discharge and the laser pulse at a hydrogen backing pressure of 100 mbar and an applied voltage of 22 kV. The time delay for best guiding is

measured to be 100 ns before the peak of discharge current. Secondly, using the same capillary, the guiding efficiency is investigated as a function of the capillary longitudinal position with respect to the laser focal spot position. As an example, Fig. 5.8 shows the guiding efficiency versus the relative capillary positions at the best delay time for the S1 capillary. In an identical manner, the same experiment is conducted for all the other capillaries.

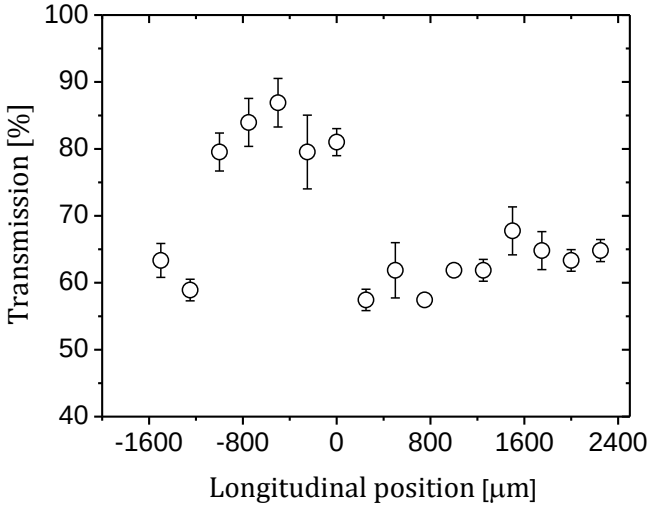

Figure 5.8: Guiding efficiency measured as a function of the longitudinal position with respect to the laser focal spot position for the S1 capillary. Zero on the x-axis indicates the entrance plane of the capillary.

From Fig. 5.8, it can be seen that the guiding performance is very sensitive to the input-beam alignment. The longitudinal alignment is important to adjust the laser focus position so that it coincides with the entrance of the channel to obtain the best coupling. Transverse alignment is also important because any misalignment can lead to the beam hitting the capillary wall and therefore to damage of the capillary. Also, even without damage, transverse misalignment leads to multi-mode guiding.

For longitudinal positions between -1500 μm and 2250 μm, the transmission varies between 57% and 88% and the best energy transmission occurs at 500 μm from the initial position defined by the imaging system. This position is then fixed as the optimal position for the electron acceleration experiment.

To determine the guiding performance for both straight and tapered plasma waveguides, the laser transmission has been measured for all capillaries described in Table 5.1 for a discharge delay ~0 ns (peak of discharge current) and ~-100 ns (for best guiding). Laser guiding efficiency results for straight and tapered capillaries for low power laser [E_{laser} ~6 mJ and 40 fs FWHM duration, which gave P ~0.15 TW (a_0 ~0.10)] are presented in Fig. 5.9(a) and (b), respectively. From these figures it can be seen that in general the guiding efficiency at the laser-discharge synchronisation timing for best guiding for all types of capillary is equally efficient, in agreement with the low-power results presented in chapter 4.

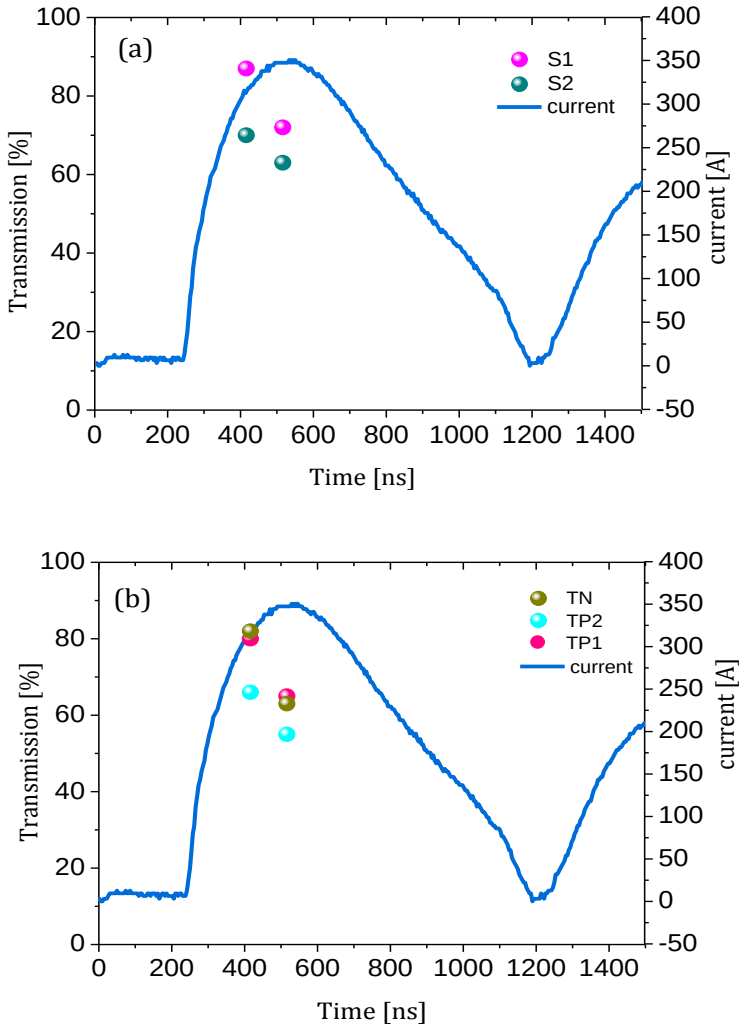

Figure 5.9: Low power guiding efficiency for two discharge delays. The discharge current (solid line, right axis) and transmission loss (circles, left axis) are shown for (a): straight capillaries S1 and S2, and (b): tapered capillaries TN, TP2 and TP1.

The maximum measured transmissions are $(87 \pm 7)\%$, $(82 \pm 10)\%$ and $(80 \pm 11)\%$ for the capillaries that have narrower entrance diameters respectively (S1, TN and TP1). For these three capillaries, later timing at discharge delay ~0 ns results in a reduced transmission of $(72 \pm 10)\%$, $(63 \pm 7)\%$ and $(65 \pm 8)\%$, respectively. The capillaries with wider entrance diameters (S2 and TP2) display lower maximum measured transmissions of $(70 \pm 12)\%$ and $(66 \pm 9)\%$, respectively, dropping to $(63 \pm 8)\%$ and $(55 \pm 7)\%$, respectively at a discharge delay ~0 ns.

The dependence of the efficiency on the entrance diameter of the capillary may be due to the mismatch between the laser focal spot size and the plasma channel matched waist size ($w_{0M} \approx 32$-64 μm compared with $w_{0L} = 20$ μm [see table 5.2]) which leads to oscillation of the beam diameter (see section 3.1.2). With larger oscillation amplitudes, part of the power can escape from the channel and intercept the capillary wall, resulting in a loss of the energy [5], as can be clearly observed for the case of the tapered capillary TP2.

When the input laser power is increased to 20 TW, the transmitted laser pulses shows a decrease in measured energy transmission for all capillaries, as presented in Fig. 5.10 (all data have been obtained for a hydrogen backing pressure of 200 mbar and an applied voltage of 22 kV). Guiding of high-power laser pulses in the narrower entrance capillaries (S1, TP and TN) are similar in terms of transmitted laser energy and mode structure. Despite being far from the matched condition, however, significant energy transmission of $(67 \pm 10)\%$ is obtained for the three capillary types at the laser-discharge synchronisation timing for best guiding [Fig. 5.10(c)], confirming that guiding is equally efficient in the presence of a density taper [section 4.3.2.2]. In each case, later timing results in a mean reduced transmission of $(30 \pm 10)\%$ due to plasma wake formation and subsequent electron beam production [6].

The wider entrance capillaries (S2 and TP2) both exhibited a smaller decrease in energy transmission under high power guiding. For the delay for best guiding, the transmission is $(60 \pm 11)\%$ for both, which is only ~7% less

than the narrower entrance capillaries. For a time delay for best acceleration, the mean transmission of (29 ± 9)% is similar to that measured for the other capillaries. This indicates that the mismatching of the channel is less significant at high powers, because relativistic self-focusing of the laser at the start of the interaction plays an important role. This is discussed in more detail later.

5.2.1.2 Transmitted laser spectra and stimulated Raman scattering

Analysis of the transmitted laser spectra provides information on the plasma characteristics. Stimulated Raman scattering (due to the Raman instability) can modify the laser spectrum [6]. Stimulated Raman scattering is the resonant decay of an incident laser photon into a scattered laser photon and a plasmon (electron plasma wave)[7]. For this to occur the frequency matching conditions

$$\omega_0 = \omega_s \pm \omega_p \,, \tag{5.6}$$

$$\boldsymbol{k}_0 = \boldsymbol{k}_s \pm \boldsymbol{k}_p \,, \tag{5.7}$$

must be met, where ω_0 , $\boldsymbol{k}_0$ are the frequency and wave number of the incident photon and ω_s , $\boldsymbol{k}_s$ are the frequency and wave number of the scattered photon. There are two types of stimulated Raman scattering that experimentally can be demonstrated by the presence of peaks known as Stokes/anti-Stokes or Raman satellites peaks located either side of the central frequency in the spectrum of a laser pulse that has propagated through the plasma [8].

Stimulated Raman scattering is a good tool for plasma diagnostics because ω_p depends on the plasma density and, therefore, the frequency of the Stokes/anti-Stokes peaks can be used to estimate the plasma density. In this work, Raman peaks have been observed and used to deduce the plasma density inside each waveguide. Comparison is made with the Stark-broadened spectroscopy results of section 4.3.

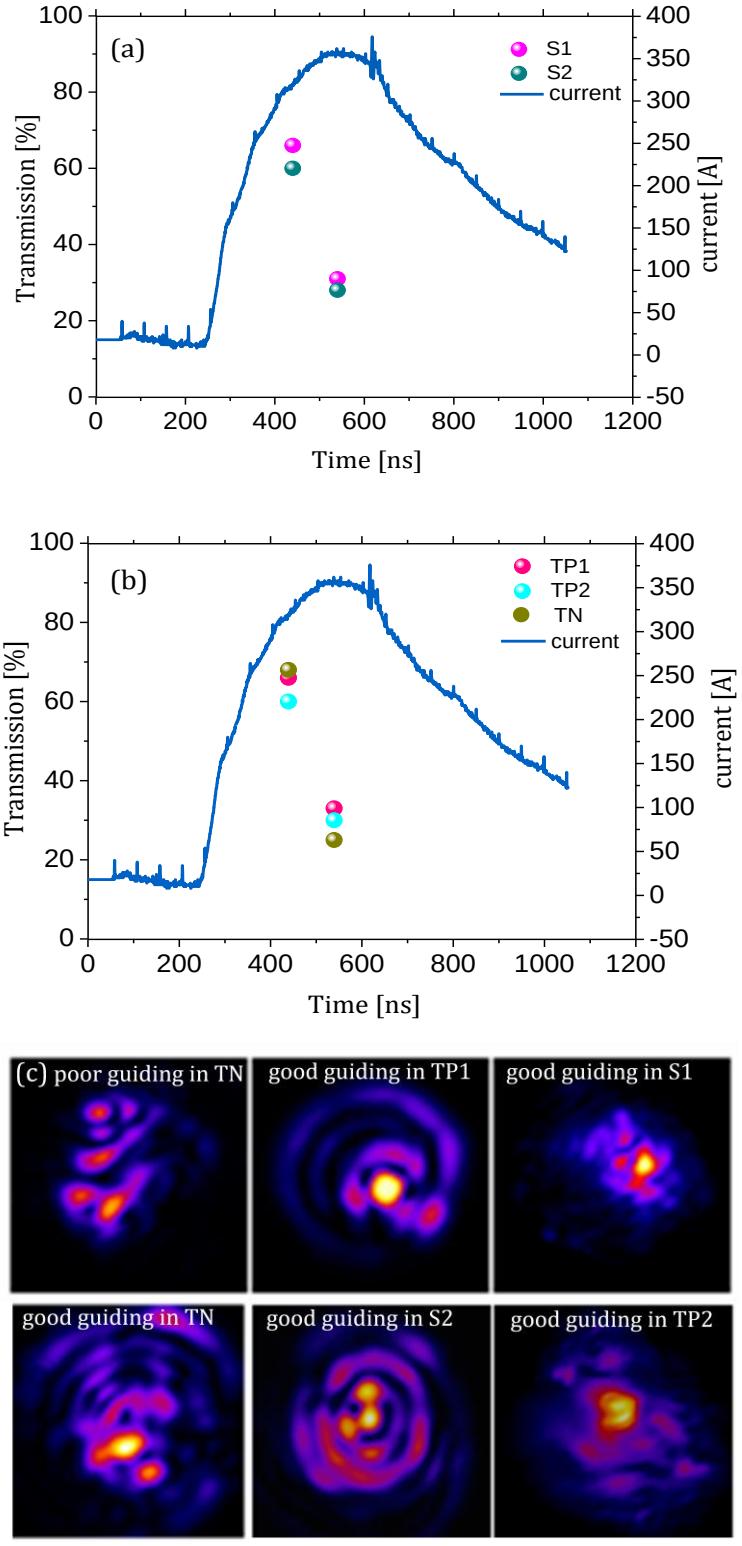

Figure 5.10: Dependence of high power guiding efficiency at two discharge delays indicating the discharge current (solid line, right axis) and transmission loss (circles, left axis). (a): For straight capillaries S1 and S2. (b): For tapered capillaries TN, TP2 and TP1. (c) Example images of: poor guiding in TN and good guiding in TP1, S1, TN, S2 and TP2.

As examples of this, two different spectra of the transmitted laser pulse compared with the original laser spectrum are presented in Figs 5.11 to 5.15 for S1, S2, TP1, TP2 and TN respectively. These figures show that at the optimum guiding delay, the spectrum of the transmitted laser pulse has not significantly broadened, meaning that excitation of plasma wave is minimal. At the delay for optimum electron acceleration, the spectrum of the transmitted laser pulse has been significantly broadened and Raman peaks appear at $\pm\,\omega_p$, mainly on the high frequency side of the central wavelength. Those peaks have been used to estimate the on-axis density.

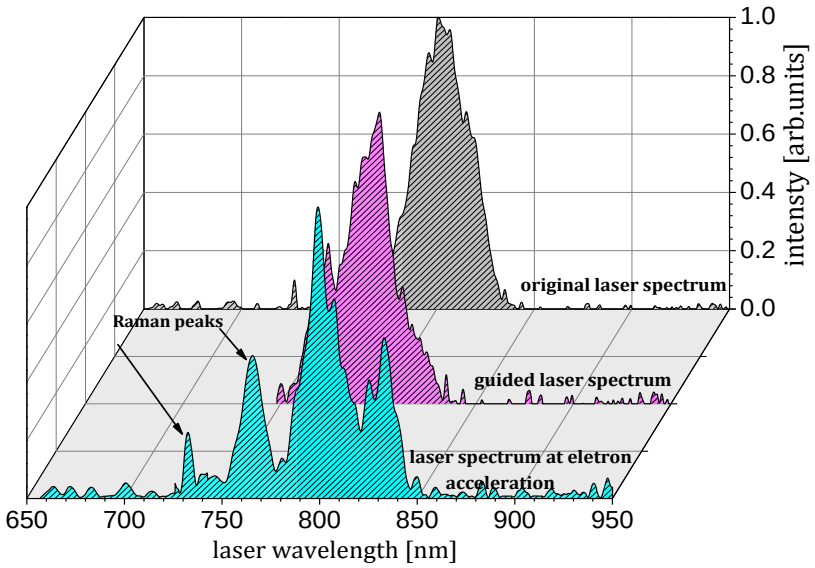

Figure 5.11: Typical transmitted laser spectra for different regions of the guiding curve produced from straight capillary S1. The grey curve is the original spectrum of the incoming laser pulse which is used as a reference. The green curve represents a spectrum for optimum electron acceleration conditions, clearly showing the Raman peaks. The pink curve represents the spectrum of a well guided pulse.

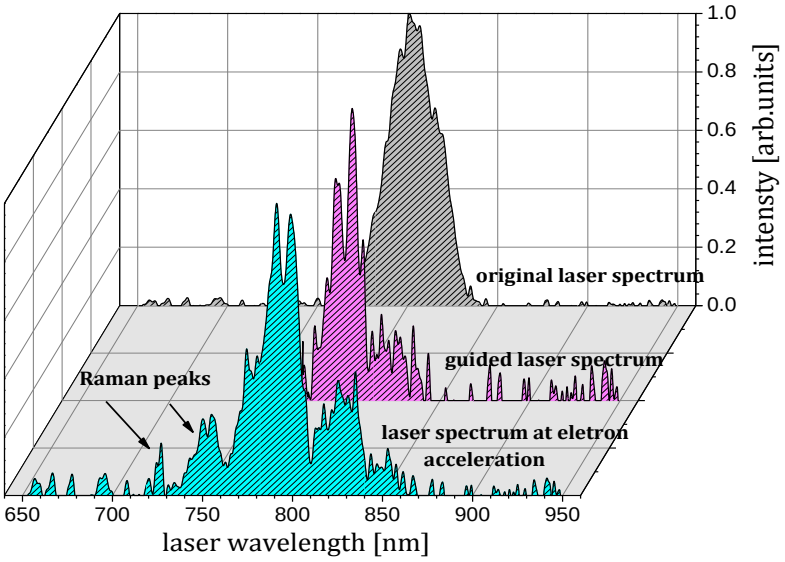

Figure 5.12: Typical transmitted laser spectra for different regions of the guiding curve produced from straight capillary S2. The grey curve is the original spectrum of the incoming laser pulse, which is presented as a reference. The green curve is the spectrum under optimum electron acceleration conditions showing Raman peaks. The pink spectrum corresponds to a well guided pulse.

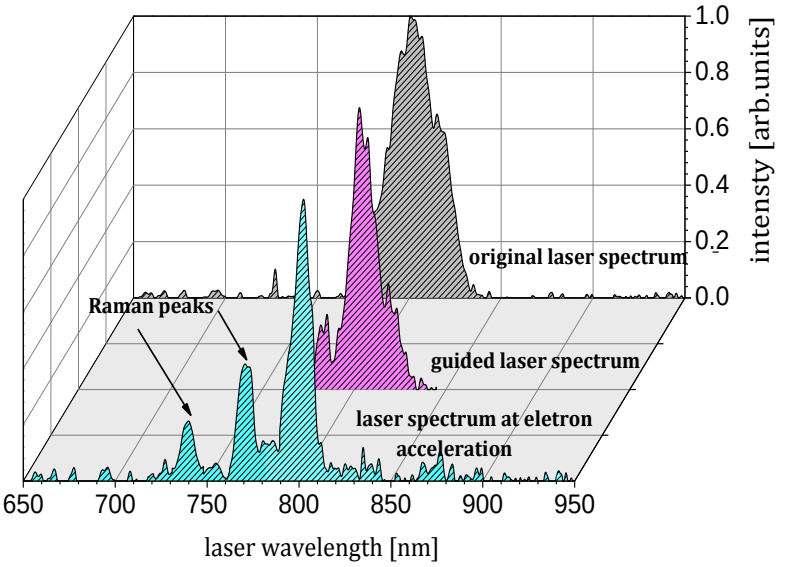

Figure 5.13: Typical transmitted laser spectra for different regions of the guiding curve for the tapered capillary TP1. The grey curve is the original spectrum of the incoming laser pulse, which is presented as a reference. The green curve indicates the spectrum measured for optimum electron acceleration conditions, showing clear Raman peaks. The pink curve is the spectrum for a well guided pulse.

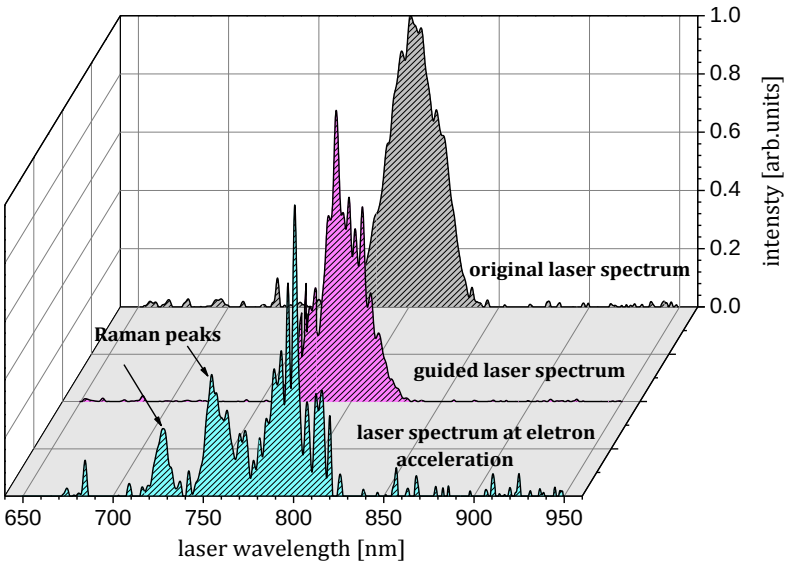

Figure 5.14: Typical transmitted laser spectra for different regions of the guiding curve produced from the tapered capillary TP2. The grey curve is the original spectrum of the incoming laser pulse, which is presented as a reference. The green curve shows the spectrum for optimum electron acceleration conditions, clearly showing the Raman peaks. The pink curve shows the spectrum of a well guided pulse.

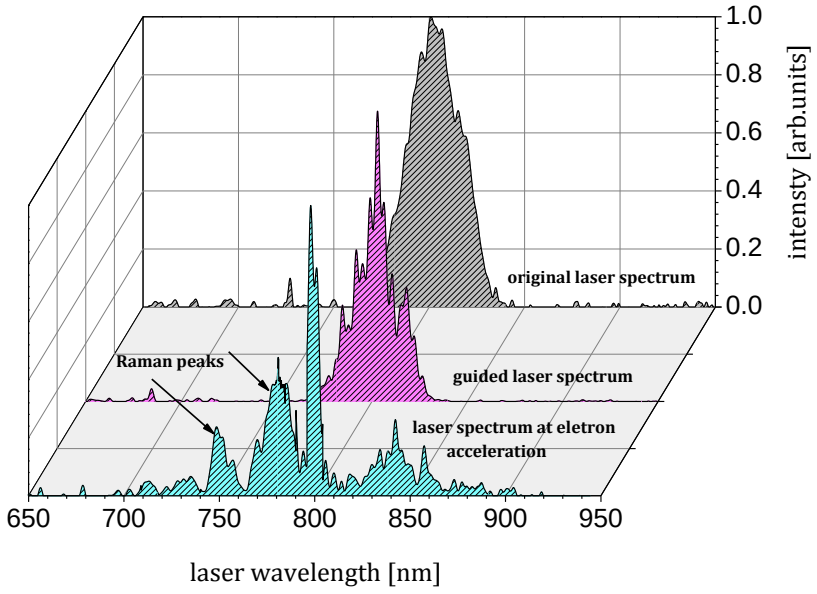

Figure 5.15: Typical transmitted laser spectra for different regions of the guiding curve produced from the tapered capillary TN. The grey curve is the original spectrum of the incoming laser pulse, which is presented as a reference. The green curve is the spectrum measured for the optimum electron acceleration conditions, clearly showing the Raman peaks. The pink curve is the spectrum measured for a well guided pulse.

At full power operation, the laser pulse is sufficiently intense to excite a strong plasma wave and electrons can be accelerated. The laser energy transmission drops due to the high energy transfer to the plasma as previously shown in the guiding section. From Fig. 5.11, the frequency up-shifted peaks give an estimated of the on-axis electron density of $n_e = 3.50 \times 10^{18}$ cm^{-3} at a backing pressure of 140 mbar and an applied voltage of 22 kV.

For the second straight capillary S2, Raman peaks are also observed as shown in Fig. 5.12. These peaks have been utilised to estimate the on-axis density as $n_e = 4.10 \times 10^{18}$ cm^{-3} at a backing pressure of 300 mbar and an applied voltage of 22 kV.

In the case of tapered channels, this diagnostic provides the average (or midpoint) density, with the estimated start-to-end density change determined by the corresponding cross-section change rate [section 4.3.1.2]. From Fig. 5.13, the estimated average electron density for positive taper capillary TP1 is $n_e = 3.10 \times 10^{18}$ cm^{-3} for a backing pressure of 150 mbar and an applied voltage of 22 kV. Also from Fig. 5.14, the average electron density for the second positive taper capillary TP2 has been estimated to be 5.60×10^{18} at a backing pressure of 300 mbar and the same applied voltage. For the negative taper TN, Raman peaks have also been observed on the high frequency side (higher than the central frequency) as shown in Fig. 5.15. At backing pressure of 175 mbar and applied voltage of 22 kV, the average electron density is estimated to be $n_e = 3.60 \times 10^{18}$ cm^{-3} .

Table 5.2 presents the on-axis estimated density of all used straight and tapered capillaries. From this table, it can be seen that the estimated on-axis densities using Raman spectroscopy of the transmitted laser pulse are consistent with the measured plasma densities using the Stark-broadened spectroscopy technique (section 4.3.1). As an example for the straight capillary S2, the averaged measured density by Stark-broadened spectroscopy at applied voltage of 21 kV and backing pressure of 60 mbar was $\sim 1.55 \times 10^{18}$ cm^{-3} and, thus, the peak density was expected to be $\sim 3.1 \times 10^{18}$ cm^{-3}. Here the measured value by Raman spectroscopy at higher backing pressure (300 mbar) and same applied voltage is 4.10×10^{18} cm^{-3}. In this case, and taking in account the

backing pressure, the two values are comparable. Our measurements here for the plasma density are also consistent with the plasma density measurements by Jang [9] who measured an electron density of 4.5×10^{18} cm^{-3} for capillary (diameter of 300-400 μm and length of 33 mm) with a hydrogen gas pressure of a few hundred mbar range at applied voltage of 25 kV using Stark-broadened spectroscopy .

Waveguide	**entrance density (10^{18} cm^{-3})**	**exit density (10^{18} cm^{-3})**	**averaged density (10^{18} cm^{-3})**	**matched spot size (μm)**	**P_{cr}[TW]**
S1	3.5	3.5	3.5 ± 0.8	37	8.70
S2	4.1	4.1	4.1 ± 0.5	40	7.41
TP1	2.5	3.8	3.1 ± 0.9	44	9.80
TN	4.7	2.8	3.6 ± 0.6	32	8.44
TP2	3.4	9.3	5.6 ± 0.9	46	5.42

Table 5.2: Capillary parameters with experimental on-axis plasma density estimated from the Raman peaks. Also on-axis plasma measured density at the entrance and the exit for tapered capillaries are estimated from the respective taper rates. Each uncertainty (shown for the averaged density only) is the standard deviation of 3 shots (4 in the case of S2). The critical laser power P_{cr} in practical units for λ = 0.8 μm case, $P_{cr}[\mathrm{TW}] = 30.4/n_e \times 10^{-18}$ [cm^{-3}] [10].

These plasma density measurements are in agreement with the on-axis density measurements by Spence *et al.* [11] who used an interferometric method to measure an on-axis electron density of 2.7×10^{18} cm^{-3} for a 300 μm alumina capillary with a hydrogen gas pressure of 67 mbar. The average discrepancy with respect to the established interferometry technique [12] is 12%. The measurement of plasma density obtained in similar capillary waveguide discharge experiments for betatron radiation production, which was 2×10^{18} cm^{-3} at 60 mbar pressure [13], compares well with our measurements of the electron density presented here and the agreement is quite acceptable.

5.2.2 Electron beam generation

As seen from the measurements to determine the guiding performance, the laser deposits a significant fraction of its energy into the plasma at high intensity, which leads to the generation of the plasma wake and accelerated electron beams. This section presents an overview of measurements of electron beam profiles and energy spectra from all the straight and tapered capillaries that have been studied.

5.2.2.1 Electron beam divergence and pointing

The beam profile of electron beams exiting each capillary has been measured on Lanex screen L1 located 0.64 m downstream, which is imaged by a CCD camera. Table 5.3 summarises the relative beam charge, divergence and pointing behaviour for large data sets collected under the optimal acceleration conditions for the three capillary types. Lanex L1 is uncalibrated for absolute charge and the charge measured at this position also includes the low energy tail of the electron beam. Most charge was injected into the bunch, on average, in the capillary TP1. The reason for this could be that, for the case of a positive density gradient, the density near the entrance is lower, resulting in a larger bubble ($R \cong (1/\pi)\sqrt{\gamma\,\lambda_p}$, where γ is the relativistic factor), into which more electrons can be injected [14].

Fig. 5.16(a), (b) and (c) show images of electron beam profiles for TP1, S1 and TN. However, for the straight capillary S1, the best three shots show that the mean beam r.m.s. divergence is less than 1 mrad with a beam divergence of 0.70 mrad r.m.s. assuming a Gaussian profile. For the tapered capillary TN, the divergence improves and the beam profiles correspond to very low divergences. An r.m.s. divergence down to just 0.5-0.6 mrad is measured as shown in Fig. 5.16 (c) for the best shots.

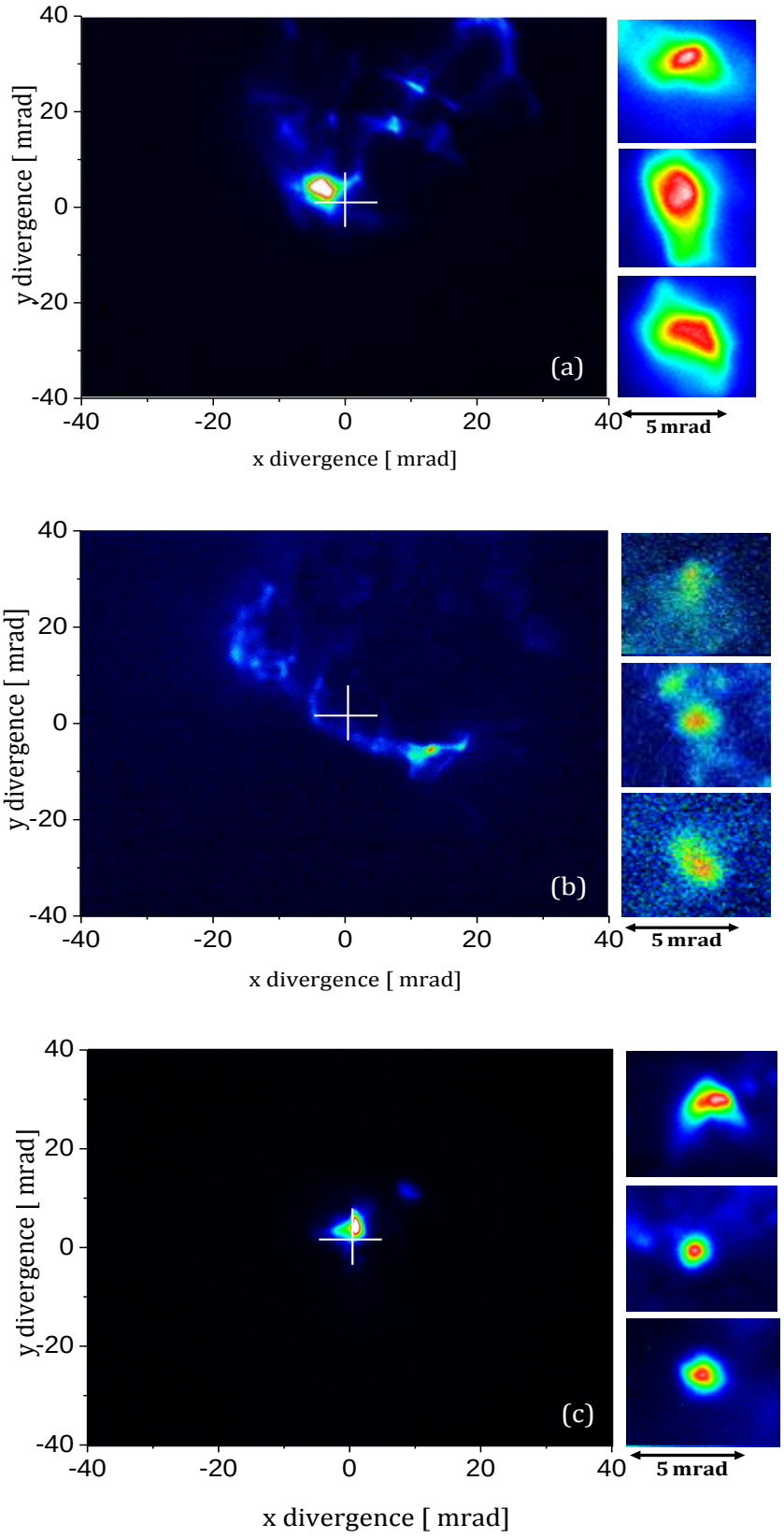

Figure 5.16: Example images of electron beam profiles for (a) TP1, (b) S1 and (c) TN. The best three shots are shown for each capillary. The beam line axis is indicated by a white cross.

Name	Number of shots	Mean Q_{rel} [a.u.]	Mean (Min.) θ_Y [mrad]	Mean (Min.) θ_X [mrad]	Mean φ_Y [mrad]	Mean φ_X [mrad]
TP1	88	2.6 ± 1.0	3.0 ± 0.6 (0.8)	3.3 ± 1.1 (0.9)	-2.3 ± 6.6	2.0 ± 7.6
S1	68	0.5 ± 0.1	1.7 ± 0.8 (0.8)	1.4 ± 0.5 (0.7)	-19 ± 10	9.0 ± 13
TN	100	1.6 ± 0.4	1.3 ± 0.5 (0.6)	1.8 ± 0.8 (0.5)	-0.4 ± 2.1	0.3 ± 1.3

Table 5.3: Beam profile measurements showing the mean (minimum) electron beam relative charges Q_{rel}, the r.m.s. divergences θ and pointing angles φ in the vertical Y and horizontal X planes, respectively, for each capillary type. The uncertainty is given as the r.m.s. standard deviation.

The dependence of the divergence on the relative electron beam charge has been studied by analysing a large number of shots for straight capillary S1 and two tapered capillaries TP1 and TN. For these three capillaries, Fig. 5.17 shows the measured beam divergence plotted as a function of the relative beam charge in the horizontal and vertical planes. As shown in Fig. 5.17(a), (b) and (c) the divergence scales proportionately with the charge. For tapered capillary TP1, it can be noticed from Fig. 5.17(a) that there is a sharp increase of divergence for low charges while, at higher charge, the data show a steady increase in the divergence.

For straight capillary S1, there is also a trend to larger divergence with higher charge [Fig. 5.17(b)]. This observation is similar for the behaviour of divergence with charge obtained from tapered capillary TN [Fig. 5.17(c)]. This behaviour, common to all the capillary types, may be the result from the space-charge effects due to Coulomb repulsion or an increase in the transverse momentum spread at injection due to the larger charge capture area on injection.

The trend to larger divergence with higher charge is similar to that seen in other experimental work [6] where a straight capillary with diameter of 200 μm and length of 15 mm was used. In gas jet accelerators, measurements of divergence as a function of beam charge have shown similar behaviour as well [15]. From all three capillary types, the divergence scaling with the charge that accounts for the larger divergence for capillary TP1 while the similar mean

divergences for lower charge S1 and TN data indicates a lower intrinsic limit for the divergence (~0.5 mrad as charge approaches zero) and, thus, the lowest transverse emittance is obtained.

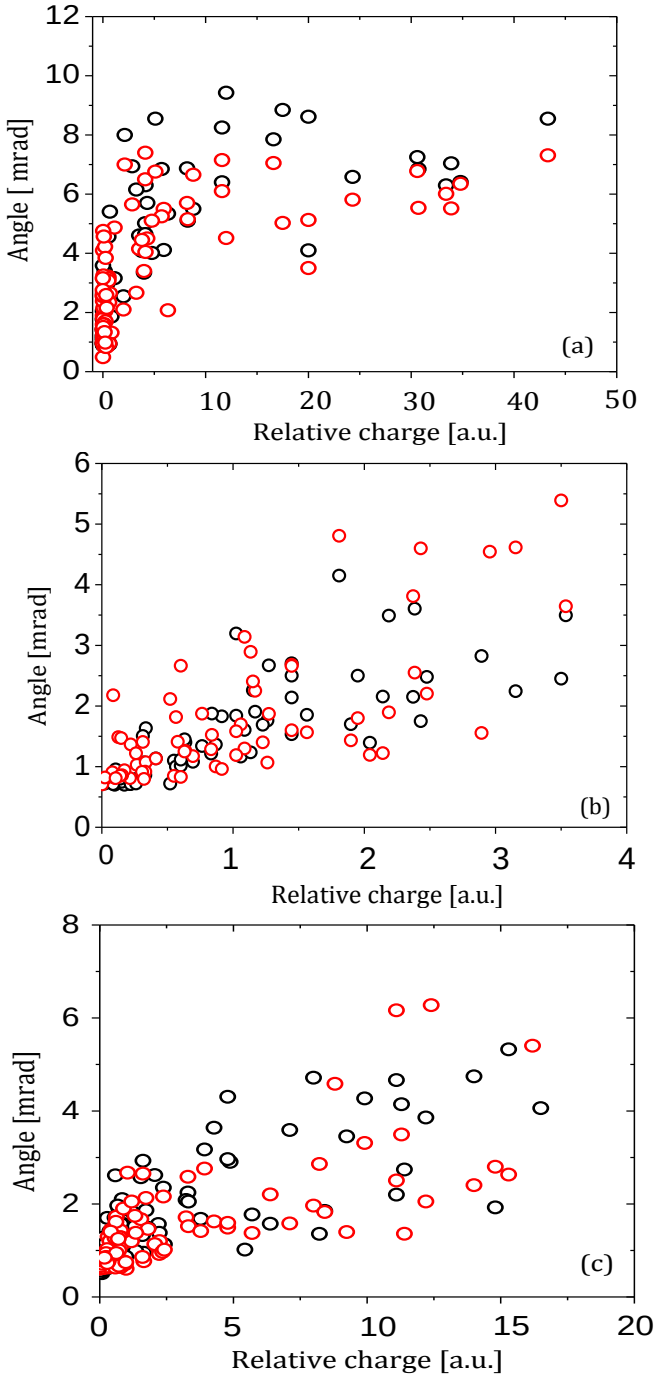

Figure 5.17: Beam divergence measured as a function of beam charge in vertical and horizontal planes for (a) TP1, (b) S1 and (c) TN. The black circles show the divergence measured in horizontal plane and the red circles show the divergence measured in vertical plane.

Very faint electron beam images have been obtained from the S2 capillary indicating extremely low charge. Under the optimal conditions, only a small number of electron beams have been captured on Lanex L1 and the beam profiles are characterised by relatively large divergences. An r.m.s. divergence up to 5-6 mrad is measured as shown in Fig. 5.18(c). Three images of electron beams at different backing pressure are shown in Fig. 5.18 with a clear dependence of the relative charge on the pressure, i.e., the total charge increased with increasing pressure. This observation is related to the probability of electron injection that increases strongly with plasma density which increases with the pressure [16] but with such high divergence, the beam quality is poor.

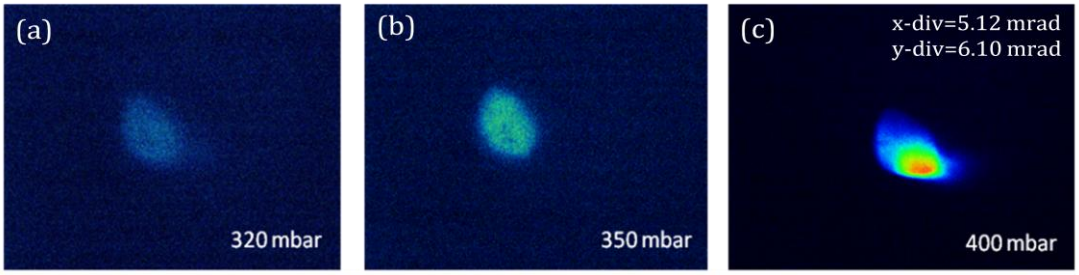

Figure 5.18: Images of electron bunches on Lanex screen L1 taken with three different relatively high backing pressures for capillary S2.

The shot-to-shot stability was poor for the strongly tapered capillary TP2 and all the electron beam properties are observed to exhibit large fluctuations. Fig. 5.19(a) shows six images of the electron beam profile where the divergence depends on the backing pressures in the range 250-420 mbar. For the minimum r.m.s electron beam divergence, the horizontal and vertical divergences are 0.46 and 0.48 mrad rms respectively. This divergence is the smallest divergence observed from all experiments described in this chapter.

From the analysis of all shots presented in Fig. 5.19(a), the divergence rises rapidly with increasing the pressure until eventually reaching a plateau at maximum pressure as shown clearly in Fig. 5.19(b). As the pressure increased from 250 to 420 mbar, the mean horizontal and vertical divergence of the beam also increased from 0.47 to 3.72 mrad rms. This behaviour indicates stronger

focussing forces creating a low divergence beam at lower pressure. The behaviour observed here is in contrast to previous work using straight capillary reported in [6].

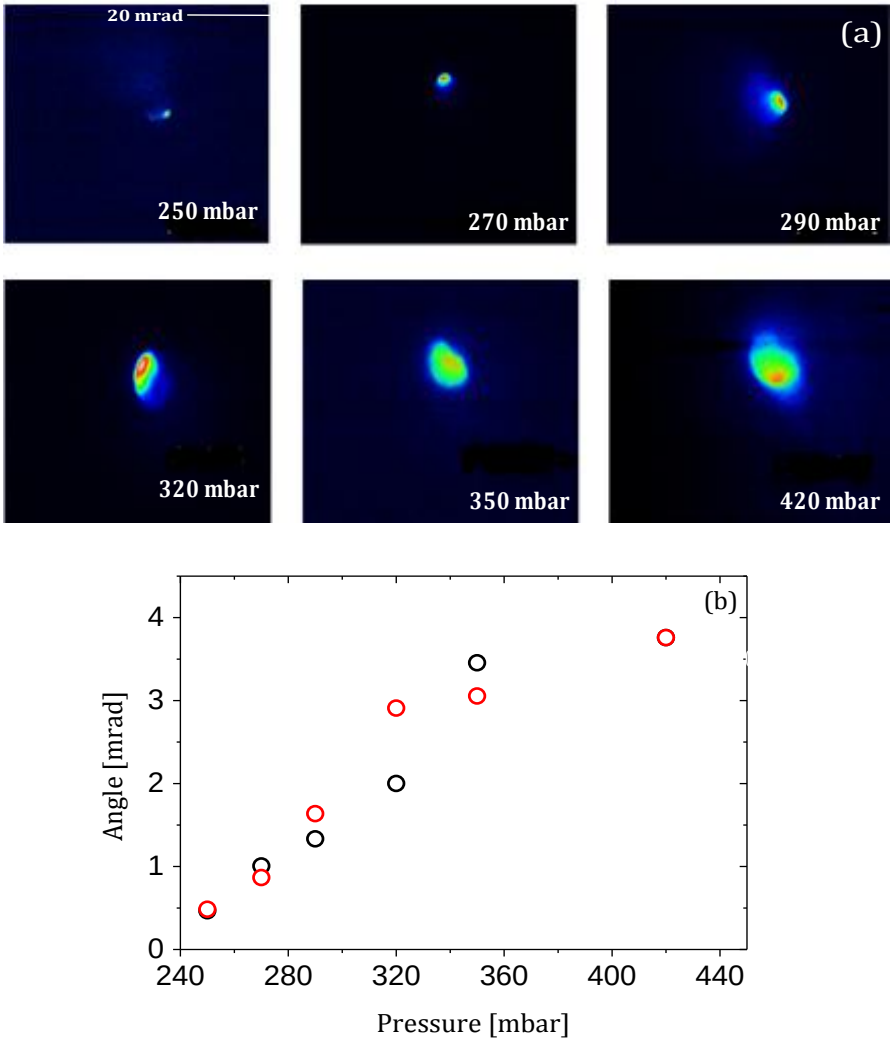

Figure 5.19: (a) Six images of electron bunches generated on screen L1 at six different backing pressures in the TP2 capillary with the laser guided from the 305 μm large end to 180 μm small end. (b) The horizontal (black circles) and vertical (red circles) divergences as a function of the backing pressure.

Shot-to-shot pointing of the electron beam fluctuations have been obtained for the three capillary types. Figure 5.20(a) and (b) illustrate the large differences in pointing angle and stability between the capillary types TP1, TN and S1 respectively. For capillary TP1, Fig. 5.20 (a) shows a large fluctuation from shot-to-shot where the beam pointing angles varies by 7.6 mrad rms and

6.6 mrad rms for the horizontal and vertical axes, respectively. The pointing angles are determined by the ratio of transverse to longitudinal momentum at the exit of the capillary. Inside the capillary, the transverse momentum oscillates according to the betatron motion, and the betatron frequency depends on the plasma density ($\omega_\beta = \omega_p/\sqrt{2\gamma}$), and thus the momentum amplitude. For the positive longitudinal plasma density gradient (TP1), the density near the capillary exit is higher and the transverse momentum is higher therefore increasing the pointing angle of the electron beam.

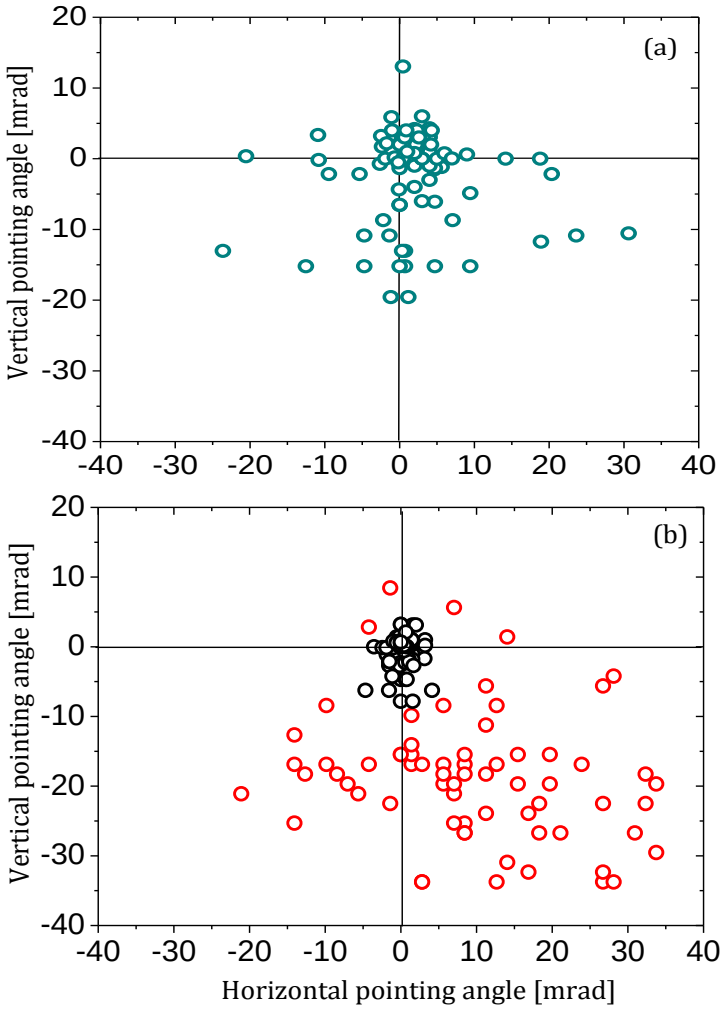

Figure 5.20: Electron beam pointing distribution for each capillary type (a): pointing distribution for 88 shots using TP1, (b): pointing distributions for 100 and 68 shots using TN (black circles) and S1 (red circles) respectively. The beam line axis is indicated by the origin.

Capillary S1 suffered from both very large angle divergence (9-19 mrad in both axes) and poor stability (10-13 mrad in both axes) and most of the electron bunches have been detected below the horizontal plane as shown in Fig. 5.20(b). This poor performance may be a product of this accelerator operating extremely close to the injection threshold (one third of shots producing no electrons, all other shots with little charge).

The largest data set (100 shots) and the highest quality electron beam in terms of close-to-axis pointing angle (0.3-0.4 mrad in both axes) and smallest pointing fluctuations (just 1.3 mrad in the horizontal axis and 2.1 in the vertical axis) have been obtained from capillary TN [Fig. 5.20 (b)]. This may be related to the negative longitudinal plasma density gradient and, as explained previously, such a decreasing longitudinal density lowers the transverse momentum near the capillary exit therefore improves the pointing angle of the electron beam upon exiting the accelerator.

5.2.2.2 Electron beam energy

At relativistic intensities, after initial waveguiding, laser beam propagation in a capillary is dominated by relativistic self-focusing (under conditions here, the critical power for self-focusing is exceeded for all capillaries [see table 5.2]), i.e., the waveguide influences the propagation only at the beginning of the interaction. This is evident in the observations that virtually no or very weak electron beam production was achieved in a larger diameter (300 μm, S2) straight capillary, in agreement with other experiments in this laser intensity range [17, 18], and the same behaviour occurred in positively tapered capillaries with a similarly wide entrance diameter (305 → 183 μm, TP2).

When the mismatch to the channel is great, the beam diffraction effect is stronger preventing strong wake generation and self-trapping of electrons (from table 5.2, note that S2 has a higher density, i.e., lower critical power for self injection, yet produced very poor electron beams). Furthermore, even the capillary type S1 with diameter 230 μm struggled to self-inject at lower plasma

densities, hence, the density was typically increased to 5.70×10^{18} cm^{-3} to facilitate injection in this capillary.

In addition to the divergence and pointing stability characteristics of the electron beams, their energy spectrum which is a very important characteristic for future applications, has been investigated. Monoenergetic electron bunches with narrow energy spread are obtained from all three capillary types (TP, S1 and TN) but with a clear difference in the mean central energy of the electron bunches.

It has been described how the injection and acceleration of electron beams depended sensitively on the discharge delay (section 5.2.1.1). If the gas backing pressure is increased, plasma-wave breaking, injection and trapping of electrons in the wake is induced. The pressure threshold above which electron acceleration occurred was around 150 mbar which gives a density around (3-6) $\times 10^{18}$ cm^{-3} ($P > P_{cr}$). It has been observed that the pressure threshold for slightly lower laser power is increased. This indicates that at lower densities electron beam generation depends more critically on the state of the plasma channel. Electron beams have been observed in a narrow window of the discharge delay ($\sim 25 \pm 5$ ns) around the peak discharge current curve which is in agreement with experiments previously performed in [17]. The experiments in general have been carried out close to the threshold for injection.

Electron beam energy for straight capillaries

For capillary S1, Fig. 5.21 shows two images of typical electron energy spectra detected by the electron spectrometer after removing the wedge while keeping Lanex1 in place. In this run, 30% of the laser shots produced an electron beam. In Fig. 5.22, four electron spectra from one run are plotted that show accelerated electron bunches with central energy for the main peak around 200 MeV with maximum value for the total accelerated charge of 0.3 pC.

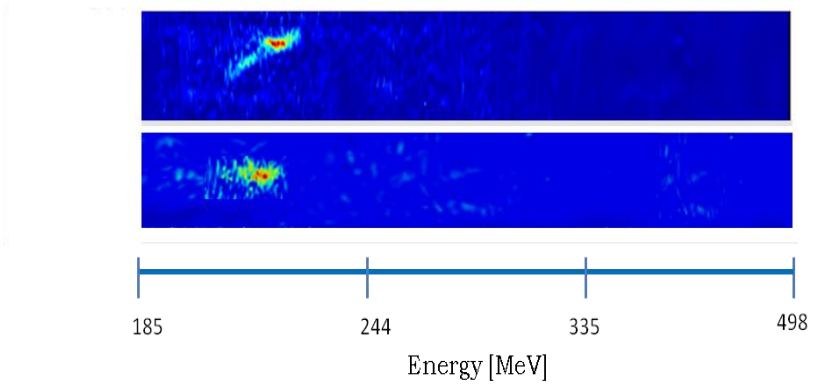

Figure 5.21: False colour images of two electron spectra captured using the electron spectrometer showing a monoenergetic electron bunch around 200 MeV for S1 capillary.

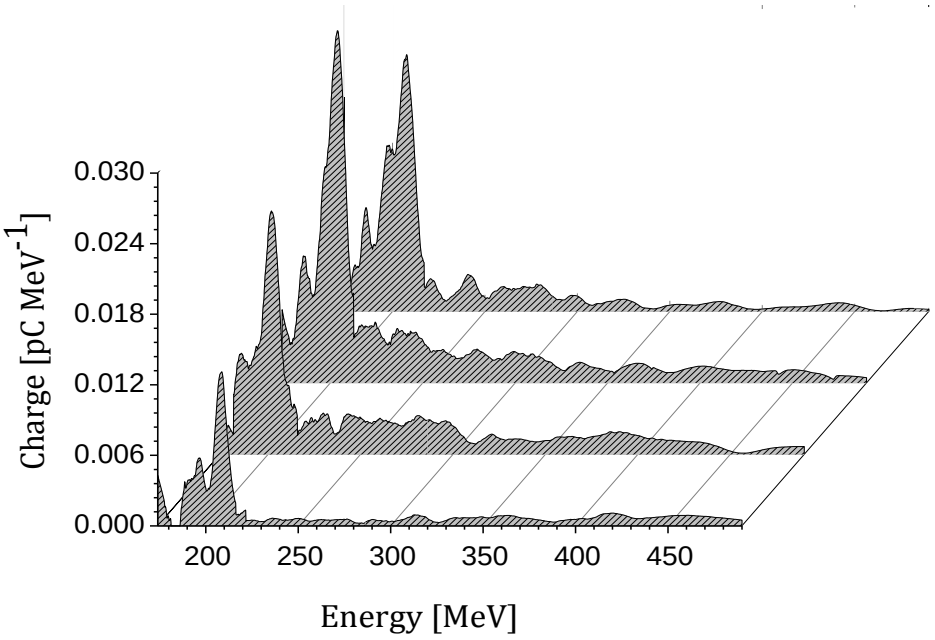

Figure 5.22: Electron energy spectra for four shots giving an average central energy of 205 MeV for straight S1 capillary.

The most of the type S1 data has been acquired at the higher end of density range ($\approx 5.7 \times 10^{18}$ cm^{-3}) where injection occurred more readily. In the density range directly comparable with the other capillary types ($\approx 3.5 \times 10^{18}$ cm^{-3}) no significant electron energy increase was observed, as might be expected for operation at lower density. Figure 5.23 shows the optimal energy spread beam

measured for S1 with central energy peaked at 205 MeV. In this case, the rms relative energy spread, $\sigma_E / E = 1.0\%$. This is the narrowest observed energy spread obtained from any of the investigated capillaries.

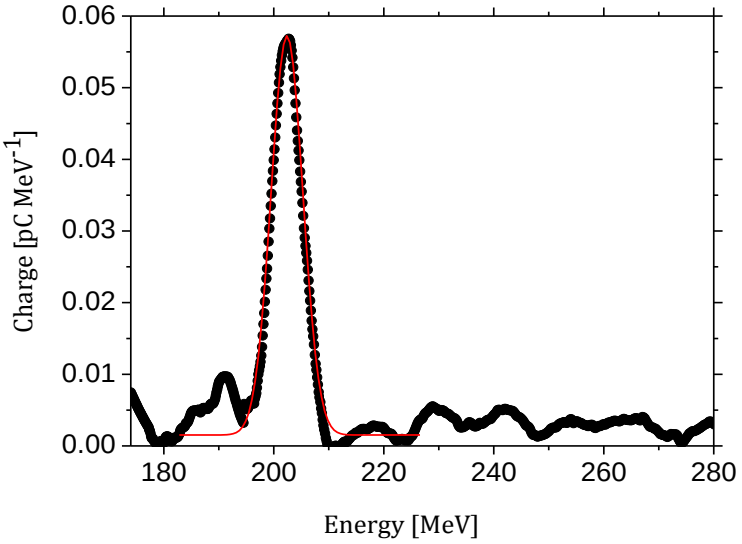

Figure 5.23: Energy spectrum for one shot giving a central energy of 205 MeV with $\sigma_E / E = 1.0\%$. The red curve is a Gaussian fit to the main peak.

No electron spectra have been observed by the electron spectrometer from capillary S2 due to the very low charge. The general poor performance of this capillary, including the extremely low charge of the electron beam, indicates the importance of matching the laser focal spot size to the plasma channel.

Electron beam energy from tapered capillaries

- **Capillary (TP1)**

Consistent with theory [19-21], the positive tapering capillary TP1 produces an energy enhancement (22% in the mean central energy of the electron bunch) with respect to capillary S1. The highest central energy for TP1 was 290 MeV with upper electron energy of 320 MeV (Fig. 5.24). If the energy enhancement is due to the taper then the enhancement obtained (20-40%) for this capillary compares well with an analytical model [21] predicting ~100-300% gain for a linearly tapered accelerator when one compares the respective taper rates (0.33×10^{18} cm^{-3}/cm in this experiment, 3.5×10^{18} cm^{-3}/cm in the model with

density range 2-8 × 10^{18} cm^{-3}). This is despite that model being solely for single particle acceleration, neglecting effects such as laser pump depletion and self-focusing. The TP1 capillary has a gentler taper rate and further optimisation of the micromachining manufacturing process [22] would increase the taper rate while hopefully still facilitating self-injection. Nevertheless, these results may provide evidence of the success of applying a positive longitudinal plasma density gradient to boost the final electron energy. This is discussed further in the Conclusions section.

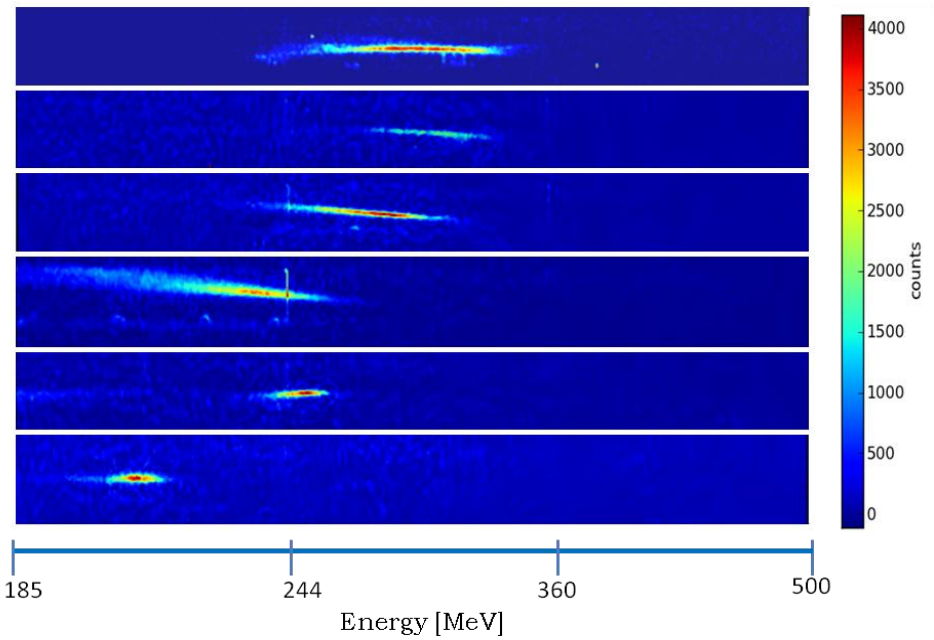

Figure 5.24: False colour images of six electron spectra measured using the electron spectrometer from TP1 through an average plasma density of 3.10 × 10^{18} cm^{-3}.

This TP1 capillary provided somewhat higher charge electron beams compared with the S1 capillary. The maximum value for the total accelerated charge was ~6.6 pC. The number of shots where quasi-monoenergetic electron beams are observed is also higher for this capillary. Here, approximately 70% of the laser shots produced electron beams. In Fig. 5.25, spectra from one run are plotted, showing accelerated electron bunches with upper electron energy ranged from 200 to 320 MeV. Figure 5.26 shows the narrowest energy spread

beams captured for central energy peak at 206 MeV. The measured rms relative energy spread, $\sigma_E / E = 1.6\%$.

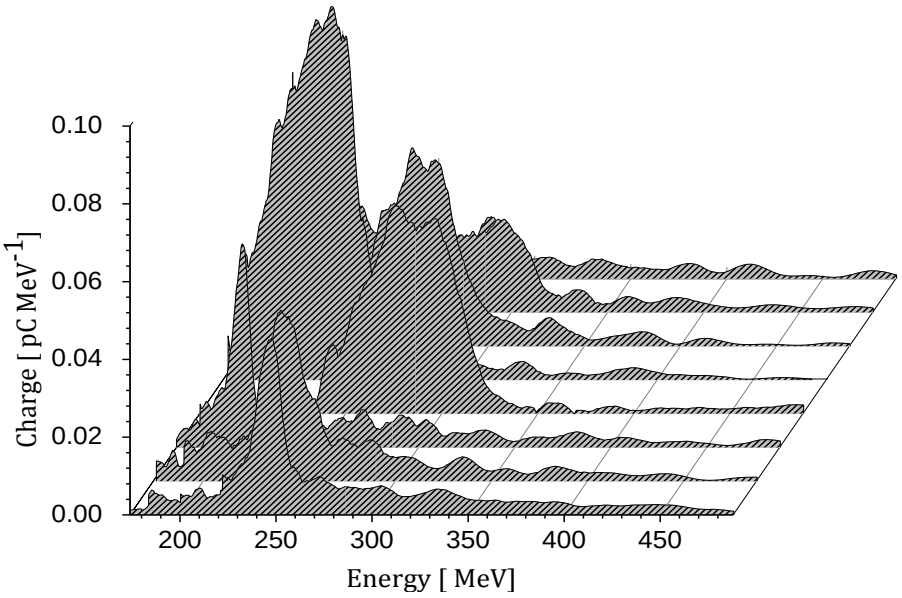

Figure 5.25: Electron energy spectra for eight shots giving an average central energy of 250 MeV for tapered capillary TP1.

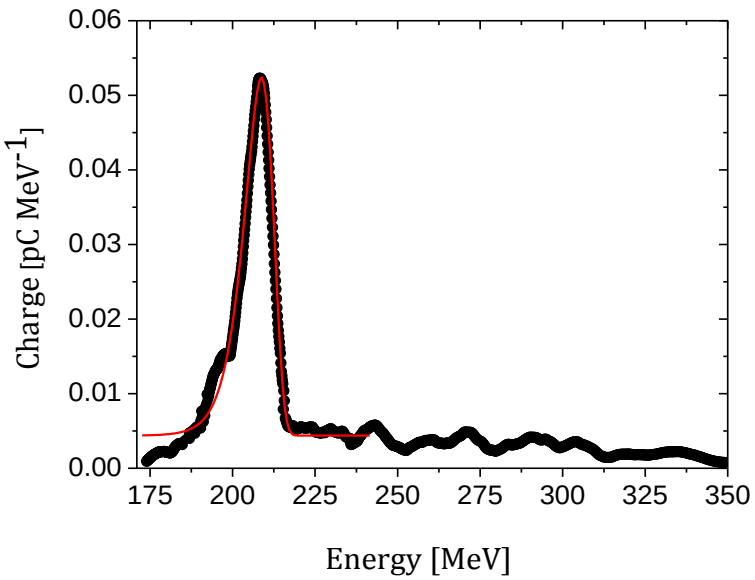

Figure 5.26: Energy spectrum for one shot giving a central energy of 206 MeV with measured energy spread $\sigma_E / E = 1.6\%$ for tapered capillary TP1. The red curve is an extreme inverted fit to the main peak.

- **Capillary (TN)**

The laser wakefield acceleration experiment has also been carried out for the tapered capillary TN. The behaviour of the electron energy obtained with negative tapering indicates a small energy reduction (–10% with respect to type S1). Stable generation of electron beams with maximum central energy of 229 MeV with upper electron energy of 250 MeV (Fig. 5.27) have been measured for this capillary. High quality (low energy spread and low beam divergence) electron beams are generated for density of 3.60×10^{18} cm^{-3}.

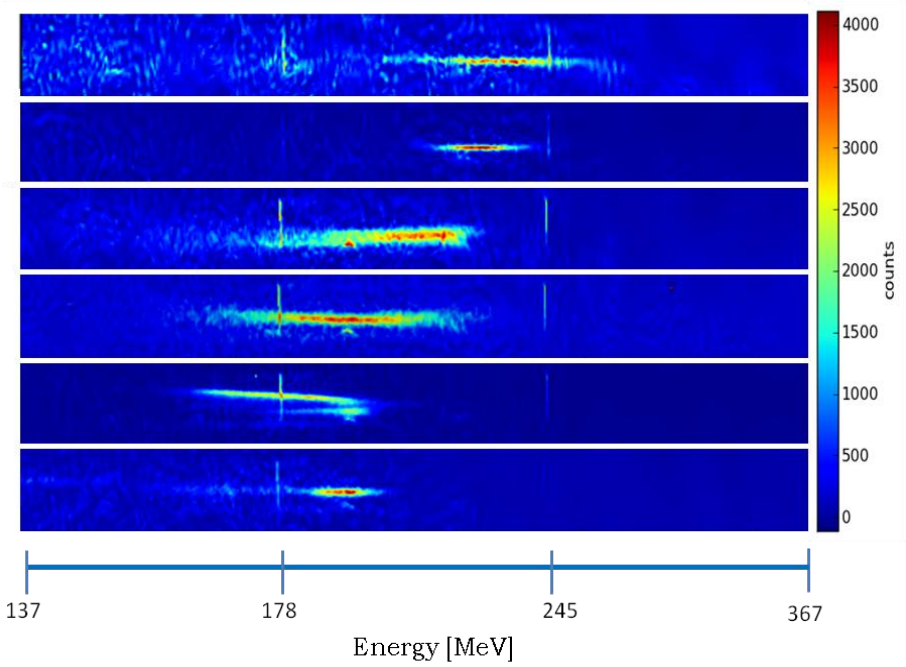

Figure 5.27: False colour images of six electron spectra captured using the electron spectrometer for capillary TN for plasma density of 3.60×10^{18}.

The capillary yielded lower charge electron beams compared with the TP1 tapered capillary. The maximum value for the total accelerated charge was ~5.1 pC. Frequent quasi-monoenergetic electron beams have been observed from this capillary with a higher shot-to-shot energy stability. An electron beam is produced on every shot. In Fig. 5.28, the electron spectra from one run at delay times corresponding to optimum beam generation are presented along with the energy calibration for energy over a wide energy range 137–367 MeV. A typical electron energy spectrum is shown in Fig. 5.29, showing a quasi-

monoenergetic beam with narrowest energy spread captured for a mean energy peak of 191 MeV. In Fig. 5.29, the measured rms relative energy spread, $\sigma_E / E = 2.6\%$.

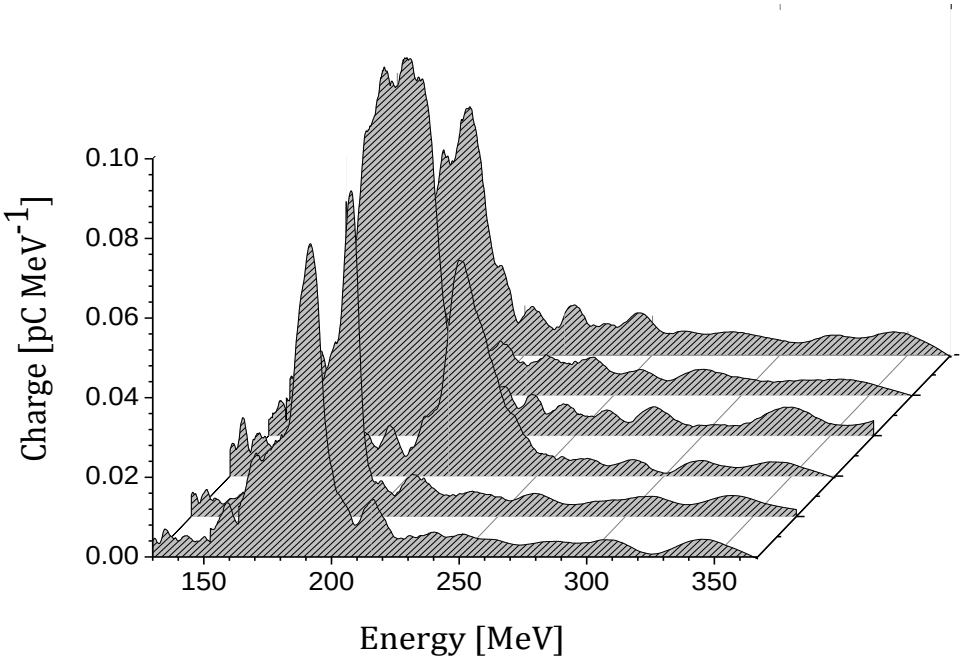

Figure 5.28: Electron energy spectra for six shots giving an average central energy of 182 MeV for tapered capillary TN.

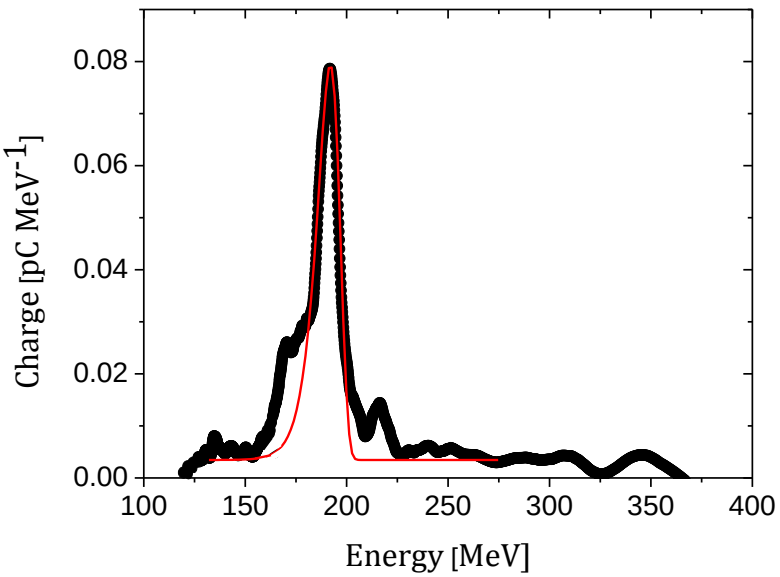

Figure 5.29: Energy spectrum for one shot giving a central energy of 191 MeV with measured energy spread $\sigma_E / E = 2.6\%$ for tapered capillary TN. The red curve is a good extreme inverted fit to the main peak.

Table 5.4 summarises the energy spectrum data for measured electron bunch charge and central energy of the electron bunch with a discernible finite energy spread for three capillary types (TP1, TN and S1).

Name	**Mean (Max.)** Q **[pC]**	**Mean (Max.)** E **[MeV]**	**Mean (Min.)** σ_E/E **[%]**
TP1	2.6 ± 2.3 (6.6)	250 ± 25 (290)	5.2 ± 2.7 (1.6)
S1	0.2 ± 0.1 (0.3)	205 ± 5 (211)	1.8 ± 0.7 (1.0)
TN	1.3 ± 1.1 (5.1)	184 ± 17 (229)	7.1 ± 3.0 (2.6)

Table 5.4. Energy spectrum data giving the mean (maximum) electron bunch charge Q and central energy E and mean (minimum) measured relative measured energy spread σ_E / E of the electron bunch for each capillary type where each uncertainty is the r.m.s. standard deviation.

In order to characterise the correlation between the electron energy and the charge, the central energy against the total electron charge has been investigated for each capillary type: TP1, TN and S1. It has been observed that the main bunch central energy had no clear dependence on the charge for all three capillaries. As an example, Fig. 5.30 shows the behaviour observed for capillary TN. In contrast, a clear decrease of the bunch central energy with increasing charge was seen for electrons produced from previous LWFA experiments using gas jet [23]. Hence, for the data sets here, there is no clear observation of beam loading effects [24] influencing the final electron energy.

The narrowest measured energy spreads are only 1-2% for electron bunches (determined solely for that bunch and ignoring lower energy bunches or pedestals) for all three capillary types, therefore, the resolution of the spectrometer must be considered. Numerical simulations have been carried out using the General Particle Tracer (GPT) code [25], to estimate the resolution of the electron spectrometer for the measured energy range. This has allowed deconvoluted of the spectra to estimate the actual energy spread of monoenergetic electron bunches.

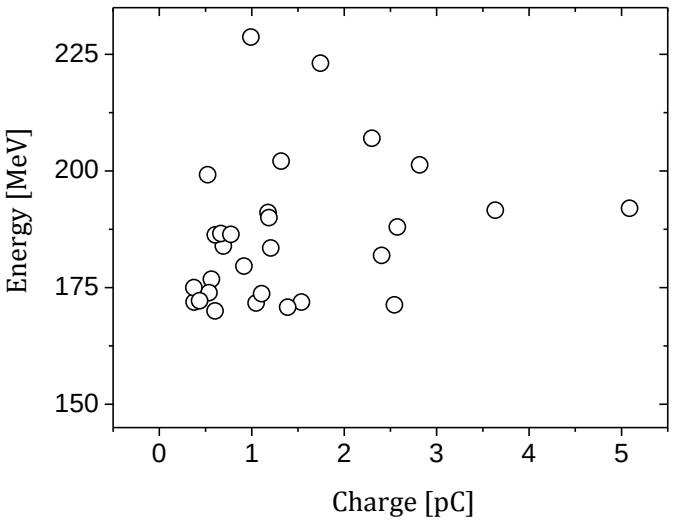

Figure 5.30: The main bunch central energy versus charge for capillary TN.

The resolution of the spectrometer has been calculated [26] by assuming a spatially Gaussian monoenergetic electron distribution in both transverse and longitudinal planes. Figures 5.31 (a) to (f) illustrate the energy resolution for different monoenergetic bunch energies over a range of divergences for the capillary TP1. It can be seen that there is a dependence of the rms energy resolution on the divergence for a constant emittance, i.e., an increase in the initial beam radius produces an increase in the resolution at a given central energy as shown in Fig. 5.31 (a), (c) and (e). On the other hand, there is no dependence of the rms energy resolution on emittance at constant divergence as presented in Fig. 5.31(a) and (b). Similar analysis has been carried out for the S1 and TN capillaries.

The dependence of the measured energy spread on the bunch charge has been investigated using all three capillary types TP1, TN and S1 and the data presented in the Fig. 5.32 (a), (b) and (c) respectively. It is clear that there are increases in the energy spread with increasing charge. This increase can be explained by the combination of two effects:

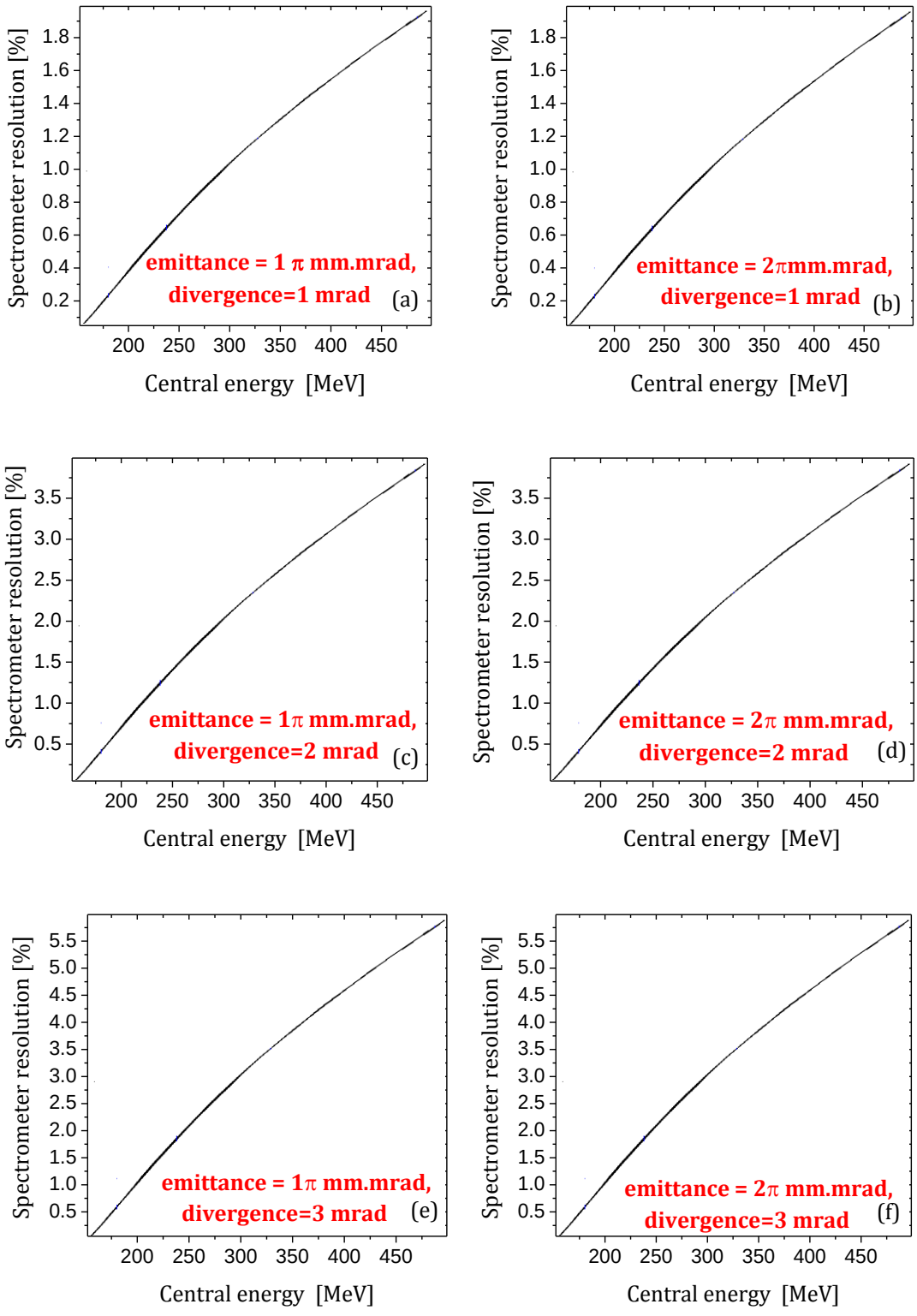

Figure 5.31: GPT simulations of the electron spectrometer instrument response calculated for electron beams of energy between 150 MeV and 500 MeV using TP1, for three different emittance values $(1 \times 10^{-6} - 3 \times 10^{-6})$ mm mrad and three different divergences (1-3) mrad.

First is the beam loading effect [24]. The Coulomb field produced by high-density accelerated electron bunch causes a local modification of the wakefield produced by the laser pulse. For a low charge bunch, optimal loading in the wake minimises the variation of the accelerating electric field along the beam thus producing a low bunch energy spread. Higher charge in the beam causes over-loading producing a fast varying field over the bunch length, leading to growth of the energy spread.

The second possible effect is that the lower charge beams have been trapped and accelerated over a small phase region in the plasma wave, leading to a decrease in the variation of the accelerating electric field across the beam, thus decreasing the final energy spread of the accelerated electrons. For electron beams generated with small energy spread, controlling the charge of trapped electrons is important.

The data for measured energy spreads using TP1 for 10 shots, presented in Fig. 5.32(a), provided values from 1.6% to 9% for the range of charge observed (0.3-6.6 pC). These measured energy spreads have been observed with a central energy in the range 180-290 MeV.

The deconvoluted measured energy spread can be estimated using:

$$\left(\frac{\sigma_E}{E}\right)^2_{meas.} = \left(\frac{\sigma_E}{E}\right)^2_{act.} + (R)^2 \tag{5.8}$$

where $\left(\frac{\sigma_E}{E}\right)_{meas.}$ is the measured spread, $\left(\frac{\sigma_E}{E}\right)_{act.}$ is the actual spread and R is the spectrometer resolution, assuming Gaussian distributions. The deconvoluted energy spreads, using the respective calculated resolution values, as a function of the electron bunch are presented in Fig. 5.33. For each capillary, mean divergence values obtained experimentally (Table 5.3) have been applied. That is, the charge dependence on divergence (Fig 5.17), obtained with the uncalibrated Lanex screen L1, has been neglected.

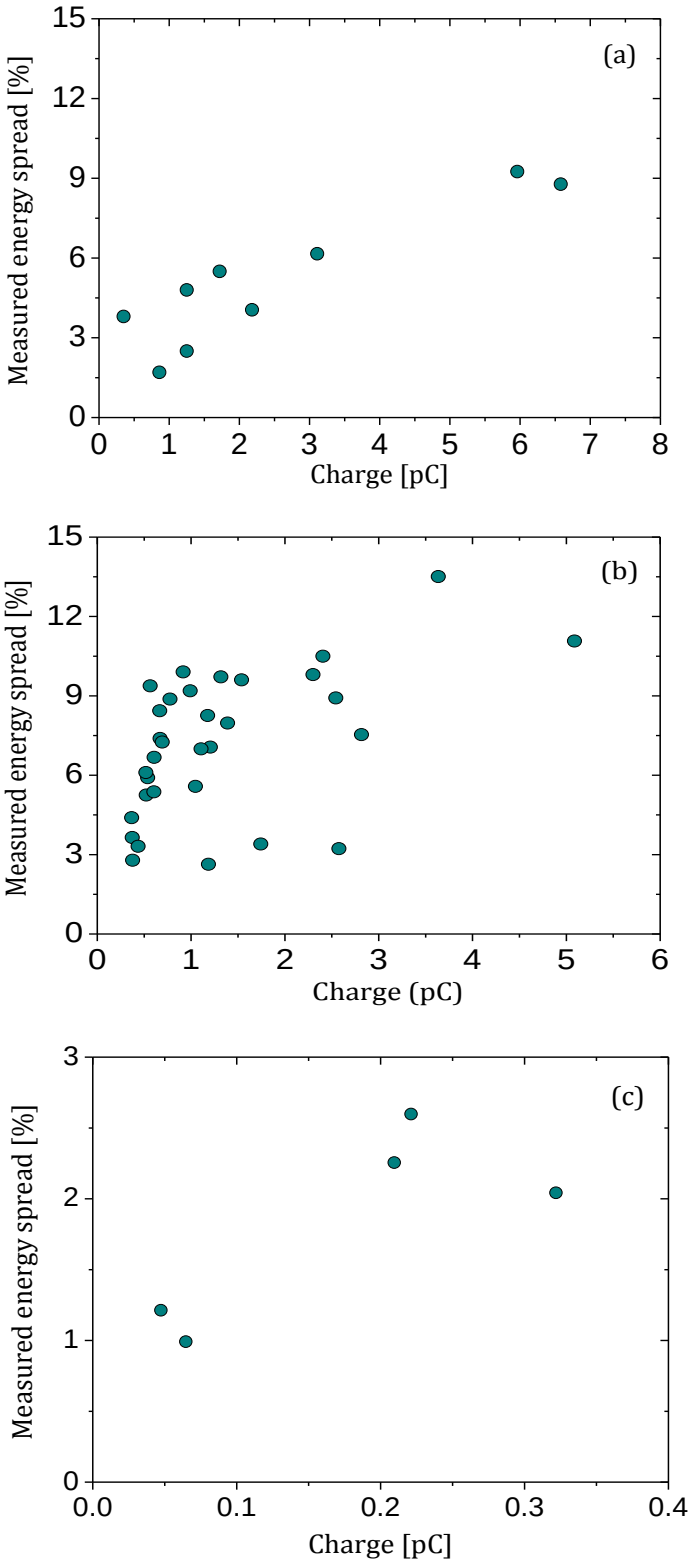

Figure 5.32: Measured energy spread dependence on charge for each capillary type: (a) TP1, (b) TN and (c) S1.

Given that the narrowest measured bunch r.m.s. energy spreads are in the range 1-2% and beam line simulations in Fig 5.31 (e) and (f) indicate that the electron spectrometer resolution is also in the 1-2% range for the typical bunch properties [central energy (180 – 290) MeV and divergence = 3 mrad] observed in the experiment, it is clear, therefore, that the narrowest spread bunches have been strongly convoluted by the detection system response. Hence, the actual energy spread is much less than 1% (see Fig. 5.33), as is the case for the gas jet accelerators driven either by single [27] or colliding [28] laser pulses. From the data presented in Fig. 5.32 (a), (b) and (c) for all three capillary types and from Table 5.4, it is interesting to note that type TN is observed to have a larger mean spread than type TP1 despite lower mean charge.

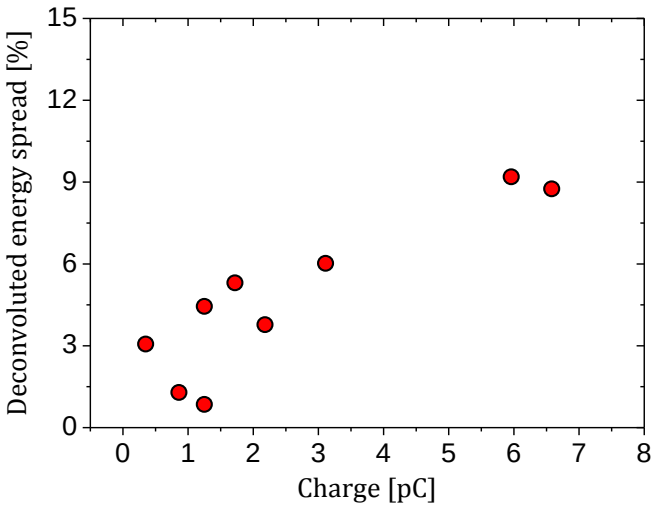

Figure 5.33: Deconvoluted energy spread dependence on charge for the capillary TP1 with the spectrometer response applied for a transverse divergence of 3 mrad.

Energy comparison with gas jet experiments at Strathclyde

Results from other experimental work [18] have reported that the hydrogen-filled capillary discharge waveguide can channel laser pulses with high intensities of the order of 10^{18} W/cm^2, and the performance of the LWFA has been significantly improved. The waveguide enabled electrons to reach around double the energy of electrons accelerated by the same laser in a gas jet.

On the ALPHA-X beam line, electrons are produced with an energy typically up to 150 MeV from a 2 mm gas jet with a density n_e ~1-5 × 10^{19} cm^{-3} [27]. Using the same laser parameters, the experimental data presented here show that electron beams in the tapered hydrogen-filled discharge capillary waveguide have a maximum energy of 320 MeV in a plasma density of ~3-5 × 10^{18}. Therefore, the highest energy of electrons accelerated in the plasma channel can be more than twice that accelerated in gas jets.

A comparison of the electron energy scaling with electron density shown in section 2.2.3 with the present data shows that the electron energy obtained here is consistent with electron energy scaling for other experimental results.

5.3 Straight and tapered capillary durability

Hydrogen-filled capillary discharge waveguides made of alumina (or sapphire) have a long lifetime compared with other waveguides for LWFA. This is due to the fact that the materials are very hard and robust and that hydrogen gas is easily ionised with heat conducted away from the plasma to the capillary walls, meaning that the temperature is peaked on axis and the lifetime of the device is greatly increased. Previous experimental work found that the discharge current widened a capillary of diameter 200 μm by approximately 20 pm per shot [29]. Additionally, the incident high-power laser pulses and variations in laser pointing can increase damage to the entrance region of the capillary.

For experiments here, to study the damage of the capillary, the main capillaries (TP1, S1 and TN) have been optically imaged after use and comparison made with images of their initial condition. Figure 5.34 shows the entrance and exit of the tapered capillary TP1, where the laser is guided from the 282 μm large end to 230 μm small end, before and after use. After 1300 shots, the capillary entrance has been broadened by 128 μm in the horizontal direction and 50 μm in the vertical direction, corresponding to approximately 0.1 μm per shot, and with no significant broadening at the capillary exit. The capillary widening by the discharge current is estimated to be 26 nm only [29] which is greatly below the resolution of the measurement.

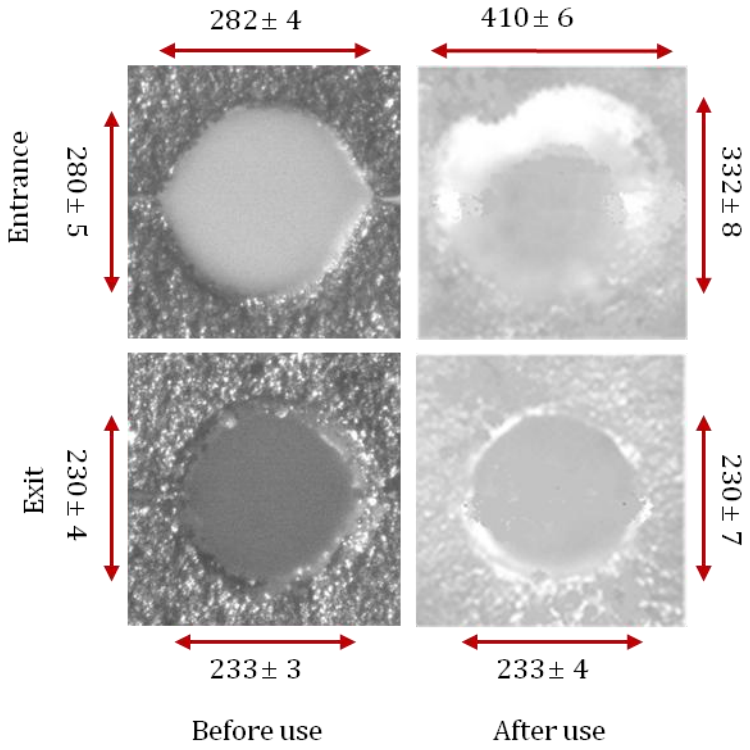

Figure 5.34: Images of the entrance and exit of the tapered capillary TP1. The left images show the entrance and the exit before use and the right images show the entrance and the exit after use. The red arrows indicate the respective diameters (in μm).

Such damage at the entrance is not negligible, however, and has been caused by the laser pulse. It is clear also that most damage at the capillary entrance is along one axis (horizontally). The first of two possible reasons to explain this observation is the laser pointing variation. As presented in section 5.1.2, the laser focal spot suffers from relatively large fluctuations in the horizontal direction (σ_x = 6.7 μm) compared with the vertical direction (σ_y = 1.5 μm). In addition, the transverse spatial profile of the focal spot displays a wing on one side of the spot, with an intensity of $\sim 2.2 \times 10^{17}$ W/cm^2 (about 7 times lower than the intensity at the waist) and a small wing on the other side with an intensity of $\sim 1 \times 10^{17}$ W/cm^2. These intensities are sufficient to ablate the walls of the capillary (the ablation threshold is about 10^{14} Wcm^{-2} as shown in chapter 3).

Additionally, the initial vacuum waist size (20 μm) is less than the matched spot size of the plasma channel (44 μm), which may lead to beam waist oscillations between 20 μm and 97 μm. This scalloping when occurring in the early stages of the capillary, with the magnitude of the pointing fluctuation in the wings as shown in Fig. 5.34, gives a finite probability that any particular laser shot will be pointed into the capillary wall causing damage to the capillary entrance shown in Fig. 5.34. The second possible explanation is that the laser alignment drifts out of optimal alignment in this direction.

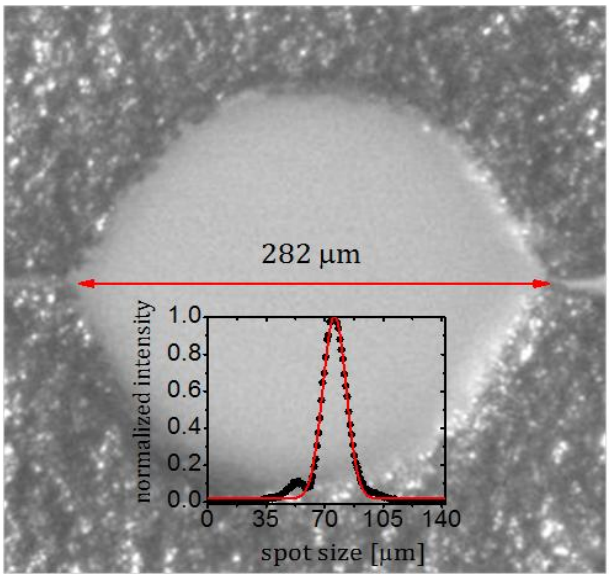

Figure 5.35: The entrance image of tapered capillary TP1 compared with the transverse spatial profile of the laser pulse at the focus (w_0 = 20 μm). The transverse spatial profile of the laser pulse shows a clear wing at one side of the pulse with a weak wing in other side.

As shown in Fig. 5.36, the shape of the damage is conical and does not penetrate deeper than ~0.6 mm along the length of the capillary. This distance of penetration may indicate the scale length of laser self-focusing that would reduce the laser beam size and, coupled with the waveguiding process, thus preventing the intensity at the walls reaching the threshold for the ablation. The bulk of the capillary appeared to be undamaged showing that the capillary has been working well as a waveguide during the experiment.

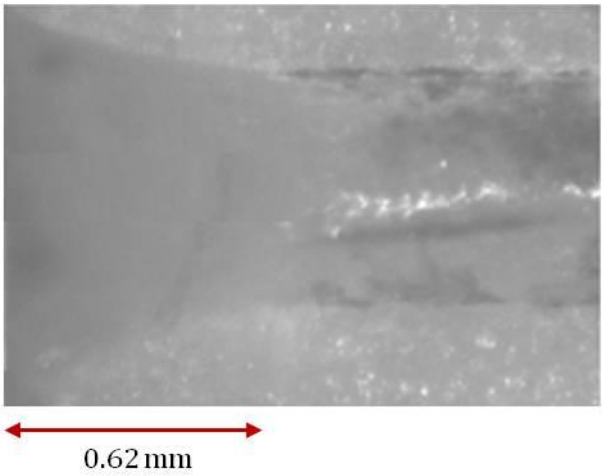

Figure 5.36: Longitudinal image along one plate of the entrance of the tapered capillary TP1. The image shows the cone shape of the damage which has not deeply penetrated. The red arrow indicates the length of the cone.

Similar damage to the entrances of the straight capillary S1 with diameter of 230 μm and the tapered capillary TN with the laser guided from the 206 μm small end to 268 μm large end are shown in Figs 5.37 and 5.38 respectively. Table 5.5 summarises the parameters for the three capillaries studied for damage. TP1 and S1 both show 23% more widening of the entrance in the horizontal direction while, for TN, the value is 35%.

In summary, it can be concluded that the capillary TN, which has a smaller initial entrance diameter than the other capillaries, suffered more extensive damage. This is most likely because of fluctuations in the laser pulse pointing and the energy in the wings of the laser spot.

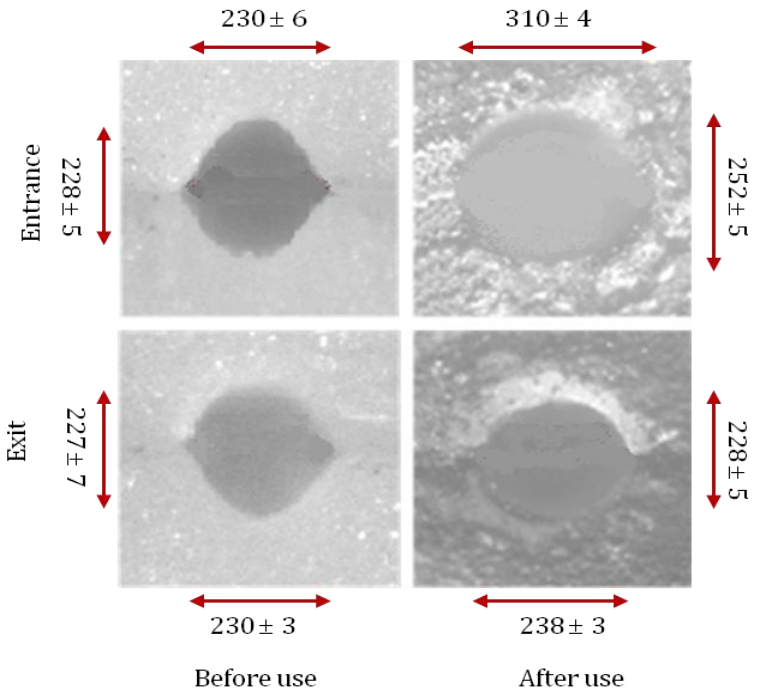

Figure 5.37: Images of the entrance and exit of the straight capillary S1. The left images show the entrance and exit before use and the right images show the entrance and exit after 2200 shots. The red arrows indicate the respective diameters (in μm).

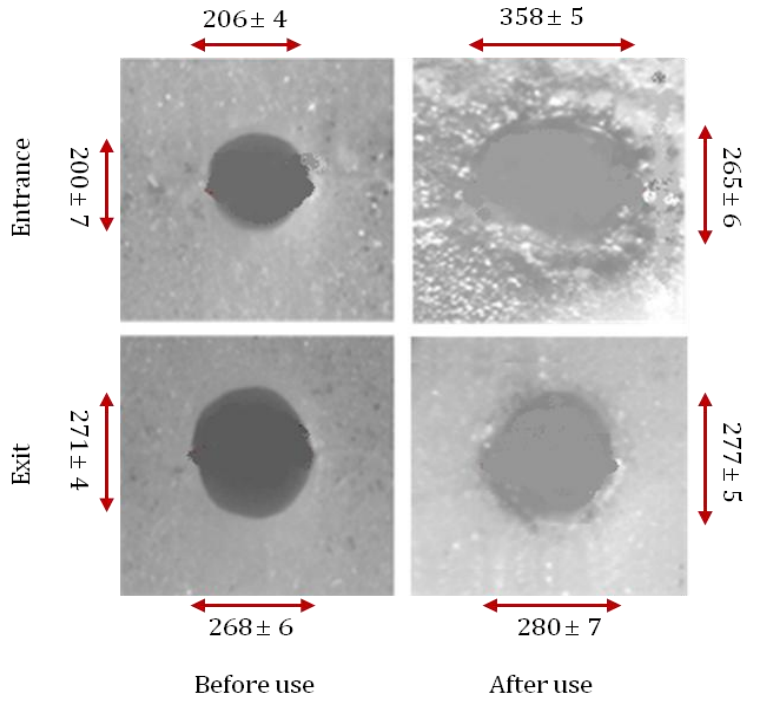

Figure 5.38: Images of the entrance and exit of the tapered capillary TN. The left images show the entrance and the exit before use and the right images show the entrance and the exit after 2000 shots. The red arrows indicate the respective diameters (in μm).

Name	Entrance before use (μm)	Entrance after use (μm)	Exit before use (μm)	Exit after use (μm)	Number of shots
TP1	282 ± 4	H 410 ± 6 V 332 ± 8	233 ± 3	H 233 ± 4 V 230 ± 7	1300
S1	230 ± 6	H 310 ± 4 V 252 ± 5	230 ± 3	H 238 ± 3 V 228 ± 5	2200
TN	206± 4	H 358 ± 8 V 265 ± 6	268 ± 6	H 280 ± 7 V 277 ± 5	2000

Table 5.5: Diameter measurements of the entrance and exit of the main used capillaries (TP1, S1 and TN) before and after use. H and V indicate the horizontal and vertical directions respectively.

5.4 Conclusions

The results from experiments discussed in this chapter represent several important achievements. Firstly, hydrogen-filled tapered capillary discharge waveguides provide good quality guiding of laser pulses with peak input intensities of the order of 10^{18} W/cm^2, which is achieved for the first time in the field. Secondly, the tapered capillary discharge waveguides show some significantly improved LWFA performance.

The mechanism of the trapping and acceleration of electrons occurring in the waveguide used in the experiments can be described as follows:

Hydrogen gas is injected into the capillary through gas slots machined into the alumina plates near the capillary ends. The flow of the hydrogen gas produces a plume at each end of the capillary. Then the high-voltage pulser which is connected across the electrodes situated at either end of the capillary with a peak voltage ~21 kV results in the breakdown of the gas within the waveguide to form plasma as shown in the schematic of Fig. 5.39.

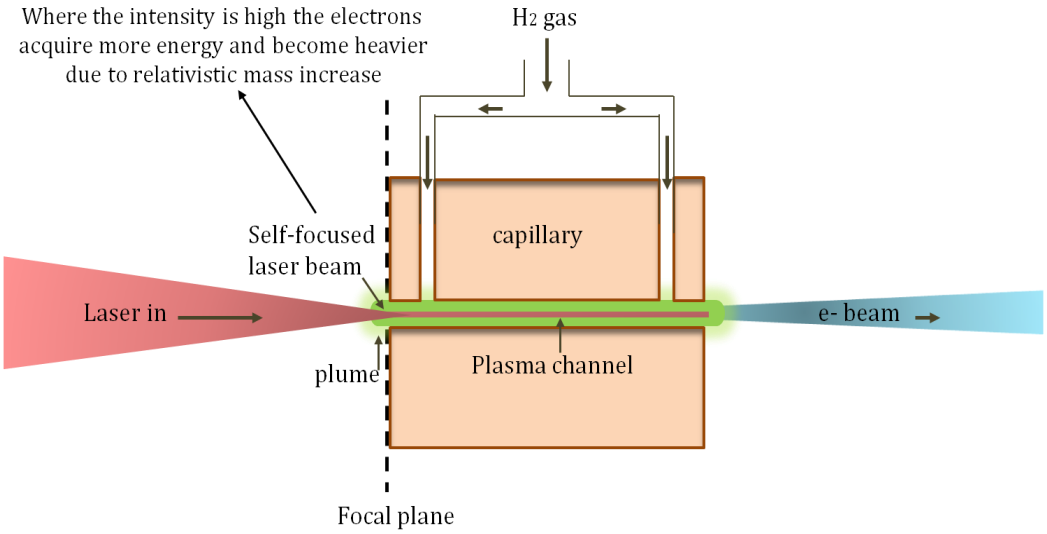

Figure 5.39: Schematic diagram showing the operation of self-focusing and the evolution of the laser spot size from the vacuum to the plasma channel.

As the current flows, the density profile evolves into a stable plasma channel. The laser pulse with energy of 0.4 J (50% of the energy in the central spot) arrives at the plume at ~1.6 mm (z_R) from the entrance of the capillary with intensity ~ 10^{18} W/cm^2 and $a_0 = 0.7$. At this high intensity (> 3 × 10^{16} W/cm^2), hydrogen ionisation occurs [5] producing the plasma with density of ~2-6 × 10^{18} cm^{-3} as shown by other measurements.

The laser pulse with this sufficient intensity will experience a refractive index that is peaked on-axis, leading to self-focusing (see chapter 2) and propagation over distances longer than the Rayleigh range. This positive focusing effect becomes stronger as the laser beam decreases in diameter and becomes more intense.

Figure 5.40 shows the results of simulations [30] for relativistic self-focusing of laser spot for different plasma densities: 1 × 10^{18} cm^{-3}, 3 × 10^{18} cm^{-3} and 5 × 10^{18} cm^{-3}. From the figure it can be seen that the laser pulse becomes more intense and the focusing effect becomes stronger with increasing the plasma density. As an example for the case here, with plasma density at the plume of 3 × 10^{18} cm^{-3}, a_0 can be increased from ~ 0.7 to ~ 1.4 at the capillary plane.

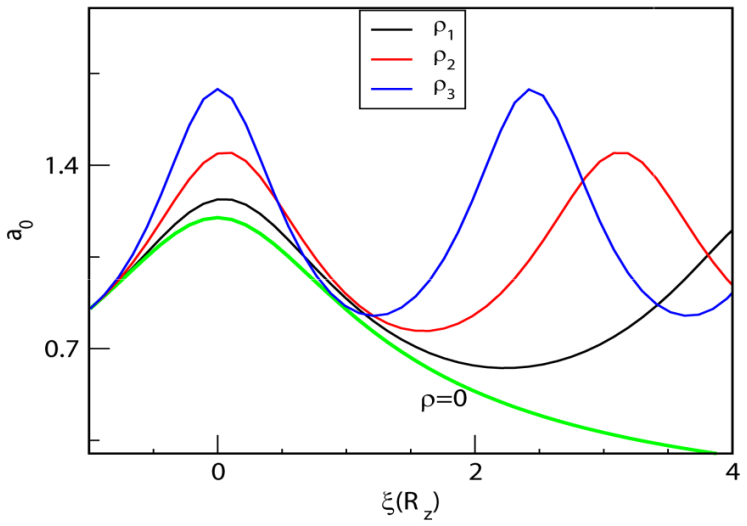

Figure 5.40: The evolution of a_0 as function of longitudinal distance normalised to the Rayleigh length for density values of $\rho_1 = 1 \times 10^{18}\,cm^{-3}$ (black curve), $\rho_2 = 3 \times 10^{18}\,cm^{-3}$ (red curve) and $\rho_3 = 5 \times 10^{18}\,cm^{-3}$ (blue curve). The $\rho = 0$ green curve shows the vacuum evolution of a_0 .

For the plasma channel inside the capillary, a_0 can increase yet further beyond that achieved when the pulse is first self-focused in the plume region. From simulations performed by other work [31], this allows a_0 to evolve sufficiently to reach the threshold for injection of electrons into the wake, which is estimated to occur at a_0 ~3–4 [32]. With respect to the laser pulse, there are competing self-focusing and diffractive (from mismatching to the channel) effects. The poor electron generation observed in the wider entrance diameter S2 and TP2 capillaries show that good initial coupling to the waveguide is important.

The experiments show that the performance of the capillary discharge channel guided accelerator strongly depends on capillary diameter, discharge delay and peak power of the laser pulses. Acceleration is reported for the first time in a tapered waveguide, with the laser guided from the 280 μm large end to 230 μm small end, which results in an electron energy around 2.2 times the energy of electrons accelerated by the same laser in a gas jet [27] and around 1.5 times the energy of electrons accelerated by the same laser in a straight capillary.

Through the data analysis for electron beam generation, regarding the electron energy, beam pointing and divergence, it is found that control of the discharge delay and input energy are critical for stable operation. A change of less than 20 ns in the discharge delay and of less than about 15% in the input energy significantly affects capillary performance. From comparison of characteristics of the electron bunches produced by straight and capillaries it was observed that:

- The 230 μm diameter straight capillary operation provided accelerated electron bunches with maximum energy around 211 MeV and an rms relative energy spread as low as 1.0% with lowest values for a charge of 0.3 pC. The average of beam divergence was also low at 1.6-1.8 mrad rms in both axes.
- Quasi-monoenergetic electron beams using tapered capillary with the laser guided from the 280 μm large end to 230 μm small end is observed. It is shown that through a plasma density gradient from 2.5×10^{18} cm^{-3} to 3.8×10^{18} cm^{-3} electron beams with energies of up to 320 MeV with maximum value for the total accelerated charge of ~6.6 pC are measured. The minimum divergence of electron beam measured is ~0.85 mrad.
- Using a negatively tapered capillary with the laser guided from the 206 μm small end to the 270 μm large end, the highest beam quality is observed, with low energy spread and low beam divergence for lower charge. It is shown from this capillary that very good shot-to-shot pointing stability with r.m.s. Pointing angles of 0.3-0.4 mrad in both horizontal and vertical axes.

Although these results are encouraging, there are important features in the data indicating that the contribution of the waveguide as a tool for extending the laser plasma interaction length is not fully understood. These features include a sensitive dependence of electron acceleration on the capillary entrance diameter. It is not entirely clear how much influence the density tapering (which is relatively gentle in the tested capillaries) is having on the acceleration.

Importantly, for the LWFA process, the longitudinal position of the injection point and subsequent acceleration is not known. Given that the dephasing

length (for a straight capillary), from Eq. 2.35, is typically only a few mm, it is then therefore not known how much of the energy enhancement in the TP1 capillary is due to the taper. Ignoring any tapering, predicted electron energies, from Eq. 2.47, for the 3 main capillaries are given in Table 5.6 for the measured or estimated plasma densities at the start, middle and end of the waveguides (intensity = 2×10^{18} W/cm^2 for $a_0 = 1$ and specific laser self-focusing effects are also neglected).

	Start (z = 0 cm)		**Middle (z = 2 cm)**		**End (z = 4 cm)**	
Name	n_e	**E (MeV)**	n_e	**E (MeV)**	n_e	**E (MeV)**
TP1	2.5	321	3.1	259	3.8	211
S1	3.5	229	3.5	229	3.5	229
TN	4.7	171	3.6	223	2.8	286

Table 5.6: Theoretical energy gains in each capillary, ignoring any tapering, for three longitudinal z positions. The plasma density n_e is in units of 10^{18} cm^{-3}.

The expected S1 electron energy is clearly independent of position because the density is uniform and the energy value of 229 MeV is quite close to the measured mean value of 205 MeV. That for TP1 decreases as the density increases and is closest to the measured mean value of 250 MeV around the middle. That for TN increases as the density decreases and is reasonably close to the measured mean value of 184 MeV at the start location.

If acceleration is occurring around the middle of the capillary, allowing for self-focusing to reach the required level for injection to happen, then there may be some evidence that positive tapering is enhancing the electron energy. The 22% energy increase from S1 to TP1 in the experiment is larger than the 13% middle increase from Table 5.6.

On the other hand, if electron injection and acceleration occur early in the propagation of the laser pulse in the plasma channel, then the larger energy found for TP1 can be explained simply by the lower density at the start, from Table 5.6. In any case, acceleration ceases close to the dephasing length, evidenced by the narrow energy spreads, probably because of pump depletion

effects destroying the bubble structure. The analysis above is very simplified but the difficulty in running particle-in-cell simulations over the very long propagation distances makes it hard to gain useful information from such computing facilities [30].

Reasonable agreements, however, with experiments for the energy ratios between capillaries can be found using the simple energy gain estimate, as shown in Table 5.7. This indicates an injection point around 1 cm into the capillary which is consistent with the ablation damage data (Fig. 5.36) that extended ~0.6 mm into the capillary entrance region. Large uncertainties in the experiment and the theoretical energy gain estimates make it impossible to determine if the density tapers are influencing the final electron energies.

	Experiment			**Theory (z = 1 cm)**		
Name	n_e	**E (MeV)**	**Ratio**	n_e	**E (MeV)**	**Ratio**
TP1	2.5	250	1.22	2.8	286	1.25
S1	3.5	205	-	3.5	229	-
TN	4.7	184	0.90	4.2	191	0.83

Table 5.7: Comparison between the experimental and theoretical (z = 1 cm) at energy gains in each capillary, ignoring any tapering. The ratios indicate the TP1 and TN energy differences with respect to the corresponding S1 energy. The plasma density n_e is in units of 10^{18} cm^{-3} and laser a_0 = 1.

Electron bunches produced from the LWFA show excellent stability when using the negatively tapered capillary. There is a marked improvement of the shot-to-shot stability of electron beam parameters (divergence, pointing direction and energy spread), which could be very important to the success of laser-driven electron sources for applications such as the free-electron laser [1].

References

1. D.A. Jaroszynski, R. Bingham, E. Brunetti, B. Ersfeld, J. Gallacher, B. van der Geer, R. Issac, S.P. Jamison, D. Jones, M. de Loos, A. Lyachev, V. Pavlov, A. Reitsma, Y. Saveliev, G. Vieux, and S.M. Wiggins, *Radiation sources*

based on laser–plasma interactions. Philosophical Transactions of the Royal Society A: Mathematical, Physical and Engineering Sciences, 2006. **364**(1840): p. 689-710.

2. R. Hofstadter, *Alkali Halide Scintillation Counters.* Physical Review, 1948. **74**(1): p. 100-101.
3. C.P. Browne and W.W. Buechner, *Broad-Range Magnetic Spectrograph.* Review of Scientific Instruments, 1956. **27**(11): p. 899-907.
4. G. Manahan, [private communication].
5. G. Vieux, *Broad-band linear Raman chirped pulse amplification in plasma.* (PhD Thesis), 2004. University of Strathclyde: Glasgow.
6. S. Karsch, J. Osterhoff, A. Popp, T.P. Rowlands-Rees, Z. Major, M. Fuchs, B. Marx, R. Hörlein, K. Schmid, L. Veisz, S. Becker, U. Schramm, B. Hidding, G. Pretzler, D. Habs, F. Grüner, F. Krausz, and S.M. Hooker, *GeV-scale electron acceleration in a gas-filled capillary discharge waveguide.* New Journal of Physics, 2007. **9**(11): p. 415-425.
7. W.L. Kruer, *Physics of Laser Plasma Interactions*. 2003, Westview Press: Redwood, California.
8. E. Miura, K. Koyama, Susumu Kato, and N. Saito, *Demonstration of quasi-monoenergetic electron-beam generation in laser-driven plasma acceleration.* Applied Physics Letters, 2005. **86**(25): p. 251501.
9. D.G. Jang, M.S. Kim, I.H. Nam, H.S. Uhm, and H. Suk, *Density evolution measurement of hydrogen plasma in capillary discharge by spectroscopy and interferometry methods.* Applied Physics Letters, 2011. **99**(14): p. 141502.
10. P. Sprangle, C.M. Tang, and E. Esarey, *Relativistic Self-Focusing of Short-Pulse Radiation Beams in Plasmas.* IEEE Transactions on Plasma Science, 1987. **15**(2): p. 145-153.
11. D.J. Spence, A. Butler, and S.M. Hooker, *Gas-filled capillary discharge waveguides.* Journal of the Optical Society of America B-Optical Physics, 2003. **20**(1): p. 138-151.

12. A.J. Gonsalves, T.P. Rowlands-Rees, B.H.P. Broks, J.J.A.M. van der Mullen, and S.M. Hooker, *Transverse Interferometry of a Hydrogen-Filled Capillary Discharge Waveguide.* Physical Review Letters, 2007. **98**(2): p. 025002.
13. S. Cipiccia, M.R. Islam, B. Ersfeld, R.P. Shanks, E. Brunetti, G. Vieux, X. Yang, R.C. Issac, S.M. Wiggins, G.H. Welsh, M.-P. Anania, D. Maneuski, R. Montgomery, G. Smith, M. Hoek, D.J. Hamilton, N.R.C. Lemos, D. Symes, P.P. Rajeev, V.O. Shea, J.M. Dias, and D.A. Jaroszynski, *Gamma-rays from harmonically resonant betatron oscillations in a plasma wake.* Nature Physics, 2011. **7**(11): p. 867-871.
14. J. Xu, B. Shen, X. Zhang, M. Wen, L. Ji, W. Wang, Y. Yu, and Y. Li, *Overloading effect of energetic electrons in the bubble regime of laser wakefield acceleration.* Physics of Plasmas, 2010. **17**(10): p. 103108.
15. E. Brunetti, R.P. Shanks, G.G. Manahan, M.R. Islam, B. Ersfeld, M.P. Anania, S. Cipiccia, R.C. Issac, G. Raj, G. Vieux, G.H. Welsh, S.M. Wiggins, and D.A. Jaroszynski, *Low Emittance, High Brilliance Relativistic Electron Beams from a Laser-Plasma Accelerator.* Physical Review Letters, 2010. **105**(21): p. 215007.
16. A.J. Gonsalves, K. Nakamura, C. Toth, C.G.R. Geddes, C.B. Schroeder, E. Esarey, E. Cormier Michel, W.P. Leemans, D. Bruhwiler, J.R. Cary, and S.M. Hooker, *GeV electron beams from a centimeter-scale laser-driven plasma accelerator.* Particle Accelerator Conference, PAC. IEEE, 2007: p. 1911-1915.
17. W.P. Leemans, B. Nagler, A.J. Gonsalves, C. Toth, K. Nakamura, C.G.R. Geddes, E. Esarey, C.B. Schroeder, and S.M. Hooker, *GeV electron beams from a centimetre-scale accelerator.* Nature, 2006. **2**(10): p. 696-699.
18. T.P. Rowlands-Rees, C. Kamperidis, S. Kneip, A.J. Gonsalves, S.P.D. Mangles, J.G. Gallacher, E. Brunetti, T. Ibbotson, C.D. Murphy, P.S. Foster, M.J.V. Streeter, F. Budde, P.A. Norreys, D.A. Jaroszynski, K. Krushelnick, Z. Najmudin, and S.M. Hooker, *Laser-Driven Acceleration of Electrons in a Partially Ionized Plasma Channel.* Physical Review Letters, 2008. **100**(10): p. 105005.

19. T. Katsouleas, *Physical mechanisms in the plasma wake-field accelerator.* Physical Review A, 1986. **33**(3): p. 2056-2064.
20. P. Sprangle, J.R. Penano, B. Hafizi, R.F. Hubbard, A. Ting, D.F. Gordon, A. Zigler, and J. T. M. Antonsen, *GeV acceleration in tapered plasma channels.* Physics of Plasmas, 2002. **9**(5): p. 2364-2370.
21. W. Rittershofer, C.B. Schroeder, E. Esarey, F.J. Gruner, and W.P. Leemans, *Tapered plasma channels to phase-lock accelerating and focusing forces in laser-plasma accelerators.* Physics of Plasmas, 2010. **17**(6): p. 063104.
22. S.M. Wiggins, M.P. Reijnders, S. Abuazoum, K. Hart, G.H. Welsh, R.C. Issac, D.R. Jones, and D.A. Jaroszynski, *Note: Femtosecond laser micromachining of straight and linearly tapered capillary discharge waveguides.* Review of Scientific Instruments, 2011. **82**(9): p. 096104.
23. C. Rechatin, J. Faure, X. Davoine, O. Lundh, J. Lim, A. Ben-Ismaïl, F. Burgy, A. Tafzi, A. Lifschitz, E. Lefebvre, and V. Malka, *Characterization of the beam loading effects in a laser plasma accelerator.* New Journal of Physics, 2010. **12**(4): p. 045023.
24. S. Wilks, T. Katsouleas, J.M. Dawson, P. Chen, and J.J. Su, *Beam Loading in Plasma Waves.* IEEE Transactions on Plasma Science, 1987. **15**(2): p. 210-217.
25. S.B. van der Geer, O.J. Luiten, M.J. de Loos, G. Pöplau, and U. van Rienen, *3D Space-Charge Model for GPT Simulations of High Brightness Electron Bunches*, in *Institute of Physics Conference Series No. 175*. 2005. p. 101.
26. D. Grant, [private communication].
27. S.M. Wiggins, R.C. Issac, G.H. Welsh, E. Brunetti, R.P. Shanks, M.P. Anania, S. Cipiccia, G.G. Manahan, C. Aniculaesei, B. Ersfeld, M.R. Islam, R.T.L. Burgess, G. Vieux, W.A. Gillespie, A.M. MacLeod, S.B. van der Geer, M.J. de Loos, and D.A. Jaroszynski, *High quality electron beams from a laser wakefield accelerator.* Plasma Physics and Controlled Fusion, 2010. **52**(12): p. 124032.
28. C. Rechatin, J. Faure, A. Ben-Ismail, J. Lim, R. Fitour, A. Specka, H. Videau, A. Tafzi, F. Burgy, and V. Malka, *Controlling the Phase-Space Volume of*

Injected Electrons in a Laser-Plasma Accelerator. Physical Review Letters, 2009. **102**(16): p. 164801.

29. A.J. Gonsalves, *Investigation of a Hydrogen-filled Capillary Discharge Waveguide for Laser- driven Plasma Accelerators.* (PhD Thesis), 2006. University of Oxford: Oxford.
30. M.R. Islam, [private communication].
31. T.P.A. Ibbotson, N. Bourgeois, T.P. Rowlands-Rees, L.S. Caballero, S.I. Bajlekov, P.A. Walker, S. Kneip, S.P.D. Mangles, S.R. Nagel, C.A.J. Palmer, N. Delerue, G. Doucas, D. Urner, O. Chekhlov, R.J. Clarke, E. Divall, K. Ertel, P. Foster, S.J. Hawkes, C.J. Hooker, B. Parry, P.P. Rajeev, M.J.V. Streeter, and S.M. Hooker, *Investigation of the role of plasma channels as waveguides for laser-wakefield accelerators.* New Journal of Physics, 2010. **12**(4): p. 045008.
32. S.P.D. Mangles, A.G.R. Thomas, C. Bellei, A.E. Dangor, C. Kamperidis, S. Kneip, S.R. Nagel, L. Willingale, and Z. Najmudin, *Self-Guided Wakefield Experiments Driven by Petawatt-Class Ultrashort Laser Pulses.* IEEE Transactions on Plasma Science, 2008. **36**(4): p. 1715-1721.

CHAPTER 6

Proton and heavy ion acceleration from thin hydride targets

6.1 Introduction

As described in chapter 2, the acceleration mechanism to generate the highest energy ion beams from laser interactions with thin foils is the TNSA mechanism. Although significant progress has been made towards enhancing the ion energies obtained via the TNSA mechanism, further development is needed to increase the ion energies to the level required for some of the applications envisaged. Many different methods have been proposed to increase the number and energy of protons [1, 2]. One of the more successful techniques used for producing energetic protons is a micro-structured target that drives electrons from the bulk structure to generate proton beams from the micro-structure on the rear surface [3]. Reports of recent experiments have shown that proton beams with fluxes of approximately 10^9 protons from a single pulse for a broad spectrum [4] and 10^8 protons from shaped targets with a peak energy below 10 MeV [3] can be produced. The highest proton energy achieved to date is ~70 MeV [5], while proton oncology requires fluxes of about 10^{11} protons per second and energies of around 200 MeV to be effective [6].

In the interests of achieving the required number of protons, it has been suggested that targets could be implanted with hydrogen. There is no existing data in the literature on laser-driven ion acceleration experiments using

hydride targets and it is this subject that forms the basis of the work presented here.

In this chapter, it is determined whether implantation of hydrogen can in fact result in an increase in the proton flux and, if so, the extent of the effect. In the first section, the experimental setup featuring a description of the laser system (JETI) and targets used and diagnostics required to detect the ion beam are presented. An overview of experimental results follows in section 6.3 including, in particular, the effect of the ablation on proton production. Finally, the conclusions are presented in section 6.4.

6.2 Experimental setup and diagnostics

A different accelerator setup for the acceleration of ions than that applied for laser wakefield acceleration of electrons has been employed with a shift of target from underdense plasma to overdense plasma. The laser has been directed onto a thin solid target which enables TNSA to produce energetic ion beams (section 2.3.2). The experiment is a two-beam setup with a second laser of lower intensity used to simultaneously irradiation the back side of the target.

6.2.1 The Jena Titanium:sapphire (JETI) Laser

The experiments presented here have been performed at the multi-TW JETI laser (10^9 contrast) system at the Friedrich Schiller University, Jena, Germany [2, 3]. The JETI laser is a titanium-doped sapphire (Ti:Sa) laser with a maximum pulse energy of ≈ 1 J, a pulse duration of 80 fs, a focal spot diameter of ≈ 6 μm and a pulse repetition of 10 Hz at a wavelength of 795 nm.

The intensity I of a laser pulse is given by the pulse energy E per beam cross section A and pulse duration τ

$$I = \frac{E}{A\tau}, \tag{6.1}$$

where the smallest value for A (~28 μm^2) is in principle determined by the laser wavelength and the aperture of the focal elements. The focal mirror used at Jena

is a gold-coated off-axis f/2 parabolic mirror with a focal length of 12 cm. Increasing the intensity on the target is carried out by shortening the pulse length or increasing the pulse energy within the limits of the components of the system. For the given laser parameters, the final maximum intensity on target produced is $\approx 4.4 \times 10^{19}$ W/cm^2 giving a normalised vector potential $a_0 = 4.5$.

6.2.2 Targets and techniques

The schematic experimental setup is displayed in Fig. 6.1. The laser is incident on the target at an angle of about 23°. Three different metal foils have been chosen for the experiments, each consisting of standard isotopic abundances:

- Gold: 8 μm with hydrogen implantation and 8 μm without hydrogen implantation.
- Copper: 7 μm with hydrogen implantation and 10 μm without hydrogen implantation.
- Titanium: 10 μm with hydrogen implantation and 10 μm without hydrogen implantation.

The foils have been prepared using the following method: each foil is placed in a vacuum (2×10^{-6} atm) that is then filled with hydrogen (2 atm) and left under these condition for three weeks. This was considered to be sufficient time for hydrogen migration into the bulk material in each foil to saturate.

In addition, one has to take care of parasitic proton contributions from surrounding contamination layers such as oil or water vapour, which can be removed by controlled laser ablation of the target back side (see Fig. 6.1). By removing the proton source the screening effect caused by the protons can be suppressed and enhance maximum energy of heavier ions [7, 8]. In this technique a low intensity laser, pulsed or continuous, is focused onto the target back surface. The vacuum must be sufficiently high such that the rate of ablation is above the rate of contaminant recombination on the surface. The laser fluence on target of the cleaning pulse has to be high enough to ablate contaminants from the surface while not ionising the surface or melting the target. The

observed fluence threshold corresponds to typical values for the ablation of contaminant layers from surfaces of ~ (1.2 ± 0.3) J/cm² [2].

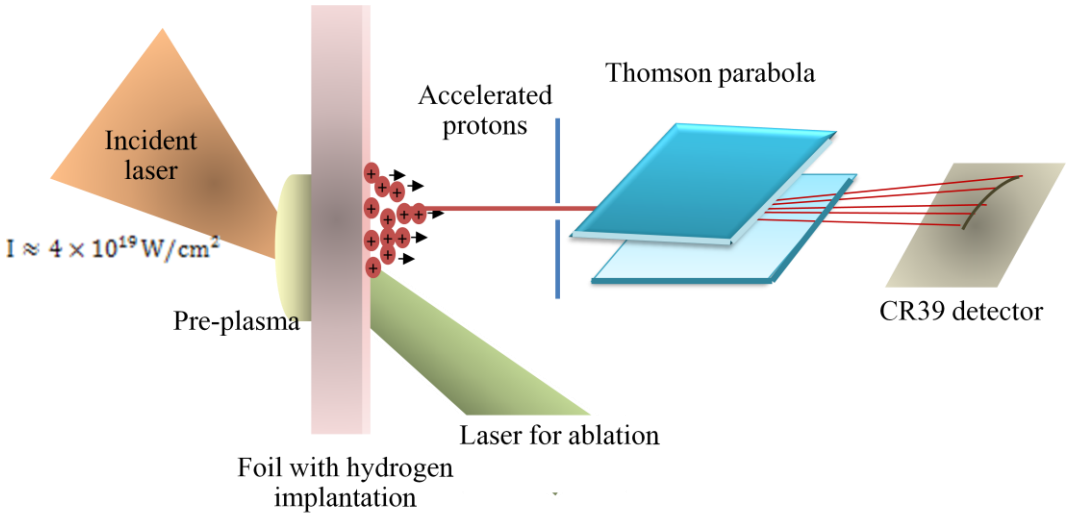

Figure 6.1: Experimental arrangement for laser proton and ion acceleration from hydride targets. A TW-laser pulse is focused to an intensity of $I \approx 4.4 \times 10^{19} W/cm^2$ onto a thin metal foil implanted with hydrogen. A second laser, which is incident on the target rear surface, is used to remove hydrocarbon contaminations. The protons and ions accelerated from the target are dispersed with respect to energy and charge-mass ratio in a Thomson parabola and then detected by nuclear track detector plastics (CR39). The aperture in front of the Thomson parabola serves as a pinhole for the Thomson spectrometer.

In this experiment, a frequency-doubled Nd:YAG ablation laser (532 nm, 5 ns pulse duration) is incident on the target rear side at an angle of 23° and co-centred with the JETI incidence laser position. The laser is weakly focused on the target to cover the whole proton source area and was attenuated with a variable set of density filters to apply a well-defined ablation fluence. Both with and without hydrogen present, the results were measured for each foil without ablation and for 10 s ablation time. Comparing the results of ions generated from both ablated and unablated targets, it is possible to determine whether the implanted protons are concentrated in the bulk structure or on the surface of the target. To have sufficient yield, a total of 5 shots of ~1 J have been fired at each of the targets.

Many different diagnostic techniques are used to study laser-accelerated protons and heavy ions [9-11]. The only technique used in the experiment described here that is able to distinguish between ion species having different charge-to-mass ratios and record their energy spectra separately is a:

- Thomson parabola spectrometer based on parallel electric and magnetic fields to distinguish the ions by their charge-to-mass ratio and energy and
- CR39 detector (nuclear track detector) which is attached to a base behind the Thomson spectrometer.

The following sections describe these two detectors.

6.2.3 Thomson parabola spectrometer

A Thomson parabola spectrometer is the ideal spectrometer for common experimental conditions in laser-solid target interaction experiments [12]. It determines the energy distributions of the particles in a single shot and consists of a superposition of electric and magnetic fields. The field lines are parallel to each other but perpendicular to the initial direction of motion of the particles. The electric field is produced by a potential difference between two electrodes and the magnetic field is produced by two permanent magnets. A schematic of a Thomson parabola ion spectrometer is presented in Fig. 6.2.

It is assumed that an ion with charge, q, and mass, m, propagating in the z direction with velocity, v, enters a homogeneous electric (E) and magnetic field (B) distribution. After the ion has moved through the field, it is deflected perpendicular to the magnetic field and parallel to electric field depending on particle parameters. The deflection is given by

$$\mathrm{D}x \approx \frac{qEld}{mv^2} \ , \tag{6.2}$$

and

$$Dy \approx \frac{qBld}{mv} \ , \tag{6.3}$$

where l, d are the length of the field and distance from the middle of the fields to the plane of the detector. Combining these equations a parabolic equation is obtained

$$Dx = \frac{mE}{qldB^2}(Dy)^2 . \tag{6.4}$$

Clearly this equation shows that the particles with the same charge-to-mass ratio and different energies are deflected on the same parabola but the particles with different charge-to-mass ratio are deflected on separate parabolas at the detector plane as shown later by the example in Fig. 6.5.

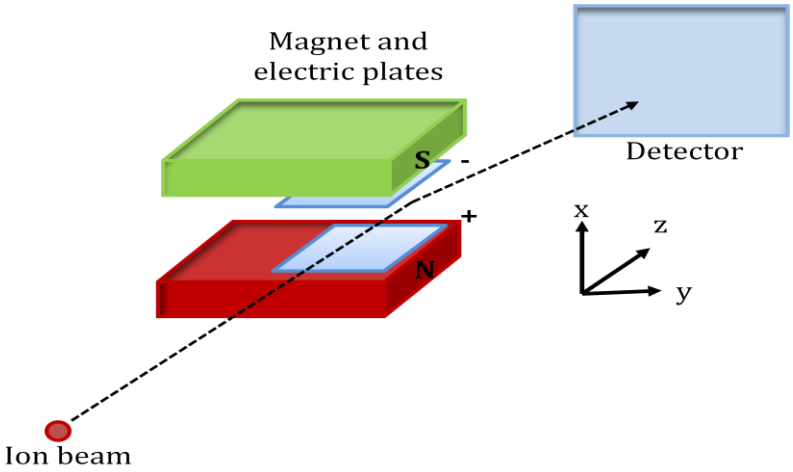

Figure 6.2: Schematic of a Thomson parabola spectrometer. Particles pass through a region with electric and magnetic fields that are parallel to each other. The particles are deflected with respect to their charge-to-mass ratio.

In these experiments, the entrance window of the Thomson spectrometer is 1 mm in diameter while the distance from the entrance window to the exit is 10 cm and the CR39 track detector is placed a further 4 cm behind. The plates of the Thomson spectrometer are separated by a 25 mm, the voltage across the copper plates is set to 7 kV and the magnets produce an average magnetic field strength of 525 mT.

6.2.4 Nuclear track detector CR39

"California Resin No. 39" (CR39) is widely used as a particle detector for ultra-high intensity laser plasma experiments to obtain beam spatial and spectral information [13-15]. The CR39 plastic track detector is formed by a $C_{12}H_{18}O_7$ polymer that has a density of 1.3 g/cm^3, which is exposed to nuclear radiation (charged particles, neutrons and gamma-rays). In the experiments described here, CR39 of typically (85 × 50 × 1) mm^3 size, which is sensitive to all heavy ions currently emitted from laser-thin foil interactions and that can detect protons up to 18 MeV [16], has been used. The main advantage of CR39 as a detector in these application areas is its insensitivity to electromagnetic radiation and lightly ionising particles such as electrons.

6.2.4.1 Track formation mechanisms and track etching

A charged particle passing through CR39 interacts with electrons and nuclei, and also with the medium as a whole (Cerenkov radiation, bremsstrahlung) through electromagnetic interaction and internuclear scattering. When the particle is highly relativistic, ionisation is the main electromagnetic contribution to energy loss. For ions with energies greater than 1 MeV, nuclear losses are small compared with electronic energy losses. On the other hand, heavy ions predominantly lose energy through Coulomb interactions with orbital electrons of the target atoms. These interactions are described in the Bethe-Bloch formula [17]

$$\left(\frac{dE}{dx}\right) = \frac{C_1 Z^2}{\beta^2}\left[ln\left(\frac{W_{max}^2}{I^2}\right) - 2\beta^2 - \delta - U\right], \tag{6.5}$$

where, $C_1 = 2\pi n_e e^4/mc^2$, n_e is electron density, m is electron mass, W_{max} is maximum of the energy transfer, Z is the charge, $\beta = v/c$, v is ion velocity, I is mean ionisation potential, δ is a correction for the polarisation effect of the media for relativistic velocities and U is a correction for small velocities.

The track formation depends on the total amount of energy deposited per unit path length by the incident particle. Total energy losses (dE/dx) in interactions with electrons are a function of particle energy and have a characteristic shape as shown in Fig. 6.3(a). This shape is directly related to the empirically observed critical value of $(dE/dx)_c$. When (dE/dx) exceeds this critical value, tracks are formed. Also, the total energy loss of the particle depends on its range, R, in CR39 material which is defined by

$$R = \int_{E_{max}}^{0} dx = \int_{E_{max}}^{0} \frac{1}{dE/dx} dE \,. \tag{6.6}$$

From this equation and Fig. 6.3(b), it can be seen that the highest energy loss occurs at low energies and at the end of the particle range. This means that particles stopping in the matter will leave the most visible tracks and, from that, information on particle species and energy can be obtained from the observed tracks.

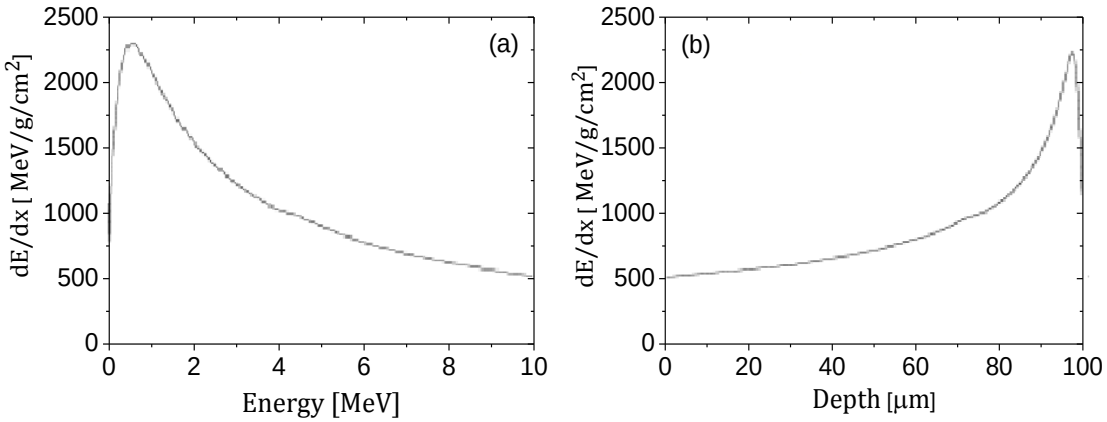

Figure 6.3: Energy loss dE/dx for heavy ion particles in CR39 (a) as a function of energy and (b) as a function of particle range [18]. The highest energy loss occurs at the end of the range at low energies, shortly before the particle is stopped.

The most common method to render the individual tracks visible is chemical etching in a suitable etchant. The etchant removes material in a very narrow region around the track at rate V_t, while it also removes material from undamaged regions at bulk etch rate V_b. As a consequence of chemical etching,

a conical etch pit appears in the CR39, as shown in Fig. 6.4(a). The track sensitivity, S, is defined as the ratio of etch rates

$$S = V_t/V_b - 1\ , \tag{6.7}$$

which is thought to be a function of the restricted energy loss, REL, of the incident charged particle [19]. REL is defined as the energy loss rate along the track core region near the particle trajectory. Using the measurable parameters, that is the cone length, L, of the etch pit and amount of bulk etch, B, the track sensitivity is obtained as

$$S = L/B - 1. \tag{6.8}$$

A damaged surface, such as an ion track, scratches, dust, dirt, etc., acts as a scattering centre that absorbs, reflects and scatters any incident light. How the light is scattered at a single etch crater depends strongly on the form of the crater as is shown, for example, in Fig. 6.4(b). Cone-shaped tracks will appear almost black since the light is not scattered back to source while, with bowl-shaped ends, tracks will develop a very bright spot in the middle which increases with increasing bowl-diameter. Tracks that have no cone walls left and consist entirely of a rounded bowl appear light and with a weak contrast with respect to an unperturbed surface.

In the experiments presented in this work, 6N NaOH solution was used at $\sim 80^0$C as an etchant. Etching times were $\sim$3 h for ions and protons analysis. After etching, charged particle tracks become visible, as is illustrated in Fig. 6.5 (a). By using an automated scanning and high-precision optical microscope, the traces can be analysed with single impact resolution, as shown in Fig. 6.5(b) and Fig. 6.5(c) for both protons and carbon ions, respectively. This system identifies and records the pits positions, lengths and other information on the pits. This information depends on particle species, its energy and angle of incidence and etching parameters.

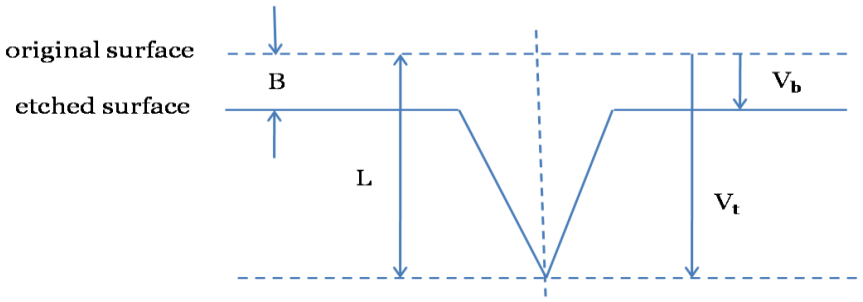

(a)

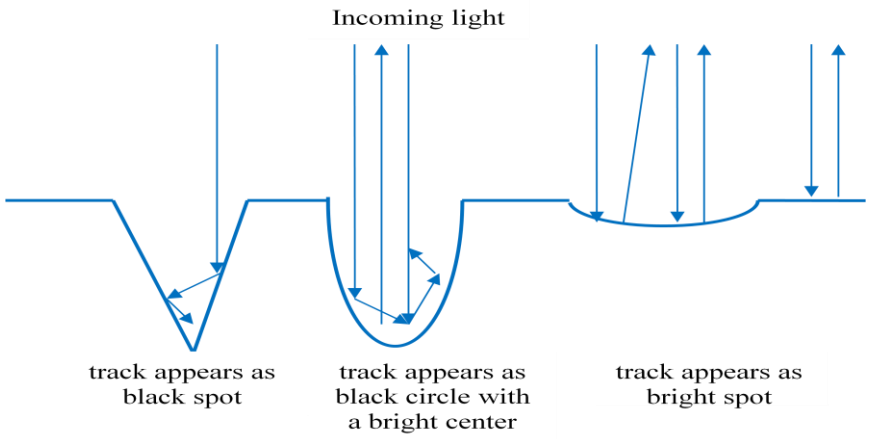

(b)

Figure 6.4: Schematic cross-sectional view of etch pit geometry. (a) An etch pit grows along the track with length L at etch rate V_t for the amount of bulk etch B at rate V_b. (b) Different track shapes show different appearances depending on how they reflect the light.

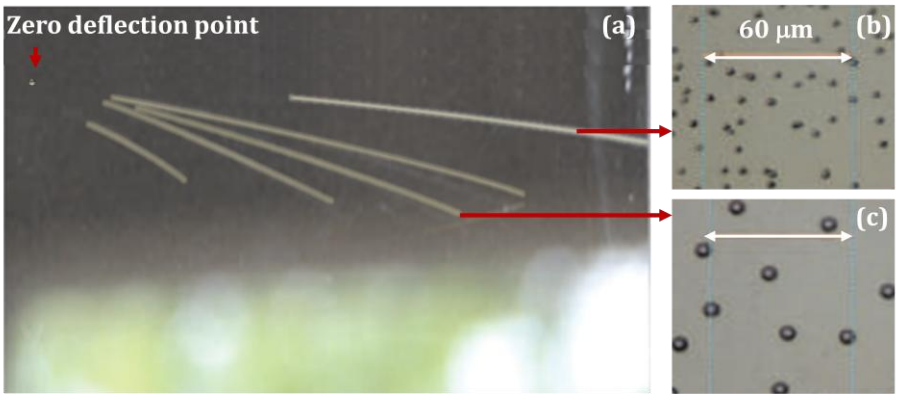

Figure 6.5: (a) Irradiated and processed piece of CR39 showing several ion traces in addition to the strong proton track (long top trace). Microscope image showing the difference between ion and proton tracks which is shown in (b) for the case of protons and in (c) for carbon ions.

The experimental data is analysed further after the scan is completed. For processing the scanning data the Software Package PlotIt was used and the Thomson parabola images obtained. The individual parabolic traces are used to determine the energy spectra. A particular example of a scanned CR39 track detector measuring protons and ions emitted from a hydride copper target is presented in Fig. 6.6.

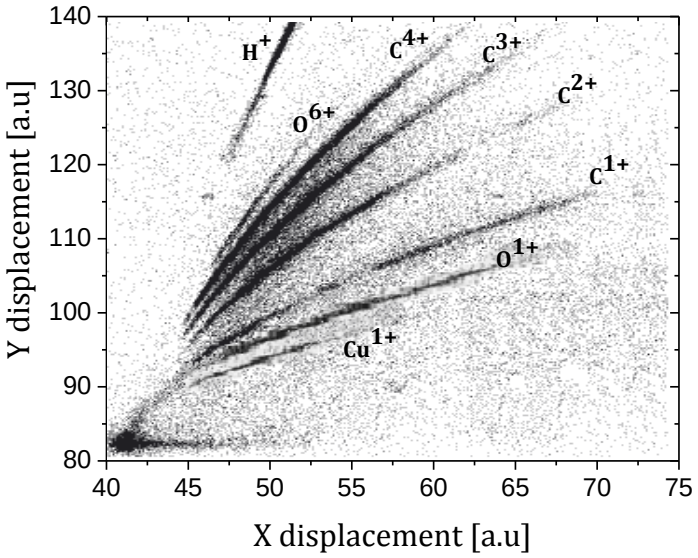

Figure 6.6: Scanned CR39 image for copper doped with hydrogen. Different ion species (Cu^{1+} , O^{1+} , C^{1+}, C^{2+}, C^{3+}, C^{4+} , O^{6+} and protons) are clearly visible and have been labelled. X-axis depends on ion energy and Y-axis depends on charge to mass ratio.

6.3 Experimental results

In this section the results of experiments obtained from the hydride and non hydride targets (gold, copper and titanium) are presented and the important trends highlighted. The protons and carbon ions peak yields without ablation are measured for all target metals and are compared with the measured protons and carbon ion peak yields with a 10 second ablation time. Also, to determine the enhancement of the proton and ion yields from hydride targets, their yields are compared with those of normal targets with and without a 10 second ablation period.

The spectral shape of each proton and ion energy distribution is generally continuous up to the cut-off energy, in agreement with the observations in similar experiments [20, 21].

6.3.1 Proton production with no ablation and with 10 second ablation

Before presenting the results of accelerated protons, the question of where the accelerated protons come from will be investigated. Measurements have shown that the accelerated protons result from contaminantes present on the target surface. As an example, the composition for a gold target can be a 12 Å thick layer consisting of 27% gold, 60.5% hydrocarbons (CH_2), and 12.2% water vapour (H_2O) [22]. Protons can also originate from prepared layers [8] or from the hydrogen implantation layers that are used here.

As will be shown next, when the high intensity laser is incident on the front surface of a foil target, it will always accelerate protons, independent of the target material type. The number of protons accelerated without ablation is expected to be reasonably high due to organic matter contaminants (hydrocarbons) present on the surface. After ablation, the number of these protons is expected to be lower due to the reduction of matter contaminants on the surface [8, 23, 24]. This effect has clearly been seen in the experiment using gold and copper targets for both cases with and without diffused hydrogen through the target, as shown in Fig. 6.7. The proton spectra also show an increase in the proton maximum energy with decreasing ablation time for all gold and copper targets.

For both cases with and without diffused hydrogen through the target, it has been observed that the maximum proton energy is 2.2 MeV from the hydride gold target and 1.9 MeV from the hydride copper target. The proton yield from the gold was about a factor of two lower than the proton yield from the copper.

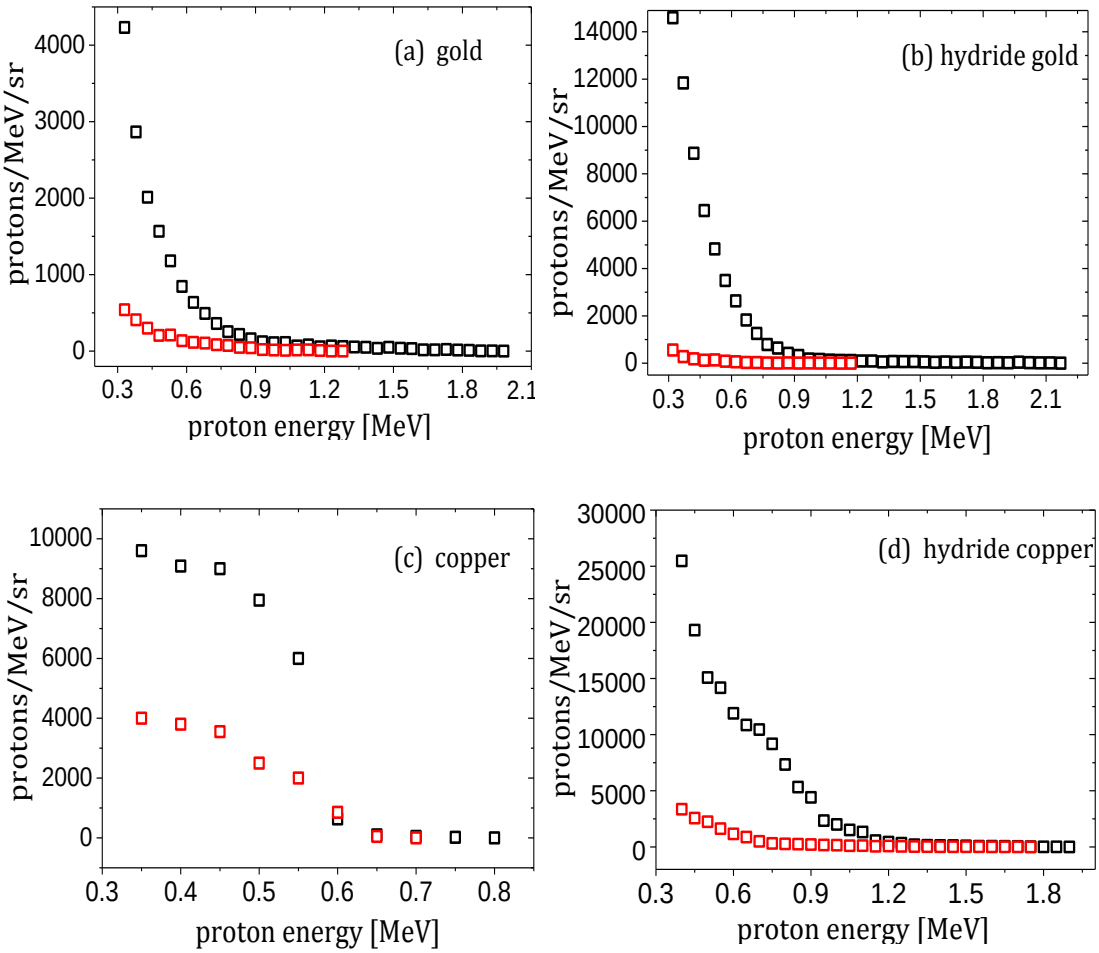

Figure 6.7: Proton spectra from the targets and hydride targets. The black open squares represent the proton production without ablation and the red open squares represent proton production with 10 s ablation. The spectra from gold and hydride gold foils are illustrated by (a,b) and the spectra from copper and hydride copper foils are illustrated by (c,d).

The effect of ablation on the number and energy of protons has been investigated for the titanium target with and without diffused hydrogen through it. From the data presented in Fig. 6.8, it can be noticed that without diffused hydrogen through the target, the number of protons and their energy decreases when contaminants on the surface are removed by 10 second period of ablation, as expected and as observed in the gold and copper targets, but with diffused hydrogen through the titanium, a decrease in the yield is not observed. The proton yield from hydride titanium did not exhibit the expected decrease while

the proton yield from hydride gold and copper did, suggesting that the effect could be related to specific properties of the metals.

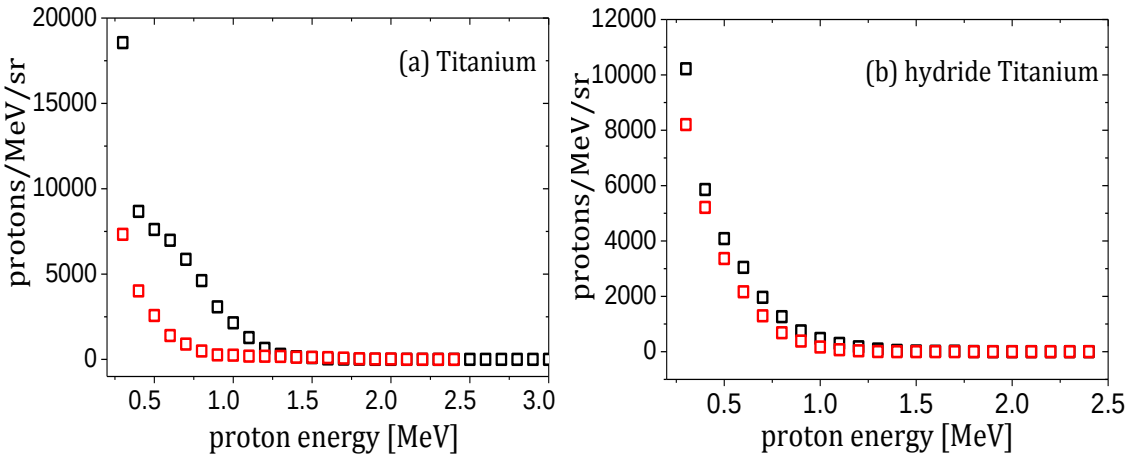

Figure 6.8: Proton spectra from the targets for two different cases, with and without ablation. The black open squares represent proton production without ablation while the red open squares represent proton production with 10 second ablation. (a) Shows proton spectra from titanium and (b) shows proton spectra from hydride titanium.

6.3.2 Proton production from hydride foils

To determine whether implantation of hydrogen results in an enhancement of the proton yield, yields from all targets with diffused hydrogen through them have been compared with the proton yields from normal targets.

The comparison between the proton production from hydride targets (gold, copper and titanium) and proton production from normal targets without ablation is shown in Fig. 6.9. In this figure, hydride gold and copper targets without ablation have been shown to give an increase both in proton yield and maximum energy [Fig. 6.9 (a, b)]. Both hydride gold and copper targets produce a proton yield of approximately 3 times higher than proton yield from normal targets. Hydride copper produces proton energy of approximately 2 times higher than proton energy from normal copper target while no proton energy increase from hydride gold target has been observed.

For the same condition, the titanium targets showed an inversion of the proton yields and energy behaviour [Fig. 6.9 (c)]. Normal titanium targets

produce proton yields and proton energy of approximately 2 times and 1.3, respectively, higher than proton yields and proton energies from hydride titanium.

The considerably increased proton yield in the hydride gold and copper targets indicates that the implanted protons are not affecting the structure of the metal and they are easily realised. While the reduced protons yield in the hydride titanium indicates that either the implanted protons are affecting the metal structure or are binding to it in a manner not previously realised.

With the addition of laser ablation on the rear surface of the targets, the expected overall increase in proton yield from hydride targets is not observed as shown in Fig. 6.10 (a, b). The figure shows that the yield from the hydride gold and copper is now smaller than from the normal targets. Here the reduction in the proton yield from hydride targets is not significant compared with the difference between the yields from the hydride and normal targets without ablation. This could suggest that implanted hydrogen is fairly evenly distributed within the target and more abundant on the surface than the bulk structure of the target.

Again, in contrast to the gold and copper targets, the titanium target showed an inversion of the proton yields after an ablation period, such that the hydride targets produced more protons than their normal equivalents. The maximum proton energy measured in the experiment was about 3 MeV which was obtained from normal titanium without ablation.

Taking all the results into account, it is clear that hydrogen implantation in targets can lead to an increase in the proton yield and maximum energy but it is not the case for all target materials. Table 6.1 presents a summary of the proton production results. There is a strong correlation between the gold and copper targets. Both hydride targets showing an increase in proton yield of about a factor of 3. Titanium shows no similarities with the gold and copper targets and, for the hydride target, the proton yield is reduced.

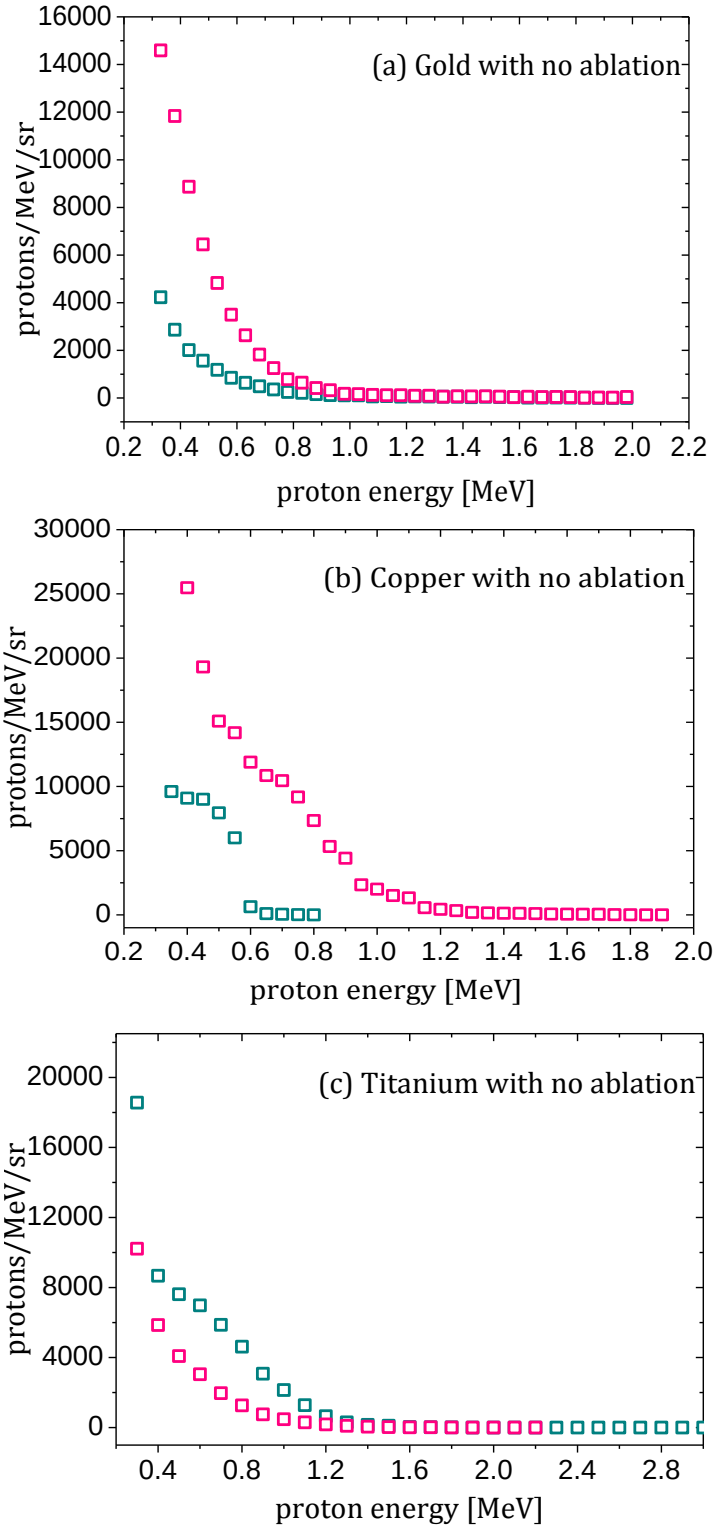

Figure 6.9: The difference between proton yield and energy from the targets with diffused hydrogen through them and from normal targets without ablation. The pink open squares represent proton production from hydride targets and the blue open squares represent proton production from normal targets. The proton spectra are from (a) gold, (b) copper and (c) titanium, respectively.

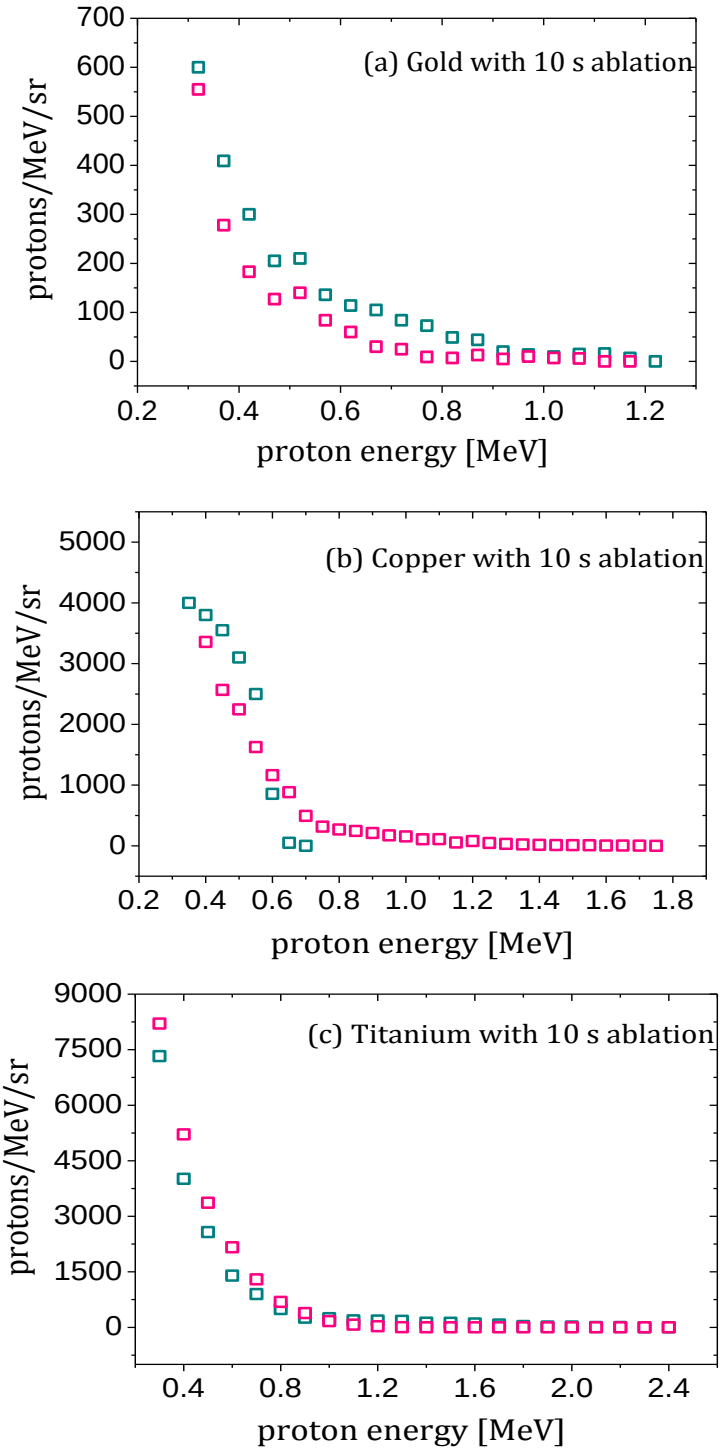

Figure 6.10: The difference between proton yield and energy from the targets with diffused hydrogen through them compared with normal targets with 10 second ablation. The pink open squares represent proton production from hydride targets and the blue open squares represent proton production from normal targets. Proton spectra from (a) gold, (b) copper and (c) titanium, respectively.

Target	proton yield (no ablation) [protons/MeV/sr]	proton energy (no ablation) [protons/MeV/sr]	proton yield (10 s ablation) [protons/MeV/sr]	proton energy (10 s ablation) [MeV]
gold	4230 ± 60	1.9	600 ± 60	1.28
hydride gold	14600 ± 120	2.17	560 ± 40	1.17
copper	9600 ± 100	0.8	4000 ± 120	0.7
hydride copper	25500 ± 150	1.9	3360 ± 100	1.75
titanium	18500 ± 140	3	7330 ± 90	2.4
hydride titanium	10000 ± 100	2.2	8200 ± 90	2.4

Table 6.1: Proton peak yield measured from all targets metals used in the experiment. The uncertainties given are the standard deviations.

This observation could be interpreted by considering that the higher mass number metals could be less porous for the hydrogen to move through, thus preventing it from penetrating into the bulk material and leaving high numbers of protons on the surface. Data from the gold and copper targets indicate that this could be a reasonable explanation for the increase in yield of protons from hydride targets. Here it may be that the mass number plays an important role for proton emission from the target. The crucial mass number where the proton yields from hydride and normal targets are the same should be seen in one of the metals with masses between titanium (Z=22) and copper (Z=29). Metals such as iron, cobalt and nickel would need to be tested to support this explanation.

6.3.3 Ion production from hydride foils

Throughout the experiment, due to their relatively large charge-to-mass ratio, protons are accelerated more efficiently and outrun other ion species thereby screening the accelerating fields for the latter. By removing the hydrogenous surface contaminants, the field coupling to heavier ions could

therefore be increased, enabling these ions to be efficiently accelerated. Using the Thomson-parabola detector, energy spectra of different ion species and charge states have been obtained and the most common of these are carbon ions due to the uncontrollable organic matter contamination on the target surfaces. Thus, carbon ions spectra were obtained from all targets with and without hydrogen.

Without ablation on the rear surface of the target, four carbon ion charge states were visible in CR39, corresponding to the C^{+1} to C^{+4} charge states. The four carbon ion charge states are observed from all hydride and normal targets. As with the proton spectra, when studying the carbon ions emerging from the hydride gold without ablation, it is possible to see a clear increase in the yield and maximum energy of carbon ions emitted from gold with diffused hydrogen. This increase is clearly visible when comparing Fig. 6.11(a) and (b) for hydride and normal gold respectively. As an example from these figures, it is clear that hydride gold has a carbon C^{+4} ion yield approaching 6 times that of the normal gold target and extending up to twice the energy.

The copper target again behaves similarly to the gold target and a larger number and higher energy ion species are observed from the hydride copper, as presented in Fig. 6.11(c) and (d). This observation confirms that hydrogen diffused through the target has a significant effect on the yield and energy of ions.

Figure 6.12(a, b) shows the carbon ion spectra with charge states 1+ to 4+ for both the natural and hydride titanium targets. Again, the titanium target shows no similarities to the gold and copper targets. Normal titanium shows a larger number and higher energy carbon ion species. By comparing carbon C^{+4} ion yields in Fig. 6.12(a, b), it can be seen that normal titanium has a carbon C^{+4} ion yield approaching 5 times that of the hydride target and extending up to one and a half times the energy.

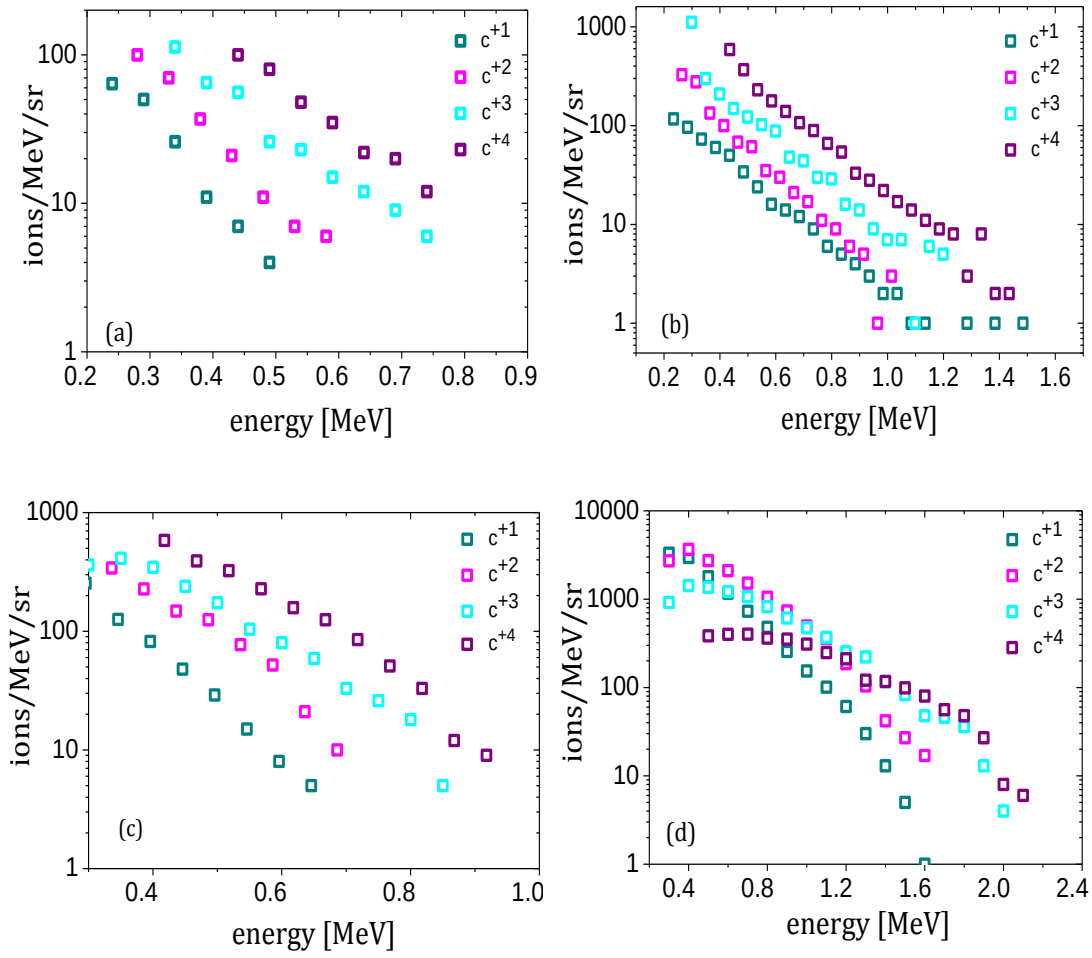

Figure 6.11: Carbon ion spectra with charge states 1+ to 4+ emitted from gold and copper foils with and without diffused hydrogen through them without ablation. (a,b) show carbon ions from gold and hydride gold respectively and (c,d) show carbon ions from copper and hydride copper respectively.

After 10 second ablation, the carbon ion spectra with charge states 1+ to 4+ for both the copper and hydride copper targets were visible [Fig. 6.13(a, b)]. From the data of carbon ions emitted from normal copper targets with and without 10 s ablation, it can be seen that the yield and maximum energy of carbon ions increase with increasing ablation time, as expected after the removal of the organic matter from the surface. This increase in both the yield and the energy is clearly visible when comparing Fig. 6.11(c) and Fig. 6.13(a), where the highest charge state (carbon C^{+4}) yield increases by a factor of ~2 and the energy increases by factor 1.5 from a copper target after 10 second ablation.

This could be interpreted by protons screening the ions from the accelerating field. By removing the contamination layer by ablation, efficient acceleration of heavier ions is facilitated [7, 8, 25].

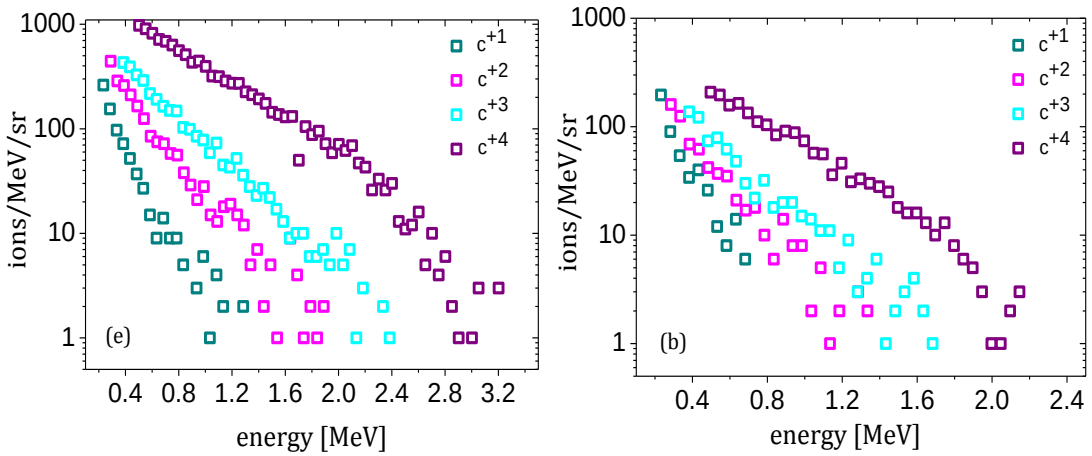

Figure 6.12: Carbon ion spectra with charge states 1+ to 4+ emitted from titanium foils with and without diffused hydrogen through them without ablation. (a) shows carbon ions from titanium and (b) shows carbon ions from hydride titanium.

Also, in Fig. 6.13(a, b), it can be clearly seen that for the hydride copper target, the increased yield and maximum energy are observed in carbon ions. This enhancement is evident by comparing the spectra in Fig. 6.13(a) and (b). From Fig. 6.13(b), it is interesting to note that for hydride copper foil there is clearly a change in the spectral shape of the ions at low energy and this change increases with increasing the ion charge as shown for the spectra C^{+3} and C^{+4}. This could be due to the fact that, for a hydride copper target, there is a difference between the mechanism to accelerate higher charge ions at low energy and the mechanism to accelerate higher charge ions at high energy. At present this explanation is not very clear and would require further experimental work on materials physics, which is out with the scope of this thesis.

In contrast to the copper target, ae different behaviour was noticed for carbon ion spectra emitted from hydride titanium, and again there is an increase of the yield and the energy of carbon ions emitted from normal titanium compared with the yield and the energy of carbon ions emitted from

hydride titanium. Table 6.2 shows a summary of the results of yields and energies of carbon ions produced from the applied targets.

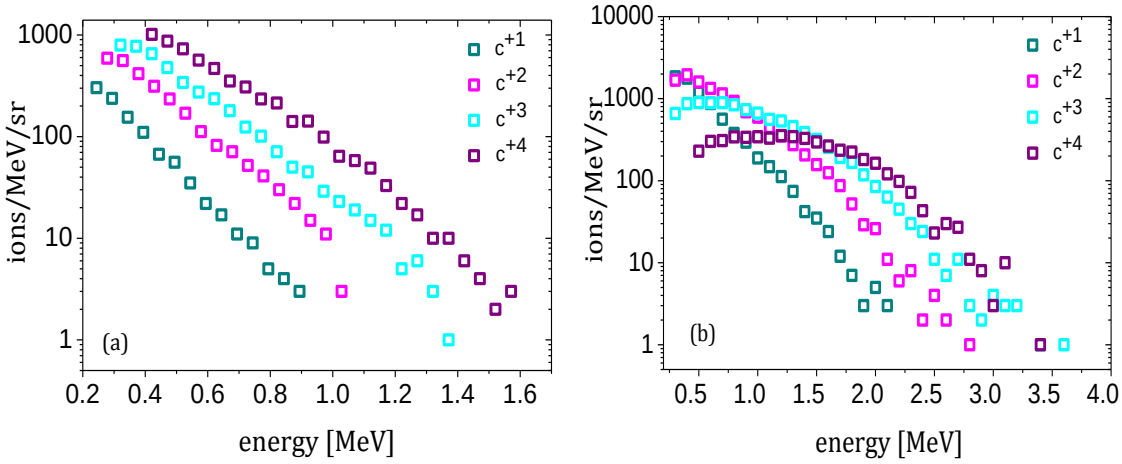

Figure 6.13: Carbon ion spectra with charge states 1+ to 4+ emitted from copper with 10 second ablation. Carbon ions from (a) copper and (b) hydride copper.

Target	Highest carbon ion yield without ablation [ions/MeV/sr]	Highest carbon ion yield with 10 second ablation [ions/MeV/sr]
gold	100±10	-
hydride gold	590±30	-
copper	580±30	1000± 70
hydride copper	3700± 100	1800± 100
titanium	1000±40	400± 30
hydride titanium	200± 25	40± 8

Table 6.2: Highest carbon ion yield measured from all targets metals used in the experiment. No carbon ions were measured from gold and hydride gold after 10 second ablation. The uncertainties given are the standard deviations.

In this experiment, measured copper ions show a higher yield observed from the hydride target compared with the copper ions yield observed from the normal target. The measured titanium ions show little difference in total yield

between the normal and hydride targets. Gold ions were not observed due to insufficient energy per pulse to ionise and accelerate them.

Analysing all the results of the carbon ions produced from all targets indicates that the hydride gold target has a thicker contaminant layer than normal gold, which produces a lower carbon ion yield. Comparing the proton yields from gold and copper targets after 10 second ablation indicates that the implanted protons and contaminant layers on the gold are much thinner than on copper. It may be for this reason that there were no observable carbon ions from both gold and hydride gold targets after 10 second ablation.

The hydride copper has an increased carbon ion yield over its normal target and this increase is still present after 10 second ablation. This indicates a higher carbon ion concentration in the contaminant layer. The titanium has increased carbon ion yield over its hydride target with and without 10 second ablation, which indicates a lower carbon ion concentration in the contaminant layer in this case.

6.4 Conclusions

It has been demonstrated from these experiments (the first of their kind), that changing the target surface properties by diffusing hydrogen into the metal foil leads to a significant increase in the yield and maximum energy of protons and ions, but these accelerated protons and ions depend strongly on the target properties.

Measurements from the copper and gold targets show a strong correlation, both hydride targets show an increase in the maximum energy and yield of protons and ions. Titanium shows no similarities with the gold and copper targets. The yield and energy of protons and ions decrease for the hydride titanium target.

The overall effect of the presence of the hydrogen in the metals remains unclear, though it is clear that it is not as simple as was originally believed. The data in these experiments should be extended with future experiments to

investigate the effect of hydride targetry in the laser proton acceleration process in more depth.

References

1. H. Kishimura, H. Morishita, Y.H. Okano, Y. Okano, Y. Hironaka, K. Kondo, K.G. Nakamura, Y. Oishi, and K. Nemoto, *Enhanced generation of fast protons from a polymer-coated metal foil by a femtosecond intense laser field.* Applied Physics Letters, 2004. **85**(14): p. 2736-2738.
2. S.M. Pfotenhauer, O. Jackel, A. Sachtleben, J. Polz, W. Ziegler, H.P. Schlenvoigt, K.U. Amthor, M.C. Kaluza, K.W.D. Ledingham, R. Sauerbrey, P. Gibbon, A.P.L. Robinson, and H. Schwoerer, *Spectral shaping of laser generated proton beams.* New Journal of Physics, 2008. **10**(3): p. 033034.
3. H. Schwoerer, S. Pfotenhauer, O. Jackel, K.U. Amthor, B. Liesfeld, W. Ziegler, R. Sauerbrey, K.W.D. Ledingham, and T. Esirkepov, *Laser-plasma acceleration of quasi-monoenergetic protons from microstructured targets.* Nature, 2006. **439**(7075): p. 445-448.
4. J. Fuchs, P. Antici, E. Humieres, E. Lefebvre, M. Borghesi, E. Brambrink, C.A. Cecchetti, M. Kaluza, V. Malka, M. Manclossi, S. Meyroneinc, P. Mora, J. Schreiber, T. Toncian, H. Pepin, and P. Audebert, *Laser-driven proton scaling laws and new paths towards energy increase.* Nature, 2006. **2**(1): p. 48-54.
5. S.A. Gaillard, K.A. Flippo, M.E. Lowenstern, J.E. Mucino, J.M. Rassuchine, D.C. Gautier, J. Workman, and T.E. Cowan, *Proton acceleration from ultrahigh-intensity short-pulse laser-matter interactions with Cu micro-cone targets at an intrinsic ~10^{-8} contrast.* Journal of Physics, 2010. **244**(2): p. 022034.
6. V.S. Khoroshkov and E.I. Minakova, *Proton beams in radiotherapy.* European Journal of Physics, 1998. **19**(6): p. 523–536.
7. P. McKenna, K.W.D. Ledingham, J.M. Yang, L. Robson, T. McCanny, S. Shimizu, R.J. Clarke, D. Neely, K. Spohr, R. Chapman, R.P. Singhal, K. Krushelnick, M.S. Wei, and P.A. Norreys, *Characterization of proton and*

heavier ion acceleration in ultrahigh-intensity laser interactions with heated target foils. Physical Review E, 2004. **70**(3): p. 036405.

8. M. Hegelich, S. Karsch, G. Pretzler, D. Habs, K. Witte, W. Guenther, M. Allen, A. Blazevic, J. Fuchs, J.C. Gauthier, M. Geissel, P. Audebert, T. Cowan, and M. Roth, *MeV Ion Jets from Short-Pulse-Laser Interaction with Thin Foils.* Physical Review Letters, 2002. **89**(8): p. 085002.
9. S.P. Hatchett, C.G. Brown, T.E. Cowan, E.A. Henry, J.S. Johnson, M.H. Key, J.A. Koch, A.B. Langdon, B.F. Lasinski, R.W. Lee, A.J. Mackinnon, D.M. Pennington, M.D. Perry, T.W. Phillips, M. Roth, T.C. Sangster, M.S. Singh, R.A. Snavely, M.A. Stoyer, S.C. Wilks, and K. Yasuike, *Electron, photon, and ion beams from the relativistic interaction of Petawatt laser pulses with solid targets.* Physics of Plasmas, 2000. **7**(5): p. 2076-2082.
10. E.L. Clark, K. Krushelnick, M. Zepf, F.N. Beg, M. Tatarakis, A. Machacek, M.I.K. Santala, I. Watts, P.A. Norreys, and A.E. Dangor, *Energetic Heavy-Ion and Proton Generation from Ultraintense Laser-Plasma Interactions with Solids.* Physical Review Letters, 2000. **85**(8): p. 1654-1657.
11. M. Roth, T.E. Cowan, M.H. Key, S.P. Hatchett, C. Brown, W. Fountain, J. Johnson, D.M. Pennington, R.A. Snavely, S.C. Wilks, K. Yasuike, H. Ruhl, F. Pegoraro, S.V. Bulanov, E.M. Campbell, M.D. Perry, and H. Powell, *Fast Ignition by Intense Laser-Accelerated Proton Beams.* Physical Review Letters, 2001. **86**(3): p. 436-439.
12. J.J. Thomson, *Bakerian Lecture: Rays of Positive Electricity.* Proceedings of the Royal Society of London. Series A, 1913. **89**(607): p. 1-20.
13. M. Zepf, E.L. Clark, F.N. Beg, R.J. Clarke, A.E. Dangor, A. Gopal, K. Krushelnick, P.A. Norreys, M. Tatarakis, U. Wagner, and M.S. Wei, *Proton Acceleration from High-Intensity Laser Interactions with Thin Foil Targets.* Physical Review Letters, 2003. **90**(6): p. 064801.
14. M. Borghesi, S.V. Bulanov, T.Z. Esirkepov, S. Fritzler, S. Kar, T.V. Liseikina, V. Malka, F. Pegoraro, L. Romagnani, J.P. Rousseau, A. Schiavi, O. Willi, and A.V. Zayats, *Plasma Ion Evolution in the Wake of a High-Intensity Ultrashort Laser Pulse.* Physical Review Letters, 2005. **94**(19): p. 195003.

15. B.M. Hegelich, B.J. Albright, J. Cobble, K. Flippo, S. Letzring, M. Paffett, H. Ruhl, J. Schreiber, R.K. Schulze, and J.C. Fernandez, *Laser acceleration of quasi-monoenergetic MeV ion beams.* Nature, 2006. **439**(7075): p. 441-444.
16. D.L. Henshaw, *Applications of CR-39 nuclear track detector in medicine and technology.* Physics in Technology, 1982. **13**(6): p. 266-280.
17. H.A. Bethe, *Theory of the passage of rapid corpuscular rays through matter.* Annals of physics, 1930. **5**(4): p. 325.
18. A.H. Khayrat and S.A. Durrani, *Variation of alpha-particle track diameter in CR-39 as a function of residual energy and etching conditions.* Radiation Measurements, 1999. **30**(1): p. 15-18.
19. E.V. Benton and R.P. Henke, *Heavy particle range-energy relations for dielectric nuclear track detectors.* Nuclear Instruments and Methods, 1969. **67**(1): p. 87-92.
20. R.A. Snavely, M.H. Key, S.P. Hatchett, T.E. Cowan, M. Roth, T.W. Phillips, M.A. Stoyer, E.A. Henry, T.C. Sangster, M.S. Singh, S.C. Wilks, A. MacKinnon, A. Offenberger, D.M. Pennington, K. Yasuike, A.B. Langdon, B.F. Lasinski, J. Johnson, M.D. Perry, and E.M. Campbell, *Intense High-Energy Proton Beams from Petawatt-Laser Irradiation of Solids.* Physical Review Letters, 2000. **85**(14): p. 2945-2948.
21. M. Roth, M. Allen, P. Audebert, A. Blazevic, E. Brambrink, T.E. Cowan, J. Fuchs, J.C. Gauthier, M. Geibel, M. Hegelich, S. Karsch, J.M. Vehn, H. Ruhl, T. Schlegel, and R.B. Stephens, *The generation of high-quality, intense ion beams by ultra-intense lasers.* Plasma Physics and Controlled Fusion, 2002. **44**(12): p. 99-108.
22. M. Allen, P.K. Patel, A. Mackinnon, D. Price, S. Wilks, and E. Morse, *Direct Experimental Evidence of Back-Surface Ion Acceleration from Laser-Irradiated Gold Foils.* Physical Review Letters, 2004. **93**(26): p. 265004.
23. A.J. Mackinnon, M. Borghesi, S. Hatchett, M.H. Key, P.K. Patel, H. Campbell, A. Schiavi, R. Snavely, S.C. Wilks, and O. Willi, *Effect of Plasma Scale*

Length on Multi-MeV Proton Production by Intense Laser Pulses. Physical Review Letters, 2001. **86**(9): p. 1769-1772.

24. M. Allen, Y. Sentoku, P. Audebert, A. Blazevic, T. Cowan, J. Fuchs, J.C. Gauthier, M. Geissel, M. Hegelich, S. Karsch, E. Morse, P.K. Patel, and M. Roth, *Proton spectra from ultraintense laser-plasma interaction with thin foils: Experiments, theory, and simulation.* Physics of Plasmas, 2003. **10**(8): p. 3283-3289.
25. B.M. Hegelich, B. Albright, P. Audebert, A. Blazevic, E. Brambrink, J. Cobble, T. Cowan, J. Fuchs, J.C. Gauthier, C. Gautier, M. Geissel, D. Habs, R. Johnson, S. Karsch, A. Kemp, S. Letzring, M. Roth, U. Schramm, J. Schreiber, K.J. Witte, and J.C. Fernandez, *Spectral properties of laser-accelerated mid-Z MeV/u ion beams.* Physics of Plasmas, 2005. **12**(5): p. 056314.

CHAPTER 7

Conclusions

The implementation of laser-plasma accelerators to drive sources of energetic particle (electrons, protons and ions), as well as the experimental investigation of the optimisation of the properties of these beams presented in this thesis, represent a significant contribution to the research in this field. It has been demonstrated that laser plasma accelerators are, in principle, capable of producing efficiently high quality beams of either relativistic electrons or fast ions.

After the important progress made for the field, the demonstration that monoenergetic particle beams from laser-plasma acceleration will open the door to a variety of applications as discussed in chapter 1. Some aspects of future work for the advancement of laser-driven particle acceleration will be discussed in this final chapter.

7.1 Summary of the main results

7.1.1 Electron acceleration

Many applications of laser systems require the pulses to be focused onto a small area in order to achieve a high intensity. In such cases the length over which the laser remains intense is fundamentally limited by diffraction. The output accelerated electrons of the laser-plasma interaction can be greatly enhanced if diffraction can be overcome by propagation in a capillary discharge waveguide. This optical guiding of the drive pulse allows acceleration over much longer distances possible and could allow the full potential of these ultra-high gradient accelerators to be realised. It has been theoretically predicted that

employing the tapered capillary discharge waveguide, as described in [1], yields increased energy gain in a single accelerator stage limited by dephasing and electron beams with multi-GeV energy could be produced for a wide range of possible applications.

In chapter 3, the production of straight and tapered hydrogen-filled capillary discharge waveguides suitable for LWFA experiments was described. Waveguides have been successfully tested for producing stable plasma. It has been demonstrated that femtosecond laser micromachining is an effective technique for producing channels and appropriate acceleration of the scanning machining laser enables the formation of a linear tapered capillary cross-section. A strong taper of mean diameter 305 μm to 183 μm over a length of 40 mm shows that the range of diameters used in LWFA can be met by this technique.

The development of the pulsed power supply unit to apply plasma channels in experiments was also described in Chapter 3. The new all solid-state pulser with TLT was successfully tested in a high voltage test chamber and it provided a stable breakdown performance, which was suitable for successful application in LWFA experiments. This is because such experiments require stable plasma for consistent synchronisation with the high-power laser pulses arriving at the waveguide entrance. Plasma generation in both straight and tapered capillaries has been shown to be comparable. Low temporal jitter in the current pulse was highly advantageous for these experiments where stable synchronisation between the formation of the plasma channel and the arrival time of the laser pulse is crucial. The temporal window for stable electron beam generation in the LWFA, for example, was as narrow as 25 ns. The pulser is relatively inexpensive, with the major costs being the high-voltage DC supply and the high voltage switch.

From the experimental data presented in chapter 4 for both straight and tapered capillaries, it can be concluded that the spectroscopic method using the Stark broadening effect is one of the most promising ways of measuring the density. The experimental data showed that the Stark broadening of the

hydrogen line H_α is a very successful diagnostic for plasma densities in the range of 10^{17}-10^{19} cm^{-3}. At these high densities, the plasma temperature can also be obtained by measuring the ratio of the two line intensities H_β/H_α. The data showed that the density increases with increasing gas pressure, while increasing the charging voltage increases the amount of light emitted, which is attributed to the increase of the temperature and not due to an increase of the plasma density. The density also increases linearly with decreased capillary diameter due to the higher current density at the smaller radius end of the capillary. From on-axis plasma density measurements, density profiles have reasonable parabolic fits, showing a radially increasing plasma density and centred on-axis with the density dropping off close to the walls. The experimental data using the tapered capillary show that measurements of the Stark-broadened Balmer line spectra confirm the existence of a longitudinal plasma density gradient, which is required in LWFA experiments exploiting a longitudinal plasma density gradient.

With a constant plasma density of $\sim 2.0 \times 10^{18}$ cm^{-3} and an internal diameter of 280 μm over a distance of 40 mm, the experimental data, obtained at laser intensity $\sim 10^{12}$ W/cm^2, show that guiding with an average energy transmission of (85 ± 5)% is suitable for LWFA driven by a laser intensity $\sim 10^{18}$ W/cm^2. The tapered capillary guided a laser pulse from an internal diameter of 325 μm to 274 μm along an increasing plasma density gradient from $(1.0 \pm 0.1) \times 10^{18}$ cm^{-3} and $(1.6 \pm 0.1) \times 10^{18}$ cm^{-3} for the wide and narrow ends respectively over 40 mm resulting in an average energy transmission of (80 ± 10)% (measured at low intensity). This transmission should increase to close to 100% at higher intensities [2, 3] where absorption due to inverse bremsstrahlung heating is reduced. However, at relativistic intensities, the transmission typically drops to ~30%-40% for ultra-short duration laser pulses due to driving a plasma wake [2-4]. Interferometric techniques that are used to measure the plasma density [5] require a square capillary cross-section with optical quality sides. However, capillaries that are usually used for energetic electron production in

LWFA experiments have circular cross-sections, which preclude the use of interferometric techniques. For this reason, the spectroscopic method using the Stark broadening effect is an alternative method for direct measurement of the capillary plasma density in LWFAs.

The experiments described in Chapter 5 aimed to investigate the tapered capillary as a medium for laser-wakefield acceleration in which electron beams with higher energy and narrower energy spread can be generated. The results from these experiments showed several important achievements. Firstly, the hydrogen-filled tapered capillary discharge waveguides has good quality guiding of laser pulses with peak input intensities of the order of 10^{18} W/cm^2, which is achieved for the first time, and some improved LWFA performance. This is also the longest distance over which laser pulses with this intensity have been guided in any type of waveguide. For example, the waveguide is a factor of 2.6 longer than in the hydrogen-filled capillary discharge straight waveguides experiments performed by [6].

The performance of the capillary discharge channel guided accelerator strongly depends on capillary diameter, discharge delay and peak power of the laser pulses. The tapered waveguide with the laser guided from the 280 μm large end to 230 μm small end enabled electrons to reach around 2.2 times higher energy than electrons accelerated by the same laser in a gas jet [7] and around 1.5 times higher energy than electrons accelerated by the same laser in straight capillary used here.

A comparison of the electron energy from all capillaries used in our experiment finds that the positive tapered capillary TP1 produces the electrons with the highest energy (320 MeV). There is uncertainty about the longitudinal position at which electron injection and acceleration takes place, given the complicated interaction between laser self-focusing and waveguiding effects. Hence, it remains unclear if the higher energies observed in the TP1 capillary (and the lower energies observed in the TN capillary) are influenced by the respective density tapers.

Higher electron energies could be reached in the positively tapered waveguide if the maximum electron energy is determined by dephasing, which also sets the maximum length of the accelerator. The dephasing also scales inversely with n_e, i.e., higher energies can be achieved by lowering the density since the dephasing increases. In the TP1 capillary, where the density increasing along the accelerator results in contracting the size of the wake, the effect is of continually advancing the dephasing point. This would lead to the electron being in the accelerating region for a longer distance than in the straight capillary, thereby increasing the maximum achievable electron energy.

These experiments are in agreement with other work that demonstrated no or very weak electron beam generation by using a 300 μm diameter capillary with laser peak power of 21 TW [2]. Through the statistical analysis for electron beam generation, regarding the electron energy, beam pointing and divergence, it was found that the control of the discharge delay and input energy were critical for stable operation. A change of less than 20 ns in the discharge delay and of less than about 15% in the input energy significantly affected capillary performance. From the comparison of characteristics of the electron bunches produced by straight and capillaries it is noted that:

Using a negative tapered capillary with the laser guided from the 206 μm small end to 270 μm large end, the highest beam quality is observed with low energy spread and low beam divergence with lower charge of electron beams. It was shown from this capillary that good shot-to-shot stability in the pointing of the electron beam was obtained with pointing angles 0.3-0.4 mrad in both horizontal and vertical axes.

The data indicate that the contribution of the waveguide for extending the interaction length is not fully understood. These trends are demonstrated by a strong dependence of electron acceleration on capillary entrance diameter. The poor performance of 300 μm diameter straight capillary and strong tapered capillary with entrance diameter of 305 μm might have come from a greater difference between the spot size of the input laser pulse and the matched spot size of the plasma channel.

From the scaling laws discussed in Section 2.2, the dephasing limited energy gain with laser parameters used in the experiments can be estimated for comparison with the measured energy gain obtained from S1. With laser intensity of 4.2×10^{18} Wcm^{-2} and a_0 = 1.4 (at the capillary plane with the self focusing effect), the dephasing limited energy gain shown in Eq. 2.47 $\Delta E_d[MeV]$ = 295.5 MeV using averaged plasma density of 5.7×10^{18} cm^{-3}. This is a factor 1.4 higher than observed maximum measured central energy (211 MeV), which indicates that an accurate estimation of full plasma channel properties has been performed.

Electron bunches generated from LWFA show excellent stability upon applying the negative tapered capillary. Finally it is clear that the potential of plasma accelerators is being realised and the tapered hydrogen-filled capillary discharge waveguide developed in this thesis is opening a path to compact accelerators up to multi-GeV level. It is hoped that in the near future the electron beams from these compact device could have a significant impact for applications such as free-electron lasers [8].

7.1.2 Proton and heavy ion acceleration

Experimental investigations of laser-driven acceleration of protons and heavy ions from thin solid foil targets with hydrogen implantation using high intensity (4.4×10^{19} W/cm^2) were studied and described in chapter 6. The effect of the ablation on the rear surface of the targets on the number of produced protons and heavy ions was also tested for all targets both with and without hydrogen implantation. The aim was to discover if it is possible to enhance the number the proton and heavy ions obtained from targets by proton implantation. Such an experiment is the first of its kind in this field.

It was believed that the resulting increase in the number of protons within the target would lead to a significant rise in yield of the accelerated proton [9]. The results obtained from this experiment indicate that the hydrogen implantation in the targets is not consistently applicable to all target materials and the behaviour of the protons within the metals is very difficult to fully

understand. Both gold and copper targets with higher mass number produced the predicted increase in the proton and heavy ion yield, but the titanium target with lower mass number produced unexpected yields of proton and heavy ions.

The hydrogen implantation in the targets has another important effect on the observed protons and ions energy, where the hydride gold and copper targets produced higher proton and ion energy than the energy of the observed proton and ion from normal targets. The observation from titanium, however, was not the same which should be further studied.

7.2 Future work

7.2.1 Time-resolved plasma density

For the study of the plasma channel density profile and the effects of the capillary geometry on the plasma density and temperature, presented in the chapter 4, an optical spectrometer was used with 1.1 nm resolution and 2 ms integration time. Since the integration time is much longer than the discharge duration (900 ns), it records the time-integrated plasma light spectrum. The time-integrated measurements presented are expected to yield a smaller plasma density than the actual one (when the laser pulse is present) because the peak of the discharge is averaged out. Indeed, the peak density is expected to be approximately double the time-averaged value. Although this technique still serves well for characterising the plasma density, in many cases such as in LWFA, the exact plasma density ideally needs to be resolved in time.

The time-resolved plasma density could be obtained by using a fast gated camera to record the amplitude of the light as a function of time for each wavelength setting. The time-dependent spectrum is then retrieved by grouping the data from each wavelength for each point in time [10].

7.2.2 Guiding with matched spot size

In a fully ionised plasma, optical guiding is affected by plasma density channels, relativistic self focusing, ponderomotive forces and plasma wave generation. When considering a non-relativistic laser pulse ($a_0 \ll 1$), its

propagation is affected only by the radial density profile of the plasma channel. Monomode guiding is achieved when the beam waist, is matched to the channel dimension as : $n_e = n_e(0) + \Delta n_e \left(\frac{r}{r_{ch}}\right)^2$. A mismatched beam waist leads to oscillations of the spot size along the propagation direction (beam scalloping) with an oscillation period $\pi^2 {w_M}^2/\lambda$.

When the beam intensity is high enough ($a_0 \geq 1$) (such as the intensity used for LWFA experiments presented in chapter 5) to change the mass of electrons through relativistic effects, self-focusing will occur when the laser power P exceeds the critical power P_c. If the plasma density is too low, the condition is not met and relativistic self-focusing is ineffective in preventing pulse diffraction. This certainly explains why no electrons were obtained for the widest capillaries (S2, TP2), where mismatching is stronger.

The improvement for the LWFA at Strathclyde will be to match the laser spot size to the plasma channel and higher laser transmission with high quality electron beam could be achieved.

7.2.3 Modified discharge for LWFA

The LWFA experiment was performed using the new high voltage pulser based on a transmission line transformer. It was successfully applied for the plasma density measurements and guiding experiments presented in chapter 4 and it also provides stable plasma for consistent synchronisation with the high-power laser pulses arriving in the waveguide but there are some difficulties regarding the use of this pulser. The main difficulty was that it produces a large amount of heat leading to damage/blocking of the capillary and its perspex housing. This could be the result of the relatively long current pulse duration (900 ns). Also the discharge could easily find paths outside the main channel, possibly due to the nature of the electrode polarity (large negative cathode potential, zero anode potential).

Refinement of the solid-state pulser for a floating point configuration (no ground with $-V/2$ cathode potential and $+V/2$ anode potential for a total V discharge potential) could be made to balance the electrode potentials while

maintaining very low jitter. This could reduce the probability of breakdown paths forming outside the main channel. Replacement high-voltage switches could allow a shorter pulse duration (~100-200 ns is sufficient) thus reducing heating effects.

7.2.4 Strongly tapered capillary

In longitudinally homogeneous plasma, the electron beam velocity is not matched with the accelerating phase of the wake, resulting in electrons out-running the accelerating phase of the wake. The energy gain in a laser plasma accelerator can be limited by this dephasing between the accelerating field of the plasma wave and the phase position of an electron beam in the wave. By allowing the plasma density to increase along the propagation path (using tapering of the plasma density) electron dephasing can be deferred, potentially increasing the energy gain.

Experimentally employing the positive tapered plasma channel (TP1), as described in chapter 5, yields increased energy gain in a single accelerator stage. If the energy gain is due to the taper, then the energy enhancement obtained (20-40%) for this capillary compares well with an analytical model [1] predicting ~100-300% gain for a linearly tapered accelerator when one compares the respective taper rates (0.33×10^{18} cm^{-3}/cm in this experiment, 3.5×10^{18} cm^{-3}/cm in the model).

Experimentally, therefore, a stronger positive tapered capillary, made by the micromachining manufacturing process [11], could be investigated. In general, more studies comparing straight and tapered capillaries at various densities are required to determine the energy gain. Micromachining controllability suggests that the final waveguide parameters can be tailor-made to suit particular applications and this may extend, in the future, to non-linear capillary structures for further enhancement of accelerator, where energy gain can be significantly increased and multi-GeV energies could be achieved.

7.2.5 Staging to higher electron energy

Another challenging technique for further increase in the electron energy to go well beyond 1 GeV is staged acceleration. A possible way to this could be injecting the electron beam from one laser-plasma accelerator into another. Using this technique, TeV energies in metres instead of tens of kilometres could be achieved. A proof-of-principle experiment on staged laser wakefield acceleration was performed for the first time at the Naval Research Laboratory [12]. Electrons of energy ~1 MeV from a 2 TW laser-driven nitrogen plasma were injected in a second laser plasma accelerator driven by a 10 TW pulse in a helium gas jet, and were accelerated to about 20 MeV in the second stage.

As a future study, a possible way to increase the energy obtained with laser wakefield acceleration using a so-called two-stage laser wakefield acceleration is described here. In this configuration, a two-stage LWFA separates the electron beam formation and acceleration processes and enables more efficient generation of higher quality electron beams at higher energies.

Using the ALPHA-X accelerator beam line (TOPS 30 TW, 10 Hz laser system), the scheme considered is drawn schematically in Fig. 7.1. As the first stage, consider that the laser pulse is focused into the entrance of a hydrogen-filled capillary discharge (diameter 300 mm, length 10 mm) as the first accelerator to generate an electron bunch of moderate kinetic energy (injector stage). For such an accelerator, consider a typical bunch generated in the bubble regime, assuming a mean energy of about 100 MeV and small absolute energy spread. The bunch from the first accelerator is injected into a second stage (gas cell which will be attached to the capillary) with self-guided laser wakefield-driven acceleration.

The distance between the accelerating stages is kept as short as possible to maintain the bunch quality. When the laser is tightly focused, it will be guided so that it will have a good effect on the wakefield in the channel. The bunch from the first accelerating stage is further accelerated in the self-guided laser wakefield where the accelerator length is chosen to be considerably longer with

a plasma of a lower density compared to that in the capillary. This leads to a bunch with a high mean energy and very low relative energy spread.

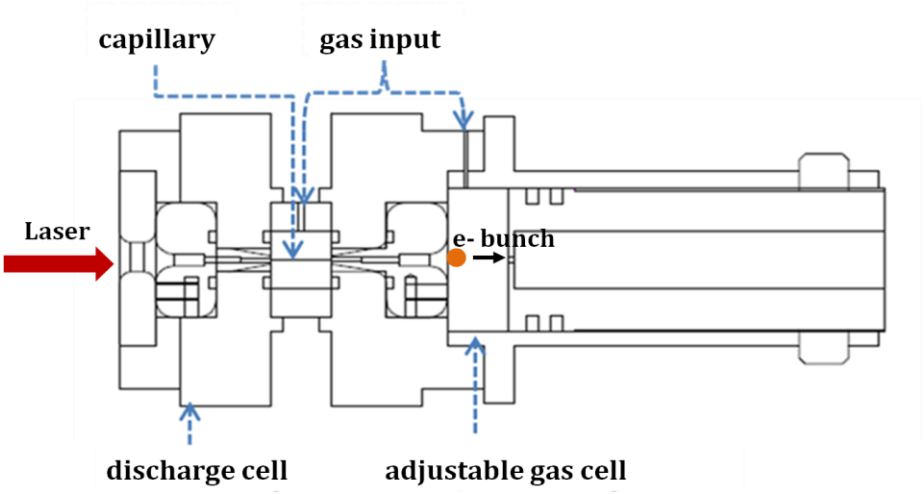

Figure 7.1: Scheme of a possible future experiment for a two-stage laser wakefield accelerator with a short distance between the stages.

7.2.6 Effect of implanted protons on proton yields

From the work carried out in the experiment described in chapter 6, it can be concluded that the presence of hydrogen in the metals remains unclear. Also, it is known that metals such as titanium are very porous. In order to determine this effect, it is necessary to acquire more data from similar experiments.

To prove that the mass is the crucial factor here, further experiments are needed that apply a range of targets to see the point where the proton yields from normal and hydride targets are the same. The target materials for investigation should have the critical mass number with masses between the lower mass tested target (titanium Z = 22) and higher mass tested target (copper Z = 29). To provide evidence, the protons and ions produced from targets such as iron, cobalt and nickel would need to be investigated.

7.2.7 Radiation generation

The electron beams produced by the laser-driven accelerator described in this thesis have a close-to-axis pointing angle (0.3-0.4 mrad in both axes), smallest pointing fluctuations (just 1.3 mrad in the horizontal axis) and low energy spread (1%).

These electron sources with more enhancements in the charge and energy could offer exciting prospects, such as sources of femtosecond radiation pulses ranging from terahertz frequencies to the X-ray region, offering the opportunity to develop very compact XFEL instruments.

It is clear that the potential of tapered plasma channel accelerators developed in this thesis is of key importance. In the near future, electrons and radiation from these compact devices could have a significant impact on the scientific and medical communities. Initial radiation studies could be carried out using the stable electron beams from the tapered capillary discharge waveguides as the source.

References

1. W. Rittershofer, C.B. Schroeder, E. Esarey, F.J. Gruner, and W.P. Leemans, *Tapered plasma channels to phase-lock accelerating and focusing forces in laser-plasma accelerators.* Physics of Plasmas, 2010. **17**(6): p. 063104.
2. W.P. Leemans, B. Nagler, A.J. Gonsalves, C. Toth, K. Nakamura, C.G.R. Geddes, E. Esarey, C.B. Schroeder, and S.M. Hooker, *GeV electron beams from a centimetre-scale accelerator.* Nature, 2006. **2**(10): p. 696-699.
3. T.P. Rowlands-Rees, C. Kamperidis, S. Kneip, A.J. Gonsalves, S.P.D. Mangles, J.G. Gallacher, E. Brunetti, T. Ibbotson, C.D. Murphy, P.S. Foster, M.J.V. Streeter, F. Budde, P.A. Norreys, D.A. Jaroszynski, K. Krushelnick, Z. Najmudin, and S.M. Hooker, *Laser-Driven Acceleration of Electrons in a Partially Ionized Plasma Channel.* Physical Review Letters, 2008. **100**(10): p. 105005.
4. T.P.A. Ibbotson, N. Bourgeois, T.P. Rowlands-Rees, L.S. Caballero, S.I. Bajlekov, P.A. Walker, S. Kneip, S.P.D. Mangles, S.R. Nagel, C.A.J. Palmer, N.

Delerue, G. Doucas, D. Urner, O. Chekhlov, R.J. Clarke, E. Divall, K. Ertel, P. Foster, S.J. Hawkes, C.J. Hooker, B. Parry, P.P. Rajeev, M.J.V. Streeter, and S.M. Hooker, *Investigation of the role of plasma channels as waveguides for laser-wakefield accelerators.* New Journal of Physics, 2010. **12**(4): p. 045008.

5. A.J. Gonsalves, T.P. Rowlands-Rees, B.H.P. Broks, J.J.A.M. van der Mullen, and S.M. Hooker, *Transverse Interferometry of a Hydrogen-Filled Capillary Discharge Waveguide.* Physical Review Letters, 2007. **98**(2): p. 025002.
6. S. Karsch, J. Osterhoff, A. Popp, T.P. Rowlands-Rees, Z. Major, M. Fuchs, B. Marx, R. Hörlein, K. Schmid, L. Veisz, S. Becker, U. Schramm, B. Hidding, G. Pretzler, D. Habs, F. Grüner, F. Krausz, and S.M. Hooker, *GeV-scale electron acceleration in a gas-filled capillary discharge waveguide.* New Journal of Physics, 2007. **9**(11): p. 415-425.
7. S.M. Wiggins, R.C. Issac, G.H. Welsh, E. Brunetti, R.P. Shanks, M.P. Anania, S. Cipiccia, G.G. Manahan, C. Aniculaesei, B. Ersfeld, M.R. Islam, R.T.L. Burgess, G. Vieux, W.A. Gillespie, A.M. MacLeod, S.B. van der Geer, M.J. de Loos, and D.A. Jaroszynski, *High quality electron beams from a laser wakefield accelerator.* Plasma Physics and Controlled Fusion, 2010. **52**(12): p. 124032.
8. D.A. Jaroszynski, R. Bingham, E. Brunetti, B. Ersfeld, J. Gallacher, B. van der Geer, R. Issac, S.P. Jamison, D. Jones, M. de Loos, A. Lyachev, V. Pavlov, A. Reitsma, Y. Saveliev, G. Vieux, and S.M. Wiggins, *Radiation sources based on laser–plasma interactions.* Philosophical Transactions of the Royal Society A: Mathematical, Physical and Engineering Sciences, 2006. **364**(1840): p. 689-710.
9. C.T. Zhou and X.T. He, *Intense laser-driven energetic proton beams from solid density targets.* Optics Letters, 2007. **32**(16): p. 2444-2446.
10. C. Hao, E. Kallos, P. Muggli, T.C. Katsouleas, and M.A. Gundersen, *A High-Density Hydrogen-Based Capillary Plasma Source for Particle-Beam-Driven Wakefield Accelerator Applications.* IEEE Transactions on Plasma Science 2009. **37**(3): p. 456-462.

11. S.M. Wiggins, M.P. Reijnders, S. Abuazoum, K. Hart, G.H. Welsh, R.C. Issac, D.R. Jones, and D.A. Jaroszynski, *Note: Femtosecond laser micromachining of straight and linearly tapered capillary discharge waveguides.* Review of Scientific Instruments, 2011. **82**(9): p. 096104.
12. D. Kaganovich, A. Ting, D.F. Gordon, R.F. Hubbard, T.G. Jones, A. Zigler, and P. Sprangle, *First demonstration of a staged all-optical laser wakefield acceleration.* Physics of Plasmas, 2005. **12**(10): p. 100702.